ADVANCED STEEL CONSTRUCTION

An International Journal

Volume 22 Number 5

***October* 2026**

CONTENTS

Technical Papers

Seismic Performance and Damage Evaluation of Irregular Steel Joints in Modern Chinese Traditional-Style Buildings with Blind Bolts
Zhan-Jing Wu, Jin-Shuang Dong, Yan Sui and Jia-Ning Wang

Application of Physics-Informed Neural Networks for Analysis Slender Steel Slope Piles
Yi Yang, Si-Wei Liu, Lei-Lei Liu and Wei-Hang Ouyang

Research on The Longitudinal Shear Behavior of Steel Grid-UHPC Composite Bridge Decks
Su-Mei Liu, Han Zhang, Peng Wang, Peng-Fei Ren and Han-Shan Ding

The Current Approach for The Design of Steel Pallet Racks
Marina Pastore, Jessey Lee, Rosario Montuori and Elide Nastri

Numerical Study on The Seismic Performance of Replaceable Energy-Dissipation Channel Steel Joints
Bi Zhang, Feng Song, Xue-Fei Sun and Bao-Wen Zhang

Experimental and Numerical Study on The Seismic Behaviour of Different Types of Strengthened Connections with Side Plates
Wang Zhang, Ai-Chao Lv, Qing-Qing Xiong, Ao-Hua Liu and Ya-Peng Wu

Study on Structural Damage Identification Using Single Sensor Data Based on Two-Dimensional Image and Convolutional Neural Network
Yu-Min He, Li Wang, Dan Luo, Nan Hu and Yi-De Chen

Mechanical Properties and Reliability Assessment of Post-Fire High-Strength Steel
Zi-Hao Xiong, Qing-Rui Deng, Ming-Yu Zhu, Yu-Feng Zhang and Pan Chen

The Load-Bearing Capacity of Latticed Column of Electric Bridge-Type Scaffold under Eccentric Compression
Li-Jun Ma, Hong-Bo Liu, Hai-Jiang Zhang, Yi-Fan Liu, Jian-Dong Li and Tian-Qi Hao

Mechanical Performance of Terminal Equipment in Ultra-High Voltage Substations
Le-Tian Wang, Ke Xin, Jun-Ming Zhang, Jun-Xiang Xu, Guan-Jun Chai and Hui-Huan Ma

Copyright © 2026 by :
The Hong Kong Institute of Steel Construction
Website: *http://www.hkisc.org*
ISSN 1816-112X
Science Citation Index Expanded, Materials Science Citation Index and ISI Alerting
Cover: Guangzhou Baiyun International Airport T3, China. Photo@ Chen Hui-Min
e-copy of IJASC is free to download at "www.ascjournal.com" in internet and mobile apps.

ADVANCED STEEL CONSTRUCTION

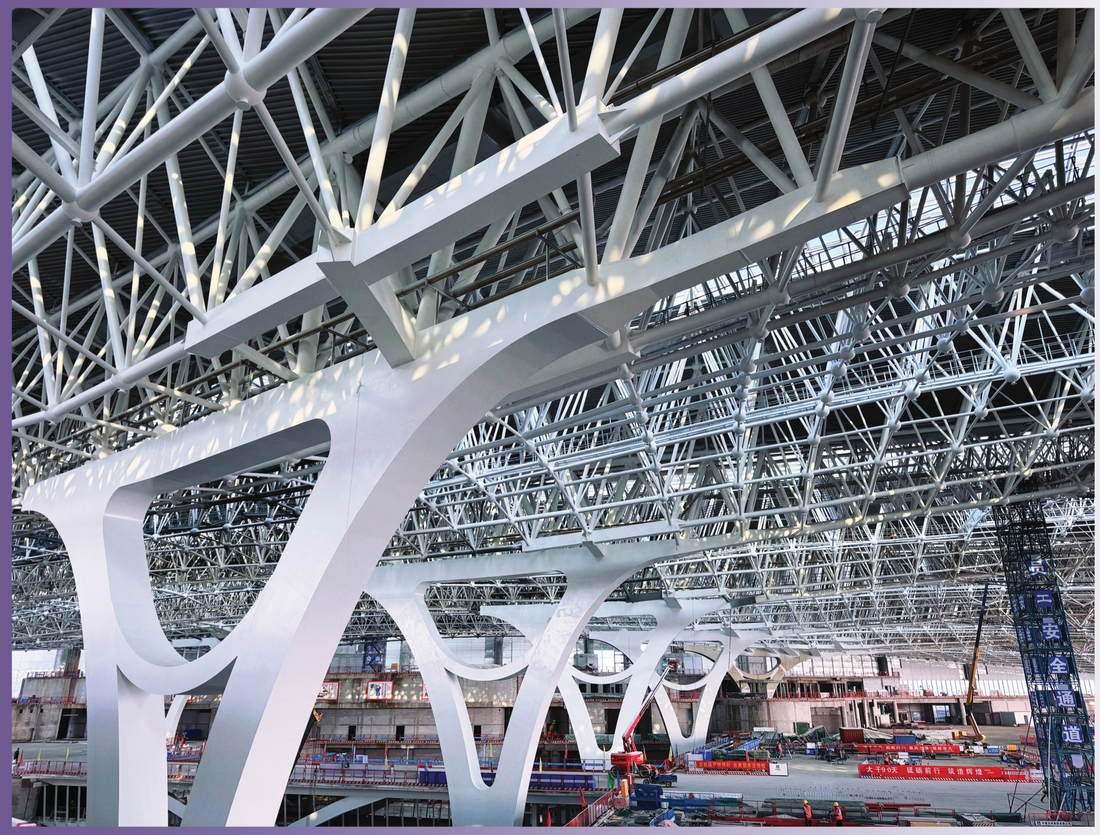
VOL.22, NO.5 (2026)

ADVANCED STEEL CONSTRUCTION

an International Journal

ISSN 1816-112X

Volume 22 Number 5 *October 2026*



Editors-in-Chief

S.L. Chan, *South China University of Technology, China*

W.F. Chen, *University of Hawaii at Manoa, USA*

R. Zandonini, *Trento University, Italy*

ISSN 1816-112X

Science Citation Index Expanded, Materials Science Citation Index and ISI Alerting

Advanced Steel Construction
an international journal

EDITORS-IN-CHIEF

Asian Pacific, African and organizing Editor
S.L. Chan
South China University of Technology, China

American Editor
W.F. Chen
Univ. of Hawaii at Manoa, USA

European Editor
R. Zandonini
Trento Univ., Italy

ASSOCIATE EDITORS

Y.P. Liu
South China University of Technology, China

S.W. Liu
The Hong Kong Polyt. Univ., Hong Kong, China

INTERNATIONAL EDITORIAL BOARD

F.G. Albermani
Central Queensland Univ., Australia

I. Burgess
Univ. of Sheffield, UK

F.S.K. Bijlaard
Delft Univ. of Technology, The Netherlands

M.A. Bradford
The Univ. of New South Wales, Australia

D. Camotim
Technical Univ. of Lisbon, Portugal

C.M. Chan
Hong Kong Univ. of Science & Technology, Hong Kong, China

T.H.T. Chan
Queensland Univ. of Technology, Australia

T.M. Chan
The Univ. of Hong Kong, Hong Kong, China

Z.H. Chen
Tianjin Univ., China

S.P. Chiew
Nanyang Technological Univ., Singapore

G.G. Deierlein
Stanford Univ., California, USA

L. Dezi
Univ. of Ancona, Italy

D. Dubina
The Politehnica Univ. of Timosoara, Romania

R. Greiner
Technical Univ. of Graz, Austria

L. Gardner
Imperial College of Science, Technology and Medicine, UK

Y. Goto
Nagoya Institute of Technology, Japan

L.H. Han
Tsinghua Univ. China

S. Herion
University of Karlsruhe, Germany

G.W.M. Ho
Ove Arup & Partners Hong Kong Ltd., Hong Kong, China

Todd A. Helwig
University of Texas at Austin, USA

B.A. Izzuddin
Imperial College of Science, Technology and Medicine, UK

J.P. Jaspart
Univ. of Liege, Belgium

S. A. Jayachandran
IIT Madras, Chennai, India

S.E. Kim
Sejong Univ., South Korea

S. Kitipornchai
The Univ., of Queensland, Australia

D. Lam
Univ. of Bradford, UK

H.F. Lam
City Univ. of Hong Kong, Hong Kong, China

G.C Li
Shenyang Jianzhu Univ., China

G.Q. Li
Tongji Univ., China

J.Y.R. Liew
National Univ. of Singapore, Singapore

E.M. Lui
Syracuse Univ., USA

Y.L. Mo
Univ. of Houston, USA

J.P. Muzeau
CUST, Clermont Ferrand, France

D.A. Nethercot
Imperial College of Science, Technology and Medicine, UK

Y.Q. Ni
The Hong Kong Polyt. Univ., Hong Kong, China

D.J. Oehlers
The Univ. of Adelaide, Australia

J.L. Peng
Yunlin Uni. of Science & Technology, Taiwan, China

K. Rasmussen
The Univ. of Sydney, Australia

J.M. Rotter
The Univ. of Edinburgh, UK

C. Scawthorn
Scawthorn Porter Associates, USA

P. Schaumann
Univ. of Hannover, Germany

Y.J. Shi
Tsinghua Univ., China

G.P. Shu
Southeast Univ. China

L. Simões da Silva
Department of Civil Engineering, University of Coimbra, Portugal

G. Shi
Tsinghua Univ., China

J.G. Teng
The Hong Kong Polyt. Univ., Hong Kong, China

G.S. Tong
Zhejiang Univ., China

K.C. Tsai
National Taiwan Univ., Taiwan, China

C.M. Uang
Univ. of California, USA

B. Uy
University of Western Sydney, Australia

M. Veljkovic
Univ. of Lulea, Sweden

F. Wald
Czech Technical Univ. in Prague, Czech

Y.C. Wang
The Univ. of Manchester, UK

B. Wu
South China University of Technology, China

Y.B. Wang
Tongji Univ., China

D. White
Georgia Institute of Technology, USA

Y.L. Xu
Southwest Jiaotong University, China

E. Yamaguchi
Kyushu Institute of Technology, Japan

Y.B. Yang
National Taiwan Univ., Taiwan, China

Y.Y. Yang
China Academy of Building Research, Beijing, China

B. Young
The Hong Kong Polyt. Univ., Hong Kong, China

X.L. Zhao
The Hong Kong Polyt. Univ., Hong Kong, China

X.H. Zhou
Chongqing University, China

S.Y. Zhu
The Hong Kong Polyt. Univ., Hong Kong, China

R.D. Ziemian
Bucknell Univ., USA

J.X. Zhao
South China University of Technology, China

Cover: Guangzhou Baiyun International Airport T3, China. Photo@ Chen Hui-Min
e-copy of IJASC is free to download at "www.ascjournal.com" in internet and mobile apps.

General Information
Advanced Steel Construction, an international journal

Aims and scope

The International Journal of Advanced Steel Construction provides a platform for the publication and rapid dissemination of original and up-to-date research and technological developments in steel construction, design and analysis. Scope of research papers published in this journal includes but is not limited to theoretical and experimental research on elements, assemblages, systems, material, design philosophy and codification, standards, fabrication, projects of innovative nature and computer techniques. The journal is specifically tailored to channel the exchange of technological know-how between researchers and practitioners. Contributions from all aspects related to the recent developments of advanced steel construction are welcome.

Disclaimer. No responsibility is assumed for any injury and / or damage to persons or property as a matter of products liability, negligence or otherwise, or from any use or operation of any methods, products, instructions or ideas contained in the material herein.

Subscription inquiries and change of address. Address all subscription inquiries and correspondence to Member Records, IJASC. Notify an address change as soon as possible. All communications should include both old and new addresses with zip codes and be accompanied by a mailing label from a recent issue. Allow six weeks for all changes to become effective.

The Hong Kong Institute of Steel Construction
HKISC
c/o Prof. SL Chan,
Unit 209B, Photonics Centre, No. 2 Science Park East Avenue,
Hong Kong Science Park, Shatin, N.T., Hong Kong, China.
Tel: 852- 3595 6150 Fax: 852- 3619 7238
Email: ceslchan@connect.polyu.hk Website: *http://www.hkisc.org/*
ISSN 1816-112X
Science Citation Index Expanded, Materials Science Citation Index and ISI Alerting
Copyright © 2026 by:
The Hong Kong Institute of Steel Construction.

ISSN 1816-112X

Science Citation Index Expanded, Materials Science Citation Index and ISI Alerting

EDITORS-IN-CHIEF

Asian Pacific, African and organizing Editor
S.L. Chan
South China University of Technology, China
Email: ceslchan@scut.edu.cn

American Editor
W.F. Chen
Univ. of Hawaii at Manoa, USA
Email: waifah@hawaii.edu

European Editor
R. Zandonini
Trento Univ., Italy
Email: riccardo.zandonini@ing.unitn.it

Advanced Steel Construction
an international journal

VOLUME 22 NUMBER 5 October 2026

Technical Papers

Seismic Performance and Damage Evaluation of Irregular Steel Joints in Modern Chinese Traditional-Style Buildings with Blind Bolts 483
Zhan-Jing Wu, Jin-Shuang Dong, Yan Sui and Jia-Ning Wang*

Application of Physics-Informed Neural Networks for Analysis Slender Steel Slope Piles 499
*Yi Yang, Si-Wei Liu, Lei-Lei Liu and Wei-Hang Ouyang**

Research on The Longitudinal Shear Behavior of Steel Grid-UHPC Composite Bridge Decks 508
Su-Mei Liu, Han Zhang, Peng Wang, Peng-Fei Ren and Han-Shan Ding*

The Current Approach for The Design of Steel Pallet Racks 522
Marina Pastore, Jessey Lee, Rosario Montuori and Elide Nastri*

Numerical Study on The Seismic Performance of Replaceable Energy-Dissipation Channel Steel Joints 538
*Bi Zhang, Feng Song, Xue-Fei Sun and Bao-Wen Zhang**

Experimental and Numerical Study on The Seismic Behaviour of Different Types of Strengthened Connections with Side Plates 547
Wang Zhang, Ai-Chao Lv, Qing-Qing Xiong, Ao-Hua Liu and Ya-Peng Wu*

Study on Structural Damage Identification Using Single Sensor Data Based on Two-Dimensional Image and Convolutional Neural Network 561
Yu-Min He, Li Wang, Dan Luo, Nan Hu and Yi-De Chen*

Mechanical Properties and Reliability Assessment of Post-Fire High-Strength Steel 572
*Zi-Hao Xiong, Qing-Rui Deng, Ming-Yu Zhu, Yu-Feng Zhang and Pan Chen**

The Load-Bearing Capacity of Latticed Column of Electric Bridge-Type Scaffold under Eccentric Compression 582
Li-Jun Ma, Hong-Bo Liu, Hai-Jiang Zhang, Yi-Fan Liu, Jian-Dong Li and Tian-Qi Hao*

Mechanical Performance of Terminal Equipment in Ultra-High Voltage Substations 597
*Le-Tian Wang, Ke Xin, Jun-Ming Zhang, Jun-Xiang Xu, Guan-Jun Chai and Hui-Huan Ma**

Advanced Steel Construction – Vol. 22 No. 5 (2026) 483–498
DOI:10.18057/IJASC.2026.22.5.1

SEISMIC PERFORMANCE AND DAMAGE EVALUATION OF IRREGULAR STEEL JOINTS IN MODERN CHINESE TRADITIONAL-STYLE BUILDINGS WITH BLIND BOLTS

Zhan-Jing Wu [1, 2], Jin-Shuang Dong [3, *], Yan Sui [4] and Jia-Ning Wang [2]

[1] *International Union Laboratory of New Civil Engineering Structure of Henan Province, Luoyang 471023, China*
[2] *School of Intelligent Construction and Civil Engineering, Luoyang Institute of Science and Technology, Luoyang 471023, China*
[3] *College of Civil Engineering and Architechture, Hainan Univerisitey, Haikou 570228, China*
[4] *College of Civil Engineering, Xi'an University of Architecture and Technology, Xi'an 710055, China*
** (Corresponding author: E-mail: mlcxll@163.com)*

ABSTRACT

Steel modern Chinese traditional-style buildings (MCTBs) commonly adopt fully welded connections. However, the use of circular hollow section (CHS) columns at beam-column joints, coupled with strict architectural aesthetic requirements, presents significant challenges for the application of conventional bolted connections. This issue represents a critical technical bottleneck that hinders the development of prefabricated construction in such buildings. To address this challenge, a novel prefabricated joint configuration based on blind bolt-T-stub assemblies was proposed. Four 1:2.6-scale specimens, including two single-beam column joints and two double-beam column joints, were fabricated and tested under low-cycle reversed loading to evaluate their seismic performance in terms of failure modes, hysteretic behavior, ductility, energy dissipation, and stiffness degradation. Furthermore, refined finite element (FEA) models were established to reproduce the experimental deformation patterns, stress distribution, and moment–rotation hysteresis behavior, including the relative slippage of the double-beam connectors. All specimens conformed to the strong-column weak-beam design principle, with damage primarily concentrated in the T-stub region. Compared to the single-beam column joints, the double-beam column joints demonstrated superior load-bearing capacity, enhanced energy dissipation, and greater safety redundancy. Moreover, increasing the T-stub thickness further improved the overall performance. Seismic damage was quantified using a modified Park-Ang damage model, confirming that the proposed prefabricated joint exhibits favorable seismic behavior and practical engineering applicability. The findings offer an effective structural solution for the industrialized seismic design of beam-column joints in steel MCTBs.

ARTICLE HISTORY

Received: 4 November 2025
Revised: 20 March 2026
Accepted: 31 March 2026

KEYWORDS

Steel modern Chinese traditional-style buildings;
Irregular steel joints;
Blind bolts;
Low-cycle reversed loading;
Seismic performance;
Damage evaluation

Copyright © 2026 by The Hong Kong Institute of Steel Construction. All rights reserved.

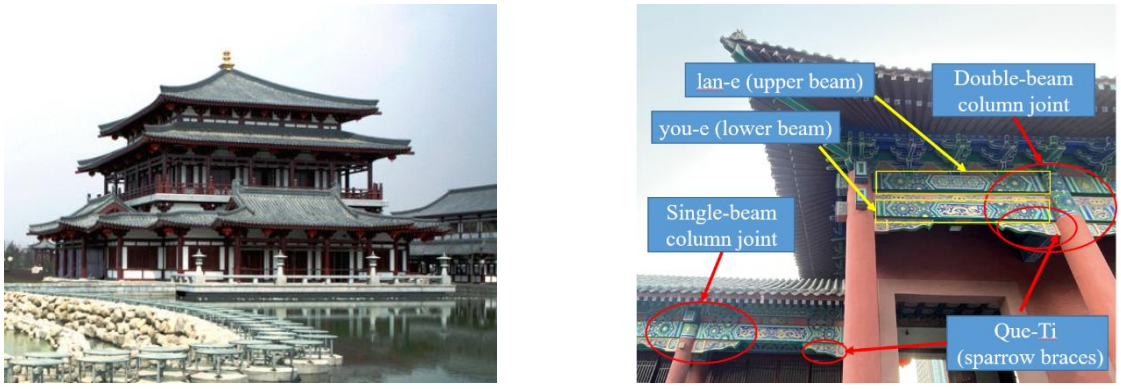
1. Introduction

Ancient Chinese architecture, characterized by its distinctive architectural style and sophisticated construction techniques, represents the remarkable artistic achievements of Chinese civilization and serves as an essential component of the architectural heritage of the world [1]. Due to the inherent shortcomings of timber, such as flammability and susceptibility to decay, along with prolonged exposure to natural disasters and human-induced damage, ancient timber structures have become extremely scarce. Moreover, most of these buildings suffer from deterioration problems including structural aging, corrosion, and insect damage, posing serious challenges to their overall safety[2]. How to preserve and inherit traditional architectural culture while satisfying the diversified demands of modern society for building functionality and aesthetics has become an urgent issue requiring resolution[3]. In response to this challenge, MCTBs have emerged, integrating contemporary construction technologies and materials while faithfully reproducing the form and appearance of ancient Chinese architecture. Meanwhile, the structural strength and durability have been significantly improved, demonstrating excellent engineering applicability and broad prospects for development. At present, representative MCTB projects such as the Chang'an Tower in Xi'an, Dingding Gate in Luoyang, Leifeng Pagoda in Hangzhou, and Tengwang Pavilion in Nanchang have been successively constructed and have become important landmarks in major historical cities[4,5]. Owing to their excellent seismic performance, including high-strength and good ductility, steel structures have been widely applied in MCTBs. These buildings adopt steel structural systems while retaining the traditional appearance and compositional principles of ancient Chinese architecture[6]. The seismic behavior of the entire structural system is largely governed by the performance of beam-column joints[7]. The roof structures of Chinese hall-style buildings are characterized by diverse forms and deep overhanging eaves, forming a "heavy roof" that occupies a significant portion of the building elevation. This prominent roof configuration is one of the most representative structural features of ancient timber architectures. To ensure the overall structural stability required by such roof systems, ancient craftsmen gradually developed a double-beam system consisting of the *Lan-e* (upper beam) and the *You-e* (lower beam) [8], as shown in Fig. 1.

Although many components of ancient timber architecture are simplified in MCTBs, the main dimensions are retained to reflect the traditional architectural style. Accordingly, the columns in steel MCTBs are typically designed in two segments. The lower column is typically composed of a circular hollow section (CHS) column with a large cross-section, whereas the upper column, which is designed to support decorative elements such as *dougong* (bracket set), generally adopts a rectangular hollow section (RHS) column with a smaller cross-section. The upper and lower columns are reliably connected through the installation of horizontal and vertical stiffening plates inside the lower column, thereby forming a "transition column". The double-beam column joint, consisting of the *Lan-e*, *You-e*, and the transition column, represents a typical and critical connection form in MCTBs. The joints in existing steel MCTBs are predominantly constructed using fully welded connections. Beams are typically made of I-sections, with the upper beam having a larger cross-sectional size than the lower beam. In smaller-scale MCTBs, only the *Lan-e* is provided, while the *You-e* is omitted, resulting in a single-beam column joint. In this study, these joints are collectively referred to as irregular steel joints in MCTBs, as the beam-column joint involves a non-standard spatial arrangement of members, including the *Lan-e* (upper beam), *You-e* (lower beam), and the transition column. The term "irregular" here describes the connection configuration and construction form, rather than the seismic irregularities (e.g., torsional or mass irregularity) defined in structural design codes. It is worth noting that non-structural components such as *dougong* (bracket sets) and *Que-Ti* (sparrow braces) primarily serve decorative purposes and do not contribute to the load-bearing system[9].

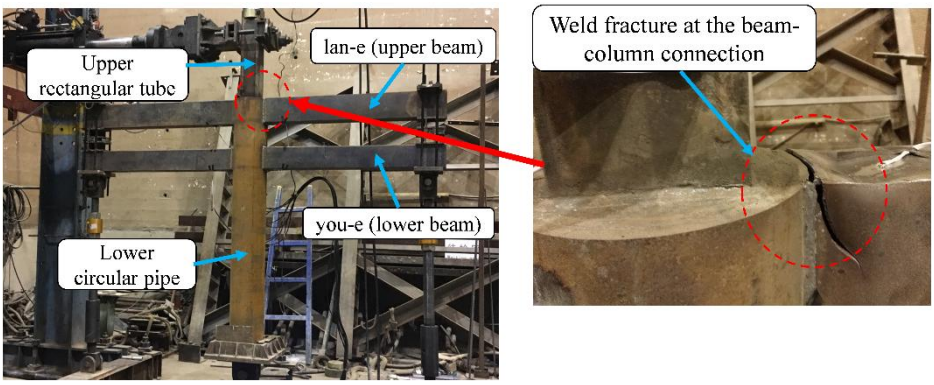
In recent years, increasing attention has been devoted to the study of MCTBs, particularly regarding the mechanical performance of irregular steel joints. These studies primarily address the hysteretic behavior, load-bearing mechanisms, and structural optimization of fully welded connections, covering a variety of joint configurations such as transition columns[10], transition columns with bracket sets[11], double-beam column joints[12-14], and joints equipped with viscous[15] or friction dampers[16-18]. Previous studies have shown that steel MCTBs with fully welded connections exhibit favorable stiffness and load-bearing capacity. However, brittle fracture of the welds and connection failure often occur in the later stages of loading. In addition, fully welded connections impose stringent requirements on site conditions. In many MCTB projects, factors such as heritage preservation and spatial constraints are frequently involved, making it difficult to ensure welding quality during on-site construction and even posing a risk of secondary damage to surrounding historical components. Therefore, MCTBs are gradually transitioning toward bolted connection systems that offer greater efficiency and structural reliability.

However, due to the widespread use of CHS columns in MCTBs, the installation of conventional bolts is often difficult or even infeasible. Blind bolts have been widely recognized as an effective solution for connecting closed-section members, as they allow for single-sided installation and are particularly well-suited for closed-section columns.



(a) Ziyun Pavilion, Tang Paradise

(b) Irregular joints in MCTB



(a) Fully welded irregular steel joint in MCTB

Fig. 1 Examples of MCTBs

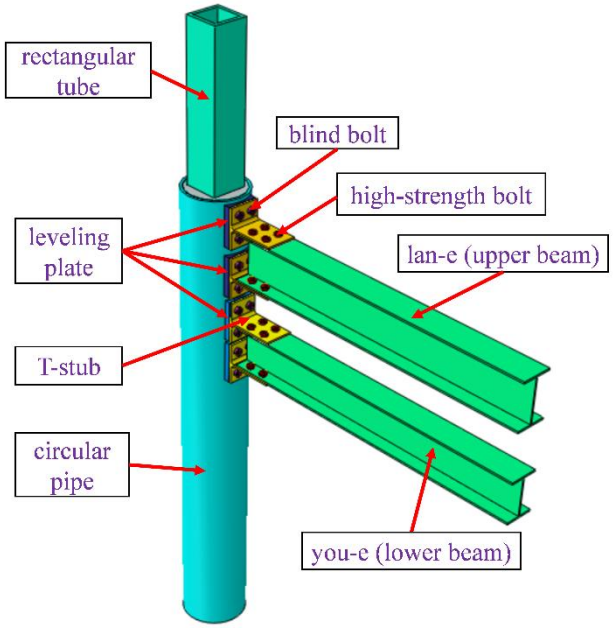
Over the past few decades, various blind bolt products such as the Hollo-Bolt, BOM, Ajax One-Side Bolt, Thread-Fixed One-Side Bolt (TFOB), and the Flowdrill series have been developed and applied in practical engineering[19]. These blind bolts are typically used in combination with endplates for connecting steel beams to closed-section columns, significantly improving assembly efficiency and construction convenience. Tizani et al. [20] developed the Extended Hollo-Bolt (EHB), which was derived from the original Hollo-Bolt.[21] It has been demonstrated that the connection performance can be significantly enhanced when the steel tube is filled with concrete, making it comparable to that of standard bolted connections. However, in hollow columns without concrete infill, the expansion legs of the EHB may fracture suddenly once the connection reaches its peak load, resulting in abrupt connection failure [22-25]. TFOBs [26,27]and Flowdrill system [28] form internal threads on the column wall, enabling bolt installation without the need for nuts. However, the Flowdrill system is only suitable for RHS tubes made of thin-walled materials. The Ajax one-side bolt features a structural configuration and load-bearing mechanism similar to those of conventional high-strength bolts, exhibiting excellent mechanical performance. Lee et al. improved the Ajax one-side bolt and developed the Headed Anchor Blind Bolt (HABB), followed by a series of studies focusing on its mechanical performance [29,30]. The Ajax one-side bolt features a structural configuration and load-bearing mechanism similar to those of conventional high-strength bolts, exhibiting excellent mechanical performance. Based on the fastening mechanism of the Ajax one-side bolt, Wang et al.[31] proposed a novel Slip-critical Blind Bolt (SCBB). This bolt incorporates a compressive washer and a pre-tightening sleeve structure[32], which not only enables a preloading effect comparable to that of conventional high-strength bolts, but also achieves a pre-tensioning force that satisfies the requirements specified in the current Chinese design code[33]. Experimental studies have demonstrated that the SCBB provides excellent connection performance under various loading conditions, including single-bolt tension, shear, and combined loading[34]. In end-plate connections between RHS columns and I-section beams, SCBB connections exhibit superior hysteretic behavior and energy dissipation capacity under cyclic loading, with overall performance significantly exceeding that of conventional blind bolt connections[35]. At present, blind bolt connections for CHS columns are typically configured as symmetrical end-plate and blind bolt assemblies. However, due to their relatively large dimensions and the projection of bolts beyond the plane of the frame, such configurations are difficult to satisfy the decorative and structural concealment requirements of MCTBs.

In this study, SCBBs were introduced into irregular steel joints in MCTBs to achieve an efficient prefabricated connection between CHS columns and I-section steel beams. Four joint specimens were subjected to low-cycle reversed loading to evaluate their seismic behavior, including failure characteristics, hysteretic response, ductility, and energy dissipation capacity. In addition, the cumulative damage behavior of the joints was preliminarily evaluated. The results provide a novel prefabricated and industrialized connection system for MCTBs, offering substantial engineering value for the preservation and continuation of traditional Chinese architectural culture.

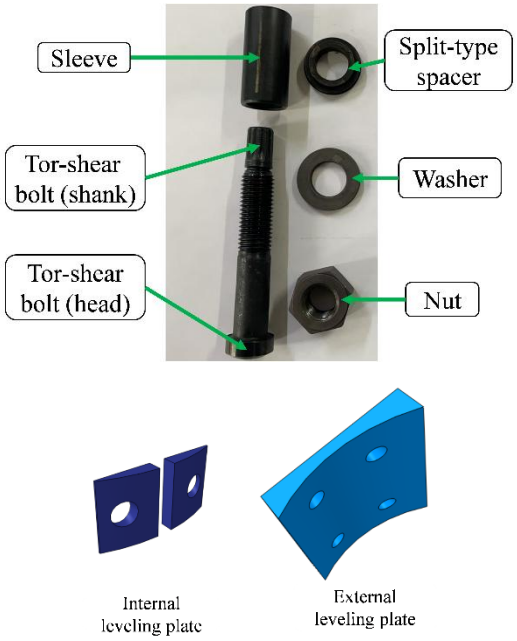
2. Experimental program

2.1. Specimen design

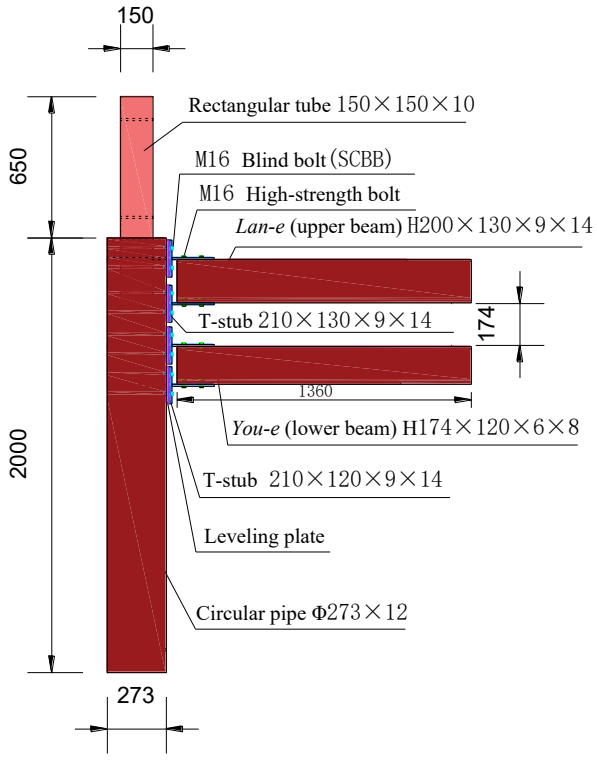
The research group previously carried out experimental and finite element studies on the seismic performance of fully welded steel MCTBs. Building upon this foundation, the present study optimizes the beam-column connection by proposing a novel prefabricated joint configuration that incorporates a blind bolt and T-stub assembly. The proposed joint is composed of a steel transition column, an I-section steel beam, and several connection components. The connection components include T-stubs, internal and external leveling plates, high-strength bolts, and blind bolts. The detailed configuration is shown in Fig. 2. The steel transition column is composed of an upper rectangular tube, a lower circular pipe, as well as horizontal and vertical stiffeners, which are welded together[36]. T-stubs serve as the connecting elements between the lower circular pipe and the I-section steel beam. Internal and external leveling plates are placed between the lower circular pipe and the web of the T-stub and are connected using SCBB blind bolts. The flange of the T-stub is connected to the I-section beam by high-strength bolts.



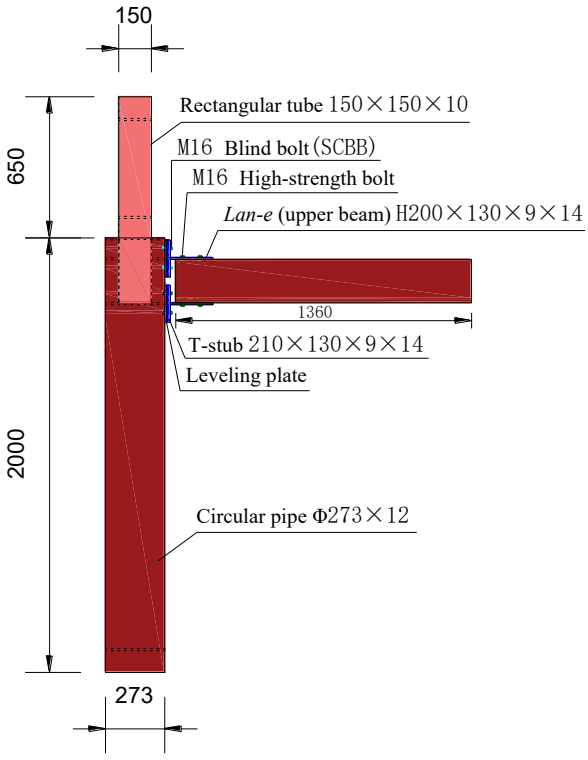
(a) Configuration of Double-beam column joint



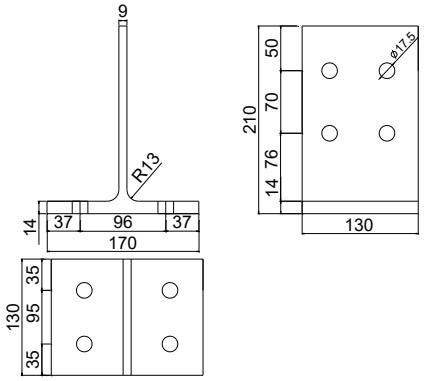
(b) Blind bolt and leveling plate



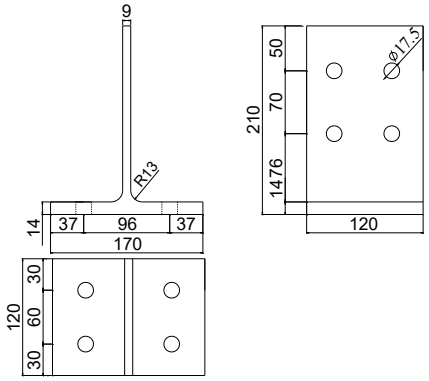
(c) Double-beam column joint（JD1、JD2）



(d) Single-beam column joint（JD3、JD4）



(e) Upper T-stub



(f) Lower T-stub

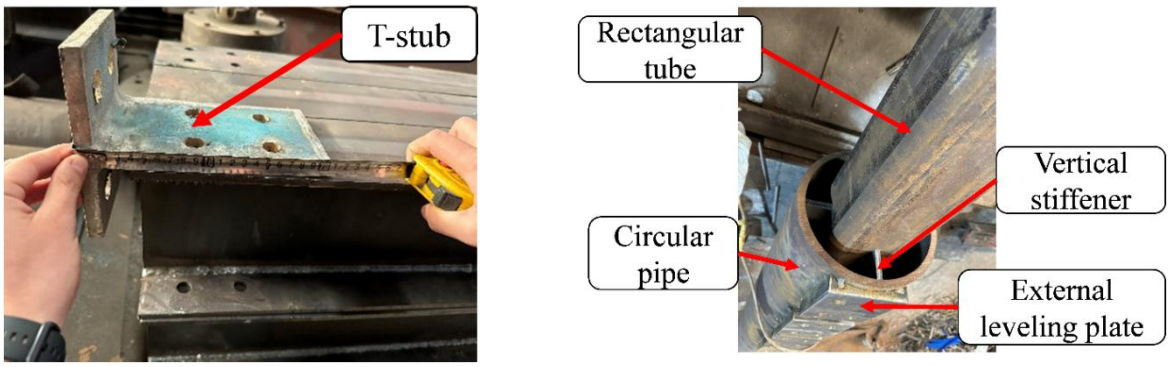
Fig. 2 Test specimens（Unit：mm）

Yingzao Fashi, issued during the Song Dynasty, is the first officially promulgated building standard in the history of ancient Chinese architecture[37]. It provides explicit specifications for architectural hierarchy, height-to-width ratios, bay spacing, as well as the structural forms and dimensional standards of key components such as beams and columns. The building standard established a modular system based on the standardized units of *ts'ai*, *chi'i*, and *fen*, which is referred to as the "material portion grading system". The dimensions of all building components were controlled according to fixed proportional relationships, thereby ensuring consistency in design and reliability in structural performance.

Once the architectural hierarchy (i.e., the rank of the building as classified in traditional Chinese standards) was determined, the height-to-width ratio and column spacing were subsequently defined, based on which the lengths of beams and columns were calculated. The width of the beam was determined by the column diameter, and the beam cross-section maintained a fixed height-to-width ratio of 3:2. For other components such as bracket sets, corresponding specifications were also explicitly provided in the *Yingzao Fashi*. This standardized design methodology reflects the advanced understanding of structural mechanics embodied in ancient Chinese architecture. For steel MCTBs constructed using modern steel materials, other parameters such as the wall thickness of circular steel tube columns and the thicknesses of beam flanges and webs need to be determined through structural calculations.

A total of four irregular steel joints in MCTBs with blind bolts were designed in this study, including two double-beam column joints and two single-beam column joints. The specimen dimensions were determined with reference to the previous experimental study on fully welded irregular steel joints in MCTBs conducted by the research group, and were further adjusted based on practical engineering requirements and the material portion grading system described in the *Yingzao Fashi*. The prototype of the specimen was based on a second-class hall-style building from the Tang Dynasty, and its structural dimensions were determined in accordance with the material portion grading system specified in the *Yingzao Fashi*. In this modular system, the smallest unit was *fen*. The diameter of the eave column was 42 *fen*, and the beam cross-section followed a fixed height to width ratio of 3:2. Specifically, the *lan-e* (upper beam) had a height and width of 30 *fen* and 20 *fen*, respectively, while the *you-e* (lower beam) measured 27 *fen* in height and 18 *fen* in width. According to the modern metric system, 1 *fen* is equivalent to 17.16 millimeters, and the eave column diameter was therefore approximately 720 millimeters.

To accommodate the capacity of the laboratory loading equipment and to comply with the current national standards for seamless circular steel tubes[38], the final scale ratio of the specimen model was determined as 1:2.6, and a seamless circular steel tube with an outer diameter of 273 mm was selected for the eave column. An axial compression ratio of 0.2 corresponds to an axial force of 275 kN. The remaining structural dimensions were determined using the same conversion method. The main parameters are summarized in Table 1, and the specimen dimensions are illustrated in Fig. 2. The total length of the steel column was 2650 mm, consisting of two segments with different cross-sections. The lower segment was a circular pipe with dimensions of Φ273 mm × 12 mm, and the upper segment was a rectangular tube measuring 150 mm × 150 mm × 10 mm. The beam adopted an I-section profile, with the upper beam and lower beam having cross-sectional dimensions of 200 mm × 130 mm × 6 mm × 8 mm and 174 mm × 120 mm × 6 mm × 8 mm, respectively. Openings were made in the connection region between the circular pipe column and the steel beam, and internal leveling plates were welded to the inner wall of the column[39]. In addition, a circular horizontal stiffening plate with a thickness of 10 mm was welded inside the circular pipe column at the height corresponding to the beam flange. The upper rectangular tube was embedded into the lower circular pipe and extended downward to the level of the lower flange of the upper beam. Its bottom perimeter was welded to the inner wall of the circular pipe column using four vertical stiffeners. During the assembly of the beam and column, internal and external leveling plates were positioned on both sides of the circular pipe column wall and precisely aligned with the predrilled holes. The circular pipe column and the T-stub were connected using M16 Grade 10.9 nested blind bolts, while the web of the T-stub was connected to the beam flange using M16 Grade 10.9 high-strength bolts. The fabrication process of the specimen is illustrated in Fig.3.



(a) T-stub (b) Column

Fig. 3 Photos at manufacturing site

Table 1
Specimen details

Specimen	Circular pipe (mm)	Rectangular tube (mm)	Upper T-stub (mm)	Lower T-stub (mm)	Upper beam (mm)	Lower beam (mm)
JD1	273×12	150×10	T210×130×9×14	T210×120×9×14	HN200×130×6×8	HN174×120×6×8
JD2	273×12	150×10	T210×130×8×12	T210×120×8×12	HN200×130×6×8	HN174×120×6×8
JD3	273×12	150×10	T210×130×9×14	/	HN200×130×6×8	/
JD4	273×12	150×10	T210×130×8×12	/	HN200×130×6×8	/

Table 2
Mechanic performance indexes

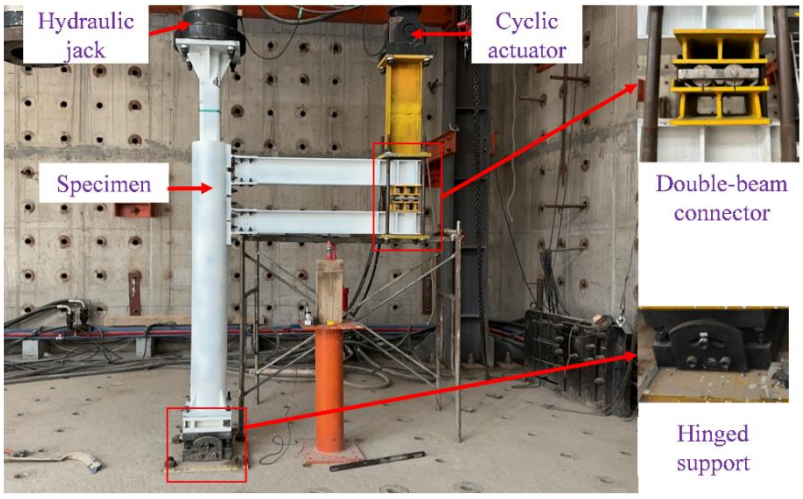
Type	Thickness (mm)	f_y (MPa)	f_u (MPa)	E_s (×10^{5}MPa)	δ (%)
Tube	12	288.3	388.1	1.92	/
Beam Flange	8	252.5	440.6	1.99	32.2
Beam Web	6	280.6	442.7	1.96	35.1
T-stub Flange	14	268.3	447.6	1.96	34.5
T-stub Web	9	271.1	445.2	2.16	37.5
T-stub Flange	12	283.3	483.3	2.21	39.5
T-stub Web	8	330.4	450.4	2.15	36.3

2.2. Mechanical properties of the material

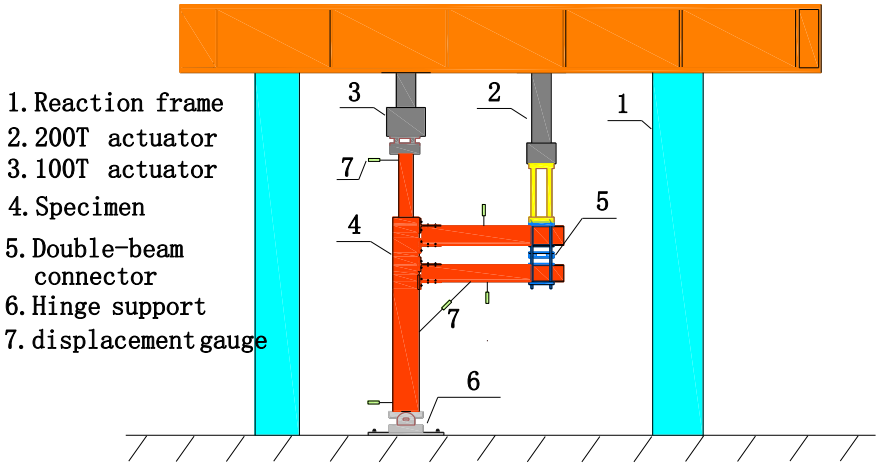
All specimens were fabricated using Q235B steel. In accordance with the relevant Chinese standards[40], tensile tests were conducted on samples taken from the upper rectangular tube, lower circular pipe, I-section steel beams, and T-stub. The measured mechanical properties of the steel materials are presented in Table 2.

2.3. Loading scheme

The test was conducted using a beam end loading method, and the on-site loading setup is illustrated in Fig. 4. A vertical axial load of 275 kN was applied to the top of the column using a hydraulic jack, corresponding to an axial compression ratio of 0.2, and was maintained at a constant level throughout the entire test to ensure axial load stability during cyclic loading. An electrohydraulic servo loading system was applied at the column top, with a maximum load capacity of 2000 kN and a displacement range of ±100 mm. The column base was connected to the ground through a unidirectional hinged support, which was anchored to the rigid floor using ground anchor bolts. Cyclic loading was applied at the beam ends using a 500 kN electrohydraulic servo actuator. The beam end reached a maximum load of 1000 kN, with a displacement range of ±250 mm. The entire testing procedure was controlled by an MTS973 electrohydraulic servo structural testing system, as illustrated in Fig. 4. To ensure that the beam end force conditions of the double beam column joints (JD1 and JD2) in the test are consistent with those in engineering practice, it is important to prevent moment transfer between the upper and lower beam ends during loading while allowing relative horizontal movement. A double-beam connector was designed and fabricated, as shown in Fig. 4(b). The extension of the hydraulic servo actuator was defined as the positive direction, whereas retraction was defined as the negative direction.



(a) On-site photograph



(b) Schematic diagram

Fig. 4 Test setup

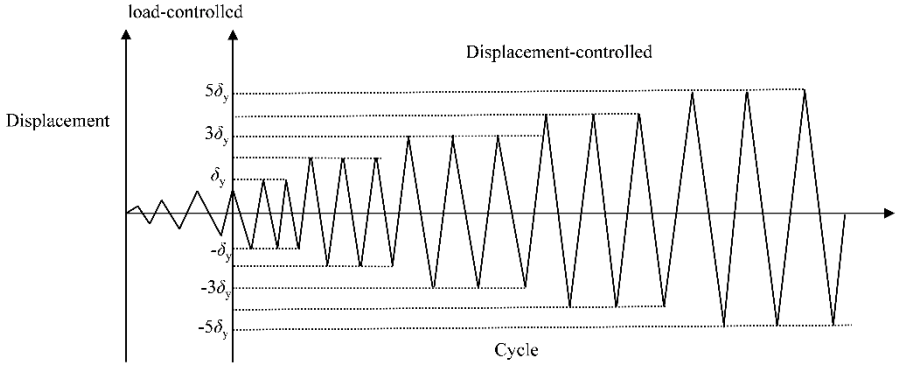


Fig. 5 Loading protocol

According to relevant standards[41], the loading protocol is shown in Fig. 5. The yield displacement (δ_y) was determined based on strain measurements obtained from strain gauges installed at critical locations of the T-stub component. Yielding of the specimen was identified when the measured strain reached the yield strain of the steel material (ε_y), and the corresponding lateral displacement was defined as the yield displacement (δ_y). The cyclic loading history was applied in a symmetric displacement-controlled pattern in both positive and negative directions.

In the initial stage, displacement controlled loading was applied. After the specimen yielded, the displacement increment was progressively increased based on multiples of the yield displacement, with each loading level repeated three times. The test was terminated when the lateral load capacity dropped to 85% of the peak load, indicating significant strength degradation, or when severe failure of the specimen occurred.

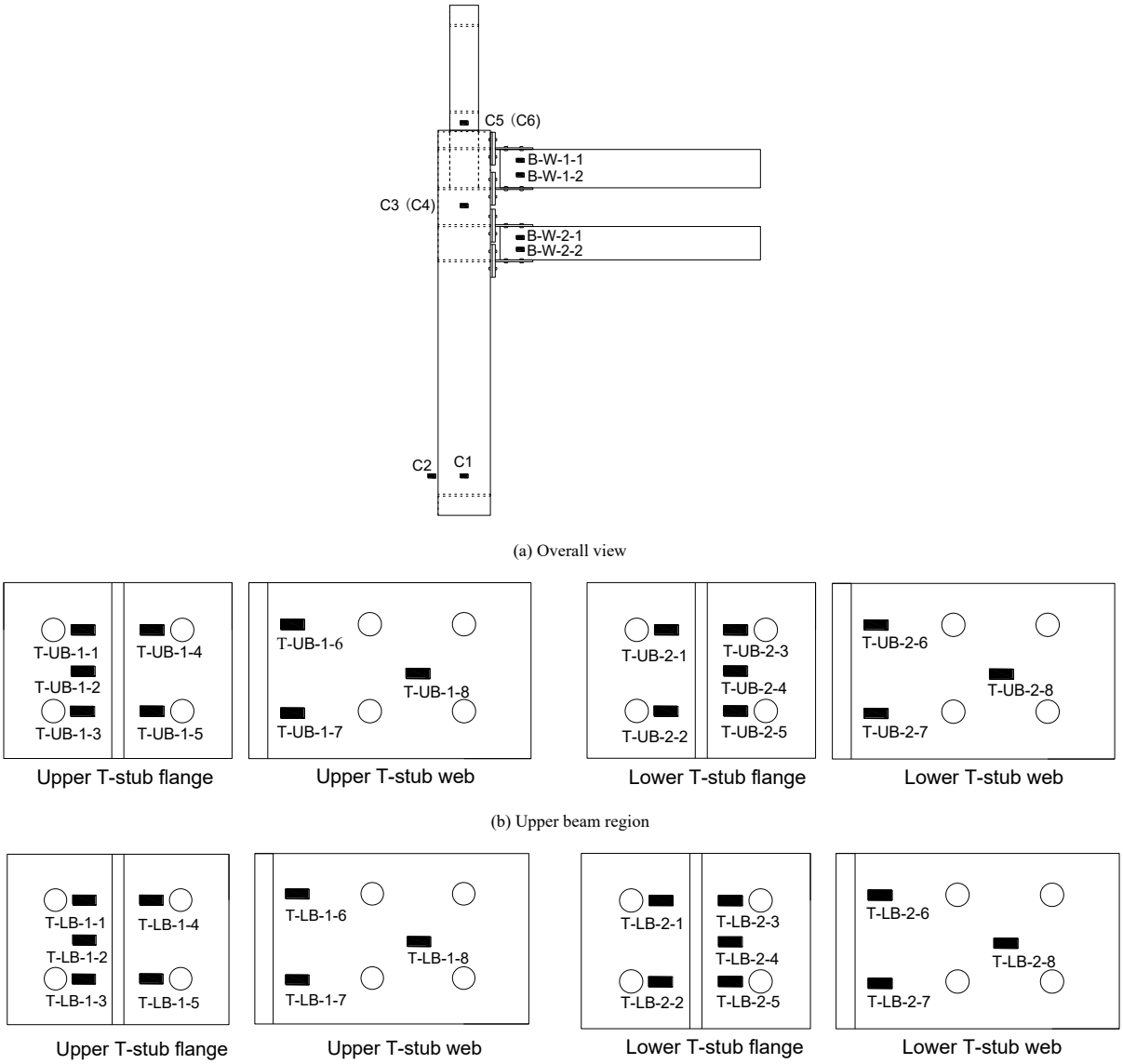
2.4. Data measurement

The DH3816N static stress and strain analysis system was used to collect data on displacement, strain, and load during the test. Displacement gauges were primarily arranged at the top and bottom of the column. A cable displacement transducer was installed at the beam end to measure the horizontal displacement at the loading point. The measurement layout is illustrated in Fig. 4(b).

The joint rotation angle was calculated based on the measured beam-end displacement assuming that the beam segment between the column axis and the loading point behaves approximately as a rigid body. The rotation angle θ was calculated as $\theta = \Delta / L$, where Δ is the beam-end displacement recorded by the displacement transducer, and L is the distance from the column axis to the loading point. In the present test setup, L = 1480 mm. The bending moment was calculated as $M = P \times L$, where P is the applied load.

Strain gauges were primarily arranged on the flange and web of the T-stub, as well as on the web and flange at the beam ends. In addition, a small number of strain gauges were installed at the top, bottom, and mid height of the column. To monitor the strain development of the blind bolts during the test, a flat surface was ground at the root of the bolt shank, and strain gauges were affixed along the axial direction of the bolt. The measurement points are illustrated in Fig. 6.

For ease of identification, each strain gauge was labeled with a concise code comprising the component type, measurement location, and sequence number. The coding system is defined as follows. C represents the column, T represents the T-stub, UB represents the upper beam, and LB represents the lower beam. For example, the code T-UB-1-1 indicates the first strain gauge installed on the upper T-stub, whereas T-LB-2-1 refers to the first strain gauge installed on the lower T-stub.



(a) Overall view

(b) Upper beam region

(c) Lower beam region

Fig. 6 Arrangement of strain gauges

3. Test results

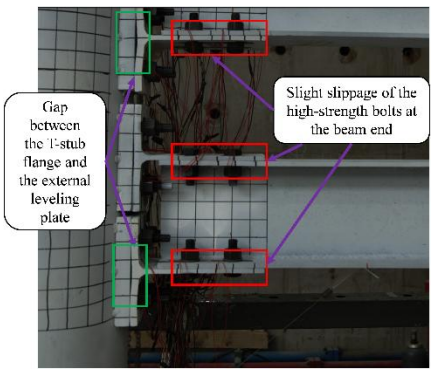
3.1. Failure process of specimens

Taking the single-beam column joint JD3 as an example, the specimen remained in the elastic stage during the initial loading phase due to the relatively small applied load. As the load gradually increased, the strain gauge on the lower flange of the T-stub was the first to reach the yield strain of the steel, indicating that local yielding initially occurred in the lower T-stub region. As the loading progressed, a slight gap appeared between the flange of the T-stub

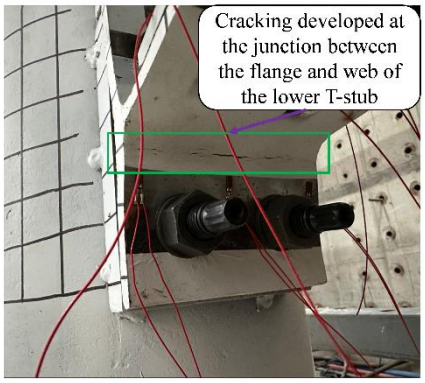
and the external leveling plate, and minor slip occurred at the high-strength bolts at the beam end, as shown in Fig. 7(a). The strain gauges on the web of the lower T-stub and on portions of the beam also reached the yield strain of the steel. When the displacement reached 100 mm, a crack appeared at the junction between the flange and web of the lower T-stub, as shown in Fig. 7(b). Meanwhile, the strain gauge at the upper flange of the beam end reached the yield strain of the steel and increased rapidly, as shown in Fig. 7(c). Significant slip was also observed at the high-strength bolts at the beam end. As the displacement increased to 120 mm, a crack also developed at the junction between the flange and web of the upper T-stub, while the crack at the junction of the lower T-stub continued to propagate. Eventually, fracture occurred at the junction between the flange and web of the lower T-stub, and the test was terminated when the load-carrying capacity dropped by more than 85 percent from the peak load, as shown in Fig. 7(d). For the double-beam column joints, yielding of the T-stub in the upper beam occurred earlier than that in the lower beam. Failure was initiated by a crack at the junction between the flange and web of the lower T-stub in the upper beam at a displacement of 80 mm. The crack propagated through the section at 100 mm and ultimately led to fracture at 120 mm.

Due to the structural characteristics of the double-beam joint, when fracture occurred at the junction between the flange and web of the lower T-stub in the lower beam, a crack had already developed at the corresponding location in the upper beam but had not yet fractured. At this stage, the specimen still maintained a relatively high load-carrying capacity. As the displacement increased to 140 mm, the crack in the upper beam further propagated and eventually fractured, marking the final failure of the specimen. The failure mode of the specimen is illustrated in Fig. 7.

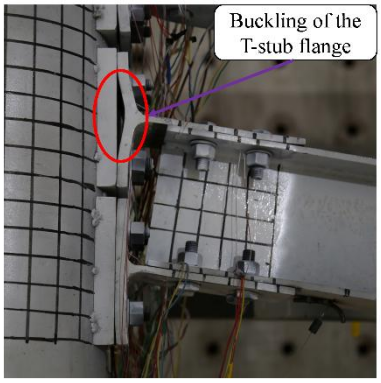
The strain measurements of the blind bolts indicate that most bolts remained within the elastic range throughout the loading process. Post-test inspection also revealed no significant plastic deformation of the bolt shanks, suggesting that the blind bolts maintained stable fastening conditions during cyclic loading.



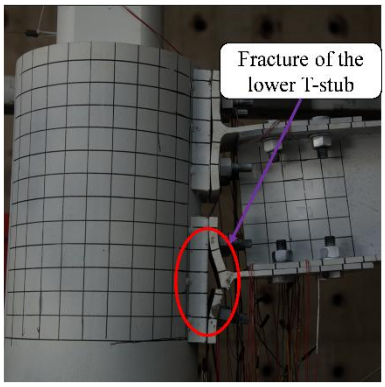
(a) Slight slippage of the high-strength bolts



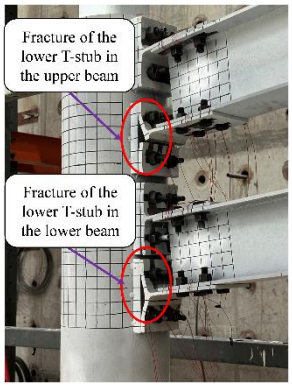
(b) Cracking developed in the lower T-stub



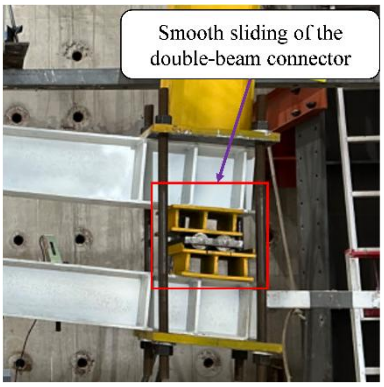
(c) Buckling of the T-stub flange



(d) Fracture occurred at the lower T-stub



(e) Final failure of the double-beam column joint



(f) The double-beam connector

Fig. 7 Failure pattern of specimens

3.2. Failure modes of specimens

The failure modes of all specimens conformed to the strong-column weak-beam design principle. During the test, deformation and damage were primarily concentrated in the T-stub region, and no significant damage was observed in the other components. Joint failure was mainly attributed to the yielding and fracture of the T-stub under the combined action of shear and bending. A summary of the observed failure phenomena is provided in Table 3.

The failure progression of the specimens can be divided into three distinct phases: (i) the initial yielding stage, (ii) the deformation development stage characterized by local buckling and bolt slippage, and (iii) the final fracture stage, involving crack initiation and localized rupture. In the early stage of loading, initial localized yielding occurred in the lower T-stub region, highlighting it as the critical zone of stress concentration. Subsequently, a gap gradually developed between the flange of the T-stub and the external leveling plate, accompanied by slight slippage of the high-strength bolts at the beam end. As the loading continued, the strain gauges on the web of the lower T-stub and on portions of the beam flange successively reached the yield strain. During this loading phase, pronounced buckling deformation developed in the T-stub flange, and the specimen exhibited a significant reduction in stiffness, marking the onset of plastic behavior.

In the later stage of loading, an initial crack developed at the junction between the flange and web of the lower T-stub, accompanied by a sharp increase in bolt slippage, which significantly accelerated the accumulation of damage in the specimen. As deformation continued to progress, crack propagation was also observed at the corresponding location of the upper T-stub. Eventually, fracture occurred at the junction between the flange and web of the lower T-stub. In the final loading stage, some high-strength bolts exhibited noticeable tensile deformation, while most of the other components remained in the elastic state without significant deformation. Although the double-beam and single-beam column joints differ in configuration, their failure modes were generally similar.

Under the same displacement loading, specimens JD2 and JD4, which had thinner T-stub webs, exhibited more pronounced slippage of the high-strength bolts at the beam ends, as well as larger gaps between the T-stub flange and the external leveling plate. The key difference was observed in the double-beam joint: after fracture occurred at the junction between the flange and web of the lower T-stub in the lower beam, the upper beam was still able to carry load, indicating a higher level of safety reserve.

To further interpret the fracture observed at the T-stub flange–web junction, the local stress mechanism of the flange was examined. In the tested specimens, the T-stub flange was connected by two rows of bolts, and the first bolt row was located approximately 48 mm from the web. Under the beam-end bending moment, the moment was transferred to the bolt group in the form of tensile forces, producing a bending effect in the T-stub flange. Because the web provides a restraint boundary for the flange, the distance between the bolt row and the web forms an effective lever arm that induces bending stresses in the flange section.

According to the equivalent T-stub model recommended in EN3 the flange bending resistance can be evaluated based on the plastic hinge mechanism of an

equivalent T-stub component. The mechanical model and the corresponding plastic hinge mechanism are illustrated in Fig. 8. Based on this mechanism, the tensile resistance of the equivalent T-stub flange can be calculated as follows:

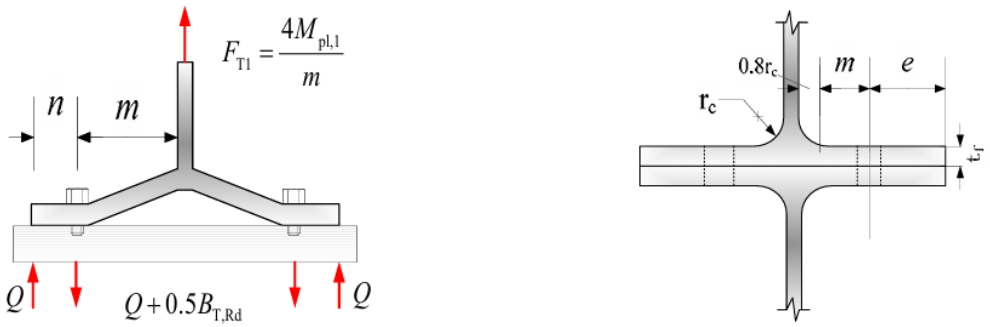
$$F_T = \frac{4M_p}{m} \tag{1a}$$

$$M_p = 0.25\sum l_{eff} t_f^2 / \gamma_M \tag{1b}$$

where F_T is the tensile resistance of the equivalent T-stub component, t_f is the flange thickness, m is the distance between the bolt row and the flange root considering the fillet radius, and l_{eff} is the effective plastic hinge length. In the present study, the T-stub has a fillet radius of 13 mm, resulting in m=48-0.8×13=37mm. The effective length l_{eff} is taken as the smaller value of 2πm and $4m+1.25e$. The flange thickness is t_f=14mm.

By substituting the geometric parameters of the specimen into the above equations, the tensile resistance of the equivalent T-stub flange was calculated as 234 kN. In the experiment, the actuator load corresponding to the first yielding of the strain gauge was 32 kN, which corresponds to a tensile force of approximately 227 kN in the T-stub flange. The close agreement between the calculated resistance and the experimental demand indicates that the flange-web junction approached its plastic capacity at that stage.

As the flange bends under bolt tension, contact between the flange edge and the leveling plate may develop, which can introduce a certain degree of prying action and increase the flange demand. Meanwhile, the leveling plates modify the load transfer path between the blind bolts and the tubular column by providing a flat contact interface, thereby alleviating direct bearing between the blind bolt nut and the curved column wall and reducing local stress concentration. Experimental observations show that the leveling plates remained stable during loading, and the deformation of the blind bolts after the test was comparable to that observed in conventional blind-bolted connections. Although the inclusion of leveling plates slightly increases the effective bolt length, the blind bolts adopted in the specimens were selected with a capacity higher than the design requirement, and no adverse influence on the overall mechanical behavior of the joint was observed.



(a) Yielding mechanism of the T-stub flange

(b) Plastic hinge lines and calculation parameters

Fig. 8 Mechanical model and plastic hinge mechanism of the equivalent T-stub

Table 3
Main test phenomena of joints

NO	Elastic stage		Deformation development stage				Failure stage			
	Load level	Major events	Load level	Major events	Load level	Major events	Load level	Major events	Load level	Major events
JD1	δ_y	☆	2δ_y ~3δ_y	□◆★	4δ_y	◆●★	5δ_y	▼	6δ_y	▼▽
JD2	δ_y	☆	2δ_y ~3δ_y	□◆★	4δ_y	◆●★	5δ_y	▼	6δ_y	▼▽
JD3	δ_y	☆	2δ_y ~3δ_y	□◆★	4δ_y	◆●★	5δ_y	▼	6δ_y	
JD4	δ_y	☆	2δ_y ~3δ_y	□◆★	4δ_y	◆●★	5δ_y	▼	6δ_y	

Notes：“☆”denotes the minor slippage of the high-strength bolts at the beam end; “□” denotes the minor gaps appeared between the flange of the T-stub and the outer leveling plate; “★”denotes the significant slippage occurred in the high-strength bolts at the beam end;“◆” denotes the buckling deformation of the T-stub flange;“●”denotes the cracking at the T-stub flange-web junction; “▽”denotes the fracture of the lower T-stub on the upper beam; “▼” denotes the fracture of the lower T-stub on the lower beam.

3.3. Hysteresis loops

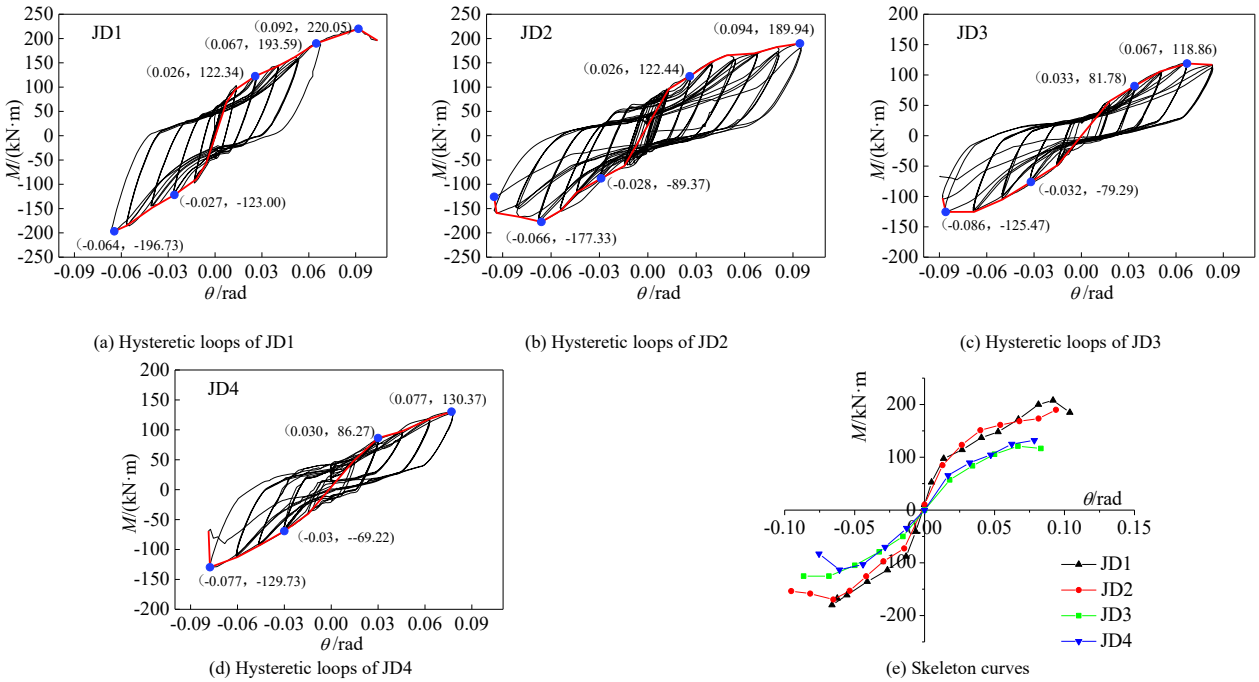
Fig. 9 presents the moment-rotation hysteresis curves at the beam ends of the specimens, where M and θ represent the bending moment and rotation, respectively. As shown in the figure, the hysteresis curves exhibit an overall spindle-shaped pattern and become progressively fuller with increasing loading, indicating favorable energy dissipation capacity. In the initial stage of loading, the specimen remained within the elastic range, and the moment-rotation relationship at the beam end was approximately linear. The hysteresis loops exhibited a small enveloped area, and no significant residual deformation was observed.

The hysteresis curves exhibit increasing fullness with the growth of loading displacement. This behavior can be attributed to three key mechanisms observed during cyclic loading: (i) progressive development of the gap between the T-stub flange and the backing plate, (ii) buckling deformation of the T-stub flange, and (iii) increasing slippage of the high-strength bolts at the beam end. In the later stage of loading, a crack developed and eventually fractured at the junction between the T-stub flange and web, resulting in a sharp drop in the hysteresis curve under negative loading.

Similar experimental observations have been reported in Ref. [44], where T-stub single-sided bolted connections with square steel tubular columns were investigated. Since the surface of the square steel tube is flat, leveling plates were not required in that study. The reported failure modes and hysteresis characteristics suggest that the cyclic behavior of such connections is mainly governed by T-stub deformation and bolt slip mechanisms.

3.4. Skeleton curve

From the moment-rotation hysteresis curves of the specimens (Fig. 9), the peak points of the first cycle at each loading level were selected and sequentially connected to generate the skeleton curves, as shown in Fig. 9. As illustrated in Fig. 9(e), the skeleton curves of all specimens exhibit similar trends, each undergoing three typical development stages: the elastic stage, the yielding stage, and the failure stage. Before slippage of the high-strength bolts at the beam end occurred, the skeleton curves of similar joints were nearly identical, indicating comparable initial stiffness and load-bearing capacity. As bolt slippage developed and the T-stub began to yield, the skeleton curves started to bend. With continued loading, significant plastic deformation gradually developed in the T-stub flange, and the growth of the skeleton curves became progressively slower. Ultimately, under repeated cyclic loading, fracture occurred at the junction between the flange and web of the lower T-stub, resulting in a rapid reduction in load-carrying capacity and a clear descending segment in the skeleton curve. In addition, compared with the single-beam column joint, the double-beam column joint exhibited significantly higher load-carrying capacity. Furthermore, an appropriate increase in the thickness of the T-stub was found to effectively improve the load-carrying capacity of the joint.



(a) Hysteretic loops of JD1 (b) Hysteretic loops of JD2 (c) Hysteretic loops of JD3

(d) Hysteretic loops of JD4 (e) Skeleton curves

Fig. 9 Hysteretic loops and Skeleton curves of specimens

3.5. Deformation and energy dissipation capacity

In this study, rotational ductility was used to evaluate the deformation capacity of the joint. It is defined as the ratio of the ultimate rotation to the yield rotation, and is calculated as follows:

$$\mu = \frac{\theta_u}{\theta_y} \tag{2}$$

where: θ_u is the rotation angle at joint failure, θ_y is the rotation angle at the yielding of the joint, and μ is the ductility factor. The calculated ductility factors for each specimen are presented in Table 4.

The average ductility coefficient of the joints ranged from 2.62 to 3.12, with the values of the double-beam column joints significantly higher than those of the single-beam column joints. The primary reason is that after fracture of the T-stub in the lower beam, the upper beam was still able to carry load, thereby providing a higher level of safety reserve. As loading progressed, the T-stub underwent large plastic deformation and eventually fractured, leading to a relatively lower overall ductility coefficient.

The energy dissipation capacity of structural members under cyclic loading was assessed using the equivalent viscous damping coefficient h_e, calculated as follows:

$$h_e = \frac{1}{2\pi} \bullet \frac{S_{\Delta ABC} + S_{\Delta ADC}}{S_{\Delta OBE} + S_{\Delta ODF}} \tag{3}$$

where $S_{\Delta ABC}+S_{\Delta ADC}$ denote the area of hysteretic curves of ABCDA, and $S_{\Delta OBE}+S_{\Delta ODF}$ denote the merging area of triangles OBE and ODF, as shown in Figure 12. The calculated results of the test specimens are shown in Table 5.

As shown in Table 5, the equivalent viscous damping ratios of the double-beam column joints and the single-beam column joints ranged from 0.151 to 0.212 and from 0.136 to 0.241, respectively. The equivalent viscous damping ratio of all specimens initially increased and then gradually decreased during the loading process. This trend was primarily attributed to the tight connection between components during initial loading, which resulted in significant energy dissipation through friction and a slight increase in the equivalent viscous damping ratio. With the increase in loading cycles, plastic deformation of the T-stub flange continued to develop, and cracks formed at the junction between the flange and the web, resulting in localized damage. These effects weakened the energy dissipation capacity of the structure and led to a reduction in the equivalent viscous damping ratio. Under the same loading level, the double-beam column joints exhibited superior energy dissipation performance compared with the single-beam column joints. This was mainly because energy dissipation was primarily provided by the T-stubs, and the double-beam column joints contained a greater number of T-stubs due to the presence of two beams, thereby offering enhanced energy dissipation capacity.

Table 4
Ductility coefficient

Specimen ID	Yield rotation θ_y/rad	Ultimate rotation θ_u/rad	μ
JD1	0.026	0.081	3.12
JD2	0.028	0.082	2.93
JD3	0.032	0.084	2.62
JD4	0.028	0.077	2.75

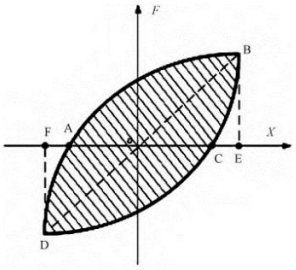


Fig. 10 Equivalent viscous damping coefficient calculation

Table 5
Equivalent viscous damping coefficient of specimens

Specimen ID	h_e				
	$1\delta_y$	$2\delta_y$	$3\delta_y$	$4\delta_y$	$5\delta_y$
JD1	0.176	0.212	0.197	0.197	0.151
JD2	0.175	0.204	0.179	0.161	0.155
JD3	0.188	0.205	0.165	0.145	0.137
JD4	0.199	0.241	0.162	0.150	0.136

The energy dissipation performance of each specimen under different loading levels is shown in Fig. 11. At the initial stage of loading, the energy dissipation of the specimens was relatively low. As the flange of the T-stub gradually entered the buckling stage, the energy dissipation capacity of the specimens was significantly enhanced. For the double-beam column joints, the

energy dissipation increment rates at each loading level compared with the previous level were 257.60%, 46.31%, 35.27%, and 29.17%, respectively. For the single-beam column joints, the corresponding increment rates were 132.00%, 84.41%, 44.48%, and 24.38%, respectively. The maximum energy dissipation of the double-beam column joints reached 11.70 kJ, which was significantly higher than the 8.69 kJ observed in the single-beam column joints, indicating that the double-beam column joints possessed superior energy dissipation capacity.

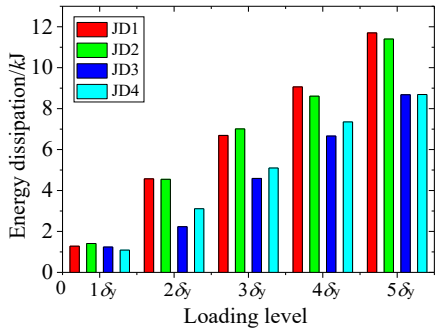


Fig. 11 Energy dissipation of specimens

3.6. Stiffness degradation

The secant stiffness was used to characterize the rotational stiffness of the joint at different load levels, as defined below:

$$K_i = \frac{|+M_i| + |-M_i|}{|+\theta_i| + |-\theta_i|} \tag{4}$$

where K_i is the moment-rotation stiffness at the ith cyclic load level; M_i denotes the maximum moment capacity at the ith cyclic load level; θ_i represents the rotation corresponding to the maximum moment capacity at the ith cyclic load level; and the sign convention follows positive for push and negative for pull directions.

The stiffness degradation curves of the specimens are shown in Fig. 12. With the gradual increase in loading levels, all joints exhibited a clear trend of stiffness degradation, which was mainly attributed to the continuous accumulation of plastic deformation in the T-stubs and the occurrence of slippage between components. Under the same loading level, the stiffness of the double-beam column joints was significantly higher than that of the single-beam column joints. For example, the initial stiffness of the double-beam column joint JD2 and the single-beam column joint JD4 was 5632.36 kN·m·rad^{-1} and 3907.99 kN·m·rad^{-1}, respectively. The initial stiffness of JD2 was approximately 44.12% higher than that of JD4.

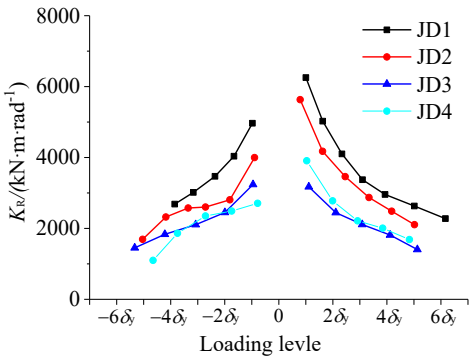
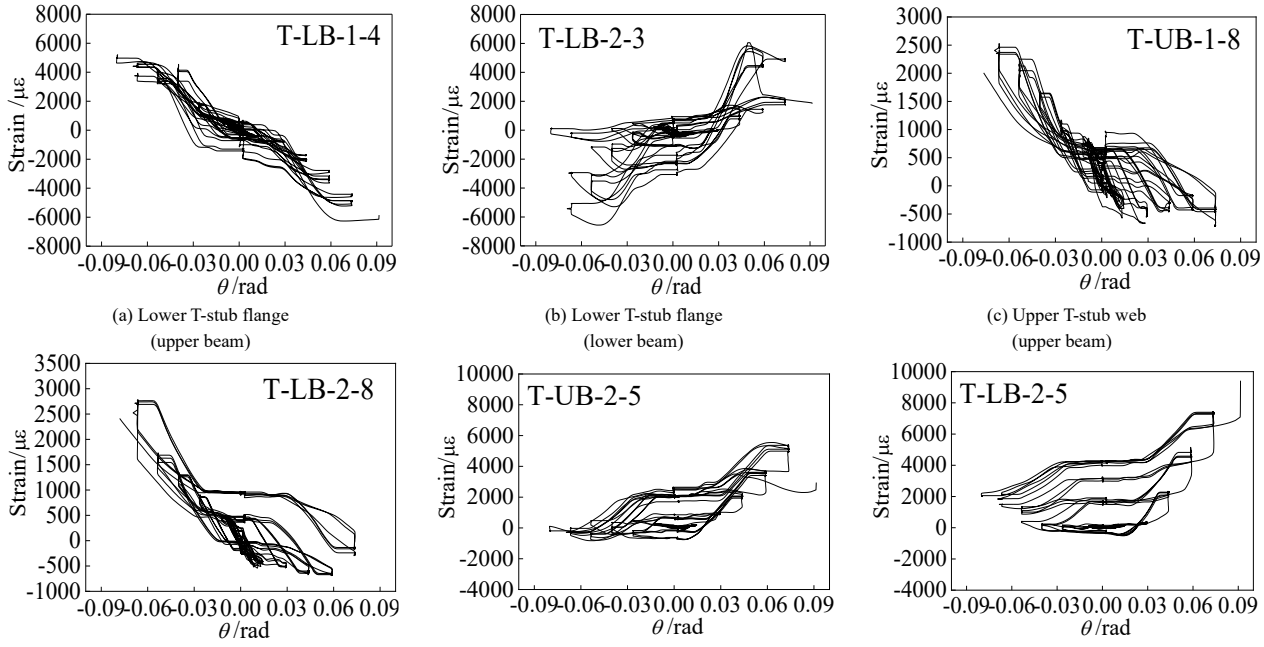


Fig. 12 Stiffness degradation

3.7. Strain analysis

The strain variations at the main measurement points of each component are shown in Fig. 13. During the test, the strain values at the beam and column locations did not exceed 500 με, indicating that these regions remained within the elastic range throughout the loading process and that the steel did not reach the yield strain.

The strain analysis indicated that plastic deformation of the joint was primarily concentrated in the flange of the T-stub. The strain in the T-stub flange was the first to reach the yield strain of the steel and increased rapidly thereafter. Most measurement points recorded strain values exceeding 4000 με, which was consistent with the buckling behavior of the T-stub flange observed during the test. As the loading progressed, the web of the T-stub also reached the yield strain. In the later stage of loading, cracks appeared at the junction between the flange and the web of the T-stub and propagated rapidly, eventually leading to fracture. This phenomenon was consistent with the experimental observations. In addition, the strain values in both the flange and the web of the lower T-stub were greater than those of the upper T-stub, which was consistent with the observed failure mode of the double-beam column specimen JD2, where fracture occurred in the lower T-stub.



(a) Lower T-stub flange (upper beam)

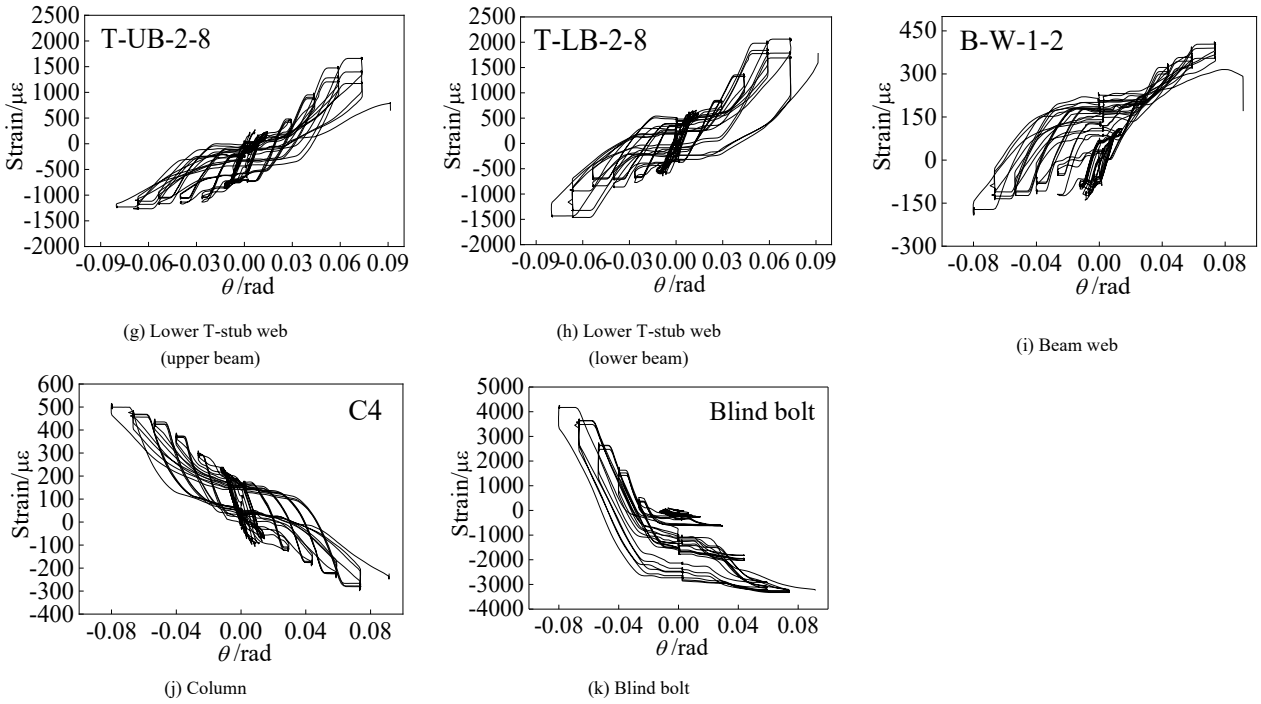
(b) Lower T-stub flange (lower beam)

(c) Upper T-stub web (upper beam)

(d) Upper T-stub web (lower beam)

(e) Lower T-stub flange (upper beam)

(f) Lower T-stub flange (lower beam)



(g) Lower T-stub web (upper beam)

(h) Lower T-stub web (lower beam)

(i) Beam web

(j) Column

(k) Blind bolt

Fig. 13 Strain curves of strain gauge

The strain in the blind bolts gradually increased with the increment of loading displacement. However, the strain values at most measurement points did not exceed 4000 με and remained within the elastic range. Only a few bolts entered the yielding stage in the later phase of loading. After the test, an inspection was conducted on the dismantled blind bolts. Slight wear was observed at the threaded portion, while no obvious deformation was found on the bolt shanks, indicating that the blind bolts exhibited good fastening performance in this type of joint.

4. Numerical analysis

4.1. Establishment of numerical model

To further investigate the plastic development and failure modes of irregular steel joints in modern Chinese traditional-style buildings with blind bolts, a refined finite element model was established in ABAQUS. The numerical model of a typical specimen is illustrated in Fig. 14. All components adopted C3D8R solid elements. Local mesh refinement was applied in the region of the T-stub connections. The mesh size in the core region of the beam-to-column joint was controlled within 5 mm to accurately capture the distribution of plastic strain fields, while the mesh size of beam and column members away from the joint gradually increased to 10-15 mm. A smooth mesh transition was adopted to achieve a balance between computational accuracy and efficiency. The circular column and the RHS column were connected through horizontal stiffening rings and vertical stiffeners, with welds simulated by tie constraints. The contact interaction among all components (including the blind bolts, beams, columns, and leveling plates) was defined as surface-to-surface contact. Hard contact was applied in the normal direction, while Coulomb friction with a penalty formulation was adopted in the tangential direction. The friction coefficient was set to 0.3, consistent with the experimental conditions.

The double-beam connectors between the upper and lower beams in the tested double beam-column joints were simulated using SLOT elements, as shown in Fig. 14. This connector allows relative horizontal displacement between the two beams while restricting vertical movement, thereby preventing the transfer of bending moments between them. Through this configuration, the beam-column joint region is subjected primarily to bending moment and shear force induced by the actuator, which reproduces the mechanical condition of a joint located between two beam inflection points in a frame structure. The effectiveness of SLOT elements in simulating this type of double-beam connection has been verified in the literature [13].

Reference points were established at the column base, column top, and beam end, which were coupled to the surrounding nodes to apply boundary conditions and loading. The loading process was divided into four analysis steps to ensure computational convergence. First, the design pretension force of 170 kN was applied to the blind bolts using the Bolt Load tool. Then, the “fix at current length” option was activated to maintain the bolt length in the subsequent analysis steps, meaning that the pretension force was assumed to remain constant during cyclic loading. In this study, the potential relaxation or loss of bolt pretension under cyclic loading was not explicitly considered. Subsequently, an axial load of 275 kN was applied at the column top. Finally, cyclic displacement loading was imposed at the beam end. To avoid stress concentration during loading, the beam end was coupled to a reference point, and the load was applied through this reference point. The column base was modeled as a hinged support (U1=U2=U3=UR2=UR3=0). The general static analysis procedure was adopted, taking into account both geometric and material nonlinearities.

Since some specimens shared the same geometric dimensions and connection details, with only a minor difference in the beam flange thickness, this variation was considered to have limited influence on the overall load-bearing mechanism and failure mode. Therefore, finite element modeling was conducted only for the typical specimens.

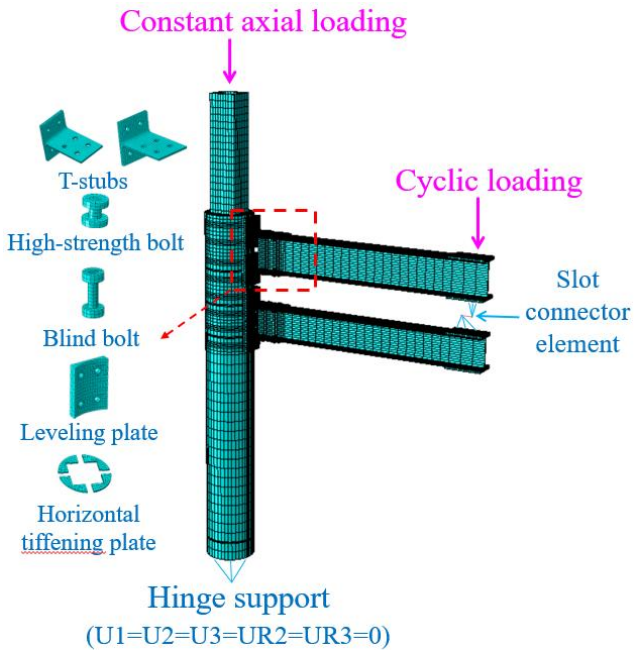


Fig. 14 Finite element model

The stress-strain relationship of the steel was represented by a three-linear-segment model proposed in literature [13], with the material parameters calibrated based on the tensile coupon tests listed in Table 2. Both the blind bolts and the high-strength bolts were modeled using a linear hardening material model.

4.2. Model verification

Taking the typical double-beam–column specimen JD2 as an example, the FEA results were compared with the experimental observations, as shown in Fig. 15. The deformation contour from FEA indicates that the specimen deformation was primarily concentrated in the T-stub region, with minor slippage observed at the high-strength bolts connecting the T-stub web to the beam end. The stress contour shows that, at the initial loading stage, the high-strength bolts at the beam end and the blind bolts at the column end reached relatively high stress levels, indicating that the T-stub effectively transferred bending moments and shear forces between the beam and column ends. As loading progressed, gaps gradually appeared between the upper and lower T-stub flanges and the outer leveling plate, accompanied by slight slippage of the beam-end high-strength bolts.

Further analysis revealed that the junction between the T-stub web and flange first reached the steel yield stress, which corresponded with the yielding detected by the strain gauges at the same location in the experiment. In the later loading stage, stress in this region continued to increase and expand, while the tension-side flange underwent significant bending, with the web arching upward. The FEA results were consistent with the experimentally observed cracking and fracture locations of the flange, and the model was able to reproduce the relative slippage between the two beams, indicating that the simulation of the double-beam connector was effective, in agreement with the findings of literature [14].

The stress distribution further demonstrated that, under cyclic loading at the beam end, both blind bolts and high-strength bolts exhibited high stress levels, with the maximum stress of the blind bolts reaching approximately 850 MPa, close to the nominal yield stress of 900 MPa. At the end of the test, slight thread wear was observed, while no noticeable deformation of the bolt shank occurred, which was consistent with the simulation. Limited by the modular constraints of traditional Chinese architecture, only four high-strength bolts and blind bolts could be arranged on each side. However, their calculated load-bearing capacity satisfied the strong-column weak-beam design principle, resulting in the primary deformation being concentrated in the T-stub.

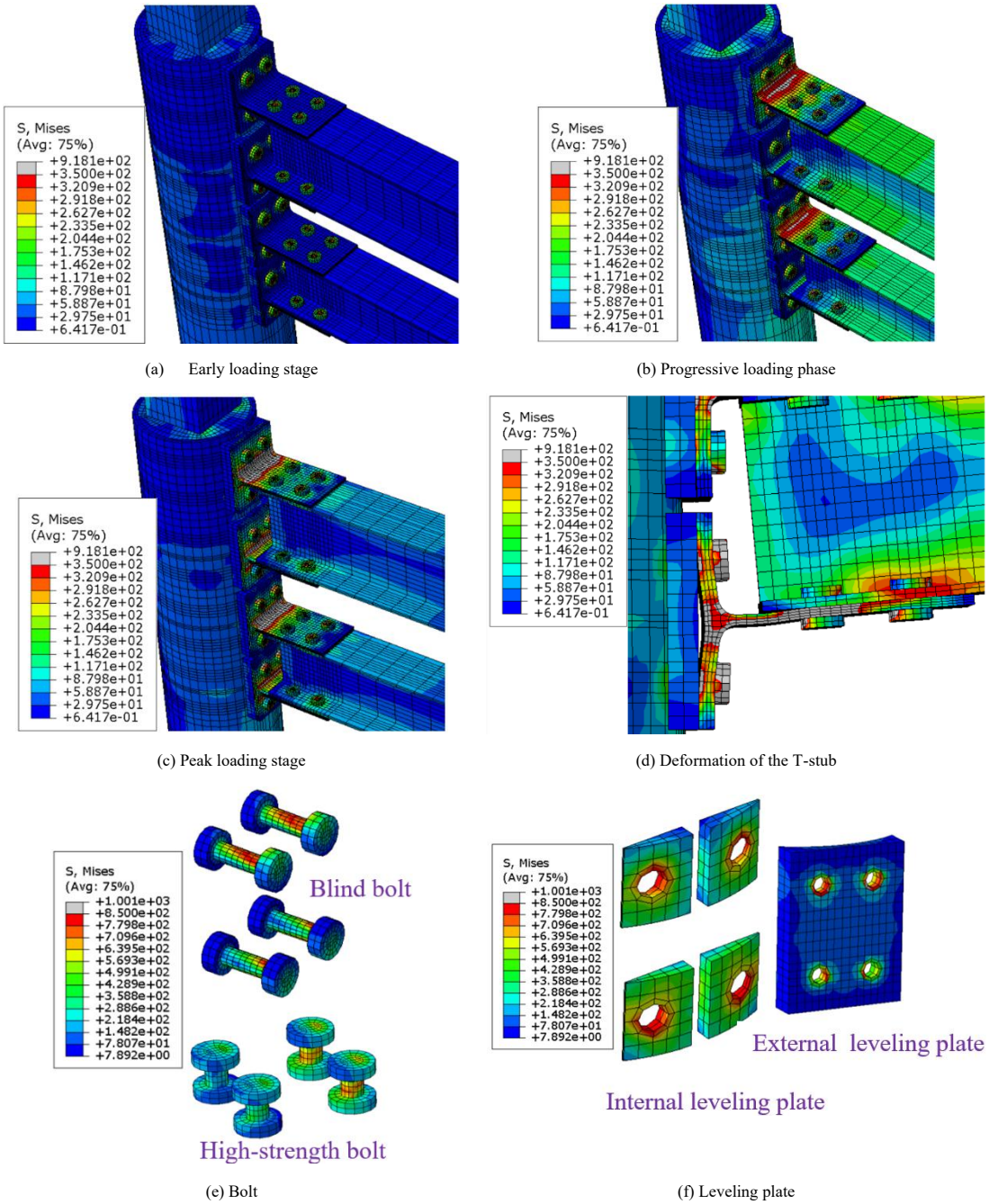


Fig. 15 Deformation of FEA

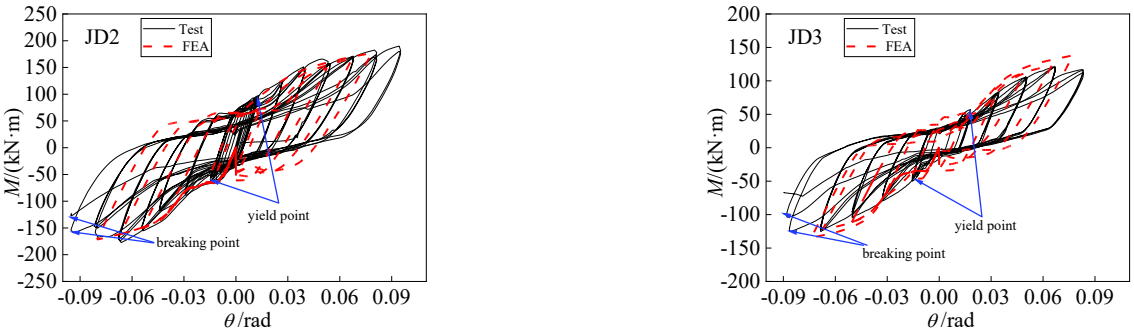
FEA also indicated that the bolt holes at the inner and outer leveling plates connecting the T-stub and the CHS column experienced high stress levels, due to the large beam-end displacements inducing significant deformation between the T-stub and the column, which caused the blind bolt shanks to press against the hole edges. Based on previous experimental experience in the research group, protective sleeves were added to the blind bolts in this test to reduce wear, and only minor wear of a few blind bolts was observed. The deformation of the core region in the FEA resembled that under monotonic loading, primarily because the simulation could not fully capture the cumulative deformation and damage under low-cycle reversed loading. Overall, however, the FEA results matched the experimental observations well, confirming the reliability of the model.

During the specimen design, the T-stub width was selected to comply with the layout requirements of traditional Chinese architecture. Based on prior studies in the research group, the flange and web thickness of the T-stub were specifically designed to ensure that the T-stub would deform preferentially, satisfying the strong-column weak-beam principle while maintaining adequate energy dissipation. Both the experimental and FEA results indicate that the blind bolt-T-stub connection in these irregular steel joints for MCTBs is structurally reasonable, with clear load transfer paths, expected deformation patterns, and favorable seismic performance.

4.3. Comparison of moment-rotation hysteresis curves

Fig. 16 presents the comparison of the moment-rotation hysteresis curves obtained from the experiment and the FEA. At the early loading stage, the hysteresis curves observed in the experiment were closely reproduced by the FEA results, indicating that the numerical model can accurately capture the initial stiffness and elastic response of the joint. As the loading progressed into the elasto-plastic stage, noticeable discrepancies between the experimental and numerical hysteresis loops were observed. The experimental curves exhibited pronounced asymmetry, with the negative peak moment being approximately 5%-8% higher than the positive peak. This asymmetry was mainly attributed to inevitable fabrication imperfections, initial geometric deviations of the specimen, and slight eccentricities in the loading system during the experiment, which were not included in the idealized numerical model. In addition, during cyclic loading, repeated opening and closing of cracks occurred in the T-stub flange region, accompanied by local plastic deformation of the flange. These cumulative damage effects led to stiffness degradation and energy dissipation in the experiment. In contrast, the finite element model adopted an idealized material constitutive relationship and did not explicitly consider crack propagation and damage evolution under low-cycle loading. Consequently, the hysteresis loops obtained from the FEA appear relatively fuller than those observed in the experiment.

Despite these differences, the overall development trend of the hysteresis curves and the peak moment values were reasonably predicted by the FEA results, indicating that the numerical model can effectively reflect the overall seismic response characteristics of the joint.



(a) JD2 (b) JD3

Fig. 16 Comparison of hysteresis curves of typical specimens

5. Damage index calculation and damage assessment

Seismic damage of structural components is typically evaluated based on deformation and hysteretic energy dissipation. To evaluate the seismic damage of components in steel MCTBs, Qi et al. [42] proposed a damage index (DDD) to evaluate the seismic damage of components in steel MCTBs, based on a two-parameter damage model that simultaneously considers deformation and energy dissipation. This index aims to quantitatively describe the influence of damage on the restoring force behavior of steel MCTB components [43]. Liu et al. [44]proposed recommended threshold ranges of the damage index for composite joints of concrete-filled steel tube columns with blind bolts under seismic action, which can be used to evaluate the damage level of structural components.

The results of this study indicated that the seismic damage of irregular steel joints in MCTBs was primarily caused by plastic deformation occurring at the T-stub region. In this study, a modified Park-Ang model that accounts for residual deformation accumulation was adopted to calculate the damage index D of the joint specimens. The calculation formula is expressed as follows in Eq. (5):

$$D=(1-\beta)\frac{\delta_{\mathrm{m}}-\delta_{\mathrm{y}}}{\delta_{\mathrm{u}}-\delta_{\mathrm{y}}}+\beta\frac{\int \mathrm{d}E}{f_{\mathrm{y}}\delta_{\mathrm{u}}} \tag{5}$$

where δ_{m} is the maximum response deformation under the seismic effect, δ_{u} and δ_{y} are the ultimate deformation capacity under monotonic loading and the yield deformation corresponding to the yield point of the specimen, respectively, f_{y} is the steel yield strength, dE is the cumulative energy dissipation of plastic deformation, and β is a non-negative weighting factor, which is taken as 0.025 for steel structures [45].

To determine a suitable value of the parameter β for the studied joints, the parameter was calibrated using the experimental results. Assuming that the damage index reaches D=1 at the ultimate failure state of the specimens, the parameter β was back-calculated for each specimen based on the experimental data using Eq. (6).

$$\beta=\frac{f_{\mathrm{y}}(\delta_{\mathrm{u}}-\delta_{\mathrm{m}})}{\int \mathrm{d}E-f_{\mathrm{y}}(\delta_{\mathrm{m}}-\delta_{\mathrm{y}})} \tag{6}$$

The calculated combination coefficients β are summarized in Table 6. The results indicate that the average value of β is 0.018 with a standard deviation of 0.003.

To further evaluate the influence of the parameter value on the damage index, a comparative analysis was carried out using two parameter values: β = 0.018 obtained from the experimental back-calculation and β = 0.025. The corresponding maximum damage indices of the specimens are presented in Table 7.

The results show that when β = 0.018, the calculated damage indices at the ultimate failure state are closer to the theoretical failure value D= 1, and the dispersion of the results is slightly reduced compared with those obtained using β = 0.025. Therefore, considering both calculation accuracy and parameter stability, β = 0.018 was adopted in the subsequent damage index analysis in this study.

The damage index D of the joints was calculated using Eq. (5), and the results are presented in Table 8. Based on the classification criteria listed in Table 6, the corresponding damage levels were determined, as illustrated in Fig. 17 and 18. The damage evolution of the joint can be divided into five stages: (i) In the initial loading stage, slight slippage occurred at the high-strength bolts connecting the web of the T-stub to the beam end. The damage index was less than 0.25, corresponding to minor damage (see Fig. 7a). (ii) Small gaps appeared between the upper and lower T-stub flanges and the external backing plate, with the damage index remaining below 0.45, still classified as minor damage (see Fig. 7a). (iii) Buckling occurred in the T-stub flange, and the joint entered a distinct plastic deformation development stage, corresponding to moderate damage (see Fig. 7b). (iv) A crack developed at the junction between the lower T-stub flange and the web, accompanied by significant slippage of the high-strength bolts. The damage expanded rapidly, corresponding to severe damage (see Fig. 7c). (v) In the single-beam joint, fracture occurred at the junction between the lower T-stub flange and the web. In the double-beam joint,

sequential fractures occurred at the corresponding junctions of the lower T-stubs in the lower and upper beams, resulting in complete damage (see Fig. 7d).

Under various loading levels, the damage indices of the double-beam joint specimens (JD1 and JD2) consistently remained lower than those of the single-beam joint specimens (JD3 and JD4), indicating a lower degree of damage. At the $4\delta_y$ loading level, the double-beam column joints were still in the moderate damage stage, whereas the single-beam column joints had already entered the severe damage stage. When the loading reached $5\delta_y$, the lower T-stub in the single-beam column joints fractured, and the damage index exceeded 1.0, indicating that complete failure had occurred. At this stage, the upper T-stub in the upper beam of the double-beam column joints remained undamaged, and the specimen had not yet reached complete failure. Further loading to $6\delta_y$ caused fracture of the upper T-stub in the lower beam of the double-beam column joints, marking the onset of complete failure.

The overall trend of the damage index curves obtained in this study was generally consistent with the experimental results reported by Liu et al. [44], primarily due to the similarity in joint configuration, as both adopted blind bolt-T-stub connections. However, RHS columns were used in the study by Liu et al., whereas CHS columns were adopted in the present study. Moreover, a pair of internal and external leveling plates was introduced at the interface between the column and the T-stub to optimize the bolt force transfer path and improve the overall mechanical stability of the connection. The similarity in damage evolution trends confirms that the proposed blind bolt–T-stub connection for irregular steel joints in MCTBs provides reliable structural performance. It achieves performance comparable to that of conventional RHS column connections and offers a feasible and adaptable solution for practical application in MCTBs.

Table 6
Calculation results of model parameter

Specimen	$f_y(\delta_u-\delta_m)$	$\int dE-f_y(\delta_m-\delta_y)$	β
JD1	655.22	38628.28	0.017
JD2	950.78	40131.50	0.023
JD3	305.18	19801.93	0.015
JD4	400.23	253.67.45	0.016

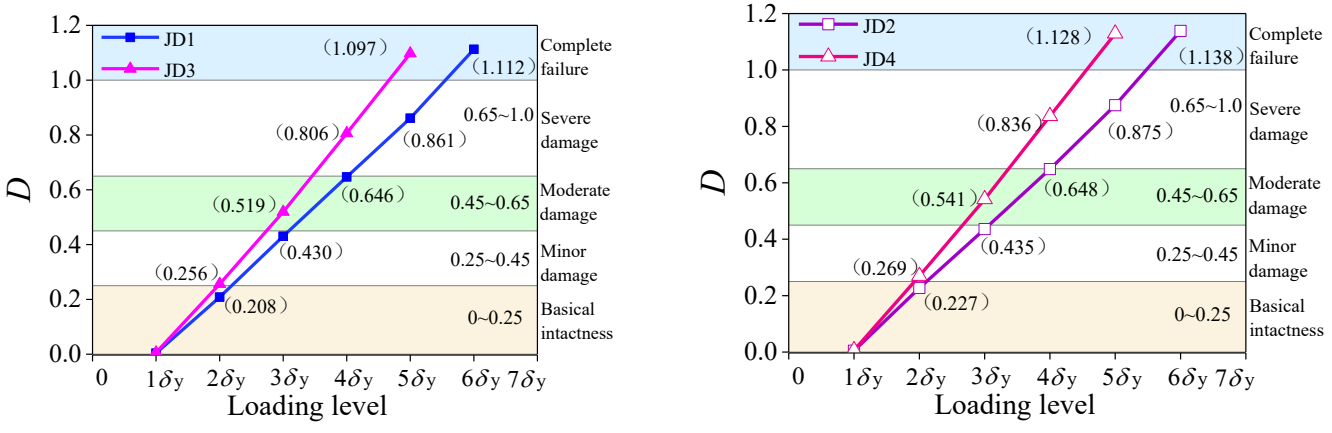
Table 7
Calculation result of damage index

Specimen No	D_{max} (β=0.018)	D_{max} (β=0.025)
JD1	1.112	1.156
JD2	1.138	1.192
JD3	1.097	1.135
JD4	1.128	1.178
Mean	1.118	1.1653
Standard Deviation	0.0180	0.0250

Table 8
Evaluation of seismic damage

Damage index	Damage description	Major events		Damage grade
		Single beam-column joint	Double beam-column joint	
0-0.25	None	☆	☆	Basical intactness
0.25-0.45	Damage occurs	☆□	☆□	Minor damage
0.45-0.65	Damage visible	□★◆	□★◆	Moderate damage
0.65-1	Damage develops	★◆●	★◆●	Severe damage
1-1.1	Destruct	▼	▼+▽	Complete failure

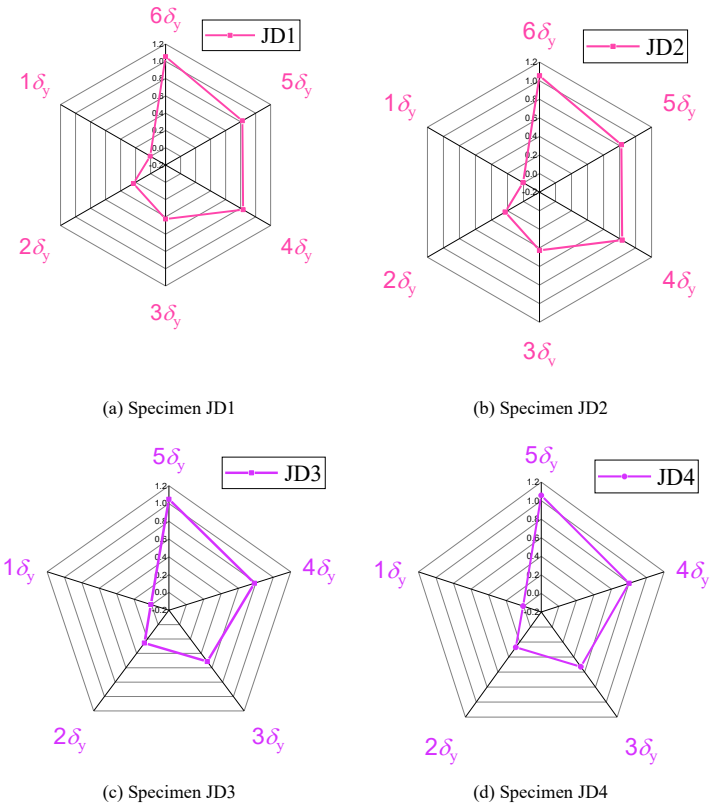
Notes：“☆”denotes the minor slippage of the high-strength bolts at the beam end; “□” denotes the minor gaps appeared between the flange of the T-stub and the outer leveling plate; “★”denotes the significant slippage occurred in the high-strength bolts at the beam end;“◆” denotes the buckling deformation of the T-stub flange;“●”denotes the cracking at the T-stub flange-web junction; “▽”denotes the fracture of the lower T-stub on the upper beam; “▼” denotes the fracture of the lower T-stub on the lower beam; “▼”+“▽” denotes the sequential fractures of the lower T-stubs on the lower beam and the upper beam.



(a) JD1 and JD3

(b) JD2 and JD4

Fig. 17 Damage index distribution



(a) Specimen JD1 (b) Specimen JD2

(c) Specimen JD3 (d) Specimen JD4

Fig. 18 Damage index curve

6. Conclusions

To address the key technical challenges associated with beam-column connections in prefabricated MCTBs, this study proposed a novel bolted connection scheme for irregular steel joints in MCTBs, based on blind bolt–T-stub assemblies. Low-cycle cyclic tests were conducted to investigate the mechanical performance of the proposed joints, and seismic damage evaluation was performed. The main conclusions are summarized as follows:

(1) All specimens exhibited failure modes primarily concentrated in the T-stub region, including flange buckling, crack initiation and propagation, and eventual fracture. These failure characteristics conformed to the strong-column weak-beam seismic design principle. In the case of double-beam column joints, the upper beam remained capable of bearing loads even after the lower beam had failed, effectively delaying overall structural failure. This behavior highlights the inherent load-carrying redundancy and improved seismic resilience of MCTBs.

(2) Under low-cycle reversed loading, all joints exhibited stable and full hysteresis loops, indicating excellent energy dissipation capacity and pronounced plastic deformation. Compared with single-beam joints, the double-beam configuration exhibited improved hysteretic behavior, higher ductility, and greater energy dissipation capacity. These enhancements are mainly due to the presence of an increased number of T-stub components in the double-beam column joints, which provided greater deformation capacity and delayed the initiation and propagation of damage.

(3) The double-beam column joints exhibited significantly higher load-bearing capacity than the single-beam column joints, and increasing the thickness of the T-stub further improved the overall structural performance. The observed stiffness degradation was primarily attributed to the accumulation of plastic deformation in the T-stub and slippage between the connecting components. Analytical results revealed that the double-beam column joints exhibited greater initial and residual stiffness, indicating enhanced deformation resistance and superior structural ductility.

(4) The refined finite element (FEA) model accurately captured the experimental deformation patterns, stress distribution, and moment–rotation hysteresis behavior of the joints, including the relative slippage of the double-beam connectors. Minor discrepancies between the numerical and experimental hysteresis loops can be attributed to material imperfections, steel fatigue, bolt slippage, and tolerances in the loading apparatus.

(5) Based on the damage assessment results obtained using the modified Park-Ang model, the double-beam column joints exhibited a significantly lower rate of damage accumulation than the single-beam column joints, along with a slower failure progression and superior seismic ductility. Notably, after the failure of the lower beam, the upper beam remained capable of bearing loads, thereby significantly enhancing overall structural stability and safety redundancy. These findings suggest that the double-beam design concept, inspired by traditional architectural practices, retains strong adaptability and practical engineering value in MCTBs constructed with steel structures.

(6) Compared with RHS column joints connected using blind bolts, the proposed irregular steel joints in MCTBs demonstrate comparable connection strength and ductility, while providing superior load-bearing capacity and enhanced safety redundancy due to the double-beam configuration, which is derived from the unique double-beam joint system evolved in ancient Chinese timber architecture. This connection strategy effectively addresses the engineering challenge of bolted assembly for closed-section columns in MCTBs and presents a practical and adaptable structural solution for their prefabricated and industrialized application.

It should be noted that only the T-stub thickness was varied in the present parametric study due to the constraints associated with using split T-sections from standard rolled H-sections and the architectural configuration requirements. The selected parameter range aims to ensure a ductile failure mechanism governed by T-stub yielding, while avoiding undesirable failure modes such as bolt pull-out or column wall damage. A more comprehensive parametric investigation will be conducted in future studies.

CRediT authorship contribution statement

Zhanjing Wu: Writing - review & editing, Resources. Jinshuang Dong: Writing - original draft, Data curation. Yan Sui: Writing - review & editing, Funding acquisition. Jianing Wang: Data curation, Formal analysis.

Declaration of competing interest

The authors declare that they have no known competing financial interests or personal relationships that could have appeared to influence the work reported in this paper.

Acknowledgments

The financial supports from the Natural Science Foundation of China (NSFC) with Grant No. 52008330 and Natural Science Foundation of Henan Province with Grant No. 252300421260 are gratefully acknowledged. This study is also supported by the Henan Provincial Department of Science and Technology Research Project with Grant No. 242102320318 and Hainan Province Major Science and Technology Program Funding Project with Grant

No. ZDKJ201803.

References

[1] Sha B, Xie L, Yong X, Li A. An experimental study of the combined hysteretic behavior of dougong and upper frame in Yingxian Wood Pagoda. Constr Build Mater 2021; 305: 124723.

[2] Zhang X, Liu L, Cui L, et al. Nonlinear dynamic analysis of ancient timber structures with rotary friction dampers. J Build Eng 2025, 100: 111707.

[3] Xue J, Qi L, Li Y, Che S, Wang G, Wei S. Quasi-static test on steel frame structure in traditional style buildings. J Build Struct 2017;38(8):133–40.

[4] Xue J, Ma L, Ge Z, Wu K, Liu Z. Experimental study on seismic performances of composite column with SRC square section and RC circular section in traditional style buildings. J Civ Eng 2018;51(2):21–31.

[5] Xue J, Ma L, Lin J, Wu K, Ge H. Experimental study on seismic behavior of imitated ancient building connections between concrete filled square steel tubular columns and reinforced concrete circular columns. J Build Struct 2018;39(4):37-44.

[6] Qi L, Xue J. Pseudo dynamic test and time-history analyses of traditional-style steel frame structures. International Journal of Steel Structures 2018;18(2):402-16.

[7] Xue J, Zhai L, Li H, Zhao X, Wu K. Seismic performances of RC-CFST composite frame in traditional style building under low cycle reversed loading. J Build Struct 2019;40(9):53-62.

[8] Qi L, Cao Y, Xue J, et al. Seismic performance evaluation and engineering application of modern Chinese traditional-style buildings: The state-of-art review. Structures, 2023, 56: 105022.

[9] Xue J, Wu Z, Sui Y, Ge H, Wu K. Experimental study and numerical analysis on aseismic performance of steel double-beams-column interior-joints in traditional style building. Eng Mech 2016;33(5):97-105.

[10] Qi L, Xue J, Leon RT. Experimental and analytical investigation of transition steel connections in traditional-style buildings. Eng Struct 2017;150:438-450.

[11] Xue J, Ma L, Wu Z, et al. Influence analysis of bracket set on seismic performance of steel eave columns in Chinese traditional style buildings[J]. Struct Des Tall Spec Build 2018, 27(8): e1462.

[12] Xue J, Ma L, Wu Z. Seismic Performance of Steel Joints Between Double Beams and Column in Chinese Traditional Style Buildings. Int J Steel Struct 2018;18(2):417-432.

[13] Xue J, Wu Z, Sui Y, Liu Z. Experimental study on seismic performance of steel double-beams column exterior joints in antique style building. J Build Struct 2015; 36(3):80-89.

[14] Xue J, Qi L, Yang K, Wu Z. Dynamic experimental study on single and double beam-column joints in steel traditional-style buildings. Struct Eng Mech 2017;63 (5):617-628.

[15] Qi L, Xue J, Sui Y, Wu Z. Smart retrofitting of irregular steel joints in traditional Chinese buildings by viscous dampers. Eng Struct 2021;228:111526.

[16] Yuan Z, Qi L, Xue J. Seismic performance of steel semi-rigid friction-damped joints with replaceable angles in modern Chinese traditional-style buildings. J Constr Steel Res 2023;207:107948.

[17] Yuan Z, Qi L, Xue G, et al. Resilient joints with SMA bar-shear friction damper (SSFD) device in steel modern Chinese traditional-style buildings: Seismic performance evaluation and optimized design. J Build Eng 2024, 82: 108300.

[18] Qi L, Yuan Z, Xue J. Experimental and numerical study on seismic performance of steel semi-rigid joints equipped with SMA bars and friction dampers. Eng Struct 2024, 301: 117320.

[19] Liu Y, Sun L, Zhang Y, et al. Proposed analytical models for bolted T-stubs to square hollow section column connection using thread-fixed one-side bolts under tension. J Build Eng 2022, 52: 104398.

[20] Tizani W, Wang Z, Hajirasouliha I. Hysteretic performance of a new blind bolted connectionto concrete filled columns under cyclic loading: an experimental investigation. Eng Struct 2013, 46(1): 535-546.

[21] Mahmood M, Tizani W, Sansour C. Effect of tube thickness on the face bending for blind-bolted connection to concrete filled tubular structures. Int J Civ Archit Struct Constr Eng 2014, 8(9): 897-903.

[22] Pitrakkos T, Tizani W. Experimental behaviour of a novel anchored blind-bolt in tension. Eng Struct 2013, 49: 905-919.

[23] Tizani W, Mahmood M, Dionysios B. Effect of concrete infill and slenderness on column-face component in anchored blind-bolt connections. J Struct Eng 2020, 146(04): 1-39.

[24] Cabrera M, Tizani W, Mahmood M, et al. Analysis of Extended Hollo-Bolt connections: Combined failure in tension. J Constr Steel Res 2020, 165: 105776.

[25] Cabrera M, Tizani W, Ninic J, et al. Experimental and numerical analysis of preload in Extended Hollo-Bolt blind bolts. J Constr Steel Res 2021, 186: 106885.

[26] Zhang Y, Liu M, Ma Q, et al. Yield line patterns of T-stubs connected by thread-fixed one-side bolts under tension. J Constr Steel Res 2020, 166: 105932.

[27] Liu M, Zhu X, Wang P, et al. Tension strength and design method for thread-fixed one-side bolted T-stub[J]. Eng Struct 2017, 150: 918-933.

[28] Dhanapal J, Das S, Ghaednia H, et al. Experimental study on structural performance of flow drilled connections in HSS members. J Constr Steel Res 2020, 164: 105786.

[29] Lee J, Goldsworthy HM, Gad EF. Blind bolted T-stub connections to unfilled hollow section columns in low rise structures. J Constr Steel Res 2010;66 (8):981-992.

[30] Lee J, Goldsworthy HM, Gad EF. Blind bolted moment connection to unfilled hollow section columns using extended T-stub with back face support. Eng Struct 2011;33(5):1710-1722.

[31] Wang W, Li M, Chen Y, et al. Cyclic behavior of endplate connections to tubular columns with novel slip-critical blind bolts. Eng Struct 2017, 148: 949-962.

[32] Gao X, Wang W, Teh L H, et al. A novel slip-critical blind bolt: Experimental studies on shear, tensile and combined tensile-shear resistances. Thin-Walled Struct 2022, 170: 108630.

[33] JGJ82-2011, Technical specification for high strength bolt connections of steel structures, 2011.

[34] Gao X, Wang W, Teh L H. Experimental and numerical investigations of tensile behavior of slip-critical blind bolts anchored in concrete-filled steel tubes. Structures 2023, 55: 354-369.

[35] Jiao W, Wang W, Chen Y, et al. Seismic performance of concrete-filled SHS column-to-beam connections with slip-critical blind bolts. J Constr Steel Res 2020, 170: 106075.

[36] GB 50017-2017, National Standard of People's Republic of China. Code for Design of Steel Structures, China Plan Press, Beijing, 2017. (In Chinese)

[37] Liang, S. A Pictorial History of Chinese Architecture; MTT Press: Boston, MA, USA, 1984.

[38] GB50011-2010; Code for Seismic Design of Buildings. China Architecture & Building Press: Beijing, China, 2010. (In Chinese)

[39] GB50661-2011; Code for Welding of Steel Structures. Standards Press of China: Beijing, China, 2011. (In Chinese)

[40] GB/T228.1-2021; Metallic Materials-Tensile Testing at Ambient Temperature. Chinese Standard Press: Beijing, China, 2021. (In Chinese)

[41] JGJ101-2015; Specification of Testing Methods for Earthquake Resistant Building. China Building Industry Press: Beijing, China, 2015. (In Chinese)

[42] Qi L, Xue J, Xu D. Experimental study and theoretical model of seismic behavior of steel transition columns considering damage effect. J Build Struct 2021;42(S1): 239-248

[43] Usami T, Kumar S. Inelastic seismic design verification method for steel bridge piers using a damage index based hysteretic model. Eng Struct 1998;20(4-6): 472-480.

[44] Liu H, Yan S, Wang X, et al. Experimental study on the seismic damage behavior of composite joints of concrete-filled steel tube column with blind bolts. Structures 2024;70: 107767.

[45] Xiao S, Bu X, Chen Y, et al. Investigating the damage-based seismic performance of the blind bolt-connected steel framework. Structures 2024, 69: 107388.

[46] EN 1993-1-8; Eurocode 3: Design of Steel Structures-Part 1-8: Design of Joints. European Committee for Standardization (CEN): Brussels, Belgium, 2005.

Advanced Steel Construction – Vol. 22 No. 5 (2026) 499–507
DOI:10.18057/IJASC.2026.22.5.2

APPLICATION OF PHYSICS-INFORMED NEURAL NETWORKS FOR ANALYSIS SLENDER STEEL SLOPE PILES

Yi Yang [1], Si-Wei Liu [2], Lei-Lei Liu [3] and Wei-Hang Ouyang [2, *]

[1] *School of Science, Harbin Institute of Technology, Shenzhen 518055, P. R. China*
[2] *Department of Civil and Environmental Engineering, The Hong Kong Polytechnic University, Hong Kong SAR, P. R. China*
[3] *Key Laboratory of Metallogenic Prediction of Nonferrous Metals and Geological Environment Monitoring, Ministry of Education, School of Geosciences and Info-Physics, Central South University, Changsha, 410083, P.R. China*
** (Corresponding author: E-mail: weihang.ouyang@connect.polyu.hk)*

ABSTRACT

Physics-informed neural networks (PINNs) have emerged as an efficient and powerful tool for solving partial differential equations by seamlessly integrating governing physical laws with machine learning frameworks, differing from traditional data-driven approaches. In mountainous regions prone to landslides, such as Hong Kong, steel slope-stabilizing piles are critical for enhancing slope stability against sliding forces and complex soil-structure interactions (SSI). Conventional numerical methods, including the finite element method (FEM) and limit analysis method (LAM), have effectively evaluated the stabilizing effects of slope piles on slope reliability and failure mechanisms, often relying on continuum constitutive models. However, these approaches are computationally intensive and struggle with nonlinear behaviors and uncertainties in spatially variable soil properties. This study advances the application of PINNs to the nonlinear analysis of slender slope-stabilizing piles, incorporating complex SSI and distributed sliding forces. A comprehensive PINN framework is developed, embedding the governing equations, boundary conditions, and external loading effects (uniform, trapezoidal, and parabolic distributions) into the network architecture. The methodology is verified against analytical solutions and benchmark FEM simulations, demonstrating robust predictions of deflection patterns, internal forces, and bending moments under highly nonlinear SSI. Furthermore, uncertainty quantification reveals competitive predictive accuracy and computational efficiency compared to conventional FEM. Numerical results indicate that the PINN framework reliably captures nonlinear responses, even in scenarios with depth-dependent soil stiffness and p-y relationships, offering a promising alternative to FEM for real-time geotechnical challenges. This represents a novel application of PINNs in slope engineering, bridging physical constraints with data efficiency to enhance design optimization and landslide disaster mitigation.

ARTICLE HISTORY

Received: 1 December 2025
Revised: 14 February 2026
Accepted: 14 February 2026

KEYWORDS

Physics-informed neural networks;
Soil-structure interaction;
Steel slope piles;
Nonlinear analysis;
Machine learning

Copyright © 2026 by The Hong Kong Institute of Steel Construction. All rights reserved.

1. Introduction

In mountainous cities, natural and cut slopes are commonly reinforced with slope-stabilizing steel piles, which are widely used in slope upgrading and maintenance projects to meet required safety standards [1]. Slope piles play a pivotal role in enhancing slope stability by resisting sliding forces from unstable soil masses, particularly in high-steep rock slopes prone to landslides triggered by rainfall, earthquakes, or engineering excavations [2,3]. For instance, field investigations and monitoring have shown that faults near the rear edge of slopes exacerbate crack propagation and hydraulic conductivity, leading to platform collapse, where slope piles combined with anti-slide measures (e.g., anchor cables) effectively mitigate these risks [2]. Similarly, physical model experiments demonstrate the synergistic action between tap-like arbor root systems and anti-slide piles, improving anti-sliding forces and slope integrity [4]. The failure mechanisms of such systems often involve complex soil-structure interactions (SSI), including asymmetric failure modes in laterally loaded piles near slope crests, where soil resistance is influenced by slope gradients and embedment depths [5,6]. Beyond traditional geotechnical settings, recent structural mechanics studies have highlighted the criticality of second-order (geometric nonlinearity) effects and their tight coupling with SSI in slender members; for example, PINN-enabled second-order analysis of steel beam-columns demonstrates that embedding governing equations and boundary conditions can yield accurate large-deflection predictions without dense data, offering a compelling paradigm for pile-like members under lateral actions [7].

Extensive research has investigated the stabilizing effects of slope piles using traditional numerical methods. Finite element methods (FEM) and finite difference methods (FDM) have been employed to simulate slope stability, accounting for soil-pile interactions and width-limited failure modes [8,9]. These approaches rely on continuum mechanics constitutive models or discrete element contact models to predict pile bearing capacity, deflection, and internal forces under lateral loads. For example, modified strain wedge models have analyzed laterally loaded piles in sloping ground, revealing asymmetric failure modes and the influence of slope gradients on capacity ratios [5,6]. Reliability-based optimizations, such as first-order reliability methods (FORM) and weighted uniform simulations, have further quantified uncertainties in soil strength, providing Pareto-optimal designs for pile parameters like length, spacing, and diameter [9,10]. Hybrid response surface methods combining support vector machines and Kriging have assessed system reliability in pile-reinforced slopes, highlighting critical reinforcement ratios and optimal pile locations [11]. Displacement-based methods have evaluated the stability of finite soil slopes in front of piles, considering landslide thrust and factors like slope gradient and pile spacing [3]. These methods yield accurate results for deterministic and probabilistic analyses but are computationally demanding, especially for nonlinear SSI, spatial variability in soil properties, and repeated simulations in reliability assessments. On the modeling side of SSI itself, element-level formulations that directly incorporate nonlinear p–y and t–z relationships and realistic earth pressure distributions have proven highly efficient for laterally loaded piles and sheet piles, reducing the need for dense spring discretization while preserving second-order effects [12]. Such advances motivate physics-based learning frameworks that can inherit these SSI regularities while avoiding heavy meshing.

Recently, the rapid development of artificial intelligence has introduced data-driven methods, such as neural networks, for geotechnical predictions [13,14]. However, these approaches often require large datasets from experiments or numerical simulations, limiting their applicability when data is sparse. To address this, physics-informed neural networks (PINNs) embed governing physical equations directly into the network, enabling solutions to partial differential equations (PDEs) without extensive data [15]. PINNs have been applied in fluid mechanics, consolidation analysis, and tunneling-induced deformations, demonstrating advantages in handling nonlinearities and uncertainties [16-18]. Despite these advances, PINN applications in slope engineering remain limited, particularly for nonlinear slope-stabilizing piles under distributed sliding forces. In the pile engineering, Ouyang et al. [19] recently established a PINN framework capable of handing non-differentiable soil-structure interactions (SSI). However, while Ref [19] successfully resolved the discontinuity issues in soil resistance, it focused primarily on simplified loading conditions. It did not address the mathematical complexity of integrating depth-dependent, distributed sliding forces (landslide thrusts) into the large-deflection governing equations, which is a critical requirement for realistic slope stability analysis.

Building upon the foundational work on SSI in Ref [19], this study introduces a distinct mathematical advancement: the integration of complex, spatially varying sliding force distributions into the PINN architecture. Unlike previous studies that modeled external loads as concentrated forces or simple constants, this work derives and embeds novel integral formulations for trapezoidal and parabolic landslide thrusts directly into the loss function's equilibrium constraints. This represents a significant physical and mathematical leap, enabling the PINN to capture the cumulative shear and moment effects

induced by realistic landslide geometries. This study develops a PINN framework for the nonlinear analysis of slender slope-stabilizing piles, incorporating complex SSI and sliding force distributions (uniform, trapezoidal, parabolic). Unlike traditional FEM, which depends on mesh-based computations and constitutive models, the PINN integrates PDEs, boundary conditions, and loading effects into a loss function, optimized via automatic differentiation. This offers several benefits: (1) computational efficiency, reducing simulation times for uncertainty quantification; (2) scalability for real-time engineering, handling non-differentiable SSI without explicit meshing; (3) robustness to sparse data, leveraging physical constraints for accurate predictions of deflections, bending moments, and forces; and (4) enhanced uncertainty handling, outperforming FEM in probabilistic scenarios (as verified against benchmarks). The framework is validated against analytical solutions and FEM for various loading cases, with uncertainty quantification assessing predictive accuracy. Results underscore PINNs as a scalable alternative for geotechnical challenges, filling a gap in slope engineering applications. The present PINN framework for large-deflection analysis of slender slope-stabilizing piles can be seen in Fig. 1.

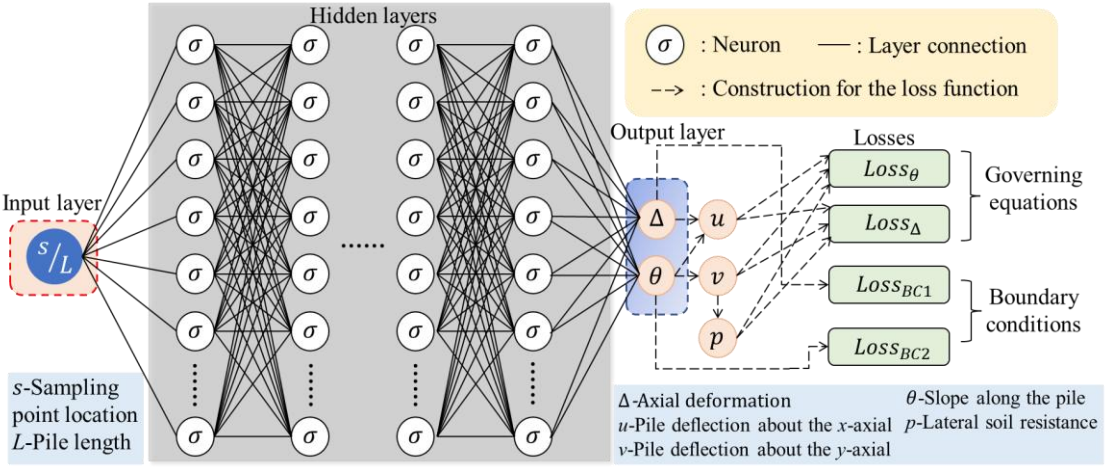


Fig. 1 The architecture of the corresponding PINN

2. Governing equations

This study develops a Physics-Informed Neural Network (PINN) methodology for analyzing slender slope-stabilizing piles, explicitly incorporating both nonlinear soil-structure interactions (SSIs) and soil sliding forces. The neural network (NN) architecture rigorously embeds fundamental physical constraints to ensure solution reliability. Subsequent sections present comprehensive derivations of the governing equations that mathematically formalize these underlying physical phenomena.

2.1. Assumptions

The following assumptions are employed, including:

(1) Pile materials exhibit homogeneous and isotropic linear elastic behavior, conforming to Hooke's constitutive law.
(2) Structural deformation adheres to Euler-Bernoulli beam kinematics, neglecting shear deformation effects (large-diameter piles).
(3) Soil-pile interaction is characterized by p-y curves representing lateral soil resistance distribution along the pile shaft.

2.2. Mechanical model

This mechanical model develops formulations for both deflections and internal force distributions along the pile. Deflections are described in the global O–x–y frame and the local O–u–v frame. As shown in Fig. 2, the total deflection along the x- and y-axes splits into two contributions: one from the rotation of each pile segment and another from its axial deformation after rotation. Hence, the deflections in the u and x directions can be written as:

$$u(y)=\int_0^y du_\theta+\int_0^y du_\Delta \tag{1}$$

$$x(y)=\int_0^y dy_\theta+\int_0^y dy_\Delta \tag{2}$$

The internal force equilibrium conditions for any pile segment above depth y (Fig. 2) can be derived from the computed displacement field along the pile length:

$$M(y)=-F_{y,Top}[x|_{y=L_p}-x(y)]+F_{x,Top}[u|_{y=L_p}+L-u(y)-y]+M_{Top}+M_s(y) \tag{3}$$

$$F_y(y)=F_{y,Top} \tag{4}$$

where M represents the bending moment distribution along the pile; F_x and F_y denote the internal forces in the x and y directions, respectively; $F_{x,Top}, F_{y,Top}$, and M_{Top} correspond to the applied external forces and bending moment at the pile head; M_S and F_S are the forces induced by the lateral soil resistance; and L_p indicates the length of the pile. When the $p-y$ relations are given, M_S and F_S can be written as:

$$M_S(y)=\int_y^{L_p}[t+u(t)-y-u|_{t=y}][p(t)+q(t)]dt \tag{5}$$

$$F_S(y)=\int_y^{L_p}[p(t)+q(t)]dt \tag{6}$$

where p represents the distributed lateral soil pressure acting on the pile, q denotes the imposed sliding force distribution along the pile length

Through vector decomposition following the parallelogram law, the resultant axial force (P) and shear force (V) acting on the pile can be expressed as:

$$P(y)=\cos\theta F_y(y)-\sin\theta F_x(y) \tag{7}$$

$$V(y)=\sin\theta F_y(y)+\cos\theta F_x(y) \tag{8}$$

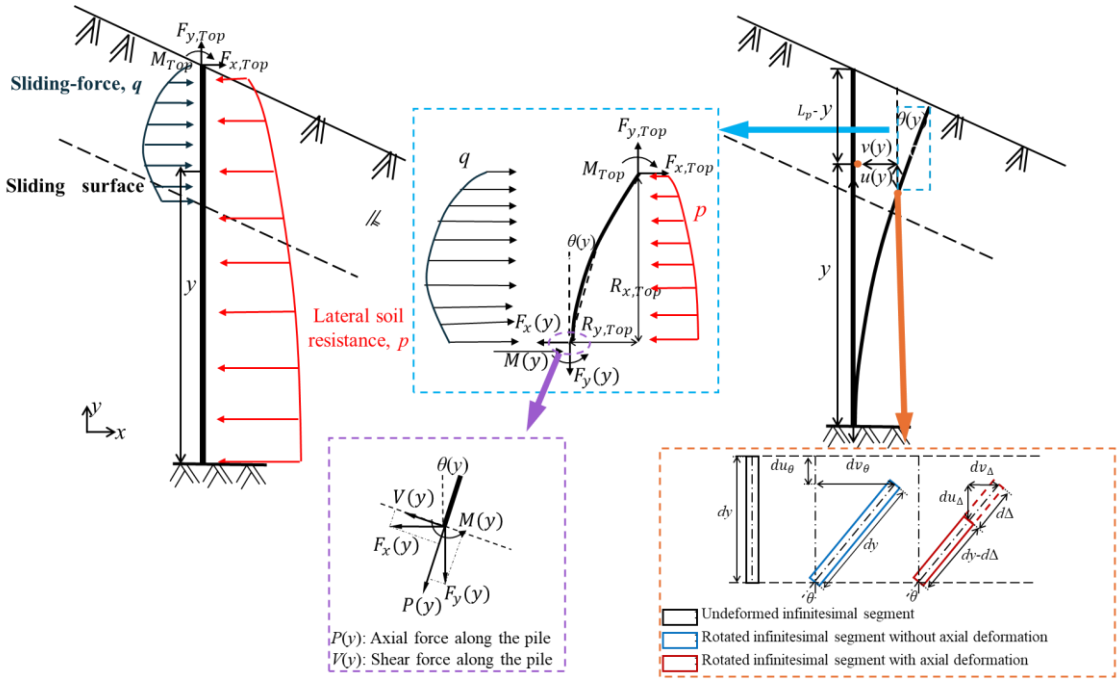


Fig. 2 Mechanical model of slender slope pile

2.3. Governing equation

The pile cross-sections maintain planarity following deformation, with the slope along the pile axis characterized by:

$$\frac{M(y)}{EI}=\frac{d\theta(y)}{dy} \tag{9}$$

The axial strain distribution is governed by the normal force relationship:

$$\frac{P(y)}{EA}=\frac{d\Delta(y)}{dy} \tag{10}$$

where A represents the pile's cross-sectional area.

2.4. Boundary condition

Since the rotation and displacement at the base of a slender slope pile are fixed, they are neglected here. Consequently, the base boundary conditions are prescribed as:

$$\Delta\big|_{y=0}=0 \tag{11}$$

$$\theta\big|_{y=0}=0 \tag{12}$$

At the pile head, three distinct boundary condition cases are considered, as detailed below:

$$EA(\cos\theta\frac{d\Delta}{dy}\Big|_{y=L_p}-EI(\sin\theta\frac{d^2\theta}{dy^2})\Big|_{y=L_p}=F_{y,Top} \tag{13}$$

$$EA(\sin\theta\frac{d\Delta}{dy}\Big|_{y=L_p}+EI(\cos\theta\frac{d^2\theta}{dy^2})\Big|_{y=L_p}=F_{x,Top} \tag{14}$$

$$EI\frac{d\theta}{dy}\Big|_{y=L_p}=M_{Top} \tag{15}$$

3. Physics-informed neural networks framework

3.1. Networks architecture

The developed PINN for slope pile analysis consists of two fundamental components:

(1) Artificial neural network architecture and (2) Physics-constrained loss functions.

The neural network employed in this machine learning solution represents a layered mathematical model, where data propagates unidirectionally from input nodes through multiple hidden layers to the output layer (Fig. 3).

Accordingly, we can train a Neural networks (NN) model written as:

$$N(y^0;\theta):=[\Delta_N,\ \ \theta_N]\approx x(y^0) \tag{16}$$

where $[\Delta_N,\ \ \theta_N]$ describes the NN model output to approximate the exact solution; and y^0 as the input feature describes the normalized embedded depth:

$$y^0:=(\bar{y})\ \text{where}\ \bar{y}=\frac{y}{L_p} \tag{17}$$

where y represents the spatial coordinate along the pile axis; and $N(y^0;\theta)$ denotes a fully connected neural network operator mapping input feature y to outputs through parameter set θ.

As illustrated in Fig. 3, this network comprises N hidden layers followed by an output layer. Each i^{th} hidden layer contains n_i neurons and receives from the previous layer a vector $y_{i-1}\in\mathbb{R}^{n(i-1)}$, which is first subjected to a linear transformation:

$$f_i(y^{i-1}):=W^i y^{i-1}+b^i \tag{18}$$

Here, f_i represents the linear transform at layer i; its weight matrix $\boldsymbol{W}^i\in\mathbb{R}^{n_i\times n_{i-1}}$ and the bias vector $\boldsymbol{b}^i\in\mathbb{R}^{n_i}$ are parameters set $\theta=\{W^i,b^i\}_{i=1}^{N+1}$. $\sigma_i(\cdot)$ is applied element-wise activation function to $f_i(x^{i-1})$ output before it's passed to the next layer. Consequently, the network can be written as the following composition:

$$N(y^0,\theta)=(f^{N+1}\circ\sigma^N\circ f^N\circ\sigma^{N-1}\cdots\circ\sigma^1\circ f^1)(y^0) \tag{19}$$

where $\circ$ denotes the composition operator.

Common activation functions in PINN literature include Sigmoid, ReLU, Tanhshrink and Tanh. Following comprehensive evaluations by Ouyang et al. [20], this study adopts distinct activation functions as follows:

$$\sigma^i(y)=\begin{cases} Tanhshrink(y) & when\ i\ =\ 1\ or\ N \\ Tanh(y) & when\ i\ =\ 2,3,...,N\text{-}1 \end{cases} \tag{20}$$

in which:

$$Tanh(y)=\frac{e^{y}-e^{-y}}{e^{y}+e^{-y}} \tag{21}$$

$$Tanhshrink(y)=Tanh(y)-y \tag{22}$$

The PINN architecture comprises 3 hidden layers, with each layer containing 50 neurons. The network is trained using the Adam optimizer with an initial learning rate of 0.0005. The computational domain is discretized using 50 collocation points distributed along the pile shaft. The training process allows a maximum of 50,000 epochs, implemented with an early stropping mechanism (patience = 2000) to prevent overfitting and enhance computational efficiency. A hybrid activation configuration is employed: *Tanhshrink* for the first and third layers, and *Tanh* for the second layer.

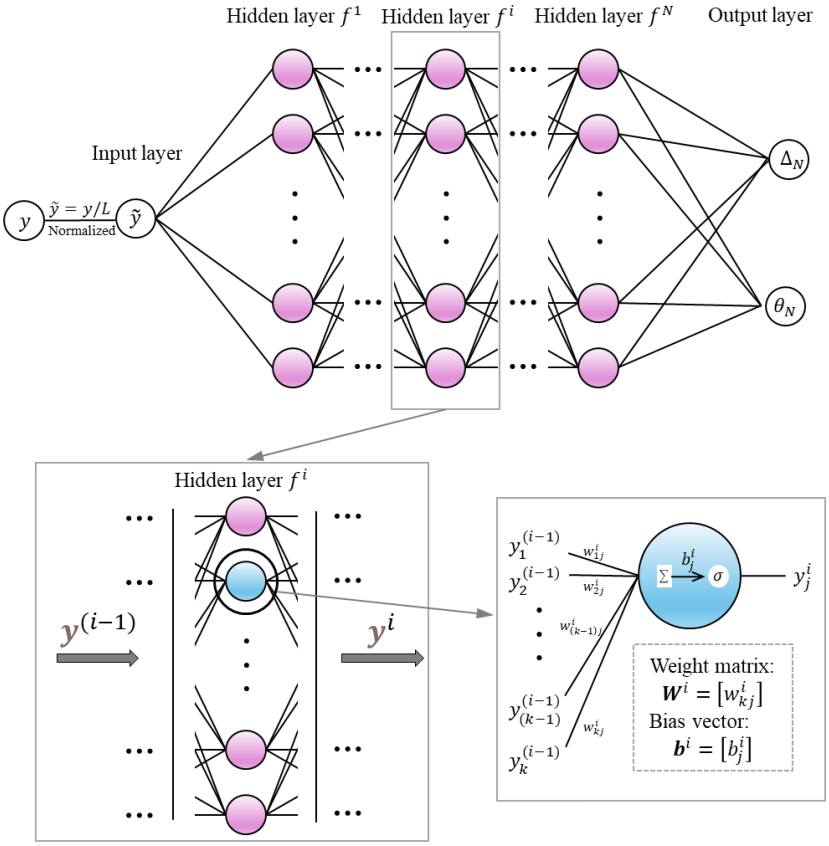


Fig. 3

3.2. Loss function

The PINN architecture incorporates a composite loss function that simultaneously quantifies [20]:

(i) the residual error in satisfying the governing differential equations, and

(ii) the deviation from prescribed boundary conditions.

$$L=L_G+L_B+L_T \tag{23}$$

where L is the loss function; and the subscripts $_G$, $_B$ *and* $_T$ denote the loss terms by the governing equation, the bottom boundary condition, and the top boundary condition.

$$L=MSE_\theta+MSE_\Delta+MSE_{B,\theta}+MSE_{B,\Delta}+MSE_{T,\mathrm{u}}+MSE_{T,\mathrm{y}}+MSE_{T,\theta} \tag{24}$$

In this study, the loss function formulation inspired by finite element method (FEM) convergence criteria. Unlike conventional approaches that directly minimize mean squared error (MSE), our proposed formulation establishes the loss function as normalized residual terms relative to their current magnitudes. Furthermore, we introduce a set of factors to properly normalize each component of the loss function.

$$L_G=MSE_\theta N_\theta+MSE_\Delta N_\Delta \tag{25}$$

$$L_B=MSE_{B,\theta}N_{B,\theta}+MSE_{B,\Delta}N_{B,\Delta} \tag{26}$$

$$L_T=MSE_{\mathrm{T},u}N_{\mathrm{T},u}+MSE_{T,x}N_{\mathrm{T},u}+MSE_{T,\theta}N_{\mathrm{T},u} \tag{27}$$

Where the related normalization factor of the governing Loss denote as N_θ and N_Δ; the bottom normalization factor describe as $N_{B,\theta}$ and $N_{B,\Delta}$; and the free top normalization factor represent $N_{\mathrm{T},u}$, $N_{\mathrm{T},x}$ *and* $N_{\mathrm{T},\theta}$ are set as:

$$N_\theta=\frac{1}{n}\sum_{i=1}^{n}\left(\frac{M}{EI}\Big|_{\bar{y}=\bar{y}_i}\right) \tag{28}$$

$$N_\Delta=\frac{1}{n}\sum_{i=1}^{n}\left(\frac{P}{EI}\Big|_{\bar{y}=\bar{y}_i}\right) \tag{29}$$

$$N_{B,\theta}=\frac{1}{n}\sum_{i=1}^{n}\left(\theta_N\big|_{\bar{y}=\bar{y}_i}\right) \tag{30}$$

$$N_{B,\Delta}=\frac{1}{n}\sum_{i=1}^{n}\left(\Delta_N\big|_{\bar{y}=\bar{y}_i}\right) \tag{31}$$

$$N_{T,u} = N_{T,x} = N_{T,\theta} = (F^2_{y,Top} + F^2_{x,Top} + M^2_{Top}) \quad (32)$$

The normalization factors (e.g., dividing by L^4 or EI) are fixed constants chosen to non-dimension the governing equations, ensuring numerical stability by keeping values near unity.

4. Validation examples

This section reevaluates three case studies from Ouyang et al. [21] to verify the accuracy of the proposed PINN approach for slender slope piles, focusing particularly on its treatment of sliding force distributions. This is the first study of slope piles by PINN.

4.1. Example 1 - Analytical and PINN comparative analysis of slope piles

To verify the proposed PINN framework's effectiveness in analyzing slope piles subjected to variable sliding forces, we first establish benchmark solutions by solving the governing partial differential equation:

$$EI\frac{d^4x}{dh^4} + kx - q(h) = 0 \quad (33)$$

where E and I denote the pile's elastic modulus and polar moment of inertia, respectively; x denotes the lateral deflection; h is the embedded depth; k corresponds the soil's lateral stiffness; and q defines the lateral - load intensity per unit length. Closed form analytical solutions are derived for three load distributions—uniform, trapezoidal and parabolic—assuming negligible axial loads. To quantitatively assess the PINN's predictive accuracy, multiple error metrics are evaluated, including: the relative mean squared error (rMSE); the relative mean absolute error (rMAE); the relative root mean **squared** error (rRMSE); and R^2.

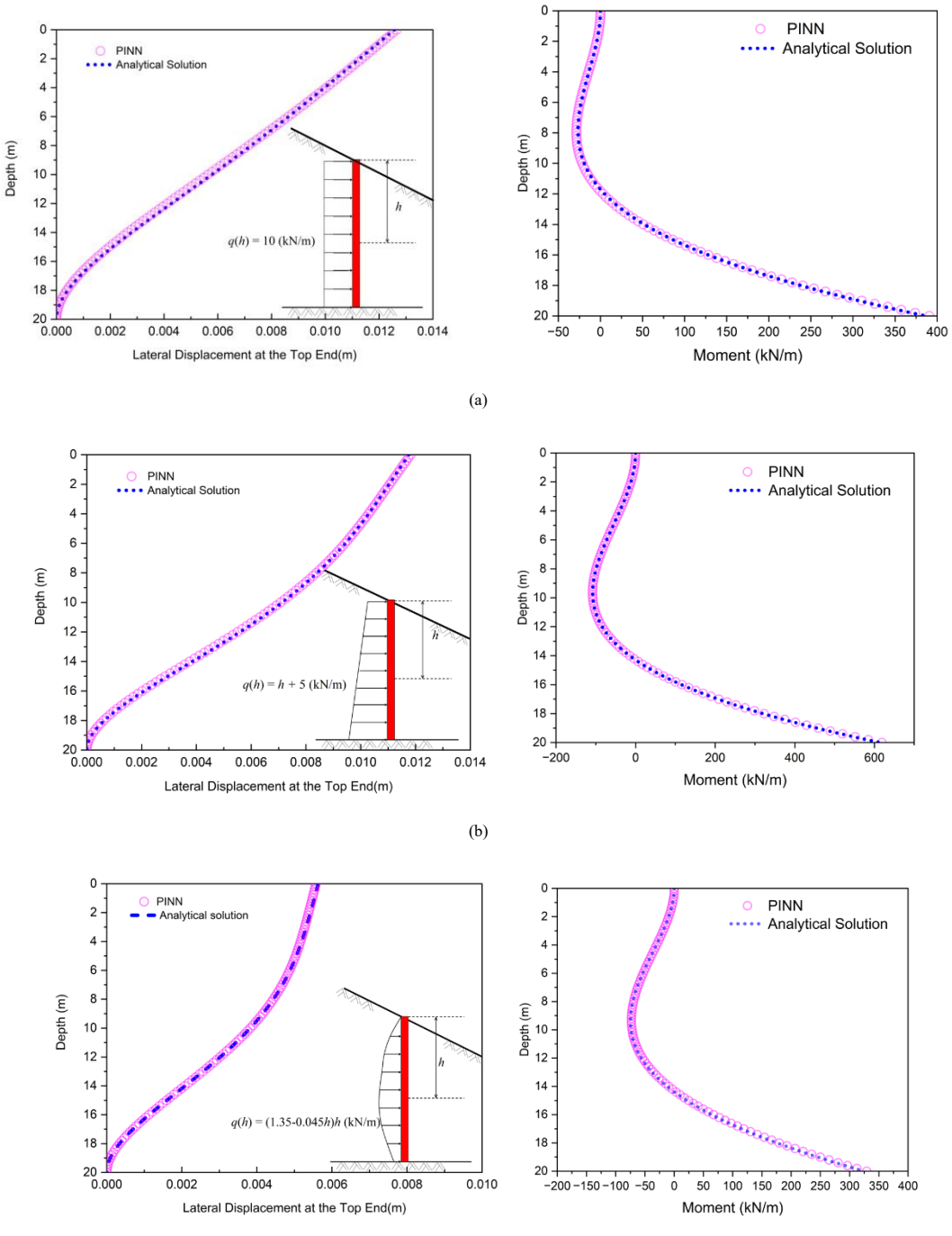


Fig. 4 Comparative analysis of pile behavior under varying lateral load distributions: (a) uniform, (b) trapezoidal, and (c) parabolic loading conditions

Table 1
Correlation analysis of analytical method and PINN

Correlations	Lateral deformation			Moment		
	Uniform	Trapezoidal	Parabolic	Uniform	Trapezoidal	Parabolic
rMSE	0.00031	0.00008	0.00005	0.00065	0.00014	0.00104
rMAE	0.01517	0.00709	0.00443	0.02071	0.00758	0.02588
rRMSE	0.01755	0.00890	0.00675	0.02546	0.01190	0.03220
R^2	0.99934	0.99977	0.99997	0.99973	0.99993	0.99948

For uniform loading the lateral deflection results predicted by the PINN align almost perfectly with the analytical solution. The maximum deflection occurs at the pile top, reflecting the constant nature of the applied sliding force along the pile length. Error metrics such as rMSE (0.00031), rMAE (0.01517), and rRMSE (0.01755) confirm the exceptional accuracy of the PINN in capturing the deflection profile. The bending moment distribution, which is linear under uniform loading, is also predicted with high accuracy, though the rRMSE for moments (0.02546) is slightly higher due to the increased sensitivity of moment calculations. Overall, the PINN demonstrates excellent performance under this simplest loading case, as shown in Fig. 4a.

Under trapezoidal loading, where the intensity of the sliding force increases linearly along the pile length, the deflection profile becomes nonlinear. The PINN effectively captures this behavior, with error metrics remaining low (rMSE ≈ 0.00008, rMAE ≈ 0.00709, rRMSE ≈ 0.00890), and the R^2 value exceeding 0.999. For bending moments, which exhibit a nonlinear distribution, the PINN predictions closely match the analytical solution, though small deviations are observed near the pile top where moments are minimal. The rRMSE for moments (0.01190) is moderate but acceptable, indicating the PINN robustness in handling more complex load distributions. These results are illustrated in Fig. 4b.

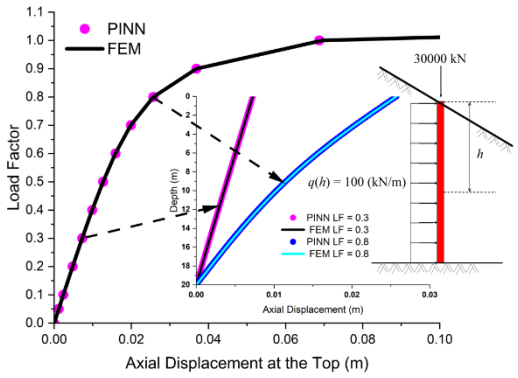
Parabolic loading introduces the greatest complexity, with the sliding force intensity varying quadratically along the pile length. Despite the nonlinear nature of this loading, the PINN successfully predicts both the deflection and bending moment distributions with high accuracy. Deflection errors remain minimal (rMSE ≈ 0.00005, rMAE ≈ 0.00443, rRMSE ≈ 0.00675), and the R^2 value for deflection is exceptionally high at 0.99997. For bending moments, the PINN captures the rapid curvature changes near the pile top, though the rRMSE (0.03220) is slightly higher compared to the other cases. These results confirm the PINN capability to handle highly nonlinear load distributions while maintaining reliable accuracy, as demonstrated in Fig. 4c.

4.2. Example 2 - Comparative nonlinear analysis of slope piles under varied sliding force distributions by PINN and FEM

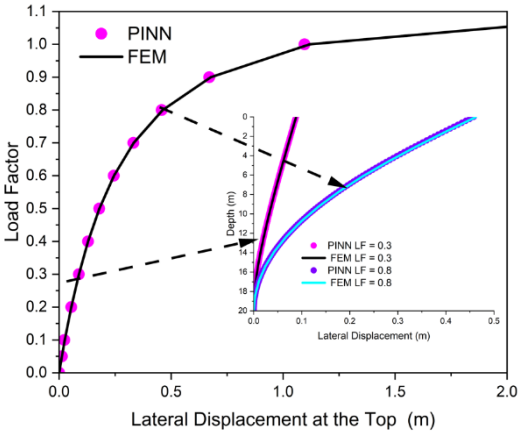
The investigation examines a 20m long reinforce concrete pile (diameter = 1 m, E = 32.5 GPa) embedded in a slope, analyzing its nonlinear deformation response under three distinct lateral loading conditions: uniform, trapezoidal, and parabolic distributions. The pile head is free and carries an axial compression of 30000 kN, while the base is fixed. The surrounding soil is assigned a lateral stiffness of 500 kN/m, and additional sliding - force components are introduced to mimic realistic slope conditions. FEM is employed as the benchmark solution against which the proposed PINN framework is evaluated.

Fig. 5 illustrates the axial displacement, lateral displacement, and bending moment results for the pile under uniform loading. Under uniform sliding force conditions, the bending moment distribution varies linearly along the pile axis. Similarly, the lateral displacement shows a smooth, parabolic curve, reaching its peak at the pile top. The PINN predictions closely match the FEM results for both axial and lateral displacements, with negligible differences in the displacement profiles. For bending moments, a slight discrepancy is observed near the pile bottom; this is attributed to the sensitivity of the moment calculation to small variations in displacement. However, the error metrics remain small, and the R^2 value indicates a near-perfect correlation between the PINN and FEM results.

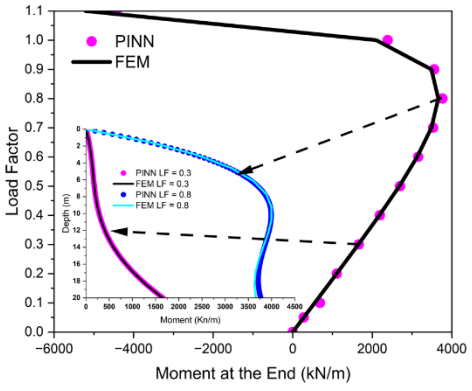
Fig. 6 presents the results for trapezoidal loading, where the sliding force intensity increases linearly along the pile length. This leads to a nonlinear variation in bending moments, with higher values concentrated near the pile bottom. The lateral displacement profile also becomes more curved compared to the uniform loading case. The PINN successfully captures these trends, and the displacement predictions align closely with the FEM results. However, minor deviations in the bending moment predictions are observed, particularly near the pile top, where moments are minimal and more sensitive to boundary condition variations. The RMSE for moments is slightly higher in this case compared to uniform loading, but the overall accuracy of the PINN remains high, demonstrating its robustness in handling more complex force distributions.



(a) Axial displacement

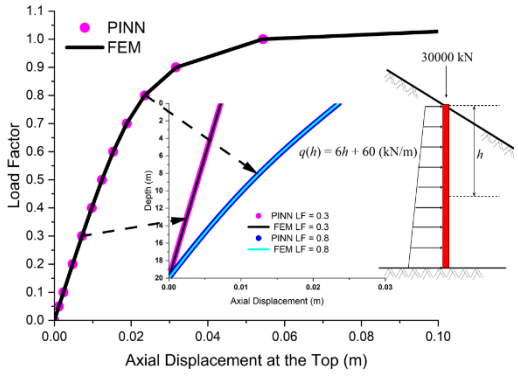


(b) Lateral displacement

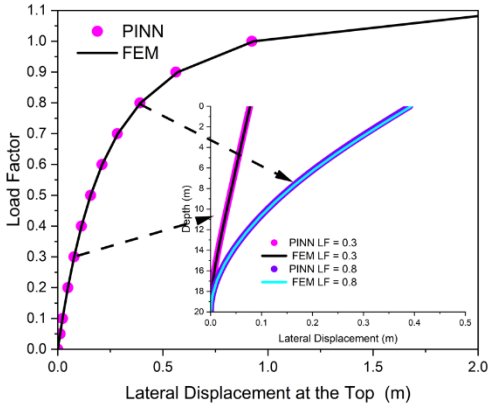


(c) Moment

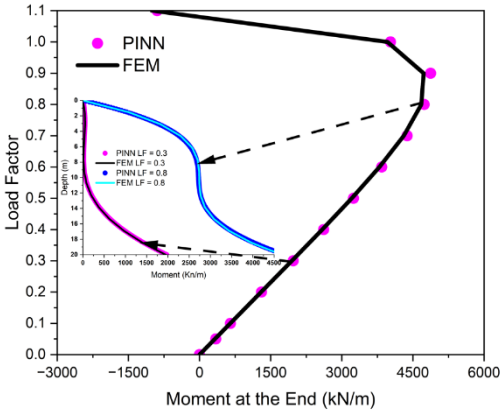
Fig. 5 Deformation analysis of the slope pile under the uniform load by PINN and FEM



(a) Axial displacement



(b) Lateral displacement

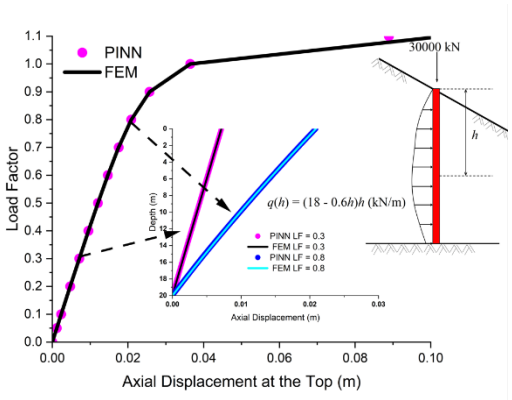


(c) Moment

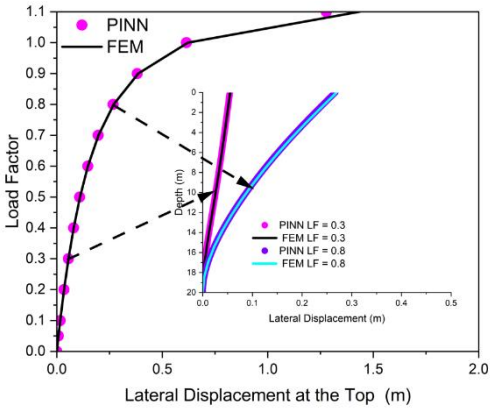
Fig. 6 Deformation analysis of the slope pile under the trapezoidal load by PINN and FEM

Fig. 7 shows the results for parabolic loading, where the sliding force intensity varies quadratically along the pile length. This loading condition introduces the highest level of complexity, as the bending moment distribution exhibits rapid changes in curvature, especially near the pile bottom. The lateral displacement profile also becomes more nonlinear, with a steeper gradient near the pile top. Despite the increased complexity, the PINN accurately predicts both the displacement and moment distributions. The FEM and PINN results for axial and lateral displacements are nearly indistinguishable, with minimal errors. For bending moments, the deviations between the PINN and FEM are slightly larger than those for uniform and trapezoidal cases, particularly in regions with high curvature. Nonetheless, the R^2 value remains consistently high, reflecting the PINN's ability to handle complex nonlinear distributions with reliable accuracy.

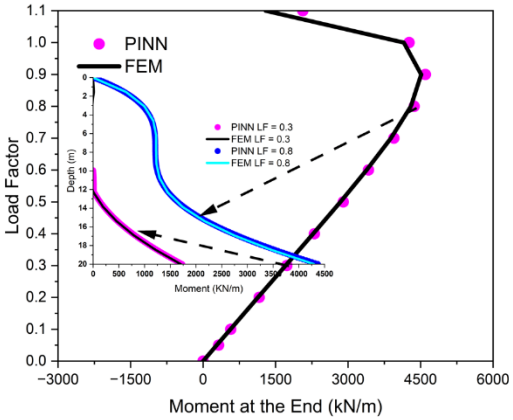
The PINN framework demonstrates excellent agreement with FEM across all three loading conditions, maintaining high accuracy even as the complexity of the force distributions increases. Axial and lateral displacement predictions align closely with FEM results, showing minimal discrepancies, while bending moment predictions exhibit slightly larger errors, particularly for trapezoidal and parabolic loading, though these remain within acceptable engineering limits. Overall, the results confirm the robustness and versatility of the PINN approach in accurately capturing nonlinear buckling and deformation behavior of slender slope piles under varying loading conditions.



(a) Axial displacement



(b) Lateral displacement

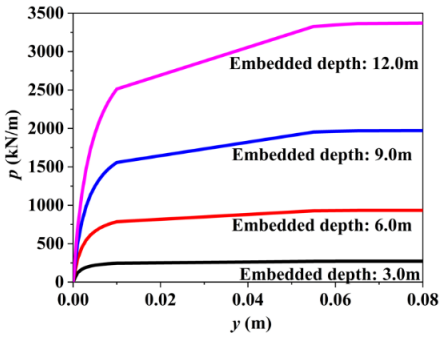


(c) Moment

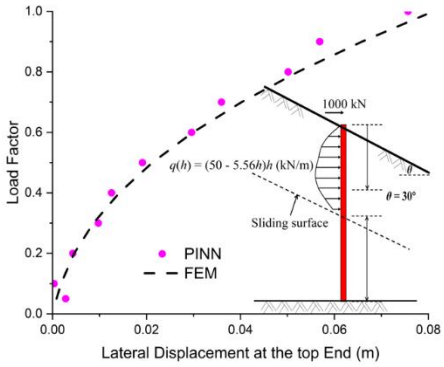
Fig. 7 Deformation analysis of the slope pile under parabolic loading load by PINN and FEM

4.3. Example 3 –Large deflection analysis of a single pile in slope with nonlinear SSI by PINN and FEM

In this example, the proposed PINN framework is assessed for accuracy and computational efficiency in modeling a single reinforced-concrete (RC) pile embedded in a slope, with nonlinear SSIs. The soil's vertical stiffness is set at k_v = 500 kN/m, while its lateral resistance is described by depth- and displacement-dependent p–y curves per Ouyang et al. (2021). Corresponding geotechnical parameters s are also taken from Ouyang et al. (2021). The pile (L = 12 m; D = 1 m; E = 30 GPa) is modeled with a free head and a fixed base and with a lateral load of 1000 kN. This configuration provides a realistic benchmark against which to evaluate the PINN's performance.



(a)



(b)

Fig. 8 Large deflection analysis results of a single pile in slope with nonlinear SSIs: (a) p-y curves; (b) applied shearing force

Fig. 8 demonstrates the lateral deflection at the pile top under a 1000kN lateral force, comparing the predictions of the PINN framework with FEM results. The figure highlights the PINN's ability to accurately capture large deflections in the pile, even under nonlinear SPI conditions. The inclusion of depth-dependent soil stiffness and nonlinear p–y relationships results in a highly nonlinear displacement profile, which the PINN replicates with excellent precision. The close agreement between the PINN and FEM results confirms the framework's robustness in handling complex SPI. Additionally, the PINN achieves this accuracy with significant computational efficiency, making it a promising tool for real-time or large-scale analysis of piles subjected to nonlinear SPI and large deformations.

4.4. Example 4 - Uncertainty evaluation of the single slope pile

In this example, an RC pile (L = 20 m, D = 1 m, E = 32.5 GPa) is subjected to the lateral and vertical loading regime illustrated in Fig. 9. To quantify the impact of load and material uncertainties on the pile's response, we employ Monte Carlo simulation (MCS) [21], a standard approach for uncertainty propagation. In the MCS, 1 000 deterministic realizations are generated by sampling from the prescribed probability distributions of the uncertain parameters. Fig. 9 shows the results from the proposed method and FEM are almost identical to each other, reinforcing the accuracy of the proposed PINN in slope pile problems. Computational costs have been quantitively discussed through the PINN and FEM by the previous study. In the current study, all the numerical simulations are executed on the same computer with AMD Ryzen 7 7730U with Radeon Graphics 2.00 GHz and 16 GB RAM without the GPU device. The FEM requires approximately 7.6h for 1000 repetitive analysis during the MCS. Conversely, the proposed PINN surrogate model achieves 1000 iterations for about 6h. It is important to not that this duration includes the transfer learning process for each sample, where the network parameters from the previous step are used as initialization. Unlike purely data-driven surrogates that infer instantly but may violate physical laws, this transfer learning strategy ensures strict adherence to governing equations for every stochastic realization. Consequently, the PINN framework offers competitive computational efficiency and provides a roughly 21% reduction in time compared to FEM. The comparisons show that PINN can be considered as a promising alternative for some computationally intensive tasks.

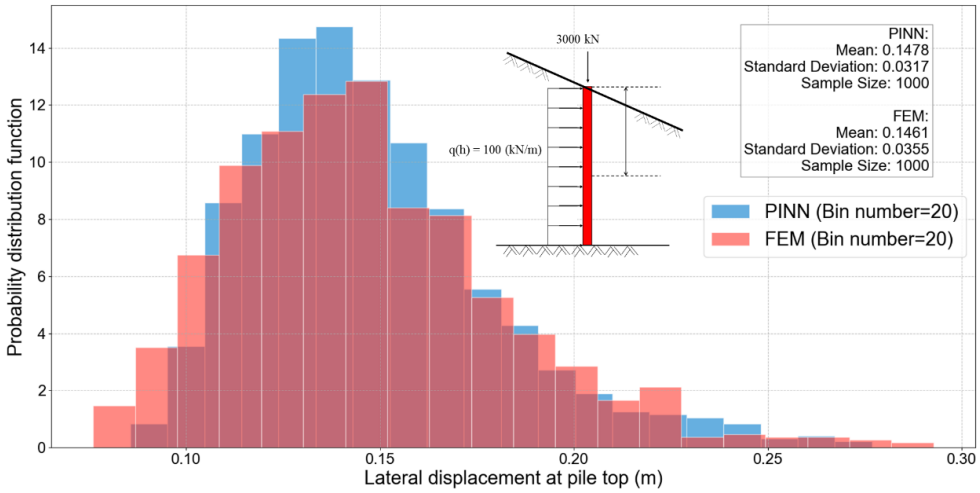


Fig. 9 Probability distribution function of lateral pile top deflection

5. Conclusion

This study presents a PINN framework for the nonlinear analysis of slender slope piles, demonstrating its potential as a precise and efficient tool for geotechnical engineering applications. The findings show that the PINN can accurately predict deflections and bending moments under various sliding force distributions—including uniform, trapezoidal, and parabolic loads. Comparisons with analytical solutions and finite element method (FEM) results confirm the framework's reliability and robustness, consistently yielding high accuracy across different loading conditions. Moreover, the uncertainty evaluation results have proven accuracy and efficiency for the application of PINN in slope pile problems which have the potential to encounter some other boundary value problems with computationally intensive tasks.

The framework effectively integrates complex nonlinear behaviors, such as large deflections and variable bending moments, thereby capturing the intricacies of SSI. Importantly, the PINN incorporates nonlinear SSI, including depth-dependent soil stiffness and nonlinear p–y relationships. This integration enables the model to predict highly nonlinear deformation and interaction effects with exceptional precision. Notably, PINN maintains excellent agreement with FEM predictions in large deflection scenarios, even under significant lateral forces, while providing competitive computational efficiency.

Beyond its demonstrated accuracy and efficiency, the PINN framework offers significant scalability and flexibility, making it adaptable to a wide array of geotechnical engineering challenges. In contrast to conventional FEM, which can be computationally prohibitive for nonlinear or large-scale problems, the PINN emerges as a faster alternative without compromising precision. Future research will focus on further enhancing the framework by integrating stochastic parameters to address variability in soil properties and loading

conditions, as well as optimizing the network architecture for even larger-scale engineering problems. These advancements will further establish the PINN as a powerful and versatile tool for nonlinear analysis in geotechnical engineering.

CrediT

Yi Yang: Conceptualization; Investigation; Data curation; Visualization; Validation; Writing – original draft. Si-Wei Liu: Project administration; Supervision; Funding acquisition; Writing–review and editing. Leilei Liu: Writing-review and editing. Weihang Ouyang: Conceptualization; Software; Supervision; Writing – review and editing.

Data availability

All data generated or used during the study are available from the corresponding author by request.

Acknowledgement

The work described in this paper was partially supported by grants from the Research Grants Council of the Hong Kong Special Administrative Region through the projects "INTACT: Intelligent tropical-storm-resilient system for coastal cities (T22-501/23-R)". The work is also partially supported by a grant from Harbin Institute of Technology, Shenzhen through ZX20250365.

Conflict of interest

The authors have no competing interests to declare that are relevant to the content of this article.

References

[1] Cheng YM, Lau CK (2008) Slope stability analysis and stabilization: New methods and insight. CRC Press, Boca Raton

[2] Li H, Yan C, Shi Y, Lan H, Bao H, Sun W, He Z, Ma D, Wen K, Hu J (2025) Failure mechanism and stability evaluation of rockslides with oblique intersecting faults as well as mitigation measures for slope-top platform collapse. Landslides 22:1227–1239.

[3] Jiang J, Zhao Q, Jiang H, Wu Y, Zheng X (2022) Stability evaluation of finite soil slope in front of piles in landslides with displacement-based method. Landslides 19:2653–2669.

[4] Ding H, Xue L, Shang J, Guo S, Liu H, Li L, Wang H (2024) Study on synergistic action of tap-like arbor root system and anti-slide piles by physical model experiment of landslides. Landslides 21:1707–1717.

[5] Peng W, Zhao M, Xiao Y, Yang C, Zhao H (2019) Analysis of laterally loaded piles in sloping ground using a modified strain wedge model. Comput Geotech 107:163–175.

[6] Peng W, Zhao M, Zhao H, Yang C (2021) Effect of slope on bearing capacity of laterally loaded pile based on asymmetric failure mode. Comput Geotech 140:104469.

[7] Chen, L., Zhang, H. Y., Liu, S. W., & Chan, S. L. (2023). Second-order analysis of beam-columns by machine learning-based structural analysis through physics-informed neural networks. Advanced Steel Construction, 19(4), 411-420.

[8] Sun Z, Huang G, Hu Y, Dias D, Ji J (2023) Reliability analysis of pile-reinforced slopes in width-limited failure mode considering three-dimensional spatial variation of soil strength. Comput Geotech 161:105528.

[9] Wang L-P, Wang T, Hu Y, Liao W, Ji J (2023) Reliability analysis of pile stabilized earth slopes using weighted uniform simulation method. Comput Geotech 162:105623.

[10] Hu Y, Ji J, Sun Z, Dias D (2023) First order reliability-based design optimization of 3D pile-reinforced slopes with Pareto optimality. Comput Geotech 162:105635.

[11] Duan X, Zhang J, Liu L, Hu J, Xue Y (2024) Hybrid response surface method for system reliability analysis of pile-reinforced slopes. J Rock Mech Geotech Eng 16(9):3395–3406.

[12] Ouyang, W. H., Yang, Y., Wan, J. H., & Liu, S. W. (2020). Second-order analysis of steel sheet piles by pile element considering nonlinear soil-structure interactions. Adv. Steel Constr, 16(4), 354-362.

[13] Raissi M, Perdikaris P, Karniadakis GE (2019) Physics-informed neural networks: A deep learning framework for solving forward and inverse problems involving nonlinear partial differential equations. J Comput Phys 378:686–707.

[14] Cai S, Mao Z, Wang Z, Yin M, Karniadakis GE (2021) Physics-informed neural networks (PINNs) for fluid mechanics: A review. Acta Mech Sin 37(12):1727–1738.

[15] Zhang ZL, Pan QJ, Yang ZH, Yang XL (2023) Physics-informed deep learning method for predicting tunnelling-induced ground deformations. Acta Geotech 18(9):4957–4972.

[16] Zhang P, Yin ZY, Sheil B (2022) A physics-informed data-driven approach for consolidation analysis. Géotechnique 74(7):620–631.

[17] Zhong LW, Lan YP, Tang XW, Huang W, He JW, Liu SW (2025) From classical models to neural operators: A study on mooring tension prediction for floating offshore wind turbine. Advanced Steel Construction 21(4):357–366.

[18] Wu M, Xu X, Han X, Du XL (2024) Seismic performance prediction of a slope-pile-anchor coupled reinforcement system using recurrent neural networks. Eng Geol 338:107623.

[19] Ouyang, W.H., Li, G., Chen, L., & Liu, S. W. (2024). Physics-informed neural networks for large deflection analysis of slender piles incorporating non-differentiable soil-structure interaction. International Journal for Numerical and Analytical Methods in Geomechanics, 48(5), 1278-1308.

[20] Ouyang, W.H., Liu, S. W., Wan, J.H., & Yang, Y. (2021). Euler–Bernoulli pile element for nonlinear buckling analysis of single piles in slope. International Journal of Geomechanics, 21(9), 04021170.

[21] Zio E. (2013). Monte Carlo Simulation: The Method. Springer

Advanced Steel Construction – Vol. 22 No. 5 (2026) 508–521
DOI:10.18057/IJASC.2026.22.5.3

RESEARCH ON THE LONGITUDINAL SHEAR BEHAVIOR OF STEEL GRID-UHPC COMPOSITE BRIDGE DECKS

Su-Mei Liu [1, *], Han Zhang [2], Peng Wang [3], Peng-Fei Ren [4] and Han-Shan Ding [4]

[1] *School of Architectural Engineering, Jinling Institute of Technology, Nanjing, 211169, PR China*
[2] *Architecture and Engineering Co., Ltd. of Southeast University, Nanjing, 210096, PR China*
[3] *Shandong Electric Power Engineering Consulting Institute Corp., Ltd., Jinan, 250013, PR China*
[4] *School of Civil Engineering, Southeast University, Nanjing, 211189, PR China*
** (Corresponding author: E-mail: smliu@jit.edu.cn)*

ABSTRACT

This study proposes a novel steel grid–ultra-high performance concrete (UHPC) composite bridge deck system. A parametric study using finite element analysis (FEA) shows that the dominant failure mode of perfobond leiste (PBL) shear connectors in this system involves shear and compressive failure of the concrete tenons. Hole shape and the presence of through rebars significantly influence shear behavior, which is enhanced with increasing hole number, hole diameter, and concrete strength. Comparative evaluation of existing design formulas against FEA results confirms their inapplicability for predicting the shear capacity of PBL connectors in this system. Accordingly, a revised formula is developed that explicitly accounts for the combined contribution of concrete tenons and through rebars. Push-out tests on three specimens demonstrate the superior longitudinal shear performance of the proposed deck. For the tested configurations, interface bonding contributes less than 5% of the total shear capacity, and may therefore be neglected in design. Furthermore, the group effect, induced reduction in capacity between adjacent holes must be considered, which can be addressed through the reduction factors incorporated in the proposed formula.

ARTICLE HISTORY

Received: 10 October 2025
Revised: 6 February 2026
Accepted: 14 February 2026

KEYWORDS

Longitudinal shear behavior;
Shear capacity;
PBL shear connectors;
FEA;
Push-out test

Copyright © 2026 by The Hong Kong Institute of Steel Construction. All rights reserved.

1. Introduction

Steel-concrete composite bridge decks have seen widespread adoption in recent years due to their ability to effectively utilize the high tensile strength of steel and the excellent compressive capacity of concrete. For example, the composite bridge deck system which consists of orthogonal anisotropic steel bridge decks combined with ultrathin reactive powder concrete proposed by Shao et al. (2013), a novel large longitudinal rib steel-concrete composite orthogonal bridge deck proposed by Zhang et al. (2015), the corrugated steel-concrete composite bridge deck proposed by Su et al. (2016) and Zhang et al. (2018).

Shear connectors are typically incorporated into steel-concrete composite bridge decks to ensure synergistic load distribution between the steel and concrete components. The perfobond leiste (PBL) shear connector, first proposed by Leonhardt et al. (1987), is widely applied in steel-concrete composite structures owning to its excellent static and fatigue properties (Zhou &Yao, 2019). Su et al. (2016) conducted a comparative analysis of the mechanical properties of corrugated steel- normal concrete composite bridge decks with PBL shear connectors against those of conventional concrete and steel bridge decks, demonstrating the feasibility of applying this type of composite bridge deck in bridge engineering.

This paper presents a novel composite bridge deck system, referred to as the steel grid-ultra-high performance concrete (UHPC) composite bridge deck is proposed, as illustrated in Fig. 1. The system comprises five components: a perforated-web T shaped steel (which its web can acts as a traditional PBL shear connector), corrugated steel plate, angular steel, rebar and UHPC. Each component serves a distinct function. Specifically, T shaped steel and UHPC are responsible for load-bearing. Corrugated steel plates function as construction formwork. Rebars passing through holes (through rebars) enhance the interfacial bond strength between the steel and concrete components. Angular steel forms a steel grid in conjunction with the T shaped steel, facilitating both construction and transportation.

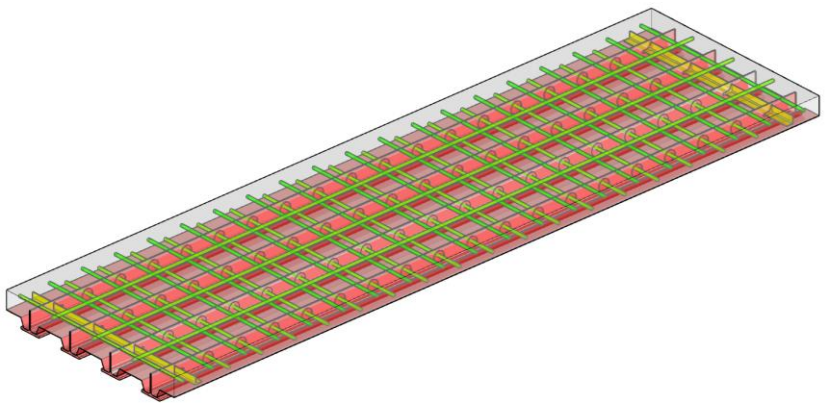


Fig. 1 Steel grid-UHPC composite bridge deck

Currently, the majority of research on the shear behavior of PBL shear connectors predominantly employs the push-out test method. Jeong et al. (2009), Kong et al. (2021), Pang et al. (2023) and Zhang et al. (2024) all conducted push-out test on the corrugated steel-normal concrete composite bridge deck with PBL shear connectors. Jeong et al. (2009) evaluated the longitudinal shear capacity of this type of composite bridge decks by adopting the *m-k* method, and carried out the push-out test and bending test with the same shear connection details. Kong et al. (2021) conducted push-out test on this type of composite bridge decks and results show that PBL shear connectors showed ductile failure pattern. Pang et al. (2023) conducted push-out test on this type of composite bridge decks. The results show that PBL shear connectors undergo elastic range, plastic range and failure range, and the predominant failure pattern of specimens is concrete shear failure, which exhibits excellent ductility during the failure process. Zhang et al. (2024) conducted test on this type of composite

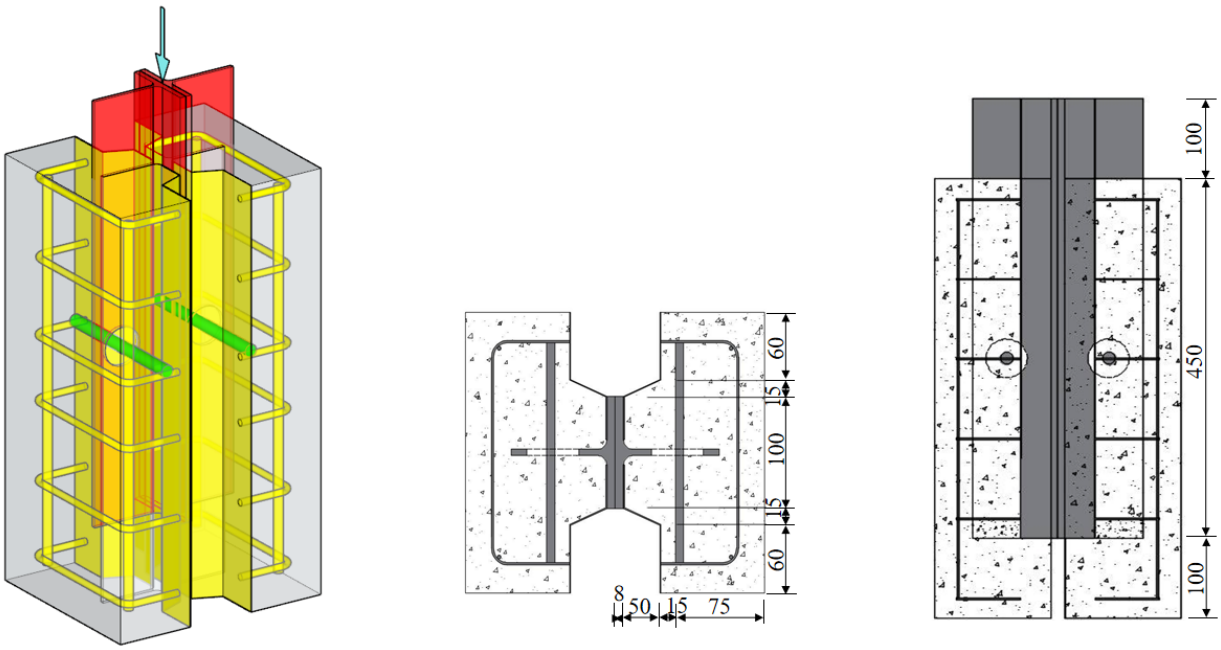
bridge decks subjected to symmetrical load at two midspan. The results indicate that the composite bridge deck with PBL shear connectors arranged in the crest had greater bending stiffness, the distribution range of concrete cracks due to the hogging moment was about twice the width of up flange of the girder, which should be paid attention to in design. Yang et al. (2024) proposed a combined shear connector for corrugated steel-UHPC composite bridge deck, and suggested to secure short studs at the wave peak of corrugated steel plates and install PBLs (Perfobond Leistes) at the wave trough. Through the push-out test and finite element analysis (FEA), the cooperative working mechanism and failure patterns of studs and PBL shear connectors in composite bridge decks were systematically elucidated. Based on these findings, a design theory and calculation method for the shear capacity of the combined shear connector were developed.

Compared to normal concrete, UHPC exhibits remarkable strength, exceptional toughness, and unparalleled durability. In addition, the mechanical property of the T shaped steel's web featuring perforations is different from that of traditional PBL shear connectors. In this paper, the failure pattern and critical influence factor of the steel grid-UHPC composite bridge decks are systematically investigated through FEA. Subsequently, the contrastive analysis of the existing formulas and FEA results is conducted. Finally, three push-out tests are conducted.

2. Finite element analysis

To research the longitudinal shear behavior of steel grid-UHPC composite bridge decks, a series of push-out test specimens are systematically designed, considering various influential factors including hole shape, hole number, hole diameter, through rebar, and concrete strength. The fundamental dimensions are as follows: The T shaped steel has a length of 550mm, with a flange plate measures 100mm in width and 8 mm in thickness, with a web plate measures 92mm in height and 5.5mm in thickness. The concrete plate measures 550mm in length, 250mm in width, and 140mm in thickness. The corrugated steel plate is characterized by a length of 550mm, a thickness of 1mm, and a wave height of 50mm. The diagrammatic drawing and the detailed dimension of specimens are presented in Fig. 2.

The values of the influencing parameters for specimens are presented in Table 1. These specimens are designated in accordance with the following rules: hole shape-hole number-hole diameter-concrete type-through rebar. For instance, the designation C-1-d30-UHPC-N indicates that the specimen features a circular hole with a diameter of 30mm, the UHPC is used, and no through rebar is present.



(a) Diagrammatic drawing (b) Planar graph (c) Elevation

Fig. 2 Diagrammatic drawing and detailed dimension of specimens. (unit: mm)

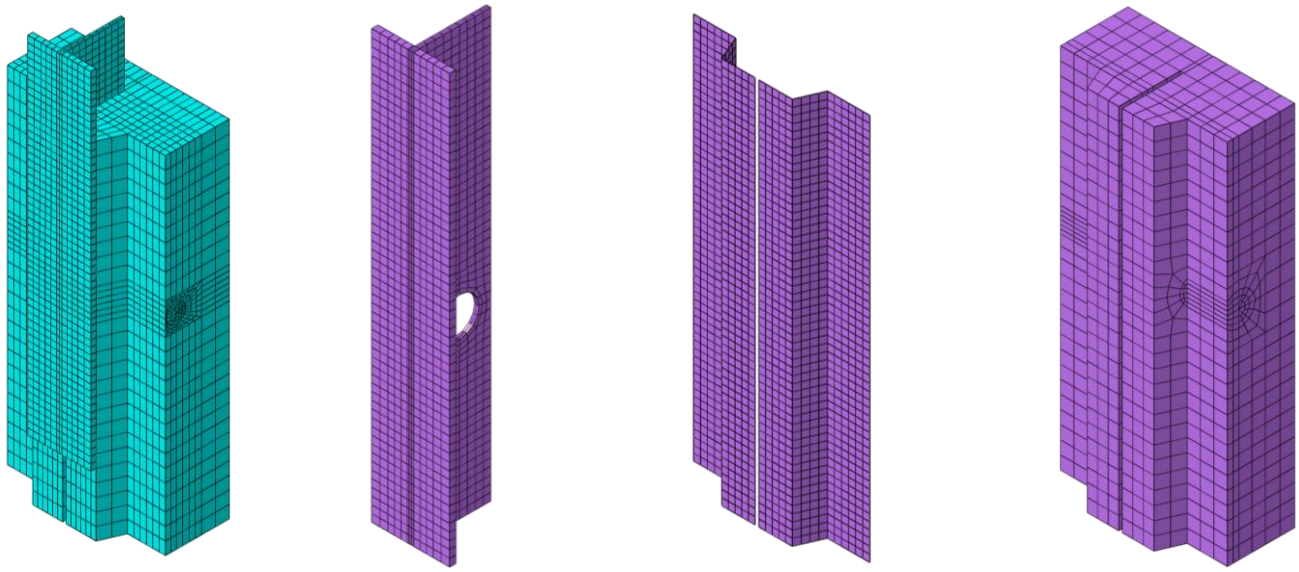
Table 1
Values of the influencing parameters for push-out specimens

Specimens	Hole shape	Hole number	Hole diameter (mm)	Concrete type	Through Rebar
C-1-30-UHPC-N	circular	1	30	UHPC	No
W-1-30-UHPC-N	widened	1	30	UHPC	No
L-1-30-UHPC-N	elongated	1	30	UHPC	No
C-2-50-UHPC-N	circular	2	50	UHPC	No
C-3-50-UHPC-N	circular	3	50	UHPC	No
C-1-35-UHPC-N	circular	1	35	UHPC	No
C-1-40-UHPC-N	circular	1	40	UHPC	No
C-1-45-UHPC-N	circular	1	45	UHPC	No
C-1-50-UHPC-N	circular	1	50	UHPC	No
C-1-55-UHPC-N	circular	1	55	UHPC	No
C-1-60-UHPC-N	circular	1	60	UHPC	No
C-1-50-UHPC-Y	circular	1	50	UHPC	Yes
C-1-50-UHPC-N	circular	1	50	C50	No

2.1. Finite element models

2.1.1. Finite element mesh division

Given that the push-out test specimen exhibits two symmetry axes and fulfills symmetrical boundary conditions, a semi-structural finite element model, which is showed in Fig. 3 is developed utilizing the ABAQUS software. T shaped steel, concrete plates and through rebars are modeled using 8-node solid element (C3D8R), whereas corrugated steel plates are represented by 4-node shell element (S3D4R). The mesh size for both the T shaped steel and corrugated steel plates is 10mm. The global mesh size of the concrete plate is 20mm, and the local mesh size in circular hole region is refined to 10mm. A mesh sensitivity analysis was carried out to ensure the reliability of the FEA results. After evaluating several mesh densities, it was confirmed that the selected mesh size provides sufficient accuracy in capturing stress gradients, particularly around the perforated regions where stress concentrations are expected. The chosen mesh configuration was therefore adopted in all subsequent analyses. The finite element model is shown in Fig. 3.



(a) Whole model (b) T shaped steel (c) Corrugated steel plate (d) Concrete plate

Fig. 3 Finite element model

2.1.2. Boundary conditions

Fig. 4 illustrates the boundary conditions applied in FEA. Here, the bottom surface of concrete plates is fixed, then $U_x = U_y = U_z = 0$. Given that the back side of flange plates of T shaped steel is symmetric about the *x*-axis, it follows that $U_x = R_y = R_z = 0$. Due to the potential for local deformation of the T shaped steel as displacement load increases, the boundary condition is designed to simulate structural displacement loading. This is accomplished by positioning the reference point RP-1 above the centroid of the upper surface of the loading plate and coupling it to that surface. Subsequently, a linearly increasing displacement is imposed on point RP-1.

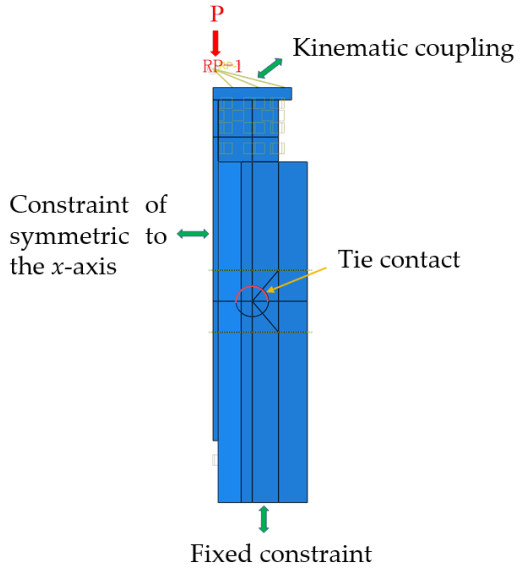


Fig. 4 Boundary conditions applied in FEA

2.1.3. Contact definition

In the interactions between concrete plates and the T shaped steel, as well as between concrete plates and corrugated steel plates, the concrete plates are designated as the primary contact surface. In this paper, given that the slip is not substantially influenced by the friction coefficient between concrete plates and corrugated steel plates, a friction coefficient of 0.1 is adopted (Katwal et al., 2018).

During the process of force-induced deformation, the upper portion of concrete tenons and the T shaped steel with open holes maintain constant contact, whereas the lower portion remains separated from it. Consequently, the upper portion of concrete tenons is in contact with the perforated T shaped steel solely through a tie contact, as indicated by the red line in Fig. 4. This simplification is adopted for two reasons. First, it models the upper interface as a non-separating compression zone, consistent with observed behavior. Second, and more importantly, it aligns with the model's objective to predict global structural capacity and failure modes, rather than local interface slip. The constraint is therefore a purposeful idealization that focuses the analysis on dominant macro-scale mechanisms.

2.2. Material property

2.2.1. Concrete

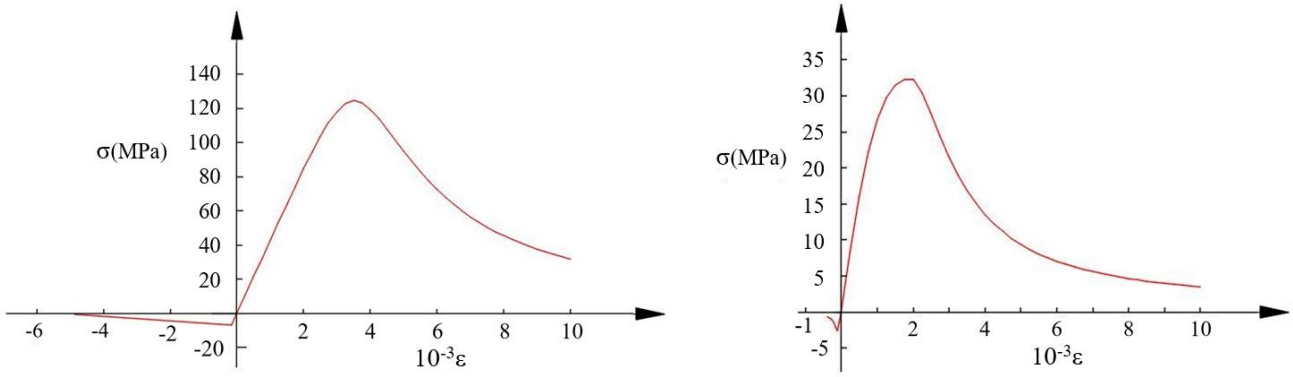
The concrete damage plasticity (CDP) model was employed to simulate the constitutive behavior of concrete in this study. For UHPC, the compressive and tensile stress-strain relationships were adopted from Shan (2002) and Sugano et al. (2007), respectively. Normal concrete C50 was modeled according to the constitutive relationship specified in the Chinese standard GB50010 (GB 50010-2010, 2010).

The key CDP parameters for UHPC were defined as follows to ensure mesh objectivity: dilation angle $\psi = 30°$, flow potential eccentricity $\epsilon = 0.1$, the ratio of initial biaxial to uniaxial compressive yield stress $f_{b0}/f_{c0} = 1.16$, the ratio of second stress invariant on tensile to compressive meridian $K_c = 0.667$, and the viscosity parameter $\mu = 0.0005$ (Li, 2020). The post-peak tensile and compressive behaviors were regularized using fracture energy criteria based on the models by Sugano et al. (2007) and Shan (2002), respectively, to eliminate mesh sensitivity.

The mechanical property parameters for both concrete types are summarized in Table 2, with their corresponding stress-strain curves shown in Fig. 5. Further details on this modeling approach are provided in Liu et al. (2025a).

Table 2
Mechanical property parameters of concrete materials

Concrete	Ultimate axial compressive strength (MPa)	Ultimate axial tensile strength (MPa)	Elastic modulus (MPa)	Poisson's ratio	Ultimate compressive strain
UHPC	124.5	6.7	46200	0.2	0.0035
C50	32.4	2.64	34500	0.18	0.00365



(a) UHPC (b) C50

Fig. 5 Stress-strain curves of UHPC and normal concrete C50

2.2.2. Steel

In this paper, the steel label of the T shaped steel and corrugated steel plate is made of Q345(GB 50017-2017, 2017), the constitutive relationship of steel is simulated through the application of an ideal elastoplastic model. The mechanical property parameters and the stress-strain curve of steel materials are illustrated in Table 3 and Fig. 6 respectively.

Table 3
Mechanical property parameters of steel materials

Steel	Yield stress (MPa)	Elastic modulus (MPa)	Poisson's ratio
T shaped steel	345	206000	0.3
Corrugated steel plate	345	206000	0.3
Rebar	465	206000	0.3

2.3. Failure pattern

Comparing the failure patterns obtained from FEA with those observed in actual structural failures serves as a robust method for validating the accuracy of the FEA approach. In FEA, the equivalent plastic strain (PEEQ) can serve as an indicator to partially characterize the fracture behavior of UHPC and steel (Luo, 2013). Typically, UHPC is deemed to have failed when its PEEQ exceeds 0.035, while steel is considered fractured when its PEEQ surpasses 0.2. Fig. 7 and Fig. 8 illustrate the failure patterns of UHPC and steel by FEA method respectively.

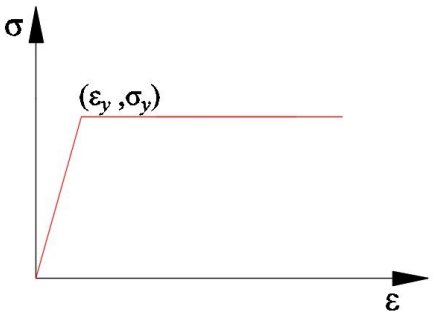
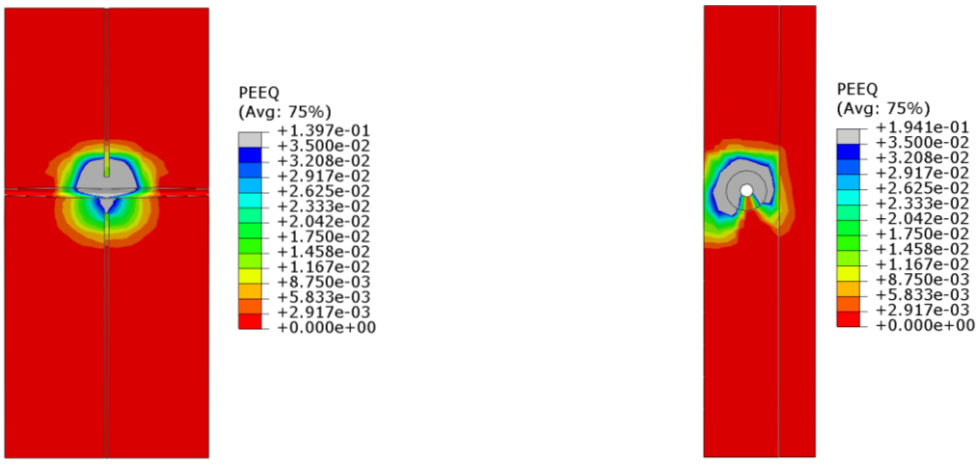
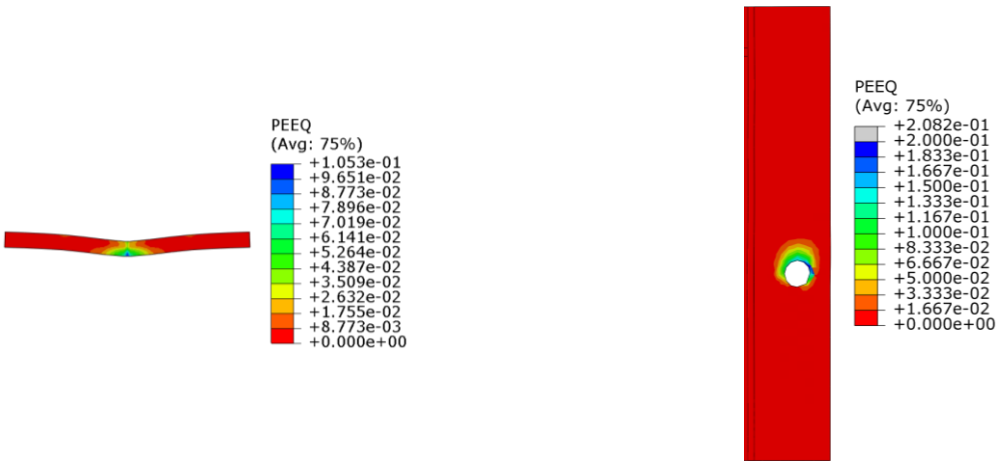


Fig. 6 Stress-strain curve of steel materials



(a) Front elevation (b) Side elevation

Fig. 7 Failure patterns of UHPC obtained through FEA



(a) Through rebar (b) T shaped steel

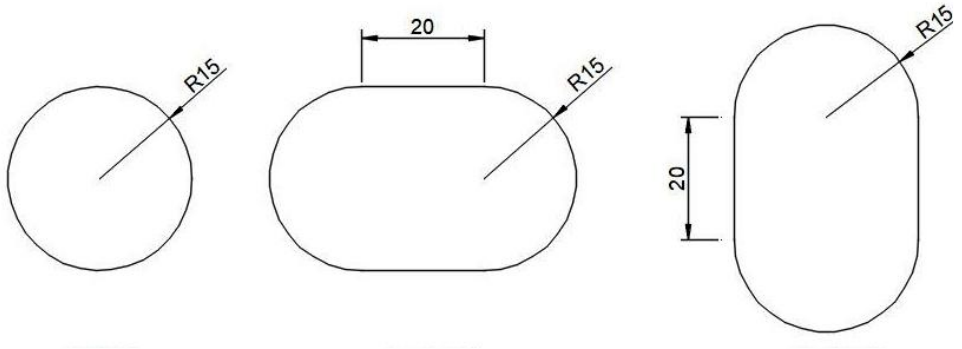
Fig. 8 Failure patterns of steel obtained through FEA

According to Fig. 7 and Fig. 8, the T shaped steel with one open hole does not exhibit any significant fracture failure. Instead, the primary modes of failure are shear and compression failure of concrete tenons within holes and shear failure of through rebars. Although UHPC demonstrates superior compressive performance compared to normal concrete, the structural failure patterns indicate that the failure patterns in both types of concrete are identical. In both cases, shear and compression failure of the concrete tenon occurs first, followed by shear failure of the through rebar. Additionally, when the concrete tenon is damaged, a conical fracture zone forms. This phenomenon is reasonable because this shear connector primarily depends on the concrete tenons within the holes to resist longitudinal shear forces. Therefore, within a specific range, concrete strength does not observably influence the failure pattern. Since the failure pattern is primarily attributed to the failure of concrete tenons, the PEEQ distribution in concrete plates is illustrated below.

2.4. Parameter analysis

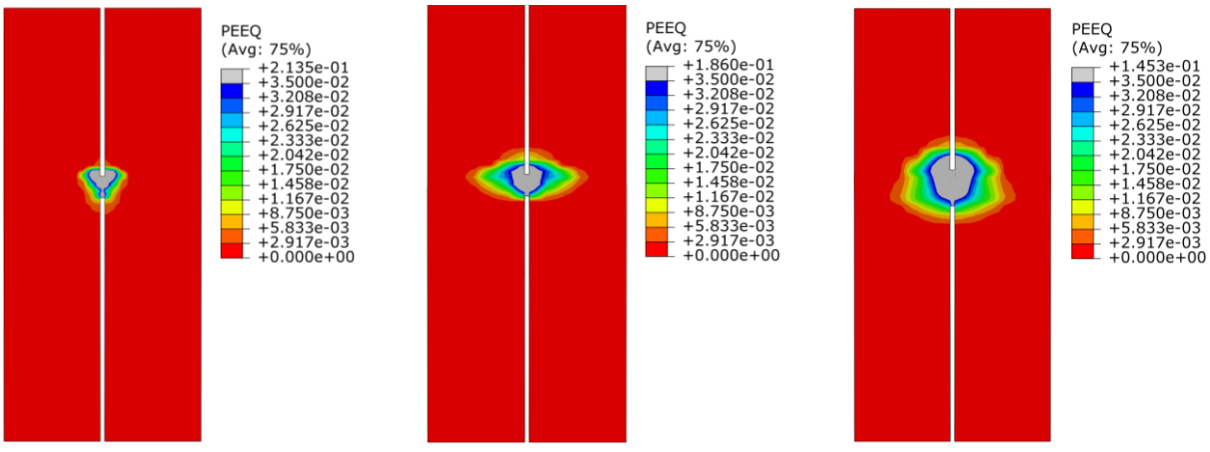
2.4.1. Hole shape

The impact of hole shape on shear behavior is studied by adopting push-out specimens featuring circular holes, widened holes and elongated holes, as illustrated in Fig. 9. In these simulations, while the hope shape is varied, other parameters are kept constant: the concrete material utilized is UHPC, a single hole with a diameter of 30mm, no rebar pass through the hole. Fig. 10 presents the PEEQ of UHPC plates obtained through FEA.



(a) Circular hole (b) Widened hole (c) Elongated hole

Fig. 9 The hole shape in the web plate of T shaped steels



(a) Circular hole (b) Widened hole (c) Elongated hole

Fig. 10 PEEQ of UHPC plates obtained through FEA (varying hole shape)

As illustrated in Fig. 10, the hole shape in shear connectors significantly influences the plastic damage area of UHPC plates (depicted as the gray region in Fig. 10). Specifically, the elongated hole specimen exhibits the largest plastic damage area, followed by the widened hole specimen, with the circular hole specimen showing the smallest. When the hole is circular, the maximum PEEQ in the UHPC plate is 0.2135. For a widened hole, this value decreases to 0.1860, and for an elongated hole, it further reduces to 0.1453. The data suggest that the hole shape has a notable effect on the plastic damage degree in PBL shear connectors.

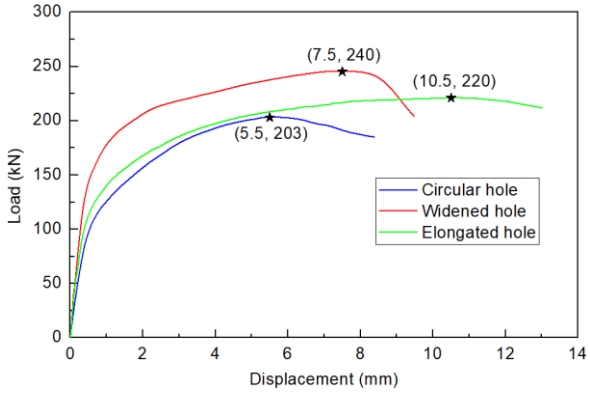


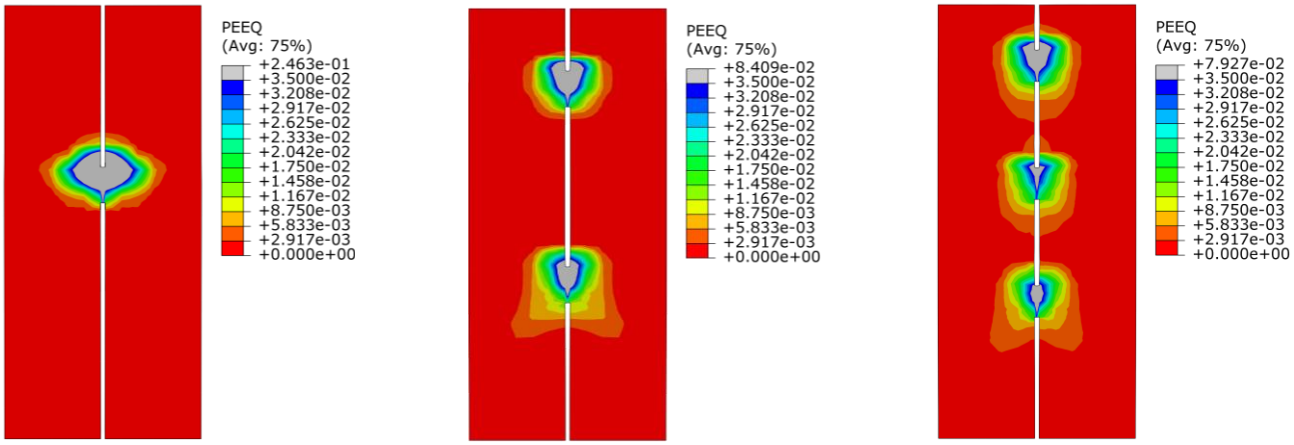
Fig. 11 Load-displacement curve (varying hole shape)

Fig. 11 illustrates the load-displacement curve, emphasizing the shear capacity and the associated displacement of each specimen. As can be observed from Fig. 11, the curve are manifested as elastic range, elastoplastic range and failure range. The elastic range exhibits no significant correlation with hole shape, whereas the elastoplastic range and failure range are substantially influenced by hole shape. The shear capacities of the shear connectors with one circular hole, one widened hole, one elongated hole are approximately 203kN, 240kN, 220kN, corresponding to displacements of 5.5mm, 7.5mm, 10.5mm. The data suggest that the hole shape significantly affects both the shear capacity and ultimate displacement. A preliminary analysis reveals that the specimen with widened hole demonstrates higher shear stiffness and capacity owing to its larger shear area. Conversely, the specimen with elongated hole may exhibit greater displacement at ultimate load owing to its extended shear length.

2.4.2. Hole number

The impact of hole number on shear behavior is studied by adopting push-out specimens with 1 hole, 2 holes, and 3 holes. When hole number is 2, hole spacing is 250mm. When the number increases to 3, the spacing decreases to 150mm. In these simulations, while the hope number is varied, other parameters are kept constant: the concrete material utilized is UHPC, the hole shape is circular with a diameter of 50mm, no rebar pass through the hole. Fig. 12 presents the PEEQ of the UHPC plate obtained through FEA.

As can be observed from Fig. 12, the hole number exerts a significant influence on the plastic damage sustained by UHPC plates. Specifically, the plastic damage area of concrete tenons decreases both with an increase in the hole number and with greater distance from the loading point. When there is one hole, the maximum PEEQ of the UHPC plate is 0.2463. With two holes, this value reduces to 0.0841, and with three holes, it further decreases to 0.0793. The data suggest that an increased hole number correlates with a reduced plastic damage degree in PBL shear connectors.



(a) 1 hole (b) 2 holes (c) 3 holes

Fig. 12 PEEQ of the UHPC plate obtained through FEA (varying hole number)

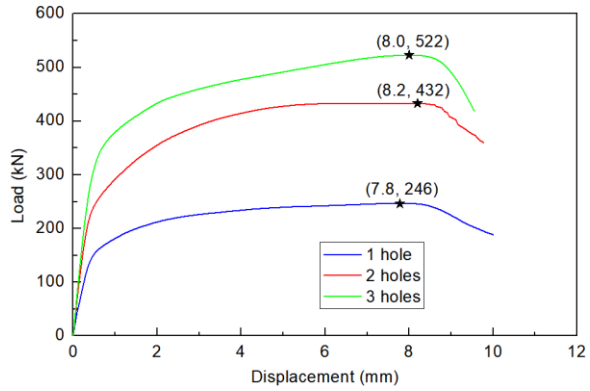


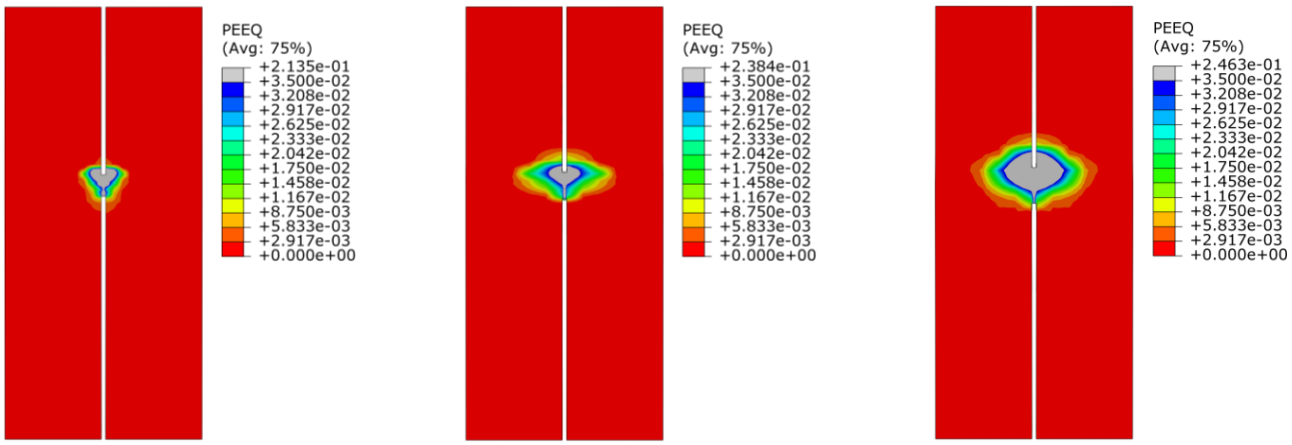
Fig. 13 Load-displacement curve (varying hole number)

Fig. 13 illustrates the load-displacement curve, emphasizing the shear capacity and the associated displacement of each specimen. As can be observed from Fig. 13, the hole number does not influence the variation tendency of load-displacement curves but significantly affects its numerical values. The shear capacities of the shear connectors with 1 hole, 2 holes, 3 holes are approximately 246kN, 432kN, 522kN, corresponding to displacements of 7.8mm, 8.2mm, 8.0mm. The data suggest that as the hole number increases, the displacement at ultimate capacity remains relatively unchanged. However, with the increasing hole number, the rate of increase in shear capacity gradually diminishes.

2.4.3. Hole diameter

The impact of hole diameter on shear performance is studied by adopting push-out specimens featuring a circular hole with a 30mm diameter, 40mm diameter and 50mm diameter respectively. In these simulations, while hole diameter is varied, other parameters are kept constant: the concrete material utilized is UHPC, the hole number is 1, no rebar pass through the hole. Fig. 14 presents the PEEQ of the UHPC plate obtained through FEA.

As can be observed from Fig. 14, the hole diameter significantly influences the plastic damage area of the UHPC plate. Specifically, with the increase in hole diameter, the plastic damage zone above and on both sides of concrete tenons progressively expands, whereas the plastic damage area below remains largely unchanged. Notably, when the hole diameter d=30mm, the maximum PEEQ of the UHPC plate reaches 0.2135. This value increases to 0.2384 when d=40mm, and further to 0.2463 when d=50mm. The date suggest that the plastic damage degree in PBL shear connectors intensifies with an increase in hole diameter.



(a) d=30mm (b) d=40mm (c) d=50mm

Fig. 14 PEEQ of the UHPC plate obtained through FEA (varying hole diameter)

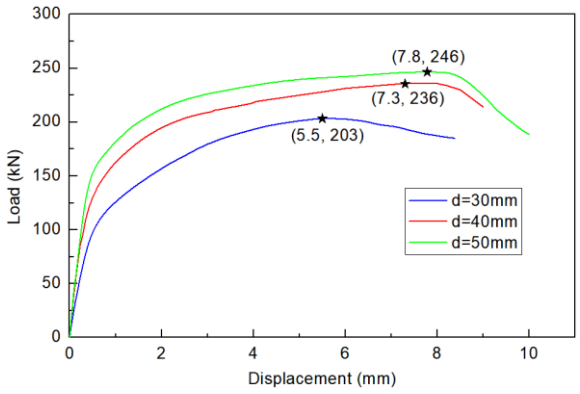


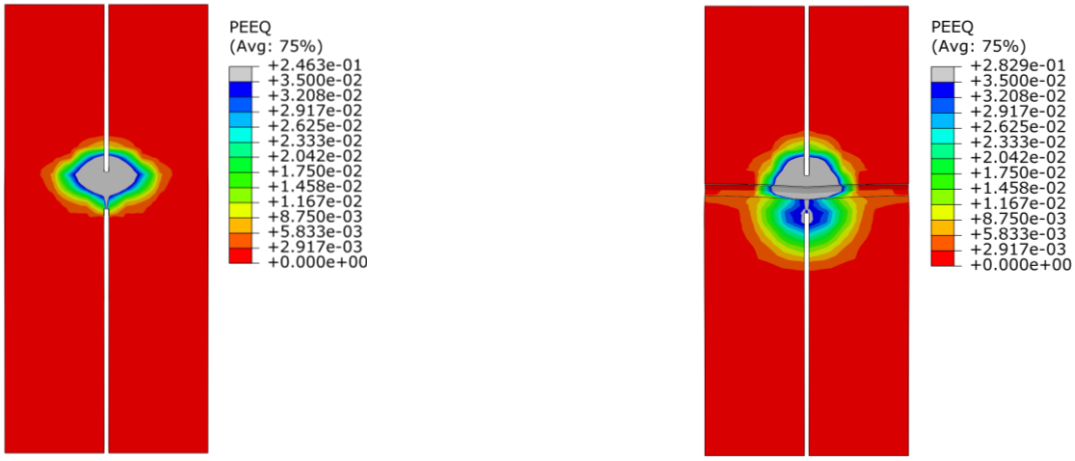
Fig. 15 Load-displacement curve (varying hole diameter)

Fig. 15 illustrates the load-displacement curve, emphasizing the shear capacity and the associated displacement of each specimen. As can be observed from Fig. 15 that the hole diameter significantly affects the specific values of the load-displacement curve but does not substantially influence its overall trend. The shear capacities of shear connectors with diameters of 30mm, 40mm, 50mm are approximately 203kN, 236kN, 246kN respectively, and the corresponding displacements are 5.5mm, 7.3mm, and 7.8mm respectively. The date suggest that while the shear capacity increases with hole diameter, the ultimate capacity and corresponding displacement progressively reach a stable state as diameter grows larger.

2.4.4. Through rebars

To study the impact of through rebars on the shear behavior, this study designed two specimens. One specimen incorporates through rebar with a diameter of 16mm, while the other does not. In these simulations, while through rebar is varied, other parameters are kept constant: the concrete material utilized is UHPC, a single circular hole with a diameter of 50mm. Fig. 16 presents the PEEQ of the UHPC plate obtained through FEA.

As can be observed from Fig. 16 that, although the through rebar does not significantly alter the plastic damage area of UHPC plates, it increases the extent of UHPC involvement in shear connectors. This indicates that the implementation of through rebars can enhance the overall stress distribution of UHPC plates, thereby effectively improving the shear behavior. Consequently, the installation of through rebars demonstrably enhances the shear behavior of steel grid-UHPC composite bridge decks.



(a) No through rebar (b) One through rebar

Fig. 16 PEEQ of the UHPC plate obtained through FEA (varying through rebar)

Fig. 17 illustrates the load-displacement curve, emphasizing the shear capacity and the associated displacement of each specimen. As can be observed from Fig. 17, that the through rebar significantly influences the failure stage of the load-displacement curve but does not affect the linear elastic stage. For the specimen with one through rebar, the shear capacity is approximately 282kN at a corresponding displacement of 13.7mm. In contrast, for the specimen without through rebar, the shear capacity is approximately 246kN, which corresponds to a displacement of 7.8 mm. The data indicates that through rebars enhance both the shear capacity and the ductility of the structure.

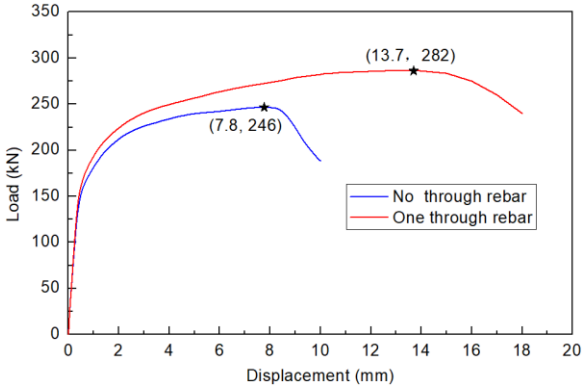
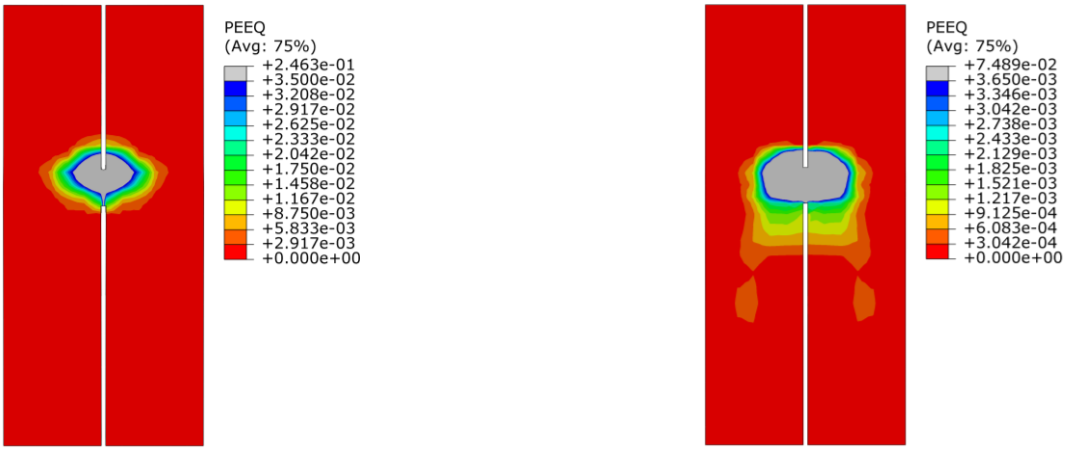


Fig. 17 Load-displacement curve (varying through rebar)

The preliminary analysis of the cause of this phenomenon suggests that prior to the structure reaching its shear capacity, the longitudinal shear force is predominantly carried by concrete tenons. Consequently, the influence of through rebars passing through holes on enhancing shear capacity is relatively limited. However, once the structure reaches its shear capacity and the concrete tenons are damaged, the longitudinal shear force is entirely transferred to the through rebar. Thus, through rebars play an important role in enhancing the ductility and overall performance of structures.

2.4.5. Concrete strength

To study the impact of concrete strength on shear behavior, FEA models are developed for both the push-out specimen with UHPC and the push-out specimen with C50 concrete. In these simulations, while concrete strength is varied, other parameters are kept constant: the hole shape is circular with a diameter of 50mm, no rebar pass through the hole. Fig. 18 presents the PEEQ of the concrete plate obtained through FEA. Fig. 19 illustrates the load-displacement curve, emphasizing the shear capacity and the associated displacement of each specimen.



(a) UHPC plate (b) C50 concrete plate

Fig. 18 The PEEQ of specimens obtained through FEA (varying concrete strength)

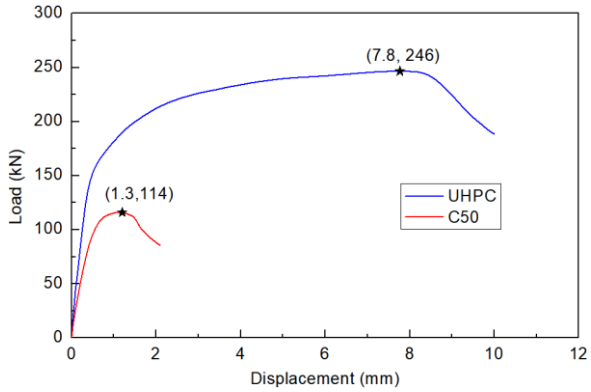


Fig. 19 Load-displacement curve (varying concrete strength)

As can be observed from Fig. 18 and Fig. 19 that compared with the PBL shear connector in normal concrete, it in UHPC exhibit a smaller plastic damage area at failure, despite the failure pattern remaining unchanged. Additionally, the ultimate bearing capacity and ductility of structures are markedly enhanced. Specifically, the PBL shear connector in UHPC demonstrate a shear capacity of approximately 246kN, corresponding to a displacement of 7.8mm. In contrast, the PBL shear connector in normal concrete has a shear capacity of approximately 116kN, corresponding to a displacement of 1.1mm.

The main reason for this difference lies in the distinct material properties of the concrete. Compared to normal concrete, UHPC exhibits significantly higher strength, greater toughness, and superior durability, which collectively result in markedly improved shear performance of PBL shear connectors in UHPC composites.

3. Shear capacity of PBL shear connectors

3.1. Existing formulas of shear capacity for PBL shear connectors

In practical engineering applications, variations exist in the construction parameters of PBL shear connectors. To date, there is no universally accepted standard for conducting push-out tests on PBL shear connectors, nor is there a unified formula for calculating their shear capacity. Current formulas typically focus on the shear contributions of concrete tenons and through rebars. Below, the shear capacity formulas for PBL shear connectors in normal concrete are presented.

3.1.1. Chinese standard-JTG/T D64-01-2015

The design formula of shear capacity for PBL shear connectors that provided in Chinese standard-JTG/T D64-01-2015 (JTG/T D64-01-2015, 2015) is as Eq. (1).

$$Q_d = 1.4(d^2 - d_s^2) f_{cd} + 1.2 d_s^2 f_{sd} \quad (1)$$

where Q_d is the design value of shear capacity for PBL shear connectors, d is the diameter of the circle hole on PBL shear connectors, d_s is the through rebar's diameter, f_{cd} is the design value of concrete's axial compressive strength, f_{sd} is the design value of the through rebar's tensile strength.

3.1.2. Chinese standard-GB 50917-2013

The design formula of shear capacity for PBL shear connectors that provided in Chinese standard-GB 50917-2013 (GB 50917-2013, 2013) is as Eq. (2).

$$Q_d = 12.2(\frac{\pi}{4}d^2 - \frac{\pi}{4}d_s^2)f_{td} + 2\cdot\frac{\pi}{4}d_s^2 f_{vd} \quad (2)$$

where d is the diameter of the circle hole on PBL shear connectors, d_s is the through rebar's diameter, f_{td} is the design value of concrete's axial tensile strength, f_{vd} and f_{sd} are the design value of the shear strength and tensile strength of through rebars respectively, and have a relationship $f_{vd} = 0.577 f_{sd}$.

3.1.3. Japanese formula

In Japan, the shear capacity of PBL shear connectors was initially proposed by Hosaka et al. (2000) as Eq. (3).

$$Q_u = 1.45(d^2 - d_s^2)f_c + 1.45 d_s^2 f_s - 26.1\times10^3 \quad (3)$$

where Q_u is the shear capacity of PBL shear connectors (N), d is the diameter of the circle hole on PBL shear connectors (mm), d_s is the through rebar's diameter (mm), f_c is the concrete's compressive strength (MPa), f_s is the through rebar's tensile strength (MPa).

3.2. Comparison of existing formulas with FEA results

Table 4 presents a comparison between the shear capacity predictions from existing formulations and FEA results. The data reveal substantial discrepancies between the analytical and numerical results, indicating that current formulas are not directly applicable for PBL shear connectors in steel grid-UHPC composite bridge decks. Among these, the shear capacity calculation formula presented in the Chinese standard-GB 50917-2013 tends to be conservative, and the calculation error decreases as the hole diameter increases. However, the formula proposed in the Chinese standard-JTG/T D64-01-2015 and that proposed by Hosaka et al. (2000) may overestimate to calculate the shear capacity, and the calculation error increases with the rise in concrete strength.

Table 4
A comparison of the calculation results obtained from existing formulas with FEA results

Specimens	Hole diameter / T-web thickness	FEA	JTG/T D64-01-2015 Eq. (1)		GB 50917-2013 Eq. (2)		Hosaka Eq. (3)	
		Result (kN)	Result (kN)	Error	Result (kN)	Error	Result (kN)	Error
C-1-d30-UHPC-N	5.5	203	157	-23%	58	-72%	136	-33%
C-1-d35-UHPC-N	6.4	218	214	-2%	79	-64%	195	-11%
C-1-d40-UHPC-N	7.3	236	279	18%	103	-56%	263	11%
C-1-d45-UHPC-N	8.2	240	353	47%	130	-46%	339	41%
C-1-d50-UHPC-N	9.1	246	436	77%	160	-35%	425	73%
C-1-d55-UHPC-N	10.0	256	527	106%	194	-24%	520	103%
C-1-d60-UHPC-N	10.9	265	627	137%	231	-13%	624	135%
C-1-d50-UHPC-Y	9.1	282	534	89%	252	-11%	552	96%
C-1-d50-C50-N	9.1	114	113	-1%	63	-45%	91	-20%

For the PBL shear connectors with one hole in steel grid-UHPC composite bridge decks, the shear capacity calculation method that incorporates the shear capacity contributions of concrete tenons and through rebars may also be employed. Based on the comparative analysis presented in Table 3, it is recommended that the affect of the hole diameter-T-web thickness ratio be incorporated into the formula. The proposed calculation formula is presented as follows:

$$Q_u = \eta(d^2 - d_s^2)f_c + \xi d_s^2 f_s \quad (4)$$

where Q_u is the shear capacity of PBL shear connectors, d is the diameter of the circle hole on PBL shear connectors, d_s is the through rebar's diameter, f_c is the concrete's axial compressive strength, f_s is the through rebar's tensile strength. ξ is the influence coefficient of through rebars, η is the influence coefficient of concrete tenons and is determined by the hole diameter- T-web thickness ratio (d/t). For the specimens with one hole and no rebar pass through the hole, the least squares method is applied to fit the parameter analysis results, and the computational formula for η is thereby derived as follows:

$$\eta = 0.0326\left(\frac{d}{t}\right)^2 - 0.755\frac{d}{t} + 4.956 \qquad (5.5 \le \frac{d}{t} \le 11) \quad (5)$$

where d is the hole diameter, t is thickness of the T-web plate. The polynomial fit was developed using d/t range from 5.5 to 11, so Eq. (5) is valid only within these ranges and should not be used for extrapolation.

Since this study focuses solely on the parameter analysis of the hole diameter of PBL shear connectors, it is only possible to derive the expression for the influence coefficient of concrete tenons η. However, the calculation formula for the influence coefficient of through rebars ξ cannot be determined, and its recommended value was only provided as a suggestion through subsequent experiments. A comparison between Eqs. (4), (5) and the FEA values is listed in Table 5.

As can be observed in Table 5, the relative errors between the shear capacities of the seven specimens calculated using Eqs. (4) and (5) and the corresponding FEA results are all within 2%. Consequently, Eqs. (4) and (5) provide a valuable reference for estimating the shear capacity of single-hole PBL shear connectors in steel grid-UHPC composite bridge decks.

In summary, the proposed Eqs. (4) and (5) are developed specifically for UHPC based on the current FEA parameter study. They are not an extrapolation of existing concrete formulas but a new formulation grounded in the observed behavior of UHPC. It should be noted that Eqs. (4) and (5) are derived from FEA, without considering the group-nail effect among multiple tenons and multiple rebars. Their effectiveness needs to be verified by subsequent experiments.

Table 5
Comparison between the results calculated by Eqs. (4), (5) and FEA restults

Specimens	$\frac{d}{t}$ = Hole diameter / T-web thickness	FEA	Eqs. (4) and (5)	
		Value (kN)	Value (kN)	Error
C-1-d30-UHPC-N	5.5	203	203	-0.2%
C-1-d35-UHPC-N	6.4	218	237	0.4%
C-1-d40-UHPC-N	7.3	236	242	1.0%
C-1-d45-UHPC-N	8.2	240	245	-0.5%
C-1-d50-UHPC-N	9.1	246	251	-2.0%
C-1-d55-UHPC-N	10.0	256	269	1.4%
C-1-d60-UHPC-N	10.9	265	203	-0.2%

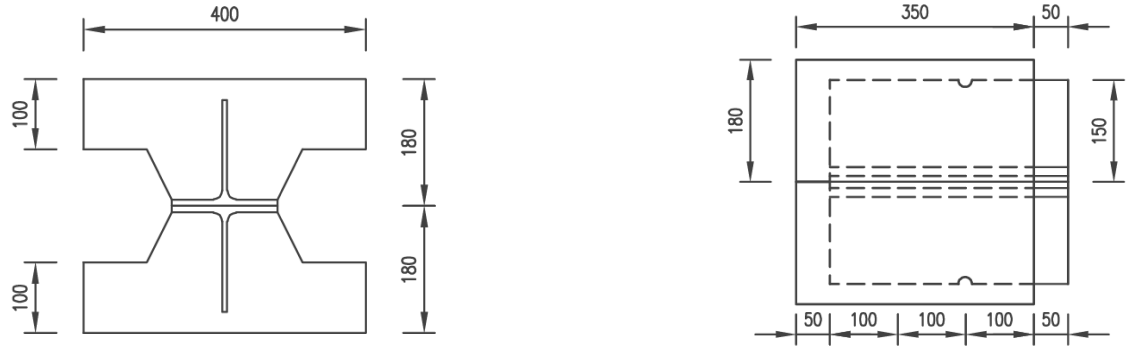
4. Experimental work

4.1. Geometric dimensioning of test specimens

This paper presents an overview of three push-out specimens design approaches. The first specimen, designated as HY-1, features no holes in the web of the T shaped steel. This configuration is intended to study the interface bonding capacity between the steel and UHPC in steel grid-UHPC composite bridge decks. The second specimen, designated as HY-2, features two holes (diameter 50mm and 60 mm) in the web of the T shaped steel but do not include the through rebars. This configuration is intended to study the shear capacity of concrete tenons and failure pattern. The third specimen, designated as HY-3, features two holes (diameter 50mm and 60 mm) in the web of the T shaped steel and include two hot-rolled ribbed bars (HRB400) conforming to Chinese standard GB/T 1499.2-2018 (GB/T 1499.2-2018, 2018), with yield strength ≥ 400 MPa and tensile strength ≥ 540MPa. This configuration is intended to study the shear capacity of PBL shear connectors with through rebars through concrete tenons and to verify whether the steel grid-UHPC composite bridge deck in this configuration satisfies the longitudinal shear resistance requirements under normal operating conditions. The specific design parameters are presented in Table 6, while the detailed dimensions are illustrated in Figs. 20-22.

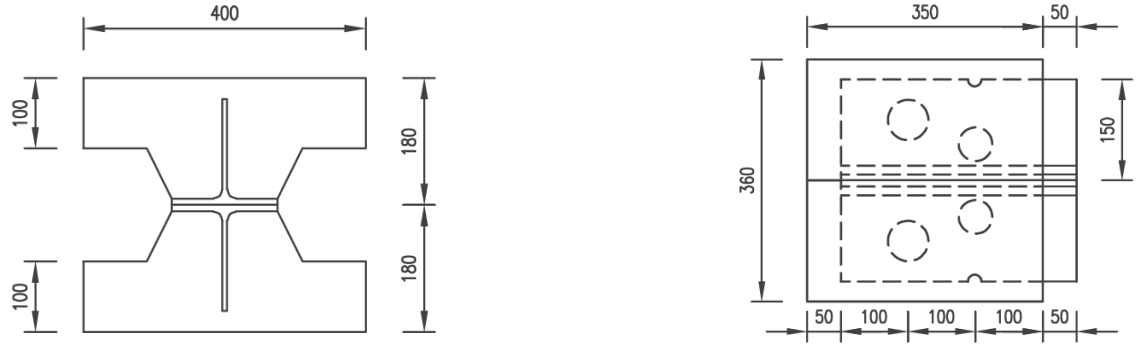
Table 6
Specific design parameters of push-out specimens

Specimens	Length (mm)	Width (mm)	T shaped steel (mm) Height*Width*Web thickness*Flange thickness	UHPC Height (mm)	Hole	Through Rebar
HY-1	350	400	150*150*6.5*9	80	No	No
HY-2	350	400	150*150*6.5*9	80	Yes	No
HY-3	350	400	150*150*6.5*9	80	Yes	Yes



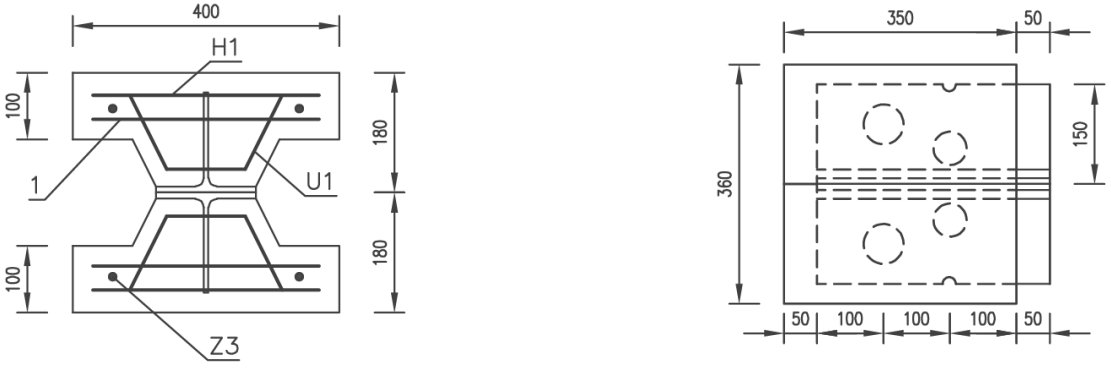
(a) Plan view (b) Elevation view

Fig. 20 Detailed dimension of specimen HY-1



(a) Plan view (b) Elevation view

Fig. 21 Detailed dimension of specimen HY-2



(a) Plan view (b) Elevation view

Fig. 22 Detailed dimension of specimen HY-3. (Rebars No. 1, H1, U1, Z3 are fabricated from HRB400, No. 1 features a diameter of 20 mm, No. H1, U1, Z3 feature a diameter of 12 mm.)

4.2. Material property

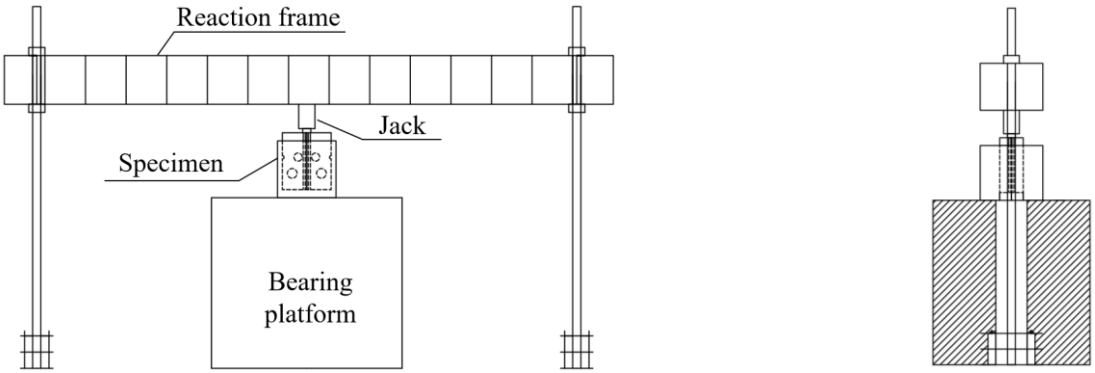
The preparation process of UHPC, along with its material characteristic test, as well as the material characteristics of T-shape steel and rebar, are thoroughly described in the authors' previously published paper (Liu et al., 2025b). Detailed material properties are presented in Table 7.

Table 7
The material characteristics of UHPC. (Unit: MPa)

Grade	Elastic modulus	Yield strength	Ultimate strength	Average compressive strength of cubic blocks during test period	Mean value of axial compressive strength	Mean value of axial tensile strength
C120	59642	/	/	153.0	105.6	11.89
Q355B	213642	357	566	/	/	/
HRB400	212753	425	631	/	/	/

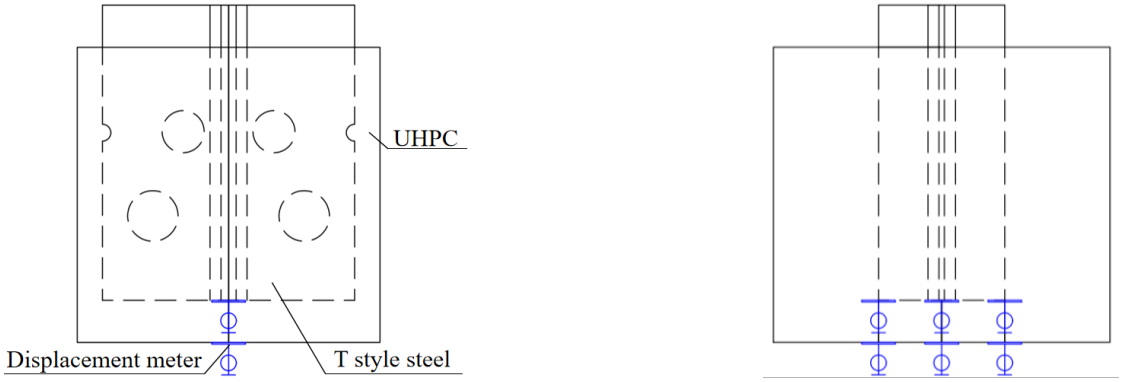
4.3. Loading device and measuring device

The loading device and measuring device for the push-out test are presented in Fig. 23 and Fig. 24 respectively.



(a) Front elevation (b) Side elevation

Fig. 23 Loading device for the push-out test



(a) Front elevation (b) Side elevation

Fig. 24 Measuring device for the push-out test

4.4. Experimental phenomena and analysis

4.4.1. Push-out specimen HY-1

Since the web of the push-out specimen HY-1's T shaped steel was not perforated, the shear force was entirely supported by the interface bonding capacity between the T shaped steel and the UHPC. The photographs depicting the specimen HY-1 in its pre-loading state and during the loading process are presented in Fig. 25 (a) and (b) respectively.

Due to the extremely brittle and rapid nature of the bond failure, a stable load-displacement curve could not be captured. Therefore, the failure progression was meticulously documented through direct observation and auditory monitoring. The chronological description of the failure mechanism, supported by post-failure examination, is provided as follows:

(1) Initial load-bearing stage (0~20kN): Under low load levels, the specimen exhibited no visible signs of distress. The behavior was presumed to be linear-elastic, based on the known material properties and analogy with the instrumented companion specimens.

(2) Onset of damage (20kN): As the load approached approximately 20kN, faint but distinct cracking sounds, characteristic of steel fiber fracture, became audible. This marked the initiation of damage within the UHPC matrix at the steel-concrete interface.

(3) Progressive interface degradation (20~40.1kN): With increasing load, the frequency of audible fiber-breakage events increased. Concurrently, visible gaps began to form and propagate at the interface between the T shaped steel and the UHPC, indicating a progressive loss of bond and interlock. The load continued to rise despite this ongoing damage, highlighting the residual load-carrying capacity provided by the fibers and friction.

(4) Catastrophic bond failure (peak load: 40.1kN): At a load of 40.1kN, a sudden, loud, and continuous tearing sound was heard. This acoustic event corresponded to the complete shear failure of the bond interface, leading to an instantaneous loss of composite action. The specimen experienced a push-out failure mode at this peak load.

(5) Post-failure behavior: Following the peak, the T shaped steel was pushed out from the UHPC block. The final separated state is shown in Fig.25 (c). The clean separation surface observed post-failure and minimal UHPC adhesion to the steel, confirms that the failure was primarily governed by bond-shear at the interface.



(a) Pre-loading state (b) During loading process (c) Post-failure state

Fig. 25 The photographs depicting the push-out specimen HY-1

4.4.2. Push-out specimen HY-2

The push-out specimen HY-2 contains perforations only in the web of the T shaped steel, with no through rebars installed. The shear force is collectively resisted by the interface bonding capacity between T shaped steel and UHPC, as well as the shear resistance offered by concrete tenons. The photographs depicting the specimen HY-2 during the loading process is presented in Fig. 26 (a). The load-displacement curve of specimen HY-2 during loading is presented in Fig. 27.

During the initial loading stage, the applied load remained relatively low and no noticeable displacement was observed. As the load gradually increased, a gap began to appear at the interface between one T shaped steel and the UHPC when the load reached approximately 30kN. This phenomenon is attributed to the unevenness of the specimen's base, which caused an imbalance in the distribution of forces during loading. The side that made contact first experienced separation between the T shaped steel and the UHPC, leading to a gap initiation. With further loading, as the force approached 150kN, it was observed that the width of the gap increased. At a load of 250kN, gaps also emerged at the interface between another T shaped steel and UHPC. It suggests that the bond between the T shaped steel and the UHPC has deteriorated further at this point, leading to a significant reduction in their interaction efficiency. When the load was raised to 350kN, one outside displacement meter provided a distinct reading. As the load continued to increase, the readings from the displacement meter progressively rose. It is evident that the failure of the bond between some steel components and UHPC led to the squeezing and deformation of the concrete tenon. Nevertheless, since the loading condition remained as eccentric compression, relative displacement initially occurred on one side. At 550kN, all interfaces between the T shaped steel and the UHPC exhibited gaps, resulting in the complete loss of bonding capacity. Consequently, the entire load was carried solely by the concrete tenons. At 600kN, another outside displacement meter started to display significant readings, which correspond to the initiation of deformation in the concrete tenon on this side. Upon reaching 800kN, the maximum gap width was measured at 1mm. At a load of 900kN, all displacement meters simultaneously recorded increased readings. Additionally, the relative displacement between the T-shaped steel and the UHPC continued to grow, indicating that the concrete tenon had been compressed and damaged. As a result, the specimen HY-2 experienced the push-out failure, and the damaged specimen was capable of withstanding a certain level of shear force, primarily due to the presence of frictional forces.



(a) During loading process (b) Post-failure status of HY-2 (c) Post-failure status of T shaped steel (d) Post-failure status of UHPC

Fig. 26 The photographs depicting the push-out specimen HY-2

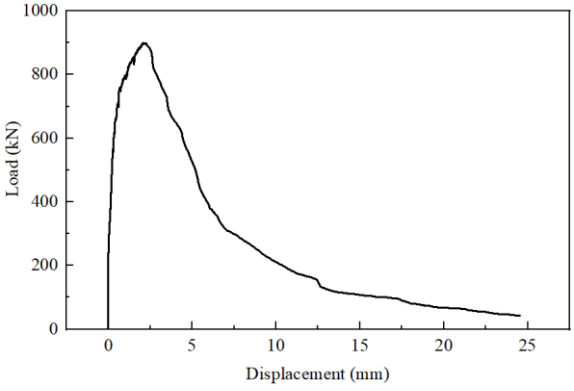


Fig. 27 The load-displacement curve for specimen HY-2 during loading

The post-failure status of the specimen HY-2 is shown in Fig. 26 (b). Post-failure examination revealed that the specimen could be disassembled, separating the T shaped steel from the UHPC. The post-failure status of T shaped steel and UHPC are illustrated in Figs. 26 (c) and (d) respectively. It is noted that there is no evident damage at the holes of the T shaped steel. The failure pattern is solely characterized by the concrete tenon being sheared by the web plate of the T shaped steel.

4.4.3. Push-out specimen HY-3

The push-out specimen HY-3 features perforations in the web of the T shaped steel, with through rebars inserted into these holes. The shear force is collectively resisted by the interface bonding capacity between T shaped steel and UHPC, the shear resistance offered by concrete tenons, and the shear resistance offered by through rebars within the concrete tenons. The photographs depicting the specimen HY-3 during the loading process is presented in Fig. 28 (a).

A continuous load-displacement curve for HY-3 is not available. This is because the test involved an unplanned interruption and repair (rewelding) following the premature failure of auxiliary welds, which made a single,

continuous curve non-representative of a monolithic structural response. Therefore, the subsequent analysis of the failure progression is based on a synthesis of recorded load levels, synchronized visual and auditory observations, and post-failure inspection.

(1) Initial elastic response and interfacial bond degradation (0~290 kN): During initial loading, the specimen exhibited negligible visible deformation, indicating an elastic response primarily governed by the bond-shear resistance at the steel-UHPC interface. The first significant damage indicator occurred at approximately 100 kN, where audible steel fiber breakage signaled the onset of interfacial bond deterioration. This process culminated at 290 kN with a loud noise, an instantaneous load drop to 280 kN, and the emergence of an interfacial gap without accompanying misalignment. Analysis reveals that, at this stage, one contributing factor is the ongoing failure of the bond between the T shaped steel and the UHPC, resulting in an increased gap at the interface. Another factor is the insufficient weld integrity, leading to the failure of certain weld points under load and producing a loud noise. This event marks the end of the interface-dominated load-transfer phase.

(2) Weld failure and structural integrity loss (410 kN): Subsequent loading to 410 kN triggered another loud noise, corresponding to the catastrophic failure of the connecting welds of the two T shaped steels, which induced component misalignment. This event underscores the critical role of connection detailing, as weld integrity became a limiting factor before the composite components could reach their full capacity. The necessary rewelding fundamentally altered the load path upon reloading.

(3) Engaged composite action and concrete tenon crushing (post-rewelding ~880 kN): Following rewelding, the reloading curve showed a renewed stiff response until approximately 880 kN, where a brief load plateau accompanied by incipient displacement indicated that the concrete tenons (mechanically interlocked via through rebars) had become the primary load-transfer mechanism. The stabilization at 880 kN reflects the progressive compressive crushing of the UHPC tenons against the steel web, a ductile yet capacity-limited process.

(4) Instability and Ultimate Buckling Failure (880 – 1050 kN): As the load increased to 910kN, a fundamental shift occurred: the load decreased despite ongoing displacement, signaling the onset of instability. When the load reduced to 812kN, the loading rate was increased. Finally, when the load sensor indicated 1050kN, the web of the top of the T shaped steel buckled, terminating the loading process. Specimen HY-3 ultimately exhibited buckling failure in the exposed web of the T shaped steel rather than push-out failure. The post-failure status of the push-out specimen HY-3 is presented in Fig. 28 (b). The recorded peak load of 1050 kN therefore represents a lower-bound estimate of the connector system's potential shear capacity. The true shear capacity of the mechanical interlock (concrete tenons and through rebars) is likely higher, as it was not fully exhausted before buckling occurred. The transition from a tenon-shear failure mode to steel web buckling as the ultimate limit state highlights a crucial design finding: for perforated web with through rebars details, member slenderness can govern failure, shifting it from the composite interface to the steel component itself.



(a) During loading process (b) Post-failure status

Fig. 28 The photographs depicting the push-out specimen HY-3

While the absence of displacement data precludes direct stiffness degradation or ductility analysis for HY-3, the coherent sequence of auditory events (fiber breakage, weld fracture) → visual evidence (gap formation, tenon crushing, web buckling) → load response (drops, plateaus) provides a robust qualitative framework. The recorded peak load of 1050 kN—significantly higher than that of non-perforated specimens—quantitatively validates the efficacy of the through rebars and tenon system in enhancing shear capacity. Ultimately, the failure narrative confirms that HY-3 failed not in push-out shear but in web buckling, a critical insight for the design of similar perforated steel-concrete composite connections.

4.5. Discussion

The specimen HY-1 without perforation of the web of the T shaped steel exhibited a push-out failure under a load of 40.1kN. This suggests that the interface bonding capacity between T shaped steel and UHPC within the current contact area was relatively low, specifically at 40.1kN. Following the failure, the specimen was unable to sustain any additional load, indicating a brittle failure pattern. This brittle failure mode, while accounting for a minor portion of the ultimate capacity, has significant implications for the long-term performance of such connections.

The brittle failure, often associated with a clean separation, indicates a lack of robustness. Environmental stressors (moisture ingress, freeze-thaw cycles, corrosion) can further degrade this already weak interface over time, accelerating the loss of composite action. The interfacial gap formed upon bond failure can also become a pathway for aggressive agents, affecting long-term durability. In addition, a weak and brittle interface is highly susceptible to fatigue cracking under cyclic loading. Micro-cracks can initiate and propagate rapidly at the interface under service loads well below the ultimate static capacity, potentially leading to premature fatigue failure of the connection. Therefore, while its contribution to ultimate static strength is minimal, the brittle nature of the bond failure underscores the necessity of mechanical interlock systems, such as the concrete tenons in HY-2 and the through rebars in HY-3, for ensuring durability and fatigue resistance in practical applications.

Compared with Specimen HY-1, Specimen HY-2 features one 60mm-diameter hole and one 50mm-diameter hole drilled in the web of the T shaped steel. Specimen HY-2 did not exhibit push-out failure until reaching a load of 900kN, which suggests that the concrete tenon possesses a relatively high shear capacity and effectively enhances the longitudinal shear capacity of the composite bridge deck. Furthermore, Specimen HY-2 retains a certain load-bearing capacity even after failure, indicating a ductile failure pattern.

By comparing the shear capacities of Specimen HY-1 and Specimen HY-2, it is evident that the proportion of interface bonding capacity between T shaped steel and UHPC contributing to the load-bearing capacity is less than 5%. When designing the longitudinal shear capacity for this composite bridge deck, for safety consideration, the contribution of the shear capacity provided by the interface bonding capacity can be disregarded in practical applications.

Two holes were introduced in the web of the T shaped steel in Specimen HY-2. The total shear capacity contributed by the two concrete tenons was calculated using Eqs. (4) and (5), yielding a value of 1150kN. The experimental value is approximately 0.78 times the theoretical prediction, indicating that the longitudinal shear capacity cannot be calculated by simply summing the shear capacities of individual concrete tenons. Additionally, the reduction in shear capacity between adjacent concrete tenons must be taken into account. This phenomenon is also evident in the parameter analysis presented in Fig. 13.

Based on the above experimental findings (a ratio of 0.78) and parametric analysis, it is clearly indicated that the basic formulas Eqs. (4) and (5) is not safe for multi-tenon design, and the reduction coefficient φ_c , φ_s for the group nail effect must be introduced. Formally present the final design formula is:

$$Q_u = \varphi_c \eta (d^2 - d_s^2) f_c + \varphi_s \xi d_s^2 f_s \tag{6}$$

where φ_c is the reduction coefficient of adjacent concrete tenons. For the two-tenon configuration in this study, a value of φ_c =0.80 is suggested. For arrangements with more tenons or closer spacing, lower values should be adopted based on the trend observed in Fig. 13, and specific values require further research for confirmation. This coefficient serves as a preliminary recommendation based on limited research and experimental data, and further calibration with more extensive data is required in the future. φ_s is the reduction coefficient of adjacent through rebars. The other parameters in Eq. (6) are the same as those in Eqs. (4) and (5).

The specimen HY-3 features two holes in the web of the T shaped steel, with through rebars inserted into these holes. Under the synergistic effect of concrete tenons and through rebars, this specimen did not exhibit push-out failure when the applied load reached 1050kN. It is evident that the through rebars within the holes substantially enhanced the longitudinal shear capacity, and this new composite bridge deck exhibits superior longitudinal shear behavior.

By comparing the shear strength of specimen HY-2 (without through rebars) and specimen HY-3 (with through rebars), the shear capacity of HY-2 is 900 kN, while that of HY-3 has a lower bound of 1050 kN. If reduction coefficients $\varphi_c = \varphi_s = 0.78$, it can be inferred that the lower limit of the through rebar influence coefficient (ξ) is approximately 1.1. This single-test estimate highlights the significant enhancing effect of through rebars but should be treated as indicative; a reliable value for ξ necessitates further systematic investigation.

For structures where fatigue, durability, or robustness are design concerns, reliance on adhesive bond strength alone is insufficient. The primary shear resistance should be provided by mechanical, ductile mechanisms (such as the perforated web with through rebars detailed in this study), with the bond considered a secondary line of defense or for serviceability conditions only.

5. Conclusions

This study proposes a novel composite bridge deck system named steel grid- UHPC composite bridge deck, and systematically investigates its longitudinal shear behavior. The main conclusion are summarized as follows:

(1) Nonlinear FEA shows that the failure pattern of PBL shear connectors in UHPC involves the shear and compressive failure of concrete tenons within the holes. The hole shape considerably influences the shear behavior of PBL shear connectors. Through rebars can substantially enhance the ductility and shear capacity. Additionally, the shear behavior improves with an increase in the hole number, an enlargement of the hole diameter, and an enhancement in the compressive resistance of the concrete.

(2) The contrastive analysis of the existing formulas and FEA results suggests that the formulas suggested in Chinese standard-JTG/T D64-01-2015, Chinese standard-GB 50917-2013 and the formula proposed by Hosaka et al. (2000) cannot be directly applied to calculate the shear capacity of PBL shear connectors in steel grid-UHPC composite bridge decks. A formula considering the shear resistance contributions of concrete tenons and through rebars taking into account the influence coefficients is proposed.

(3) Push-out tests confirm that the proposed composite deck exhibits superior longitudinal shear performance. For the configurations tested, the contribution of interface bonding to the total shear capacity was found to be less than 5%, suggesting it can be neglected in practical design for safety. Furthermore, the observed reduction in shear capacity between adjacent holes, attributed to the group effect, must be considered in design, for instance, through the reduction factors introduced in the proposed formula.

6. Limitations and future work

This study has several limitations that outline valuable directions for future research:

(1) The parametric analysis focused on key variables under typical configurations. Future work should employ nondimensional parameters and normalized capacities to generalize trends, and include cases with more holes and varied spacings to further isolate the group effect.

(2) The interface modeling simplification (tie constraint at the upper tenon-steel interface) could be refined in future studies to investigate local bond-slip behavior.

(3) The through rebar influence coefficient ξ in the proposed design formula remains uncalibrated. Future experimental and numerical studies focusing on parameters of through rebars (e.g., diameter, strength, layout) are needed to determine this coefficient reliably.

(4) Further experimental validation under a wider range of parameters and loading conditions (e.g., fatigue, long-term durability) is recommended to refine and calibrate the proposed design formula.

(5) A normalized comparative analysis between UHPC and conventional concrete, focusing on the distinct effects of fiber reinforcement, would help decouple material-specific behavior from geometric influences and further elucidate the role of UHPC in composite systems.

Acknowledgements

The study was supported by the Basic Science (Natural Science) Research Project of Higher Education Institutions in Jiangsu Province, China (Grant No. 23KJB560009), the National Natural Science Foundation of China (Grant No. 52078121), and the Scientific Research Foundation for High-Level Talents of Jinling Institute of Technology (Grant No. jit-b-202131). The financial supports are gratefully acknowledged.

References

[1] GB 50010-2010. (2010). Code for design of concrete structures. Beijing: Ministry of Housing and Urban-Rural Development of the People's Republic of China.

[2] GB 50017-2017. (2017). Standard for design of steel structures. Beijing: Ministry of Housing and Urban-Rural Development of the People's Republic of China.

[3] GB 50917-2013. (2013). Code for design of steel and concrete composite bridges. Beijing: Ministry of Housing and Urban-Rural Development of the People's Republic of China.

[4] GB/T 1499.2-2018. (2018). Steel for the reinforcement of concrete-Part 2: Hot rolled ribbed bars. Beijing: General Administration of Quality Super-vision, Inspection and Quarantine of the People's Republic of China.

[5] Hosaka, T., Mitsuki, K., Hiragi, H., Ushijima, Y., Tachibana, Y., & Watanabe, H. (2000). An experimental study on shear characteristics of perfobond strip and it's rational strength equations. *JSCE Journal of the Structural Engineering*, 46: 1593-1604.

[6] Jeong, Y.J., Kim, H.Y., & Koo, H.B. (2009). Longitudinal shear resistance of steel-concrete composite slabs with perfobond shear connectors. *Journal of Constructional Steel Research*, *65*(1), 81-88, DOI: 10.1016/j.jcsr.2008.01.031

[7] JTG/T D60-2015. (2015). General specifications for design of highway bridges and culverts. Beijing: Ministry of Transport of the People's Republic of China.

[8] JTG/T D64-01-2015. (2015). Specifications for design and construction of highway steel-concrete composite bridge. Beijing: Ministry of Transport of the People's Republic of China.

[9] Katwal, U., Tao, Z., & Hassan, M.K. (2018). Finite element modelling of steel-concrete composite beams with profiled steel sheeting. *Journal of Constructional Steel Research*, *146*, 1-15, DOI: 10.1016/j.jcsr.2018.03.011

[10] Kong, F.L., Huang, P.M., Han, B., Wang, X.Z., & Liu, C.Q. (2021). Experimental study on behavior of corrugated steel-concrete composite bridge decks with MCL shape composite dowels. *Engineering Structures*, *227*,111399, DOI: 10.1016/j.engstruct.2020.111399

[11] Leonhardt, F., Andrae, W., Andrae, H. P., & Harre, W. (1987). New, improved bonding means for composite load bearing structures with high fatigue strength. *Beton-und Stahlbetonbau*, *82*(12), 325-331.

[12] Li, L., Ye, M., Hu, F., Liao, R., Tang, J., Shao, X. Experimental study on the flexural behavior of a prefabricated large-cantilevered prestressed UHPC thin-walled bent cap. China Civil Engineering. Journal. 2020, 53, 92-104. DOI: 10.15951/j.tmgcxb.2020.02.008.

[13] Liu, S., Zhang, H., Ding, H., & Ren, Peng. (2025a). Study on the interface shear performance of corrugated steel-UHPC composite bridge decks with stud shear connectors. *KSCE Journal of Civil Engineering*, DOI: 10.1016/j.kscej.2025.100286

[14] Liu, S., Wang, P., Ren, P., & Ding, H. (2025b). Research on the Punching Shear Performance of Steel Grid–UHPC Composite Bridge Decks. Buildings, 15(18), 3398. https://doi.org/10.3390/buildings 15183398.

[15] Liu, T.X. (2017). Experimental and theoretical research on shear behavior of joints in precast UHPC segmental bridges. Master's Thesis, Southeast Universit, Nanjing.

[16] Luo, Y.B. (2013). Development of stud-SFRCC connection and its application to composite beam-to-column connections. PhD Thesis, Kyoto University, Kyoto.

[17] Pang, X., Zhang, D., Yu, C., Liu, C., & Kong. F. (2023). Mechanical performance analysis of corrugated steel composite bridge deck. *Journal of Hebei University of Engineering (Natural Science Edition)*, *40*(3): 70-76, DOI: 10.3969/j.issn.1673-9469.2023.03.010

[18] Shao, X.D., Yi, D.T., Huang, Z.Y., Zhao, H., Chen, B., & Liu, M.L. (2013). Basic performance of the composite deck system composed of orthotropic steel deck and ultrathin RPC layer. *Journal of Bridge Engineering*, *18*(5), 417-428, DOI: 10.1061/(ASCE)BE.1943-5592.0000348

[19] Shan, B. (2002). Experimental study on basic mechanical properties of reactive powder concrete. Master's Thesis, Hunan University, Changsha.

[20] Su, Q.T., Tian, L., Zeng, M.G., Shao, C.Y., & Chen, L. (2016). Research on basic performance of composite bridge decks with orthotropic corrugated steel plates and concrete. *Engineering Mechanics*, *33*(S1), 138-142, DOI: 10.6052/j.issn.1000-4750.2015.04.S014

[21] Sugano, S., Kimura, H., & Shirai, K. (2007). Study of new RC structures using ultra-high-strength fiber-reinforced concrete (UFC)-The challenge of applying 200 MPa UFC to earthquake resistant building structures. *Journal of Advanced Concrete Technology*, *5*(2), 133-147,

[22] Yang, X., He, J., Hu, D., Xiao, B., & Wang, N. (2024). Numerical study on shear performance of stud-PBL shear connector in corrugated steel plate-UHPC layer composite deck. *Journal of Railway Science and Engineering*, 21(2):697-708, DOI:10.19713/j.cnki.43-1423/u.T20230495

[23] Zhang, Q.H., Cheng, Z.Y., Liao, G.X., Bu, Y.Z., & Li, Q. (2018). Optimal design of corrugated steel deck plate-UHPC layer composite deck. *Journal of Southwest Jiaotong University*, *53*(4), 670-678, DOI: 10. 3969/j. issn. 0258-2724. 2018. 04. 002

[24] Zhang, Q.H., Guo, W.F., Cui, C., & Ye, H.W. (2015). Study on the fatigue properties of a novel large longitudinal rib steel-concrete composite orthogonal bridge deck. *Highway*, *60*(12), 71-77.

[25] Zhang, X., Wu, C., & Su, Q. (2024). Experiment on load capacity of profiled steel sheeting-concrete composite bridge decks [J]. *Journal of Jilin University (Engineering and Technology Edition)*, *54*(10): 2870-2883, DOI: 10.13229/j.cnki.jdxbgxb.20221556

[26] Zhou, Y., & Yao, C. (2019). Literature review on mechanical properties of PBL shear connectors [J]. *Journal of Chengdu University* (*Natural Science Edition*), *38*(4): 431-437, DOI: 10.3969/j.issn.1004-5422.2019.04.021

Advanced Steel Construction – Vol. 22 No. 5 (2026) 522–537
DOI:10.18057/IJASC.2026.22.5.4

THE CURRENT APPROACH FOR THE DESIGN OF STEEL PALLET RACKS

Marina Pastore [1,*], Jessey Lee [2] , Rosario Montuori [3] and Elide Nastri [1]

[1] *Department of Civil engineering, University of Salerno, Italy*
[2] *School of Engineering, Swinburne University of Technology, Australia*
[3] *Department of Pharmacy, University of Salerno, Italy*
** (Corresponding author: E-mail: marpastore@unisa.it)*

ABSTRACT

Steel pallet racking systems constitute a structural typology governed by slender perforated members, semi-rigid connections, and pronounced second-order effects. Although extensive experimental research exists on components, practical design remains dictated by regional standards embedding different modelling philosophies and reliability formats. Consequently, identical configurations may lead to significantly divergent safety assessments depending solely on the regulatory framework adopted. Despite its international relevance, a systematic comparison among rack-specific design standards is still missing. This paper addresses this gap through a critical examination of the European framework [2]-[14] , the Australian/New Zealand provisions [15]-[17], and the North American specifications [18]-[23]. The study analyses how these systems treat perforations, cross-section classification, imperfection strategies, connection characterization, and flexural–torsional instability. The comparison reveals substantial conceptual convergences—notably in design assisted by testing—but also significant divergences in safety formats and modelling assumptions affecting design margins. By clarifying the implications embedded in alternative normative approaches, the work provides a foundation for future harmonization and identifies priority areas requiring urgent experimental calibration and theoretical development.

Copyright © 2026 by The Hong Kong Institute of Steel Construction. All rights reserved.

ARTICLE HISTORY

Received: 5 March 2026
Revised: 10 July 2026
Accepted: 15 July 2026

KEYWORDS

Pallet racks;
Thin-walled sections;
Bracing system;
EN15512;
Eurocodes;
AS 4084;
AISI MH16.1-22

1. Introduction

Steel pallet racking systems represent one of the most demanding applications of cold-formed steel structures. In contrast with conventional buildings, these systems operate very close to their design resistance while exhibiting pronounced geometric slenderness, perforated uprights, semi-rigid beam-to-column connections and a high sensitivity to second-order effects. Their structural response is therefore governed by complex instability mechanisms involving local, distortional and global buckling, strongly influenced by connection deformability and installation tolerances.

During the last decades, a large body of experimental and numerical research has improved the understanding of individual components, particularly beam-to-upright joints and perforated members. However, practical design is still mainly controlled by national or regional standards, each embedding specific safety formats, modelling philosophies and levels of reliance on testing. At the international scale, three principal regulatory environments dominate the design of pallet racks: the European framework based on EN 15512 [6] and the Eurocodes [2]- [5], the Australian/New Zealand provisions represented mainly by AS 4084 [15]-[17], and the North American system centred on ANSI MH16.1 [18] together with AISI and AISC specifications [20]-[23]. Although these documents pursue comparable safety objectives, they differ substantially in their treatment of perforations, cross-section classification, imperfection strategies, connection modelling and instability verification.

This diversity leads to a crucial engineering question: can identical physical structures reach different reliability levels solely because they are designed under different regulatory frameworks?

Despite the relevance of this issue for global manufacturing and international trade, the literature still lacks a systematic and critical comparison among rack-specific standards.

The present study aims to fill this gap through a structured comparative analysis of the principal international provisions governing steel pallet racking systems. Rather than merely summarizing prescriptions, the work interprets the mechanical assumptions behind each approach, highlights conceptual convergences and inconsistencies, and identifies areas where further experimental calibration and harmonization are needed. Special attention is devoted to perforated uprights, connection characterization, imperfection modelling and flexural–torsional instability.

By clarifying how regulatory philosophies translate into practical design consequences, the paper seeks to strengthen the dialogue between research, standardization bodies and industrial practice, ultimately contributing to more transparent and reliable structural assessment of pallet racking installations worldwide.

2. Structural configuration of pallet racks

A typical pallet rack system (**Fig. 1**) features a regular and repetitive structural configuration, both in plan and elevation. The primary vertical components are known as uprights, which are generally formed with monosymmetric steel cross-sections, perforated with a specific hole array — typically proprietary to each manufacturer — which enables flexible beam positioning. Beams, having double-symmetric or boxed cross-sections, are directly linked to the uprights via connectors that are usually welded onto the ends of the beams. These connectors engage with the upright's hole pattern to create a semi-rigid or pin-connected joint. The palletized goods are placed directly on the beams: however, shelves may also be installed on the beams to support non-palletized loads or enhance load distribution. Structural spines are integral to the frame and provide essential lateral stiffness to the system. These spines typically consist of vertical and diagonal bracing elements. While additional bracing in the down-aisle direction (longitudinal to the racking row) is possible, it is not always mandatory [6]. Bracing usually has a lipped channel section to balance strength and weight efficiency. Finally, ties — which are also similar in section to braces — are installed at the top and/or at the base of the frame. Their function is to manage bending moments and to enhance the overall stability of the racking system by tying the bases of uprights together, contributing to a more rigid structural response.

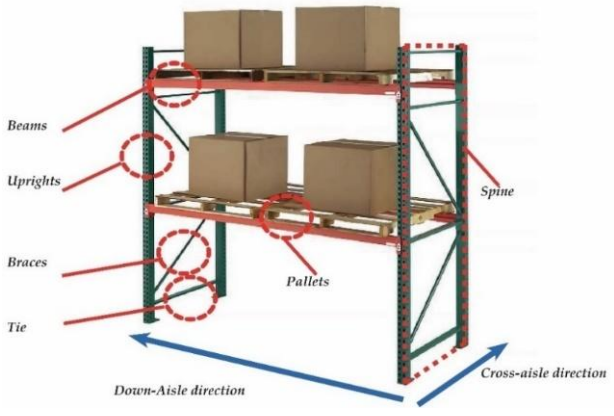


Fig. 1 Anatomy of a Pallet rack

The typical pallet rack design employs clipped (with tabs) beam-column connections, as illustrated in **Fig. 2** [24]15-[35] even if also bolted [36]-[41] and combined clipped-bolted connections [42]-[44] can be used. The most common

configuration with tabs allows for full adjustability in setting beam elevations, thereby facilitating rapid assembly and flexible use. However, these joints exhibit semi-rigid behaviour and low dissipative capacity under seismic scenarios [45]-[49]

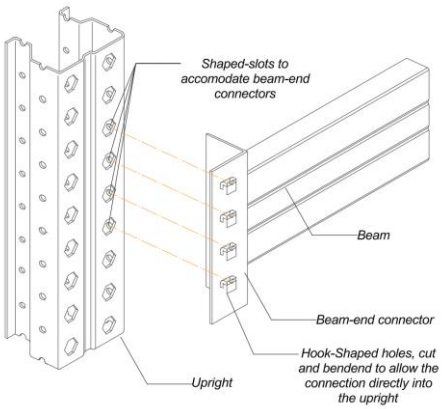


Fig. 2 A typical Beam-Column Connection

Moreover, unbraced pallet racks become highly susceptible to sway, making second-order (P-Δ) effects a critical consideration in structural design. Another characteristic of this connection system is the presence of a regular array of perforations along the uprights. These perforations, accommodate the beam connectors but also influence the structural performance of the columns [50]-[74]. Consequently, upright design typically involves analysing a singly symmetric, perforated open section, subjected to axial load combined with biaxial bending. In addition, the influence of the base-upright connections cannot be neglected [75]-[78]. The irregular stiffness distribution due to perforations requires detailed consideration in both local and global stability assessments. From both functional and design perspectives, it is essential to understand how national and international regulations influence the development and application of industrial pallet rack systems [79]-[108]. Each country tends to adopt its own regulatory approach, largely shaped by its own technical traditions and engineering philosophies. These national characteristics are often embedded in the formal standards currently in force.

3. International design frameworks for pallet racking systems

Safety - both as a design principle and a regulatory requirement- remains a central focus across all major regulatory frameworks.

This is particularly emphasized in European standards, which reflect the European Union's prioritization of structural reliability and risk mitigation[2]-[14]. However, similar safety-centric approaches are also evident in standards from other regions, such as those established in Australia [15]-[17] and the United States[18]-[23]. Despite these shared objectives, the global regulatory landscape remains highly fragmented. Within Europe, the European Committee for Standardization (CEN) has issued harmonized EN standards. Nevertheless, individual member states often maintain supplementary national regulations, which can lead to discrepancies in terms of application. Outside of Europe, the regulatory environment is different: the primary references are both the New Zealand/Australian standards and the American standards developed by organizations such as AISI (American Iron and Steel Institute) and AISC (American Institute of Steel Construction).

In the Asian context [82]-[83], the regulatory framework differs significantly. A common feature of China and Japan is the existence of a primary code governing general steel structures, which is mandatory. In addition to this main code, there are several supplementary codes or standards—that can be referred to as "satellite" documents—which primarily serve regulatory or guidance functions rather than carrying mandatory status. Another similarity between the Chinese [82]-[83] and Japanese [84] design codes lies in their treatment of cross-section classification. Although not as explicitly defined as in the Eurocode or the American/Australian standards, both codes employ a comparable approach based on the width-to-thickness (b/t) ratio. In contrast, the treatment of partial safety factors differs significantly. The Chinese and Japanese codes apply partial factors tailored to specific scenarios, which diverges from the more generalized approach adopted by the Eurocode but aligns more closely with the streamlined methodology of the American standard. Both countries address local buckling rigorously through the Effective Width Method, which serves as a functional equivalent to the design provisions for Eurocode Class 3 (semi-compact) and Class 4 (slender) cross-sections [85].

The current regulatory framework in Europe is well-defined. The primary references for the design of pallet racking systems are the EN 15512:2022 [6] (a design code for static storage systems), and the EN 15620 [7] (for specific tolerances design). These standards are supplemented by other codes — such as FEM regulations — which address more specific technical details and tolerances The Eurocodes form the backbone of the European structural design philosophy. They emphasize robustness, reliability, and are grounded in probabilistic theory. EN 15512:2022 [6] and EN 15620 [7] promote the concept of "design assisted by testing" (DAT). This approach integrates theoretical models with empirical data, allowing experimental validation to refine and support design assumptions. In practice, using EN 15512:2022 [6] and EN 15620 [7], with complementary references to Eurocodes [2]-[5] and FEM regulations [11]-[13], ensures high-quality modelling and calculation.

Additionally, the European Technical Assessment (ETA) system (formerly ETA European Technical Approval) offers performance evaluations based on the European Assessment Document (EAD) [14]. These documents define product characteristics for their intended use but do not provide structural design guidance. Instead, they ensure product quality and reliability, aligned with the values of the European Market. A recent and complex development is the introduction of EU Machinery Regulation (EU) 2023/1230 [9], which will be mandatory in 2027. Under this framework static pallet racking systems (classic racks) are excluded from the definition of machinery, while mobile racking systems or any system with motorized/movable parts are classified as quasi-machines (partially automated systems) or machines (fully mobile systems).

Therefore, such mobile systems fall under the scope of EN 15095 [10] and the EU 2023/1230 [9] regulation, while static systems remain exempt.

The regulatory frameworks for pallet racking systems in Australia and New Zealand [15]-[16] share significant similarities, primarily due to their alignment with the European standard EN 15512:2022 [6]. Since the inception of a comprehensive harmonization process in 2012, successive revisions have introduced stringent safety and reliability requirements, making many pallet racks manufactured prior to that year effectively obsolete. Both countries now apply a risk-based classification system—categorized as green, amber, or red—each of which requires specific testing, inspection, monitoring protocols, and mandatory staff training. A distinctive feature of these standards is their dual scope: they incorporate both structural engineering criteria and operational guidelines, thereby addressing the responsibilities of both engineers and facility operators. Notably, both AS 4084 [15] and EN 15512:2022 [6] offer two analytical methods for structural evaluation—the simplified method and the global analysis method—for scenarios such as instability checks. These methodologies are conceptually aligned, and the overall structure of the two standards is closely comparable. Additionally, both standards emphasize the use of design assisted by testing. Several regulatory principles also show some convergence with American practices which is for its side more fragmented and complex. The principal reference is ANSI MH16.1-23 [18] and FEMA dispositions [19], supported by related standards such as ANSI/AISC 360-22 [20] and ANSI/AISI S100-20-20 [22] , which are applied in an interconnected manner. Despite the complexity, the American standards also endorse the design assisted by testing approach, reflecting an international trend toward data-supported structural design. Two distinct design philosophies are permitted: Load and Resistance Factor Design (LRFD) and Allowable Strength Design (ASD). LRFD, based on probabilistic load modelling and safety factors, closely parallels the statistical and reliability-based approaches used in Eurocodes. Conversely, ASD represents a more traditional method. A defining characteristic of the American approach is its focus on extensive guidance and practical application. Numerous illustrative examples, typical sections, and case scenarios are provided to assist in design interpretation and implementation. While certain edge cases may not be explicitly addressed, they can often be resolved through informed interpretation of the standards. This layered and prescriptive regulatory landscape reflects the broader technical and regulatory tradition in the United States, which tends to favour comprehensive documentation and narrowly defined procedures.

It should be noted that previous research has conducted comparative assessments and inquiries on three major steel codes in particular Chinese GB 50017 [82], Eurocode 3 [2] and AISC 360 [20] with particular focus on classification of steel sections and design for local buckling [85]. However, there is a notable absence of comparable reviews addressing the rack-specific standards that govern cold-formed, perforated, and highly slender structural components. Noticing said gaps, and by embracing the insights and contributions of previous authors, this article gathers their intellectual legacy and expands the comparative analysis of the regulations, providing a comprehensive comparative review. In addition to normative comparisons, safety has been investigated using reliability-based approaches, which provide a robust framework for managing uncertainties inherent in structural design parameters. These methods allow for a more systematic evaluation of variability

in material properties, loading conditions, and geometric imperfections. However, existing reliability-focused studies are devoted to in-depth comparisons between the European and Australian standards, emphasizing a gap in the literature regarding similar evaluations involving other international codes [86]-[87].

3.1. European regulatory framework

The European approach to pallet rack design is deeply rooted in the reliability philosophy of the Eurocodes, where safety is expressed through partial factors, calibrated limit states, and explicit control of instability phenomena. Within this environment, EN 15512 [6] represents the sector-specific translation of general steel design principles to the peculiar world of storage systems, characterized by perforated uprights, semi-rigid joints, and highly repetitive structural layouts.

A central role in this framework is played by the FEM documents[11]-[13], which act as a technical bridge between the general prescriptions of Eurocode 3[2]-[5] and the operational needs of racking manufacturers and designers. In practice, FEM provisions frequently adopt Eurocode formulations, terminology, and safety formats, while adapting them to configurations that are rarely covered explicitly in building-oriented standards. This continuous cross-referencing generates a harmonized yet multi-layered system, in which global reliability concepts descend from the Eurocodes and are subsequently refined through rack-specific adjustments.

One of the most distinctive features of the European model is the institutionalization of design assisted by testing (DAT). The code implicitly recognizes that the mechanical response of thin-walled perforated members and connector-dominated assemblies cannot always be captured through closed-form expressions originally calibrated for more conventional structural typologies. As a result, experimental evidence is not treated as an exceptional validation tool but as an integral component of the design pathway.

This hybrid nature—probabilistic consistency at the global level combined with empirical calibration at the component scale—defines both the strength and the complexity of the European regulatory philosophy. On the one hand, it ensures theoretical coherence with the broader structural safety framework of the Union; on the other, it places significant responsibility on the availability, interpretation, and transferability of test results.

Recognizing this balance between codified generality and experimentally informed specialization is essential for any meaningful comparison with non-European approaches.

3.2. Australian regulatory framework

The Australian approach, embodied in AS 4084 [15], adopts the limit states philosophy but interprets it through a markedly pragmatic and application-driven perspective. Instead of prescribing a unique analytical pathway, the standard allows multiple calculation methodologies, whose adoption depends on installation tolerances, structural configuration, and the degree of refinement required. This plurality reflects a regulatory culture that privileges adaptability to industrial reality over strict procedural uniformity.

Although different routes are formally available, AS 4084 [15] accompanies them with recommendations intended to orient professional judgement. The designer is therefore granted a relatively wide interpretative responsibility, while remaining within a framework aimed at ensuring consistent and reliable outcomes. Compared with the European environment—where procedures are embedded in a more hierarchical and cross-referenced normative structure—the Australian model provides greater flexibility in how global behaviour is represented.

Experimental verification remains fundamental. Testing provisions are deeply integrated into the design philosophy, acknowledging that the behaviour of perforated thin-walled members and connector-dominated assemblies cannot be exhaustively captured through simplified analytical formulations. However, the interaction between empirical evidence and codified expressions is often presented in a more direct, practice-oriented manner, favouring usability in routine engineering activities.

AS 4084 [15] relies on AS/NZS 4600 [17] for the design of cold-formed members, thereby extending the admissible material strength range beyond that typically considered in Eurocode-based approaches. The possibility of employing steels up to G550 implies different non-dimensional slenderness values, alternative reduction factors, and potentially distinct instability predictions. Consequently, even when identical geometries are analysed, variations in assumed yield strength may translate into non-negligible differences in calculated resistance and global safety margins.

The Australian framework can thus be interpreted as a system in which codified reliability, practical applicability, and designer-driven choices coexist in a dynamic equilibrium. This position, while sharing the international trend toward design assisted by testing, contrasts with the more formally structured European hierarchy of norms and prepares the ground for further divergences when compared with North American prescriptions.

3.3. The American Standards: AISI MH16.1-23, ANSI/AISC 360-22, AISI/AISC S100, AISI/AISC S200

The North American system, primarily represented by ANSI MH16.1 [18] and supported by AISI and AISC specifications [20]-[23], adopts a regulatory architecture that is both comprehensive and strongly oriented toward practical implementation. Rather than being organized through a hierarchical chain of documents as in the European environment, the American approach operates through a network of interdependent standards that collectively define member design, connection behaviour, fabrication requirements, and analysis strategies.

A distinctive characteristic of this framework is the formal coexistence of two design philosophies: Load and Resistance Factor Design (LRFD) ($R_u \leq \Phi R_n$ where R_u required strength by LRFD load combinations, R_n Nominal strength and Φ resistance factor) and Allowable Strength Design (ASD) ($R_a \leq R_n/\Omega$ where R_a required strength by ASD load combinations, R_n Nominal strength and Ω safety factor). While LRFD follows a probabilistic format conceptually comparable to European limit state principles, ASD preserves a more traditional safety representation based on global factors applied to nominal resistances. The availability of both methods reflects the intention to accommodate a wide spectrum of industrial products, historical practices, and professional preferences.

From an engineering perspective, this duality implies that identical structural configurations may be evaluated through alternative safety lenses, potentially leading to different utilization ratios and intervention thresholds. In contrast with the European tendency toward methodological unification, the American system prioritizes inclusiveness and continuity with established design routines.

The analytical procedures are typically accompanied by extensive commentary, application guidance, and worked examples. This prescriptive richness facilitates implementation and reduces ambiguity in everyday design, but at the same time may limit the degree of abstraction in the treatment of complex phenomena such as perforation-driven instability or connection nonlinearity. In this context, the contributions of Peköz et al. [18]-[20],[88], [110]-[111] are particularly relevant, because they helped establish a mechanically grounded framework for the design of cold-formed steel members, combining experimental evidence, elastic buckling analysis and design-oriented strength formulations. Their work is especially important for rack uprights, where local, distortional and global buckling modes interact with perforations, slenderness and boundary conditions. The North American design philosophy, including the development and application of the Direct Strength Method, reflects this broader research background by linking experimentally observed behaviour with stability-based design procedures. The present review builds upon this line of research by examining how such mechanically based concepts are incorporated, simplified or complemented by testing within the European, Australian and American rack-specific standards.

Within this environment, testing remains essential, yet it is often framed as a means of qualifying components inside predefined procedural boundaries rather than as a mechanism for redefining analytical formulations. The result is a regulatory culture where clarity of application, repeatability, and industrial operability become primary objectives.

Understanding this practice-oriented orientation is crucial when comparing North American prescriptions with the more formally structured European model and the judgement-driven flexibility characterizing the Australian framework.

4. Structural idealization in pallet rack design

Before numerical verification is carried out, each regulatory framework transforms the physical pallet rack into an analytical model. This translation requires assumptions regarding geometry, boundary conditions, connection behaviour, stiffness distribution, and imperfection patterns. Far from being neutral, these modelling choices govern internal force paths, second-order amplification, and the instability mechanisms that ultimately define structural safety.

Therefore, the design of pallet racking systems does not depend solely on the intrinsic mechanical response of individual components, but on how that response is represented, simplified, and formalized within codified procedures. Understanding this process of idealization is essential for any meaningful comparison among international standards.

The following sections analyse how different regulations prescribe

tolerances, define upright modelling strategies, characterize connections, introduce imperfections, and assemble load scenarios. Rather than reproducing literal provisions, the discussion focuses on the mechanical implications embedded in these modelling frameworks and on their potential influence on predicted reliability.

4.1. Tolerances

Tolerances are a critical aspect of pallet rack design, particularly because thin-walled cold-formed steel sections are highly sensitive to global and local imperfections [1], as well as to torsional and flexural-torsional bending effects [1]. The European approach emphasizes precision through highly detailed standards governing tolerances, deformations, and permissible gaps. These strict acceptance criteria aim to minimize errors in installation and placement, as well as structural flaws or unexpected loads, all of which can significantly impact the static and dynamic performance of pallet racking systems. The EN 15620 [7] standard is primarily focused on these tolerances, along with deformations and gaps. It includes detailed guidance on how to account for additional forces that arise due to disproportional unloading and operational actions. EN 15620 [7] also outlines requirements for the proper placement of pallet racks to ensure safe and efficient manoeuvring of lift trucks. The emphasis here is operational rather than analytical; it does not delve deeply into structural modelling or calculations. Instead, it often references FEM [11]-[13] dispositions, which are used primarily for checking pallet racks in terms of service conditions and maintenance. A closely related standard is EN 15635 [8], which also addresses tolerances, deformations, and clearances. Like EN 15620 [7], it provides recommendations for handling the effects of uneven loading and dynamic operational actions, and how to position racking systems to accommodate lift truck movements. However, while the two standards overlap significantly, their intended audiences and primary purposes differ. EN 15635 [8] is more concerned with the ongoing safety and maintenance of storage systems and is typically aimed at warehouse operators and safety personnel, whereas EN 15620 [7] targets the installation and layout stage. In contrast, FEM codes—such as EN 15512:2022 [6] (developed under the umbrella of the European Racking Federation, or FEM)—serve a different purpose. While many EN standards refer to FEM guidance, these codes are technically oriented, designed mainly for use by engineers and designers. Their focus is on structural analysis, load-bearing capacity, and compliance with design principles, well before the system is operational. FEM codes provide the technical backbone that supports the broader, more practical guidelines found in EN 15620 [7] and EN 15635 [8]. The main differences between the codes are reported in **Table 1**.

The current global design approach increasingly relies on FEM dispositions, largely due to their flexibility and ease of updating. These standards serve as the foundation for several national codes. The Australian standard AS 4084 [15] aligns closely with FEM guidelines and references EN 15620 [7] for clearance and tolerances and EN 15635 [8] for operation and maintenance of racking systems. However, it introduces specific provisions, particularly for seismic response and fire resistance, reflecting local risk considerations. A unique aspect of AS 4084 [15] is that it imposes strict and detailed requirements for both designers and operators, covering the full lifecycle of the racking system.

Table 1
Main differences between EN15620 [7], EN15635 [8] and FEM regulations [11]-[13]

Aspects	EN 15620	EN 15635	FEM Regulations
Focus	Tolerances, deformations, clearances	Application, operation, maintenance	Design, testing, and engineering
Purpose	Ensures proper installation and fit	Ensures safe use and maintenance	Ensures structural safety and design
Target Audience	Installers, manufacturers	Operators, maintenance personnel	Designers, engineers, manufacturers
Key Topics	Tolerances, clearances, deformations	Inspections, training, repairs	Load capacity, testing, seismic behavior

In the United States, tolerances and structural requirements are addressed primarily through AISI/AISC 360-22 [20], which outlines the design specifications for cold-formed and structural steel. While tolerances are generally permitted, the second-order effects (such as those arising from imperfections or deformations) must still be explicitly considered, as emphasized in the general provisions of AISI 360-22 [20].

4.2. The uprights

Uprights are usually cold formed-steel, and usually those parts are affected by a regular hole array, which means that usually the modelling is a bit more complicated. Firstly, in the analysis of specific structural sections, it is critical to identify the appropriate cross-sectional area for evaluating the nominal strength of the upright member. In many cases, the use of net area alone is inadequate, as it may not accurately capture the effective resistance of the section under applied loads. A thorough consideration of all relevant section properties is therefore necessary to ensure a reliable and accurate strength assessment. Furthermore, the effective area, typical for thin walled cold-formed sections, must still necessarily taken into consideration.

Eurocodes shows a series of solutions concerning these kinds of sections, mainly centred on FEM method analysis and/or design assisted by testing, specifically in Eurocode 3 part 1-5 [4], annex C.

About the EN 15512:2022 [6], the code introduces the so called “equivalent Section”, i.e. a “virtual section” without holes but considering the effects of the hole arrays.

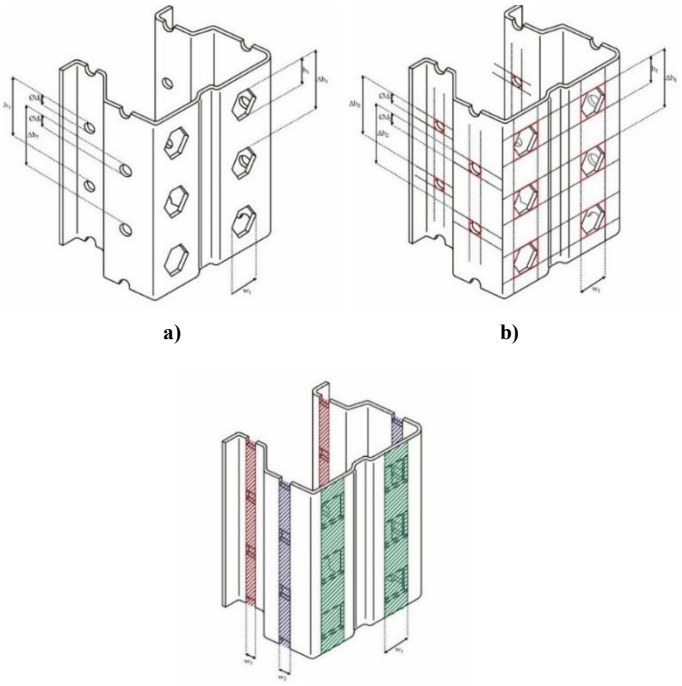


Fig. 3 The construction (in phases) of the “equivalent section” according to Annex G of EN15512:2023[6]

In EN 15512:2022 [6], Annex G (“Equivalent section properties”), the procedure for deriving an equivalent section of the uprights is presented in an explicit and practical way. In essence, the actual hole pattern is first “linearised” and simplified. The upright cross-section is then divided into strips; for each strip an equivalent thickness is calculated by redistributing the solid and void areas along the entire height of the member. This transforms the perforated section into a continuous section with equivalent mechanical properties that can be used for structural checks. While conceptually similar to the commonly used “equivalent strip method” found in other standards, the EN 15512:2022 [6] approach is formulated in a clearer and more operational manner.

No comparable approach exists in the other standards. Generally, all section properties should be derived from this equivalent value, except when the effective area is smaller than the equivalent one (with some specific exceptions, such as in flexural–torsional verifications). In line with the general philosophy of “design assisted by testing,” [86]-[108] the design must ultimately be validated by physical tests. The use of the finite strip method, among other advanced analytical tools, is also permitted and actively encouraged [101]-[108].

In the Australian Standard [15]-[17] the presence of hole arrays is generally considered indirectly through the assumptions made in the analysis. In some cases, a “net area” is also defined—typically as the sum of the products of the

material thickness and the net width of each component, adapted to the specific configuration. This calculation explicitly accounts for local reductions caused by holes, retainers and other detailing. The section is regarded as valid provided that the surrounding constraints and boundary conditions are properly evaluated, with the exception of joint imperfections. In contrast, some methods—such as GMNIA-C (geometric and material non-linear analysis for compact sections) require explicit consideration of member imperfections. This differs from the approach taken in EN 15512:2022 [6], where such imperfections are generally not included directly in the analysis of individual members.

The American standard refers to AISI S902-17 [23], which addresses the determination of the "*effective area"* of cold-formed steel columns typically derived from experimental testing—most notably the stub column test. This approach is appropriate given that the sections in question are generally Class III or IV (according to international classification) or, in American terms, *slender sections*. In such cases, not all the cross-sectional area effectively resists the applied loads, due to susceptibility to local and global buckling. Therefore, using the effective area ensures a more realistic assessment of the member's strength under compression and other solicitations. In some cases, reference is also made to another parameter, A_{net}, which is essentially the same as that used in the Australian codes but adapted to the specific phenomenon under consideration. (i.e. A_{netg} is for buckling).

The correct assessment of the section properties of perforated uprights is a central issue in rack design. However, the difference between the European [6] and North American [18] approaches should not be interpreted only in terms of whether a larger or smaller effective area is obtained. The most relevant mechanical distinction concerns how each method represents the geometry of the resisting section and, consequently, whether the shift of the centroidal axes and the associated secondary moments are explicitly captured.

In the European framework, EN 15512 [6] adopts an equivalent-section approach. The perforated upright is transformed into a continuous reduced section by redistributing the solid and void areas along the member. This procedure modifies the geometry of the cross-section itself. As a result, the centroidal axes, moments of inertia, torsional properties and, where relevant, the position of the shear centre can be recalculated on the equivalent section. If the perforation pattern is asymmetric with respect to one or both principal axes, the equivalent section may exhibit a centroidal shift relative to the gross section. Under axial compression, this shift generates an additional eccentricity, and therefore secondary bending moments may arise even when the external axial load is nominally applied through the gross-section centroid.

This mechanism is particularly relevant for monosymmetric open uprights, where the centroid and shear centre are already separated and where perforation-induced stiffness reductions may further modify the effective load path. In such cases, the equivalent-section approach provides a direct mechanical route for accounting for secondary moments associated with centroidal axis shift. Nevertheless, this representation remains approximate, because the real perforation pattern is smeared into a continuous fictitious geometry and local stress concentrations around holes are not explicitly resolved.

The North American approach [18] is based on a different philosophy. When the effective area is derived from stub column tests, the influence of perforations is introduced mainly through the experimentally observed reduction in compression resistance. This strength-based parameter can reflect the combined effect of local buckling, distortional deformation, stress concentration and hole geometry on the ultimate axial capacity. However, it does not automatically reconstruct the geometry of the effective resisting section. Therefore, the shift of centroidal axes caused by asymmetric perforations is not necessarily made explicit in routine design calculations. Its effect may be implicitly included in the tested resistance if the test specimen and loading conditions activate the same eccentricity mechanism, but the corresponding secondary moments are not separately identified unless a refined rational analysis or numerical model is used.

The mechanical consequence is that the European equivalent-section approach tends to make eccentricity effects more visible in the design process, while the American effective-area approach tends to incorporate perforation effects as a lumped resistance reduction [80][81]. The former is more transparent in tracking centroidal shift and secondary moments, but may oversimplify local perforation effects. The latter is more directly calibrated to test resistance, but may conceal the specific contribution of centroidal shift, particularly in asymmetric sections. For this reason, the two approaches are not merely different area-reduction procedures; they embody different assumptions about how perforations alter the load path, stiffness distribution and instability response of rack uprights. In general, uprights shall be designed to resist critical combinations of vertical and horizontal loads under the most unfavourable conditions. All forces and moments induced in the columns must be considered to ensure structural integrity. Stability requirements must be met, including resistance to wind and seismic actions. However, according to most applicable standards, it is not necessary to analyse both directions (cross-aisle and down-aisle) simultaneously in most cases. The use of finite element methods is permitted—and encouraged—for design analysis, although physical testing is also recommended to validate performance.

4.3. The connections (Beam-Uprights, Uprights- Base Plate)

In the design of steel structures, connections are critical components that significantly influence the overall structural behaviour, stability, and integrity. Accurate assessment of these factors necessitates a rigorous approach to the modelling and evaluation of connections. Each design standard implements its own methodology, which is often influenced by regional practices, historical experience, and prevailing assumptions regarding failure modes. The following section provides an overview of the various design approaches to connections as adopted by prominent international standards. Below there is an overview of the different design approaches to connections as adopted by key international standards.

4.3.1. Beam-Upright connections

The approach to this topic is consistent between Standard EN 15512:2023 [6] and Standard AS4084 [15]. Starting from experimental results and curves, some corrections may be necessarily made in AS 4084 [15] to obtain behavioural curve that are also statistically correct. With that information it is possible to have a full display of the connection behaviour and eventually can be easily implemented in specific software (such as SAP2000). As said, the statistical treatment of data is the same, for both European and Australian Standards.

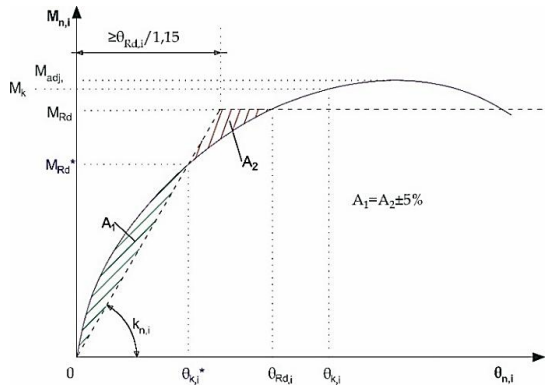


Fig. 4 Bilinear procedure as seen both in EN 15512:2022 [6] and AS 4084 [15]. The procedure suggests finding finding M_{Rd} as the difference between A1 and A2 is the smallest possible (around 5% max)

As seen in **Fig. 4**, M_{Rd} should be calculated allowing the least difference between the area A_1 (enhanced in green) and A_2 (enhanced in red) and simultaneously, must be verified that:

$$k_{n,i} \leq 1{,}15 \frac{M_{Rd}}{\theta_{Rd,i}} \tag{1}$$

where $k_{n,i}$ is the stiffness of the tested connection and $\theta_{Rd,i}$ is the rotation corresponding to the intersection between the test curve and the horizontal straight line corresponding to M_{Rd}. Since there is a minimum of 3 test (as reported in the code), the Final $k_{n,i}$ value is an average value. This procedure is valid for all the connection typologies. In addition, there are some corrections that should be made according to the Australian standard, in terms of rotation.

It should also be noted that the reliability of test-derived properties depends not only on the experimental setup, but also on the statistical treatment adopted by each standard: EN 15512 [6] requires characteristic values based on confidence-level evaluation, AS 4084 [15] allows simplified procedures in some applications, whereas ANSI MH16.1 [18] relies on protocol-specific testing, so that stiffness and resistance values should be transferred to global models only when the test assumptions are mechanically consistent with the analysed rack configuration.

Turning to the American codes, ANSI MH16.1 [18] states that rotational capacity is the primary performance criterion for connections. This capacity, which is determined through testing, must not be less than the rotational demand, denoted as θ_D.

$$\theta_D = \frac{I_e(1+\alpha_s)\delta_{x,s}}{h_{total}} \leq \theta_{max} \quad (2)$$

where θ_D is the actual rotational demand, α_s is the first order amplification term (where 1 + α_s term estimates the effects of gravity loa amplification); $\delta_{x,s}$ is the maximum inelastic seismic displacement at the height of the top loaded storage level, h_{total} is the height to the top load storage level; lastly, θ_{max} is the rotation or rotational capacity sustained at maximum moment during cyclic testing of the beam-to- column connection over at least two cycles.

For sake of clarity, the formula to compute the first order amplification factor, on FEMA 460 disposition [19]:

$$\alpha_s = \frac{\sum_{i=1}^{NL} W_{pi} h_{pi} \left(\frac{k_c + k_{be}}{k_c k_{be}}\right)}{\left(N_c + N_b \left(\frac{K_b k_{ce}}{k_c k_{be}}\right)\left(\frac{k_c + k_{be}}{k_b + k_{ce}}\right)\right)} \leq \theta_{max} \quad (3)$$

to which refences are demanded to MH16-1[18] to facilitate the reading of this article. Since there are no provision like EN 15512:2022 [6] or AS 4084 [15] about the testing curves, it is rational saying that test curves should be treated in a canonical statistical manner.

A critical issue in the interpretation of beam-to-upright tests is that the rotational stiffness obtained from the experimental moment–rotation curve cannot be regarded as an intrinsic property of the connection alone. It is a structural parameter that depends on the complete test arrangement, including the boundary conditions imposed on the upright, the load introduction system, the moment-to-shear ratio at the connector, the deformation of the perforated upright wall, and the local engagement mechanism between connector tabs and upright holes. Consequently, different standardized test protocols may lead to different apparent stiffness values even when the same nominal connection is considered [63]-[72].

This aspect is particularly relevant when comparing European/Australian and North American approaches. The European and Australian procedures generally idealize the experimentally obtained moment–rotation response through a bilinear curve that is then used in global frame analysis. However, the measured response is influenced by the prescribed test configuration and by the way in which bending and shear are transferred to the connector [72]-[73]. North American procedures may adopt different boundary conditions and load application schemes, which can modify the relative contribution of connector rotation, upright wall deformation, bearing around perforations and local prying effects. Therefore, the resulting rotational stiffness is partly protocol-dependent.

From a mechanical point of view, this implies that connection stiffness values obtained according to one standard should not be transferred directly to models developed under another framework without checking the compatibility of the underlying test assumptions. The issue is not limited to statistical treatment of test data, but concerns the representativeness of the experimental boundary conditions themselves. Design assisted by testing remains essential for pallet rack connections, but the reliability of the derived stiffness and strength parameters depends on the degree to which the test setup reproduces the actual force transfer mechanism occurring in the rack frame.

For this reason, differences among standardized testing methodologies may affect the predicted global response of the rack, particularly in terms of sway stiffness, second-order amplification and instability resistance. Future harmonization should therefore address not only the reduction and statistical processing of test curves, but also the mechanical equivalence of the test configurations used to derive beam-to-upright connection properties [73].

4.3.2. Upright – base plate connections

The design of upright-base plate connections presents a considerable complexity. According to EN 15512:2022 [6], the preferred general assumption is to consider the floor as semi-rigid, consistent with the guidelines outlined in the FEM regulations—specifically referenced in FEM 10.2.14 Part 2 [12]. This assumption, however, must be verified; if it does not hold, the interaction effects arising from differing deformation patterns must be explicitly accounted for. Additionally, long-term effects associated with flooring materials may be incorporated into the analysis, depending on the specific design objectives. Section 12 (“Design of floor base”) of the standard specifies that the first step is to calculate the effective area response of the base plate under compression, as shown in **Fig. 5** . Here, A_{bp} denotes the effective area, which must not exceed the edge of the base plate, while c is the additional bearing width, calculated according to:

$$c = t_b \sqrt{\frac{f_{yd}}{3 f_{jd}}} \quad (4)$$

where t_b is the thickness of the base plate, f_{yd} is the design strength of the base plate with $f_{yd} = f_{yk}/\gamma_{MO}$, f_{jd} is the design strength of the floor material for contact pressure.

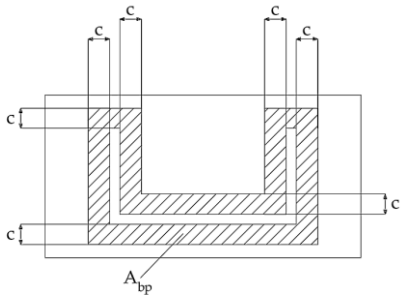


Fig. 5 A typical base plate, with the "effective area response" according to EN 15512:2022 [6]

The design upright compression force, $F_{c,Ed}$ must satisfy:

$$F_{c,Ed} \leq f_{jd} A_{bp} \quad (5)$$

where f_{jd} is the design bearing stress and A_{bp} is the effective bearing area illustrated in **Fig. 5**

Tensile forces should be evaluated subsequently, taking into account several critical factors, including the type of connection between the upright and the base plate (whether welded or bolted), the position of the upright's center of gravity, the location of the anchors, the bending resistance of the base plate, and the overall strength of the connection components, such as welds, bolts, and anchors. The standard does not prescribe a specific analytical relationship for this assessment; instead, the responsibility is placed on the designer or structural engineer to perform a case-by-case evaluation, tailored to the specific configuration and loading scenario.

Australian codes shows slightly different prescriptions: according to AS4084 [15], there still is necessity to find an “effective” area, as per EN 15512:2022 [6], as shown in **Fig. 6** but it is mandatory to consider also the distances between the upright holder and the holes for anchors as reported in the following relation:

$$e = t_b \sqrt{\frac{f_y}{2 f_{cb}}} \quad (6)$$

where e is the effective bearing width, as a product between t_b which is the thickness of the base plate, and the square root of the ratio between the yield stress of the base plate f_y, and two times the design of the bearing strength of the concrete slab f_{cb}.

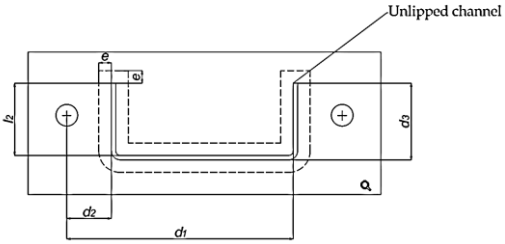


Fig. 6 Base plate effective area, according to AS 4084 [15]

where l_2 is the overall depth of upright, e is the, d_2 is the distance from the anchor bolt in tension to the nearest face of the upright; d_1 is the distance from the anchor bolt in tension to the upright flange in compression, and d_3 is the flange width of upright. The design requirement is to satisfy an equilibrium between forces, similarly to the EN 15512:2022 [6] standard, but changes if there is also bending in addition to compression:

$$A_{eff} f_{cb} \geq N^* + F_t^* \quad (7)$$

where A_{eff} is the effective area of the base plate, f_{cb} is the design bearing strength of the concrete slab, e is the effective bearing width, F_t^* is the design tension in the anchor bolt of the base plate, N^* is the design value of the vertical action on the frame, or the axial design action.

If more complexity is added to the profiles, distance (d_1) measured from the centre of the effective area of the base plate adjacent to the compression flange must be considered or alternatively choose appropriate tests to determine the minimum thickness of the base plate. Also, AS 4084 [15] adds explicit specifications to the plates' anchorage, while EN 15512:2022 [6] refers to Eurocodes [2]-[5] and similar codes. The ANSI MH16.1 [18] at the *§ C11, "column base design"* outlines the requirements for designing base plates in accordance with American standards. The standard identifies three primary loading conditions for which the thickness of the base plate must be designed:
(a) downward vertical load,
(b) uplift or tensile force, and
(c) combined axial load and bending moment.

The relationship which needs to be fulfilled is , which is centred on the rotational demand. In the down-aisle frame analysis the base plate is modelled as a rotational spring with stiffness K_b. The base moments, M_b, are determined from the structural analysis of the down-aisle model. The rotational demand of the base (θ_b) is:

$$\theta_b = \frac{M_b}{K_b} \quad (8)$$

This approach allows for a semi-rigid modelling of the column-base connection, reflecting the actual moment-rotation behaviour and ensuring that the base plate can accommodate the imposed rotational deformations under service and ultimate limit states. If bending moments are assumed in the design, the base plate should also satisfy a rotational demand which consider the peculiar strain conditions:

$$\theta_b = \frac{C_d(1+\alpha_s)M_b}{K_b} \quad (9)$$

where C_d is the deflection amplification factor, while α_s is the gravity load amplification term using the plastic modulus of the section, M_b is the base moment from analysis, while K_b is the base rotational stiffness used in the structural analysis that determined M_b.

American Standards provides also more than two anchors, and the casing is usually made with a hollow section (**Fig. 7**).

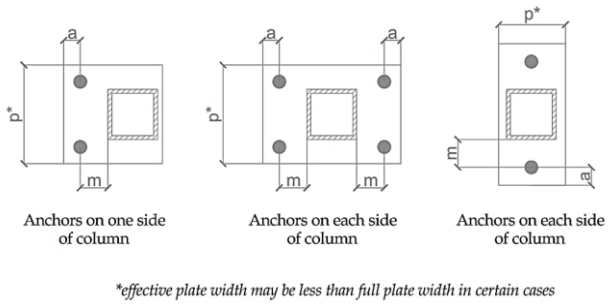


Fig. 7 Base-to-plate column attachment, according to ANSI MH16.1-2023 [18]

The standard also refers to AISI 360-22 [20] to address a wider range of structural scenarios. In *§ M – "Fabrication and Erection", particularly § M.8*, the standard outlines specific requirements for column base design, including tolerances, positioning, and installation conditions. These guidelines ensure precision in fabrication and are characteristic of American standards, which tend to provide detailed examples and require strict interpretation. For bolted connections, the standard directs users to *§ J – "Design of Connections"* of AISI 360-22 [20]. This consolidates the relevant provisions for all types of bolted and welded connections, ensuring consistency across different structural applications. Of particular importance is the design of anchors, which are essential for ensuring structural stability and transferring loads effectively to the foundation.

4.4. The imperfections

In accordance with the Eurocodes, imperfections are expressed as angular deviations (for both local and global imperfections), from which equivalent forces are derived. These equivalent forces are then applied directly to the model nodes. Local imperfections are mainly associated with the behaviour of individual bracing elements and, in most cases, can be regarded as negligible for the overall analysis. Global imperfections, by contrast, are more significant and relate to the overall geometry of the frame — such as the layout of the spine, the size and pattern of the hole arrays, bolt dimensions, and the general configuration of brace-to-upright connections. The calculation is rather complex and requires consulting both Annex A and Annex G of EN 15512 [6]. While local imperfections can be determined using the specific procedure provided, the European code gives little explicit guidance for the general calculation of global imperfections. Nevertheless, they can be estimated by multiplying the imperfection angle by the distributed load pattern (assuming the goods are evenly distributed on the beams, with minimal error according to FEM [11]-[13] and EN 15512:2022 [6]) and by the bay length in the two principal directions. This implemented solution is broadly consistent with the general instructions of Eurocode 3 [2]-[5].

The Australian Standard explicitly requires that both local and global imperfections are considered in the structural analysis and design process—aligning closely with the provisions of EN 15512:2022 [6]. The Australian framework accounts for multiple contributing factors, including overall structural geometry, the role of bracing systems in both down-aisle and cross-aisle directions, the pattern of perforations (hole arrays) in uprights, potential connection looseness, and general frame configurations.

American standards address these aspects with varying degrees of specificity. Global imperfections are generally considered under ANSI/AISI S100-20 [22], primarily through alignment tolerances and geometric assumptions. However, the treatment of local imperfections is addressed in a less explicit manner. The ANSI MH16.1-23 standard [18] does not provide explicit calculation methods but addresses imperfection effects indirectly through methods such as second-order analysis (with a proper magnification factor) and the use of Notional Loads. Additional guidance can be found in ANSI/AISC 360-22 [20], which provides a broader framework for incorporating geometric and material nonlinearity in structural systems, although it is not tailored specifically for racking structures. According to *§ C, Section 2*, of ANSI/AISC 360-22 [20] consideration of initial out-of-straightness (member imperfections) is not required in structural analysis when applying the provisions of this section, as these imperfections are already accounted for in the compression member design provisions of § E—provided they remain within the limits specified in the Code of Standard Practice. However, Appendix 1, Section 1.2, extends the Direct Analysis Method by requiring explicit modelling of member imperfections (initial out-of-straightness) within the structural analysis. Furthermore, Advanced Analysis (Appendix 1) specifies that, in all cases, the analysis must directly incorporate the effects of both system imperfections (displaced member intersections from nominal locations) and member imperfections (out-of-straightness or offsets along member lengths). The magnitude of initial displacements must reflect the maximum considered in design, and their pattern should be configured to produce the greatest destabilizing effect. Since geometric imperfections and the choice of analysis method are inherently linked, the ANSI/AISC 360-22 [20] provides a clear summary of the applicable provisions for each method, outlining how different design approaches, such as the Direct Analysis Method (DM) and the Effective Length Method (ELM), incorporate stability requirements through assumptions about member imperfections, stiffness reduction, and second-order effects. It serves as a practical reference for ensuring compliance with the stability provisions set forth in Section C of the Specification (*in the commentary, specifically Chpt C1, General Stability requirements*).

In **Table 2** some differences in terms of the out-of-plumb ratio are reported.

Table 2
Differences of the minimum out-of-plumb between the European, Australian and American Standards

Standard	Ratio	Deviation (10m height)	Notes
EN 15512:2022	1/200	50mm	Common in Europe
AS 4084	1/400	25mm	Stricter tolerance
ANSI MH16.1	1/240	~41.67 mm	Measured under load

The Australian Standard AS 4084 [15] imposes the strictest tolerances, particularly in terms of installation and alignment. While EN 15512:2022 [6]

(Europe) and ANSI MH16.1-23 [18] (USA) share similar principles, they differ slightly in specific tolerance values and interpretation. All three codes include defined limits for out-of-plumb conditions, which are critical for ensuring structural stability—especially under quasi-rigid floor assumptions or where precise vertical alignment is necessary to prevent excessive secondary stresses or instability. For example, shows the out-of-plumb for EN 15512:2022 [6] (and partially, AS 4084 [15]).

Table 3
Out-of plumb limit and limiting rotation in serviceability according to EN15512 [6] (but also cited in AS 4084 [15])

Specified installation Out-of-plumb	Limiting rotation Φ_{Floor} in serviceability limit state
1/350	1/700
1/500	1/1000
1/750	1/1500
1/1000	1/2000

NOTE: 1/350 out of plumb is related to class 400, 1/500 and 1/750 for class 300 and 1/1000 for class 100 and class 200, for additional information see EN 15620
* *Those specifications are also cited in the AS 4084, for unloaded racks. For all the standards it must be intended for FULLY UNLOADED RACKS.*

In general, the connection between the Upright and the Floor is to be considered pinned.

It needs to be noted that if the rotation of the floor slab (Φ_{Floor}) is less than the limit given in Table 5 then the floor slab may be considered to provide a rigid foundation and, for the purposes of rack design, no consideration of floor slab deformation is required. Conversely, if the floor slab deformation exceeds the limit only the deformation in excess of the limit needs to be considered.

For the sake of brevity, **Table 4** presents a summarized calculation framework, specifically addressing the imperfection angle in the down-aisle direction for the three approaches.

Table 4
Differences about the Down-Aisle imperfection angle between the three standards (European, Australian and American)

Standard	EN 15512:2022	AS 4084	ANSI MH16.1
Imperfection's angle	$\varphi_i = \varphi_s + \varphi_l$	$\varphi_i = \varphi_{su}\alpha_h\alpha_{nu} + \varphi_l$	$\varphi_i = 1/240$

* *these angles should be intended as a general assumption. For Specific condition (such as the loading condition) should be adapted.*

Both EN 15512:2022 [6] and AS 4084 [15] present similar computational algorithms, acknowledging that instability occurs in both directions—down-aisle and cross-aisle. Regarding the specific case of the down-aisle imperfection angle, EN 15512:2022 [6] defines this angle as the result of two components: one related to geometric factors (such as looseness, general design of the spine, etc.), and the other addressing global imperfections, typically taken as 1/350. AS 4084 [15] proposes a very similar formulation (with the presence of α_h and α_{nu} as correction factor, specifically depending on the geometry of the structure) but additionally incorporates three tolerance grades (φ_u), which are generally expressed as out-of-plumb ratios. While EN 15512:2022 [6] and AS 4084 [15] share comparable methodologies and operational calculations, the American standard, in contrast, adopts a fixed value for this parameter.

In the European [6] and Australian [15] frameworks, the imperfection angle is evaluated through calculation procedures that depend on the rack configuration, loading condition, tolerance class and structural arrangement. This makes the imperfection model more directly related to the actual geometry and expected sway sensitivity of the system. In this respect, the design assisted by testing philosophy and the use of configuration-dependent parameters allow the imperfection model to be adapted to different practical cases.

The American framework adopts a more direct approach, based on a prescribed out-of-plumb ratio, with additional qualifications and modifications provided in the commentary to ANSI MH16.1 [18]. This fixed-ratio formulation has the advantage of simplicity and repeatability, but it is less explicitly dependent on the specific slenderness, bracing arrangement and connection flexibility of the rack. Therefore, for highly slender or sway-sensitive systems, the adequacy of the prescribed imperfection value should be checked through second-order analysis, since differences in the assumed initial imperfection may directly affect the PΔ contribution to the bending demand.

Consequently, the comparison between the standards should not be interpreted only as a difference in numerical imperfection values. It reflects two different modelling philosophies: the European and Australian approaches use configuration-dependent imperfection models, whereas the American approach relies on a prescribed reference imperfection combined with subsequent stability verification. Both approaches can be appropriate if applied consistently, but their sensitivity to rack height, vertical load level, bracing stiffness and connection deformability should be explicitly considered in design.

4.5. The loads

Loads and their combination are explicated in *§ 6.4 Combination of actions*, EN 15512:2022 [6]. About the ultimate limit state, and are almost similar to the Eurocodes, and perfectly identical for AS 4084 [15], in *§ 2.7.2 Combination of actions for ultimate limit states* (this is not unusual, since the code AS4084 [15] follows EN 15512:2022 [6]):

1. The most unfavourable actions:

$$\sum \gamma_G G_k + \gamma_q Q_{k,1} \tag{10}$$

2. All unfavourable variable actions which can occur simultaneously:

$$\sum \gamma_G G_k + 0.9 \sum_{i\geq 1} \gamma_Q Q_{k,i} \tag{11}$$

3. Design accidental loads:

$$\sum \gamma_G G_k + 0.9 \sum_{i\geq 1} \gamma_A Q_{k,1} + \gamma_A A_k \tag{12}$$

where G_k is the characteristic value of permanent action (dead load), $Q_{k,1}$ is the characteristic value of one of the variable loads, $Q_{k,i}$ is the characteristic value of a typical variable load, A_k is the characteristic value of an accidental load; γ_G, γ_q, γ_A are all partial factors, respectively for permanent loads, variable loads and accidental loads.

ANSI MH16.1-23 [18] presents two approaches (*§. 7, "Loading"*), according to both Load and Resistance Factor Design (LRFD) method and Allowable Stress Design (ASD) Method for the limit load:

- **The LRFD (Load and Resistance Factor design) method**

$$1.4\,D + 1.2P \quad (dead\ Load) \tag{13}$$

$$1.2\,D + 1.4P + 1.6L + 0.5(L_r\ ,S\ or\ R) \quad (gravity, product\ or\ live\ load) \tag{14}$$

- **The ASD (Allowable Stress Design) method**

$$D + P \quad (dead\ Load) \tag{15}$$

$$D + P + L \quad (gravity, product\ or\ live\ load) \tag{16}$$

Where D is the dead load, P is the maximum load from pallet stored on the racks, L is the Live load or any transportable load not considered as product load, Lr is the roof live road, S is the snow load, R is the Load from rain including ponding. The main differences between the codes (EN 15512:2022 [6] , AS4084 [15], Eurocodes [2]-[5] and ANSI MH16.1-22 [18] American standard) about the partial factors (**Table 5**) and material factors (**Table 6**).

Table 5
Main differences between EN 15512:2022 [6] , AS4084 [15], Eurocodes [2]-[5] and ANSI MH16.1-23 [18] about partial factors of Actions

	EN 15512:2022	AS 4084	Eurocode 3	American Standard *(LRFD Method)*
Actions	Ultimate limit state	Ultimate limit state	Ultimate limit state	Ultimate limit state
	RC2	RC2	RC2	
Permanent loads γ_G				
With unfavourable	1,3	1,3	1,5	1.2
effect	1,0	1,0	1.35	1

With favourable effect Imposed slab deformation	1,3	1,3	/	1.4
unfavourable effect Imposed slab deformation favourable effect	0,0	0,0	/	
Variable loads γ_Q				
Unit loads	1,4	1,4	1.5	1.6
Unit loads in a crane operated system	1,4 or 1,3	1,4 or 1,3	/	1.4
Placement loads	1,4	1,4	/	1.4
Other variable loads	1,5	1,5	/	
Accidental loads γ_A	1,0	1,0	1,0	0,5

Resistances in AS4084 [15] are not explicit reduced, but there are many reductions on the member capacity according to AS4600 [17], depending on the restraints. All information about member capacity (torsional restraint, etc.) are also deducted from AS 4100 [16], while more or less explicit instructions are present in the EN 15512:2022 [6]. In **Table 5** and **Table 6** some comparisons between the codes are shown, even if the values of American ones may not quite overlap perfectly.

Table 6
Main differences between EN 15512:2022 [6], AS4084 [15], Eurocodes[2]-[5] and AISI MH16.1-22 [18] about partial factors of resistance

	EN 15512:2022	AS 4084	Eurocode 3	American Standard (LRFD Method)
Resistance	Ultimate limit state	Ultimate limit state (∗)	Ultimate limit state	Ultimate limit state (∗∗)
	RC2	RC2		
Resistance of cross-sections whatever the class is γ_{M0}	1,1	$\frac{1}{0.6}/\frac{1}{0.9}$	1	$\frac{1}{0.75}/\frac{1}{0.9}$
Resistance of members to instability assessed by member checks γ_{M1}	1,1	$\frac{1}{0.6}/\frac{1}{0.9}$	1	$\frac{1}{0.75}/\frac{1}{0.9}$
Resistance of connections γ_{M2}	1,25	$\frac{1}{0.5}/\frac{1}{0.9}$	1,25	$\frac{1}{0.75}/\frac{1}{0.9}$
Resistance of connections subject to testing and quality control (es. beam end connectors) γ_{M2}	1,1	$\frac{1}{0.6}/\frac{1}{0.9}$	1	$\frac{1}{0.75}/\frac{1}{0.9}$

(∗) According to the Australian Standard, the partial factor of resistance is normally tailored to specific scenarios. For sake of clarity, here are reported a range value of those factors, given that in some cases those values may differ.

(∗∗) Also, for the American Standard, the partial factor of resistance is normally tailored to specific scenarios. For sake of clarity, here are reported a range value of those factors, given that in some cases those values may differ.

Table 6 summarizes the main resistance safety parameters adopted in the considered standards. It should be noted that the comparison is not a direct numerical equivalence, since the European framework uses partial resistance factors, the Australian framework adopts capacity reduction factors depending on the relevant limit state, and the American framework may be applied through either LRFD or ASD formats. For consistency, the American values reported in the table refer only to the LRFD resistance factors, φ. Typical LRFD values are approximately φ = 0.90 for cross-section resistance, φ = 0.85–0.90 for compression member resistance, and φ = 0.75 for connections, depending on the specific provision and limit state considered. ASD safety factors, Ω, are not reported in this table in order to avoid mixing different safety formats.

It should be emphasized that the European partial resistance factor γ_M and the American LRFD resistance factor φ are not strictly equivalent parameters. They belong to different reliability formats and are calibrated together with different load combinations, statistical assumptions, resistance models and target reliability levels. Therefore, the present comparison does not assume a direct equivalence between γ_M and 1/φ. The reciprocal value 1/φ may only be used as an indicative way to express the LRFD resistance reduction in a form that is easier to compare with resistance-side safety factors. ASD safety factors Ω are conceptually different from LRFD resistance factors and are therefore discussed separately.

5. Stability assessment and buckling design approaches

Instability phenomena govern the structural safety of pallet racking systems to a greater extent than in conventional steel buildings. The combination of slender perforated uprights, semi-rigid joints, limited redundancy and the frequent attainment of full design load makes second-order effects and buckling verification the central task of structural assessment. Uprights are classified according to the Eurocode section classes (**Fig. 8**), with slender Class 4 sections being particularly prone to buckling and therefore driving the design approach. The inherent uncertainty in pallet rack design is amplified by the fact that the full design load is almost always achieved during the pallet service life. Unlike traditional building structures, secondary elements such as cladding, partitions, or non-structural walls provide no significant structural benefit in pallet racks. Additionally, the upright columns are typically perforated with a regular hole pattern, which introduces geometric discontinuities and stress concentrations. These features are not explicitly considered in the Eurocode design, particularly when using generalized expressions for effective cross-sectional properties. Most upright cold-formed sections used in pallet racks fall into Class 4 (per Eurocode classification), meaning they are fully slender and prone to local buckling. However, Eurocode provisions were primarily calibrated for building typologies and may therefore require complementary procedures when applied to highly perforated rack uprights. The current approach involves classifying individual parts of the cross-section and assigning the governing class to the whole section—but this may oversimplify the real behaviour of highly perforated, cold-formed uprights. As a result, the standard Eurocode framework can be inadequate for capturing the true instability phenomena in pallet racking systems, referring to FEM-specific methods or specialized testing increasingly necessary.

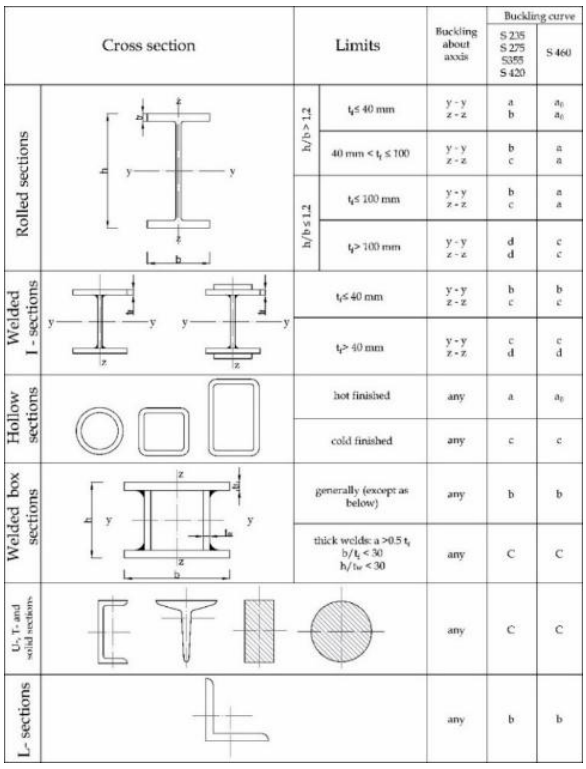


Fig. 8 Selections of buckling curves for cross section, Eurocode 3[2]

Generally, in EN 1993-1-3 [2] if the buckling factor is:

$$\alpha_{CR} = \frac{N_{Cr}}{N_{Ed}} \leq 3 \tag{17}$$

a second order analysis is required. EN 15512:2022 [6]. handles instability differently from general Eurocodes. It uses a strong design assisted by testing approach, meaning actual tests are often required to validate models in perforated cold-formed sections. The standard includes its own buckling curves (see **Fig. 9**), tailored specifically for pallet rack structures, unlike the generic curves in EN 1993-1-1 [2]. This allows for more accurate consideration of local, global, and torsional instability in racking systems.

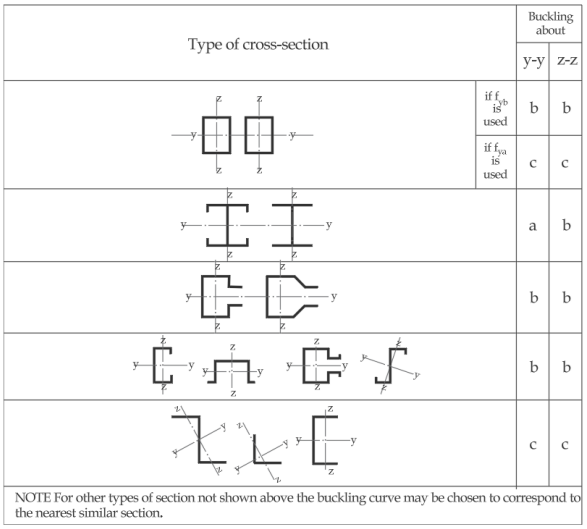


Fig. 9 Buckling curves, up to EN 15512:2022 [6]

The distinction between Eurocodes and EN 15512:2022 [6] is evident when addressing member instability, particularly for Class 4 cross-sections. In the Eurocode framework, such sections typically require the adoption of the "c-type" buckling curve, reflecting their susceptibility to local and global instabilities. However, EN 15512:2022 [6] prescribes the use of the "b-type" instability curve under similar conditions. In addition, said code introduces a more detailed classification of instability modes, explicitly dividing them according to the failure mechanism—including local, global, and distortional buckling—allowing for a more nuanced approach to design. Despite these differences, there are specific scenarios where the approaches of the Eurocodes and EN 15512:2022 [6] may converge, leading to identical or near-identical design outcomes.

The Australian Standard AS 4084 [15] adopts a distinct approach to the verification of member instability, which depends on multiple factors, including the presence and type of restraints as well as the effective length factor, the latter of which may be determined through experimental testing. Unlike EN 15512:2022 [6], AS 4084 [15] does not explicitly classify members into Section Classes (e.g., Class 1 or 4), even though there's a more general classification in AS4100 [16] . However, it provides detailed analytical procedures and simplified calculation methods to assess instability in both the down-aisle direction (Appendix A) and the cross-aisle direction (Appendix C). These procedures, though different in formulation, often yield results comparable to those produced under EN 15512:2022 [6], and in some respects align more closely with the methodology of American standards, such as those found in AISI and AISC provisions. The treatment of second-order effects under AS 4084 [15] is method-dependent. Certain design methods account for geometric nonlinearity (e.g., P–Δ effects), while others may permit its exclusion under specific conditions. The standard provides guidance for determining whether second-order effects must be considered, based on the slenderness of the member and the magnitude of expected displacements. Where necessary, these effects can be incorporated using either approximate methods (e.g., effective length factors) or through more advanced numerical analysis techniques.

The American standard differs significantly from the Eurocode framework in its approach to cross-section classification. Unlike the Eurocodes, ANSI/AISC 360-22 [20] does not adopt such an explicit classification system. Instead, it introduces a functional classification based on loading conditions, which inherently reflects the design philosophy underlying American structural codes. According to ANSI/AISC 360-22 [20], members are categorized as follows:

- Members subject to axial compression, classified as either slender or non-slender.
- Members subject to flexural strength, classified as compact, non-compact, or slender.

This classification determines the appropriate design methodology, particularly in relation to local buckling behaviour. It indicates whether local buckling is expected to occur before or after yielding, which in turn influences whether plastic, elastic, or reduced-strength design models are applicable. Like the Eurocode provisions, the width-to-thickness (b/t) ratio remains a fundamental parameter in guiding classification and design decisions. However, while Eurocodes assign a fixed class based on b/t thresholds and material properties, AISC allows more flexibility in selecting the appropriate limit states and design equations, depending on the expected failure mode and load combination.

As a comparison between Eurocodes and American Standards: Compact sections can be assumed like the I class and II class sections in Eurocodes, while non-compact can be assumed similar to III class section in the code; Slender sections can be more similar to IV classes. Unfortunately, the overlapping is not always perfect, and in some cases may diverge.

Table 7
Main differences between EN 15512:2022 [6] , AS4084 [15], Eurocodes [2]-[5] and AISI MH16.1-22 [18] about partial factors of resistance

Section Classifications (∗)		
Eurocodes	AS/NZS standard	AISI standard
Class 1	Compact	Compact
Class 2	Non-compact	Non-compact
Class 3	Slender	Slender
Class 4	-	Non-slender

(∗) Chinese standard and Japanese standards also have a similar classification with Eurocodes, since the classification is based also on the b/t ratio and through the Effective Width Method.

A common approach between Eurocodes, AISI standards, and AS4084 [15] is classifying sections according to their width-to-thickness ratios. While the specific terminology and threshold values vary among them, this classification plays a key role in determining the applicable design rules. In practice, pallet rack uprights almost invariably fall within the slender (Class 4) domain, making instability-driven design unavoidable. The comparison above demonstrates that, although instability verification is universally recognized as crucial, the modelling philosophy, safety formats and calibration strategies vary significantly among standards. These differences become even more evident when flexural–torsional phenomena are examined in detail.

5.1. Focus on Flexural-torsional instability

Across all major design standards, the determination of the effective buckling length is a fundamental requirement for verifying member stability. Modern codes—including EN 15512:2022 [6] , AS 4084 [15], and ANSI/AISC 360-22 [20] / ANSI/AISI S100-20 [22]—explicitly permit the use of the Finite Strip Method (FSM) for this purpose, aligning with contemporary developments in structural engineering research and analytical tools. Also, all the three codes have in common the chance to design according to the "amplify sway method", even in the stability analysis.

The approach adopted in EN 15512:2022 [6] places particular emphasis on the verification of flexural-torsional buckling in slender members, especially in the context of progressive collapse mechanisms [90], [107]. While many design checks, such as those for axial compression or tension, closely mirror the procedures outlined in the Eurocodes (e.g., EN 1993-1-3 [3]), the flexural-torsional resistance verification introduces more specialized requirements. Specifically, *Annex E, Section E.4.3*, of EN 15512:2022 [6] outlines a methodology that begins with a preliminary characterization of the member's susceptibility to instability. The design buckling resistance, denoted as $N_{b,\mathrm{Rd}}$, is determined as the minimum value between the resistances against:

- *Pure torsional buckling (Eq.* (18)*)*
- *Flexural-torsional buckling (Eq.* (19)*)*

This dual-check framework ensures a conservative and robust assessment of member stability under combined loading and geometric imperfections, particularly relevant in the case of perforated, cold-formed steel uprights commonly used in racking systems.

$$N_{cr,T} = \frac{1}{{i_0}^2}\left(GI_{T,eq} + \frac{\pi^2 EI_{w,eq}}{L_{eT}^2}\right) \tag{18}$$

$$N_{cr,TF} = \frac{N_{cr,y}}{2\beta}\left[1 + \frac{N_{cr,T}}{N_{cr,y}} - \sqrt{\left(1 - \frac{N_{cr,T}}{N_{cr,y}}\right)^2 + 4\left(\frac{y_0}{i_0}\right)^2 \frac{N_{cr,T}}{N_{cr,y}}}\right] \quad (19)$$

Where $N_{cr,T}$ is the critical force for torsional buckling, $N_{cr,TF}$ is the critical force for torsional-flexural buckling; $N_{cr,y}$ is the elastic critical load of the upright based on buckling lengths, i_0 is a polar radius of gyration, calculated in reference to the position of the shear centre, y_0 is said distance, β is the amplification factor for second-order effects. Lastly, $I_{T,eq}$ and $I_{w,eq}$ are, respectively, the equivalent St. Venant torsion constant and equivalent warping constant, both taking account of the effects of perforation. The lesser between Eqs. (18) and (19)is used for the preliminary verification displayed in the Annex E, §E.1 Cross sectional verification (20)

$$N_{Ed} \leq N_{c,Rd} \quad (20)$$

where N_{Ed} is the design load.

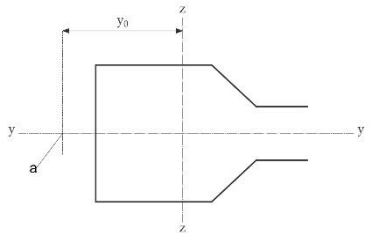


Fig. 10 Reference for the main characteristic to compute the flexotorsional resistance, EN15512[6]

Basing on **Fig. 10**, for members in combined compression and bending should be satisfied both the Eqs. (21)- (22) (if the cross-section is symmetrical, which it is in the majority of cases):

$$\left(\omega_{x,y}\frac{N_{Ed}}{\chi_y N_{Rd}}\right)^{\alpha_y} + \left(\omega_{x,LT}\frac{M_{y,Ed}+\Delta M_{y,Ed}}{\chi_{LT} M_{y,Rd}}\right)^{\beta_y} + \left(\frac{M_{z,Ed}+\Delta M_{z,Ed}}{M_{z,Rd}}\right)^{\delta_y} \leq 1{,}0 \quad (21)$$

$$\left(\omega_{x,z}\frac{N_{Ed}}{\chi_z N_{Rd}}\right)^{\alpha_z} + \left(\omega_{x,LT}\frac{M_{y,Ed}+\Delta M_{y,Ed}}{\chi_{LT} M_{y,Rd}}\right)^{\beta_z} + \left(\frac{M_{z,Ed}\Delta M_{z,Ed}}{M_{z,Rd}}\right)^{\delta_z} \leq 1{,}0 \quad (22)$$

where $\omega_{x,y}$, $\omega_{x,LT}$, $\omega_{x,z}$ are coefficient obtained by **Table 9**, $\alpha_y, \beta_y, \delta_y, \alpha_z, \beta_z, \delta_z$ are exponents calculated as per **Table 8**, χ_y, χ_z, χ_{LT} are, respectively, the reduction factors for flexural buckling (or torsional buckling where necessary) in the two main direction and the reduction factor linked with the lateral-torsional buckling; N_{Ed} is the design value for the compression force; N_{Rd} is the axial design resistance of the cross-section, considering the Area for not fully effective cross-section. $M_{y,Ed}$ and $M_{z,Ed}$ are the design values for bending moments in its direction, or conservatively the maximum design values for both bending moments, $\Delta M_{y,Ed}$ and $\Delta M_{z,Ed}$ are additional bending moments in the two directions due to shift of the centroidal axes of the effective cross section in certain condition (usually negligible); $M_{y,Rd}$ and $M_{z,Rd}$ are, of course, the bending moment resistance of the cross section about the two axes.

Table 8
Exponents to be used in the interaction formulae, EN 15512:2022 [6]

Exponents	General provisions (NDP)	Conservative
$\alpha_y{}^a$		
$\beta_y{}^a$	$0{,}85 \leq {}^{\chi_y}/_{\omega_{x,y}} \leq 1$	0,85
$\delta_y{}^a$		
$\alpha_z{}^a$		
$\beta_z{}^a$	$0{,}85 \leq {}^{\chi_z}/_{\omega_{x,z}} \leq 1$	0,85
$\delta_z{}^a$		

[a] in the case of torsional-flexural buckling, the relevant reduction factor for flexural buckling χ_y or χ_z should be replaced with χ_{TF}

Table 9
Interpolation factors $\omega_{x,y}$ and $\omega_{x,LT}$, EN 15512:2022 [6]

Factor	for a specific cross-sections location along the member	Conservative for all cross-sections
$\omega^a_{x,y}$	$\chi_y + (1-\chi_y)\sin\left(\frac{\pi x_s}{l_{cr,y}}\right)$	1,0
$\omega^a_{x,z}$	$\chi_z + (1-\chi_z)\sin\left(\frac{\pi x_s}{l_{cr,z}}\right)$	1,0
$\omega^a_{x,LT}$	$\chi_{LT} + (1-\chi_{LT})\sin\left(\frac{\pi x_s}{l_{cr,LT}}\right)$	1,0

Where:
$l_{cr,y}, l_{cr,z}, l_{cr,LT}$ are buckling lengths for the relevant buckling mode.
x_s (= x_A, or x_B) is the distance from the studied cross-section to a simple support or point of contraflexure of the buckling curve for elastic buckling for relevant mode. For end moments only ($M_{Ed,1} \geq M_{Ed,2}$), the distance x_s to the design section may be obtained from:

$$\cos\left(\frac{x_s \pi}{l_{cr}}\right) = \frac{(M_{Ed,1} - M_{Ed,2})}{M_{Rd}} \times \frac{N_{Rd}}{N_{Ed}} \times \frac{1}{\pi\left(\frac{1}{\chi} - 1\right)} \; ma \; x_s \geq 0$$

[a] In the case of torsional.flexural buckling, the relevant reduction factor for flexural χ_y or χ_z should be replaced with χ_{LT}

Eqs. (21) and (22) are conceptually related to the Eurocode 3 [2]-[5] beam-column interaction checks, but they are adapted in EN 15512 [6] to account for the specific behaviour of pallet rack uprights. In particular, rack-specific coefficients and instability reduction factors are introduced to reflect the effects of thin-walled perforated open sections, including local/distortional buckling, flexural–torsional instability, possible centroidal-axis shifts, and reduced torsional and warping stiffness. Thus, these equations should not be considered a direct reproduction of the Eurocode formulation, but a rack-specific adaptation of the same general interaction concept.

The preliminary characterization reported in Eqs. (14) and (15) should help identify in advance which failure mode dominates—this is essential for correctly selecting the exponents or interaction factors that account for flexural-torsional buckling, particularly in uprights near the base of pallet racks, where such failures are most common.

Assuming a flexural-torsional failure dominion is a common approach across multiple standards.

However, flexural–torsional buckling should not be assumed as universally governing. The assumption may break down for short or torsionally restrained members, nearly concentric loading, or sections in which local or distortional buckling occurs at lower critical loads. The governing instability mode must therefore be selected according to geometry, slenderness, restraint conditions and load eccentricity.

For instance, the Australian Standard AS 4084 [15] implicitly adopts this assumption, though it is not directly stated. Further clarification can be found in AS/NZS 4600 [17], specifically in Clause 3.5.1 (*Combined axial compression and bending*). While this approach is somewhat simplified, it includes section-specific criteria, unlike the more generalized method in European codes. In the most general cases, the dominion is:

$$\frac{N^*}{\phi_c N_c} + \frac{C_{mx} M_X^*}{\phi_b M_{bx} \alpha_{nx}} + \frac{C_{my} M_y^*}{\phi_b M_{by} \alpha_{ny}} \leq 1.0 \quad (23)$$

$$\frac{N^*}{\phi_c N_s} + \frac{C_{mx} M_X^*}{\phi_b M_{bx}} + \frac{C_{my} M_y^*}{\phi_b M_{by}} \leq 1.0 \quad (24)$$

where N_c is the nominal member capacity of the member in compression determined according to the specific case, C_{mx} and C_{my} are coefficient for unequal end moment (whose value shall be tailored according to the specific case); M_x^* M_y^* are the design bending moment about the x- and y- axes of the effective section (obtained by a first order analysis); M_{bx} and M_{by} are the nominal member moment capacity about the x- and y- axes, respectively; ϕ_b is the capacity reduction factor for bending, while ϕ_c is the capacity reduction factor for member in compression (equal to 0.85); α_{nx} and α_{ny} are moment amplification factors.

In Appendix G of AS 4100 [16], guidance is provided for the evaluation of

braced members within buckling frames. While certain provisions also address beam elements, the general expression for determining the elastic flexural buckling load N_{om} (eq.(25)) of a braced compression member within a frame is given as follows:

$$N_{om} = \frac{\pi^2 EI}{(k_e l)^2} \tag{25}$$

where k_e is the member effective length factor obtained by indication of the code.

A further clarification, about Eurocodes is the fact that whereas there are dominion formulae in analogy with the one proposed by the EN 15512,
Turning to American Standards, there is no explicit reference to a flexural-torsional dominion. Because an upright is subject to both axial and flexural-torsional action, in the ANSI MH16.1-23 [18] code, §8.2.2 Concentrically-loaded perforated compression members, there are some indications about the calculus of the nominal axial strength resistance for cold- formed steel open sections; P_n shall be the lesser of the nominal flexural (Eqs. ((26)(27)) and local buckling strength (resistance (Eq.(28)) and the notional distortional buckling strength:

$$P_{ne} = 0.658^{\lambda_c^2} P_y \quad \left(if\ \lambda_c = \sqrt{\frac{P_y}{P_{cre}}} \leq 1.5\ \right) \tag{26}$$

$$P_{ne} = \left(\frac{0.877}{\lambda_c^2}\right) P_y \quad \left(if\ \lambda_c = \sqrt{\frac{P_y}{P_{cre}}} > 1.5\ \right) \tag{27}$$

$$P_{nlg} = P_{ne}\left[1 - (1-Q)\left(\frac{P_{ne}}{P_y}\right)^{\frac{Q}{1-Q}}\right] \tag{28}$$

In addition, Q shall be calculated by the formula provided in MH16.1:2023[18]:

$$Q = \frac{ultimate\ compressive\ strenght\ of\ stub\ column\ by\ test}{F_y A_{netg}} \leq 1 \tag{29}$$

where F_y is the actual yield stress of the material as determined from a coupon test using a coupon test from the same coil or cut from the same sample coil, and A_{netg} is the area calculated for the global buckling in accordange with the same norm. Said factor should not be greater than 1.

To calculate distortional (Eq. (30)) and global buckling (Eq. (31)) for open cold-formed steel sections (typically uprights):

$$P_{lnd} = P_{ne} \quad \left(if\ \lambda_d = \sqrt{\frac{P_{ne}}{P_{crd}}} \leq 0.561\ \right) \tag{30}$$

$$P_{lnd} = \left[1 - 0.25\left(\frac{P_{crd}}{P_{ne}}\right)^{0.6}\right]\left(\frac{P_{crd}}{P_{ne}}\right)^{0.6} P_{ne} \quad \left(if\ \lambda_d = \sqrt{\frac{P_{ne}}{P_{crd}}} > 0.561\ \right) \tag{31}$$

where λ_d is the slenderness factor of distortional buckling; P_{crd} is the lesser of the axial elastic global flexural or torsional flexural buckling strength calculated according to ANSI/AISI S100-20 [22] or ANSI/AISC 360-22[20]; P_{ne} is the lesser of the global buckling axial flexural or torsional-Flexural buckling strength; P_y is the axial Yeld load, $P_y = F_y A_{net,g}$; P_{crd} is the elastic critical distorsional buckling strength calculated in accordance with ANSI/AISI S100-20 [22] (properly calculating the thickness of the strips), P_{lnd} is the nominal distortional buckling strength and F_y is the yield stress, $A_{net,g}$ is the area calculated for buckling strength, Q is the local buckling factor. P_{cre} is the lesser of the axial elastic global flexural or torsional-flexural buckling strength calculated according to ANSI/AISI S100-20 [22] or ANSI/AISC 360-22 [20].

Also, in ANSI MH16.1-23 [18] § 8.2.3 Perforated members bending about the centroidal axis perpendicular to the axis of symmetry there are some indication about the nominal flexural strength in terms of momentum is M_n, and shall be the lesser of M_{nlg} for local and distorsional buckling and M_{nld} for distorsional buckling as calculated using the following Eqs. (32)- (34):

$$M_{nlg} = M_{ne}\left[1 - \frac{1}{2}(1-Q)\left(\frac{M_{ne}}{M_y}\right)^{\frac{Q}{1-Q}}\right] \tag{32}$$

$$M_{nld} = M_{ne} \quad \left(for\ \lambda_d = \left(\frac{M_{ne}}{M_{crd}}\right)^{0.5} \leq 0.673\right) \tag{33}$$

$$M_{nld} = M_{ne}\left[1 - 0.22\left(\frac{M_{ncd}}{M_{ne}}\right)^{0.5}\right]\left(\frac{M_{ncd}}{M_{ne}}\right)^{0.5} \left(for\ \lambda_d = \left(\frac{M_{ne}}{M_{crd}}\right)^{0.5} > 0.673\right) \tag{34}$$

The problem becomes significantly more complex due to the absence of a clearly defined interaction domain specific for pallet rack structures. A solution, specific for cold-formed members, can be found among the standards such as ANSI/AISI S100-20 [22] and ANSI/AISC 360-22 [20]. Both documents refers to some of the provisions outlined in Annex F of ANSI/AISI S100-20 [22], but is at § H of ANSI/AISI S100-20 [22] (specifically, in the commentary) which provides some guidance on the interaction between axial forces and bending moments.

According to ANSI/AISI S100-20 [22], for a beam-column subjected to an axial load and end moments M as shown in **Fig. 11** the combine axial and bending stress in compression is given by the eq. (35):

$$\bar{f} = \frac{\bar{P}}{A} + \frac{\bar{M}}{S} = \bar{f}_a + \bar{f}_b \tag{35}$$

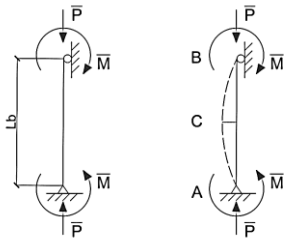


Fig. 11 Beam-Column Subjected to axial load and end load Moments, according to ANSI/AISI S100-20 [22]

where $\bar{f}$ is the Combined stress in compression, $\bar{P}$ is the required axial load determined in accordance with ASD, LRFD or LSD load combination, S is the section modulus, $\bar{f}_a$ is the Axial compressive stress and $\bar{f}_b$ is the bending stress in compression. In the context of the design, the combined stress should be limited, either way, by a certain value ratio. The procedure shows two ways of obtain said threshold value (by stress ratio or by strength ratio, which is more similar to the European procedure/dominion). This procedure is not conservative.

An alternative procedure *(§H1.2 Combined Compressive Axial Load and Bending*) –more conservative – shows some analogies with the European and Australian ones, given that the members are subjected to local buckling :
Therefore, the formulation is the following:

$$\frac{\bar{P}}{P_a} + \frac{\overline{M_x}}{M_{ax}} + \frac{\overline{M_y}}{M_{ay}} \leq 1 \tag{36}$$

where $\bar{P}$ is the required compressive axial strength, P_a is the available axial strength, $(\overline{M_x})$,$(\overline{M_y})$ are the required flexural strengths, while M_{ax}, M_{ay} are the available flexural strengths about the centroidal axes.
Nevertheless, the approaches remain predominantly conservative, often favouring stress-based checks over more comprehensive interaction formulations involving combined axial and bending actions.

5.2. Comparative benchmark of column verification procedures

To provide a more systematic and reproducible basis for comparing the three design frameworks, the qualitative discussion presented in the previous sections was complemented by an illustrative numerical benchmark. The aim of this benchmark is not to reproduce all possible rack configurations, nor to perform a full parametric study, but to quantify how the different code-based verification procedures affect the structural safety assessment of rack uprights under the same reference geometry, loading scheme and material properties.

The reference structure adopted for the comparison is shown in **Fig. 12** while in **Fig. 13** the arrangement of the column sections is reported. It consists of a three-level pallet rack frame with two bays in the down-aisle direction and one bay in the cross-aisle direction. The same structural geometry, steel grade and

nominal loading scheme were adopted for all three models. The only differences introduced in the analyses are those strictly required by the application of the European, Australian and American design provisions.

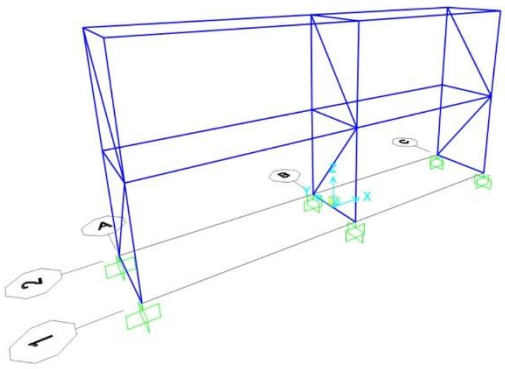


Fig. 12 Representation of the case study to provide as benchmark

The selected configuration is representative of a relatively lightweight rack system, commonly encountered in the European market. This choice was made to obtain a common benchmark geometry compatible with the available information and with the comparative purpose of the study. The main geometric, mechanical and loading parameters of the benchmark structure are summarized in **Table 10** and **Table 11**.

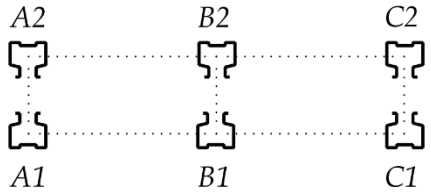


Fig. 13 Scheme adopted to clarify all the upright a location and arrangement

Table 10
Main characteristic of the benchmark rack

General information of the structures	
Number of storeys	2
Number of bays (X direction)	2
Number of bays (Y direction)	1
Storey's Height	1.3 m
Bay's Length (X direction)	2.70 m
Bay's Length (Y direction)	1 m

Table 11
Other general assumption for the adopted modelling

General information of the structures	
Steel grade	S355
Upright section	Omega, perforated
Beam section	Closed box, rectangular
Braces section	Simple lipped channel
Assumption for the beam-upright joint	Pinned down-aisle, Pinned cross-aisle
Assumption for the baseplate joint	Encastre down-aisle, pinned cross-aisle
Nominal load	3 kN/m

For the initial comparison, a uniformly distributed nominal load of approximately 3.00 kN/m was applied to the beams. The same load distribution was used in the European, Australian and American models. Each model was then adapted according to the corresponding standard, starting from the calculation of the initial imperfections. This step is particularly relevant because the three design frameworks introduce different assumptions for global imperfection angles and for their distribution in the down-aisle and cross-aisle directions.

The imperfection values obtained for the three approaches are reported in **Table 12**. These values were subsequently introduced into the numerical models and used to perform nonlinear static analyses including large-displacement effects. For each regulatory framework, the governing load combination was adopted: Eq. (10) for the European and Australian approaches, and Eq. (14) for the American LRFD-based approach.

Table 12
Imperfection values adopted in the three code-based models for a nominal load of 3 kN/m and 6 kN/m

		Imperfections [kN]	
	Location	3 kN/m	6 kN/m
European Model	Down-Aisle	0.062	0.124
	Cross-Aisle (external)	0.058	0.116
	Cross-Aisle (internal)	0.116	0.233
Australian Model	Down-Aisle	0.181	0.362
	Cross-Aisle (external)	0.078	0.157
	Cross-Aisle (internal)	0.157	0.315
American Model	Down-Aisle	0.080	0.160
	Cross-Aisle (external)	0.02	0.04
	Cross-Aisle (internal)	0.04	0.08

The resistance checks were then carried out according to the interaction formulae prescribed by each standard. In particular, the European verification was performed using Eqs. (21) and (22), the Australian verification using Eqs. (23) and (24), and the American verification using Eq. (36). The upright positions considered in the comparison are identified in Fig. 13. The resulting utilization ratios are reported in **Fig. 14**, where the colour scale indicates the percentage of the available resistance domain used by each upright.

Fig. 14 also shows that, under the reference load level, all uprights satisfy the relevant code-based resistance checks. Although the three standards lead to different utilization ratios, all members remain well below the corresponding resistance thresholds. This confirms that, for the selected benchmark structure and loading condition, the different regulatory frameworks provide safe outcomes, even if the predicted safety margins are not identical.

To further investigate the sensitivity of the results to the applied load level, the analysis was repeated by increasing the nominal beam load from 3.0 kN/m to 6 kN/m. This second analysis allows the comparison to move closer to the resistance limits of the structure and makes the influence of the different imperfection and verification procedures more evident.

The imperfection values obtained for the increased load condition are reported in **Table 12**.

Using the same structural layout, the results obtained for the increased load condition are reported in **Fig. 15.** Outcome of the analysis performed for the 3 different case study a) Europe, b) Australia c) America, for a nominal load of 6kN/m.. In this case, the divergence among the standards becomes more pronounced. The European and American models still satisfy the corresponding resistance checks, although with higher utilization ratios than in the initial loading condition. Conversely, the Australian model reaches the resistance threshold in one upright, namely column B2, which does not satisfy the required verification.

This outcome demonstrates that the differences among the standards may become structurally significant when the rack approaches its resistance limit. In particular, the combination of larger imperfection values and the specific interaction checks adopted in the Australian framework produces a more demanding safety assessment for the selected benchmark. By contrast, the European and American procedures provide less severe results for the same geometry and loading condition, although through different mechanical assumptions.

Overall, the numerical benchmark confirms that the three standards do not merely differ in terminology or formal layout. Their different treatments of imperfections, second-order effects, effective section properties and resistance interaction formulae may lead to different utilization ratios and, under increased loading, even to different acceptability outcomes. Therefore, the benchmark supports the main thesis of the paper: identical rack configurations may receive different structural safety assessments depending on the regulatory framework

adopted.

At the same time, the results should be interpreted within the limits of the present study. The benchmark is intentionally restricted to a single representative rack configuration and focuses on upright verification. It does not replace a broader parametric study involving multiple geometries, connection stiffness values, upright perforation patterns, base-plate behaviours and loading scenarios. Nevertheless, it provides a first quantitative comparison of the practical consequences of applying the three design frameworks to the same structural system and identifies the need for future benchmark studies based on refined finite-element or finite-strip models.

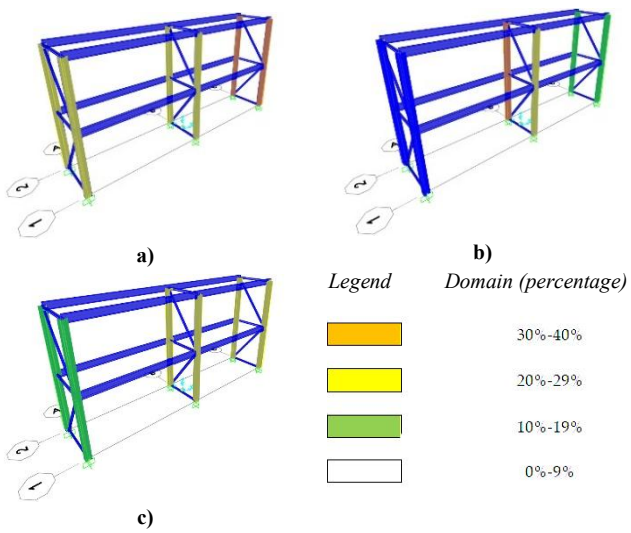


Fig. 14 Outcome of the analysis performed for the 3 different case study a) Europe, b) Australia c) America, for a nominal load of 3kN/m

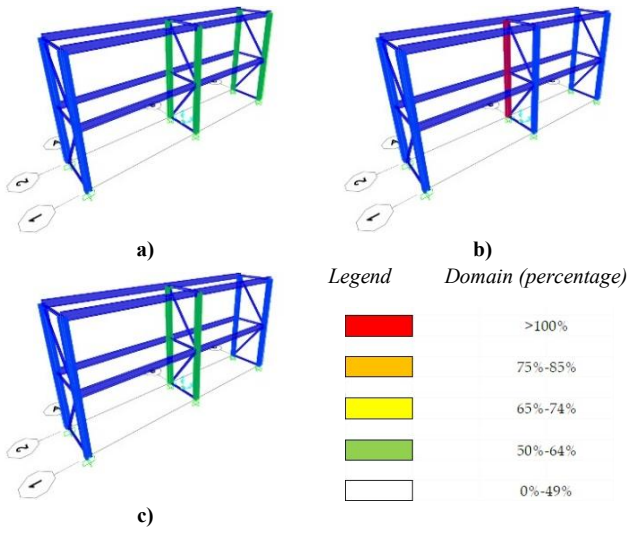


Fig. 15 Outcome of the analysis performed for the 3 different case study a) Europe, b) Australia c) America, for a nominal load of 6kN/m

5.3 Treatment of post-buckling reserve and elastoplastic effects in perforated rack uprights

A further critical aspect in the stability assessment of pallet rack uprights is the possible contribution of post-buckling reserve strength and elastoplastic stress redistribution. This issue is particularly relevant because rack uprights are thin-walled, open, highly perforated members, commonly subjected to axial compression combined with biaxial bending and, in many cases, torsional or flexural–torsional effects. Since pallet racks are often operated close to their full design load, the distinction between elastic buckling prediction, code-based resistance reduction, and actual post-buckling response becomes mechanically significant.

In conventional thin-walled steel members, post-buckling reserve strength may arise from stress redistribution after local plate buckling. However, in pallet rack uprights, the presence of repeated perforations strongly modifies this mechanism. Hole arrays interrupt the continuity of plate elements, alter the effective stress paths, induce local stress concentrations, and interact with distortional and torsional deformation modes. As a result, post-buckling behaviour cannot be reliably inferred from the formulations developed for unperforated cold-formed members or for conventional plated steel elements.

Within the European framework, Eurocode 3 [2]-[5] provides refined models for some post-buckling phenomena, such as effective width formulations and tension-field action in plated elements. Nevertheless, these models are not directly transferable to pallet rack uprights, because the regular perforation pattern prevents the development of the continuous plate mechanisms assumed in conventional formulations. EN 1993-1-3 provides effective width methods for cold-formed members, but these approaches are mainly suited to members with isolated openings or regular plate elements and do not fully represent the continuous longitudinal perforations typical of rack uprights. EN 15512 [6], therefore, adopts a more specific, but still simplified, approach: perforations are represented through equivalent section properties, while the remaining uncertainty is addressed through conservative coefficients and design assisted by testing. In this sense, the European approach does not explicitly model post-buckling reserve strength; rather, it incorporates its effects indirectly through empirically calibrated design procedures.

The North American framework follows a different philosophy. ANSI MH16.1[18] refers to AISI provisions for cold-formed member design, where the Direct Strength Method represents a more advanced alternative to the traditional effective width method. The Direct Strength Method is particularly valuable because it relates nominal strength to elastic buckling modes, including local, distortional and global buckling. This makes it conceptually suitable for thin-walled members whose behaviour is governed by interacting instability phenomena. However, its application to pallet rack uprights remains limited by the complexity of perforated sections and by the combined action of axial load, biaxial bending and torsion. While the method provides a rational basis for compression-dominated problems, the treatment of beam-column interaction, torsional effects and post-buckling reserve in highly perforated open sections remains less explicit. Consequently, the North American approach is more mechanically oriented in its use of elastic buckling modes, but still does not provide a complete analytical description of the elastoplastic post-buckling response of perforated rack uprights.

The Australian framework, through AS 4084 [15] and AS/NZS 4600 [17], shares several features with both the European and North American approaches. It relies on cold-formed steel design principles and includes empirical or semi-empirical reductions to account for the influence of perforations and instability. However, as in the European framework, the most complex effects are generally handled through testing or conservative design assumptions rather than through an explicit elastoplastic post-buckling formulation. This is particularly evident for biaxial bending and torsion, where the interaction between perforation-induced local effects, distortional buckling and global flexural–torsional instability is not fully captured by simplified analytical expressions.

A common limitation of all three frameworks is therefore the incomplete treatment of torsion and flexural–torsional interaction in the post-buckling range. This limitation is especially relevant for monosymmetric open section uprights, where the shear centre does not coincide with the centroid and where eccentric loading, connection flexibility and perforation patterns can amplify torsional effects. Although EN 15512 [6] includes specific interaction formulae and reduction factors for flexural–torsional instability, these remain essentially design-oriented and conservative. Similarly, the North American and Australian provisions provide practical routes for resistance verification, but they do not explicitly resolve the combined problem of perforation, biaxial bending, torsion and post-buckling stress redistribution. [73]

Therefore, the present comparison confirms that the current standards address post-buckling and elastoplastic effects mainly in an indirect manner. The European and Australian frameworks compensate for modelling limitations through equivalent or effective section properties, conservative coefficients and design assisted by testing. The North American framework provides a more explicit connection with elastic buckling modes through the Direct Strength Method, but still leaves unresolved the complete beam-column-torsion interaction problem for highly perforated uprights. In all cases, refined finite-element analysis, finite strip analysis calibrated for perforated members, or experimental testing remains necessary when the post-buckling response is expected to govern the design. [109]

This represents one of the most important research gaps identified by the present review. Future standard developments should move toward mechanically consistent models capable of accounting for the interaction between local buckling, distortional buckling, flexural–torsional instability, biaxial bending and elastoplastic stress redistribution in perforated open-section uprights.

6. Conclusions

The comparative investigation presented in this study demonstrates that the

design of steel pallet racking systems is influenced as much by regulatory philosophy as by structural mechanics. Although European, Australian, and North American standards pursue comparable safety objectives, they embed markedly different strategies for translating physical behaviour into analytical models. These divergences emerge in the treatment of geometric tolerances, the representation of perforated uprights, the characterization of semi-rigid connections, the introduction of imperfections, and the format of stability verification. As a result, identical rack configurations may experience different predicted force distributions, utilization levels, and intervention thresholds depending solely on the normative environment adopted. [73] [109]. This aspect was further confirmed by the numerical benchmark introduced in this study, in which the same rack configuration was analysed according to the European, Australian and American verification procedures. Although all models satisfied the resistance checks under the reference loading condition, the calculated utilization ratios were not identical. When the nominal load was increased, the differences among the standards became more evident, leading to a non-satisfactory verification in one upright according to the Australian [15] procedure, while the European[6] and American[18] checks remained satisfied. This result confirms that the divergences among the standards are not only formal or terminological, but may lead to different safety assessments for the same structural system.

The analysis also highlights that the international convergence toward design assisted by testing does not necessarily imply methodological uniformity. Experimental data are integrated within distinct interpretative frameworks, reflecting regional traditions, industrial practices, and historical development paths. [109] Consequently, direct transferability of design assumptions across jurisdictions cannot be taken for granted. From a scientific perspective, the findings underline the need for further research aimed at clarifying the interaction between system-level behaviour and codified simplifications, particularly for perforation-sensitive instability phenomena, post-buckling reserve, elastoplastic stress redistribution, and connection-driven nonlinearity. From a regulatory standpoint, the work supports ongoing efforts toward greater transparency, harmonization, and mutual recognition of safety formats in an increasingly globalized market. By exposing how modelling philosophies shape engineering outcomes, and by providing a first quantitative benchmark of their practical implications, this review contributes to a more informed dialogue between researchers, manufacturers, and standardization bodies, fostering the development of more coherent and reliable design approaches for pallet racking structures worldwide.

References

[1] Ghersi A., Landolfo R., Mazzolani F. M., Design of Metallic cold-formed thin-walled members, Spon Press, Taylor and Francis group, London and New York 2002

[2] Eurocode 3 - Design of steel structures Part 1-1: General rules - and rules for buildings

[3] Eurocode 3 - Design of steel structures Part 1-3: General rules - Supplementary rules for cold-formed members and sheeting

[4] Eurocode 3: Design of steel structures - Part 1-5: "Design of steel structures —Plated structural elements."

[5] Eurocode 3: Design of steel structures - Part 1-8: Design of joints, 1993

[6] EN 15512:2020 + A12022: Steel static storage system- Adjustable pallet racking systems, Principles for structural design

[7] EN 15620: Steel static storage systems- Tolerances, deformations and clearances

[8] EN 15635: "Steel static storage systems — Application and maintenance of storage equipment."

[9] Regulation Machinery UE 1230/2023, now L 165 of 29 June 2023

[10] EN 15095:2021 Power-operated mobile racking and shelving, carousels and storage lifts - Safety requirements

[11] FEM 9.841 -10.2.10_2012 Storage Systems with rail dependent storage and retrieval equipment- interfaces

[12] FEM R&S Guide, 10 Storage Equipment Information Bulletin No. 10 – warehouse building-storage areas for racking – guidance for stakeholders

[13] FEM position paper 22/09/23

[14] EAD 200059-00-0302: Steel components for pallet racking systems

[15] AS 4084: Steel storage racking_ part 1 Design

[16] AS 4100: Steel Structures

[17] AS/NZS 4600: Cold formed steel structures

[18] ANSI MH16.1-23: Design, testing and utilization of Industrial Steel Storage Racks

[19] FEMA 460 - Seismic Considerations For Steel Storage Racks Located In Areas Accessible To The Public, 2005

[20] ANSI/AISC 360-22 Specification for Structural steel buildings

[21] ANSI/AISC S202-20 Code of Standard practice for Cold-Formed Steel Structural Framing

[22] ANSI/AISC S100-20 North American Specification for the Design of Cold-Formed Steel Structural Members

[23] AISI S902-17: Test Standard for Determining the Strength and Stiffness of Cold-Formed Steel Connections.

[24] X. Zhao, T. Wang, Y. Chen, and K. S. Sivakumaran, "Flexural behavior of steel storage rack beam-to-upright connections," J. Constr. Steel Res., vol. 99, pp. 161–175, 2014, doi: 10.1016/j.jcsr.2014.04.007.

[25] S. N. R. Shah, N. H. Ramli Sulong, R. Khan, M. Z. Jumaat, and M. Shariati, "Behavior of Industrial Steel Rack Connections," Mech. Syst. Signal Process., vol. 70–71, pp. 725–740, 2016, doi: 10.1016/j.ymssp.2015.08.026.

[26] F. D. Markazi, R. G. Beale, and M. H. R. Godley, "Experimental analysis of semi-rigid boltless connectors," Thin-Walled Struct., vol. 28, no. 1, pp. 57–87, May 1997, doi: 10.1016/S0263-8231(97)00003-7.

[27] C. Bernuzzi and C. A. Castiglioni, "Experimental analysis on the cyclic behaviour of beam-to-column joints in steel storage pallet racks," Thin-Walled Struct., vol. 39, no. 10, pp. 841–859, Oct. 2001, doi: 10.1016/S0263-8231(01)00034-9.

[28] P. Prabha, V. Marimuthu, M. Saravanan, and S. Arul Jayachandran, "Evaluation of connection flexibility in cold formed steel racks," J. Constr. Steel Res., vol. 66, no. 7, pp. 863–872, 2010, doi: 10.1016/j.jcsr.2010.01.019.

[29] Yazici, C., Gusella, F., & Özkal, F. M. (2025). Effect of beam-to-connector weld position on the flexural response of boltless rack connections. Journal of Constructional Steel Research, 237 (Part B), Article 110141. https://doi.org/10.1016/j.jcsr.2025.110141.

[30] X. Zhao, L. Dai, and K. J. R. Rasmussen, "Hysteretic behaviour of steel storage rack beam-to-upright boltless connections," J. Constr. Steel Res., vol. 144, pp. 81–105, 2018, doi: 10.1016/j.jcsr.2018.01.006.

[31] S. Giordano, F. Gusella, G. Lavacchini, M. Orlando, and P. Spinelli, "Experimental tests on beam-end connectors of cold-formed steel storage pallet racks," Ce/Papers, vol. 1, no. 2–3, pp. 669–678, 2017, doi: 10.1002/cepa.105.

[32] N. A. Mohamad Rosli, C. G. Tan, H. Hashim, and N. H. Ramli Sulong, "Experimental investigation and parameter analysis of boltless steel pallet rack beam-to-column connection," J. Constr. Steel Res., vol. 231, no. April, p. 109578, 2025, doi: 10.1016/j.jcsr.2025.109578.

[33] L. Ślęczka and A. Kozlowski, "Experimental and theoretical investigations of pallet racks connections" Adv. Steel Constr., vol. 3, no. 2, pp. 607–627, 2007.

[34] M. Shariati et al., "Experimental investigations on monotonic and cyclic behavior of steel pallet rack connections," Eng. Fail. Anal., vol. 85, pp. 149–166, Mar. 2018, doi: 10.1016/j.engfailanal.2017.08.014.

[35] S. N. R. Shah, N. H. Ramli Sulong, R. Khan, and M. Z. Jumaat, "Structural performance of boltless beam end connectors," Adv. Steel Constr., vol. 13, no. 2, pp. 144–159, 2017, doi: 10.18057/IJASC.2017.13.2.

[36] Nuñez, E.; Mata Lemus, R. D.; Sanhueza, M.; Hernández, M.; Maureira-Carsalade, N.; Guerrero, N. (2025). Cyclic behavior of beam-to-upright bolted connections: Experimental study of Chilean steel storage racks. Engineering Structures, 323(A), 1-25. https://doi.org/10.1016/j.engstruct.2024.119310.

[37] L. Dai, X. Zhao, and K. J. R. Rasmussen, "Flexural behaviour of steel storage rack beam-to-upright bolted connections," Thin-Walled Struct., vol. 124, pp. 202–217, 2018, doi: 10.1016/j.tws.2017.12.010.

[38] Gilbert, B.P. & Rasmussen, K.J.R., 2010. Bolted moment connections in drive-in and drive-through steel storage racks. Journal of Constructional Steel Research, 66(6), pp.755-766. https://doi.org/10.1016/j.jcsr.2010.01.013.

[39] Dai, L., Zhao, X. & Ren, C., 2016. Experimental investigation into steel storage rack beam-to-upright bolted connections. Proceedings of the Wei-Wen Yu International Specialty Conference on Cold-Formed Steel Structures – Recent Research and Developments in Cold-Formed Steel Design and Construction, St. Louis, Missouri, USA.

[40] Zhao, X., Huang, Z., Wang, Y. & Sivakumaran, K.S., 2019. Flexural behaviour of steel storage rack base-plate upright connections with concentric anchor bolts. Steel and Composite Structures, 33(3), pp.357-373. https://doi.org/10.12989/scs.2019.33.3.357

[41] L. Yin, G. Tang, M. Zhang, B. Wang, and B. Feng, "Monotonic and cyclic response of speed-lock connections with bolts in storage racks," Eng. Struct., vol. 116, pp. 40–55, 2016, doi: 10.1016/j.engstruct.2016.02.032.

[42] Yazıcı, C., Arik, E. & Özkal, F. M., 2023. Influence of design parameters on beam-to-column connections of steel storage rack systems. Engineering Failure Analysis, 152, 107439. https://doi.org/10.1016/j.engfailanal.2023.107439.

[43] V. Mohan et al., "Cold-formed steel pallet rack connection: an experimental study," Int. J. Adv. Struct. Eng., vol. 7, no. 1, pp. 55–68, 2015, doi: 10.1007/s40091-015-0082-9.

[44] L. Dai, X. Zhao, and K. J. R. Rasmussen, "Cyclic performance of steel storage rack beam-to-upright bolted connections," J. Constr. Steel Res., vol. 148, pp. 28–48, Sep. 2018, https://doi.org/10.1016/j.jcsr.2018.04.012.

[45] Aguirre, C., 2005. Seismic behavior of rack structures. Journal of Constructional Steel Research, 61(5), pp.607–624. https://doi.org/10.1016/j.jcsr.2004.10.001.

[46] Bové, O., López-Almansa, F., Ferrer, M. & Roure, F., 2022. Ductility improvement of adjustable pallet rack speed-lock connections: Experimental study. Journal of Constructional Steel Research, 188, 107015. https://doi.org/10.1016/j.jcsr.2021.107015.

[47] Tsarpalis, D. & Vamvatsikos, D., 2025. A codifiable methodology for estimating pallet sliding displacements on steel racking systems. Earthquake Engineering & Structural Dynamics, 54, pp.363–388. https://doi.org/10.1002/eqe.4261.

[48] Tagliafierro, B., Montuori, R. & Vayas, I., 2024. Seismic design-assisted-by-testing approach for racks with dissipative baseplates in the cross-aisle direction. Thin-Walled Structures, 202, 112126. https://doi.org/10.1016/j.tws.2024.112126.

[49] Bernardi, M., Baldassino, N., Zandonini, R. & di Gioia, A., 2023. Full-scale tests of industrial steel storage pallet racks. Structures, 57, 105128. https://doi.org/10.1016/j.istruc.2023.105128.

[50] Aruna, G. (2020), Stub Column Tests of Cold-Formed Steel Built-Up Square Sections with Intermediate Stiffeners. Strength of Materials, n° 52, pp 281–290 DOI: 10.1007/s11223-020-00176-9

[51] Hancock G.J., Kwon Y.B., Stefan Bernard E. (1994), Strength design curves for thin-walled sections undergoing distortional buckling, Journal of Constructional Steel Research, n°31, pp. 169-186 DOI: 10.1016/0143-974X(94)90009-4

[52] Wang, D., Wang, J., Liu, S. & Liu, Z., 2025. Experimental investigation into the axial compressive buckling behavior of LQ550 cold-formed channel columns with web openings. Thin-Walled Structures, 218, 114017. https://doi.org/10.1016/j.tws.2025.114017.

[53] Matsubara, G.Y. & Batista, E.d.M., 2025. Local-distortional-global buckling interaction of steel cold-formed columns. Thin-Walled Structures, 217, 113735. https://doi.org/10.1016/j.tws.2025.113735.

[54] Ren, C., Liu, Y., Liu, W., Dai, L., Cheng, L. & Xu, J., 2025. An experimental and numerical investigation into cold-formed steel upright frames with semi-rigid joints. Thin-Walled Structures, 216 (Part B), 113586. https://doi.org/10.1016/j.tws.2025.113586.

[55] Batista E.M., Rodriguez F.C., (1995) Buckling Curve for Cold-Formed Compressed Members, Journal of Constructional Steel research, n° 28 , pp. 121-136 DOI:10.1016/0143-974X(94)90038-8

[56] Batista E.M., Camotim D., Prola L.C., Vaz E.(1998), On the stability and strength of steel columns affected by distortional buckling, Journal of Constructional Steel Research n°46 pp. 129-131 DOI: 0.1016/S0143-974X(98)00048-0

[57] Pu Y.,Godley M.H.R., Beale R.G., (1988) Experimental Procedures for Stub Column Tests,

14th International specialty Conference on Cold-Formed Steel Structures
[58] Gilbert B. P., Rasmussen K.J.R. (2009), Experimental tests on steel storage rack components, University of Sydney, research report n°R899
[59] Roure F., Pastor M.M., Casafont M., Somalo M.R. (2011) , Stub column tests for racking design: Experimental testing, FE analysis and EC3, Thin-walled Structures n°49 pp 167-184n DOI: 10.1016/j.tws.2010.09.002
[60] Crisan A., Ungueanu V., Dubina D. (2012), Behaviour of cold-formed steel perforated sections in compression: Part 1: numerical investigations and design considerations, Thin-walled Structures n°61, pp-86-96 DOI: 10.1016/j.tws.2012.07.016
[61] Crisan A., Ungueanu V., Dubina D. (2012), Behaviour of cold-formed steel perforated sections in compression: Part 2: numerical investigations and design considerations, Thin-walled Structures n°61, pp 97-105 DOI: 10.1016/J.TWS.2012.07.013
[62] Ungueanu V., Dubina D , Sensitivity to Imperfections of Perforated Pallet Rack Sections, Mechanics and Mechanical Engineering n°7, 2, pp 209–222 DOI:10.2478/amtm-2018-0010
[63] Torabian, S., Zheng, B. & Schafer, B.W., 2015. Experimental response of cold-formed steel lipped channel beam-columns. Thin-Walled Structures, 89, pp.152–168. https://doi.org/10.1016/j.tws.2014.12.003
[64] Fan, S.G. & Fan, S.G., 2014. Capacity of stainless steel lipped C-section stub column under axial compression. Journal of Constructional Steel Research, 103, pp.251–263. https://doi.org/10.1016/j.jcsr.2014.09.013.
[65] Liu J.Z, Fang H., Chan T.M., (2022), Warping Influence in the static design of unbraced steel storage pallet racks, Thin-Walled Structures n°180 DOI: 10.1016/j.tws.2022.109770
[66] Ma J.-l., Chan T.-M., Young B., ASCE M. (2015) Experimental Investigation on Stub-Column Behavior of Cold-Formed High-Strength Steel Tubular Sections, American society of Civil Engineers, DOI:10.1061/(ASCE)ST.1943-541X.0001456
[67] Manikandan P., Arun N. (2016) Behaviour of Partially Closed Stiffened Cold-Formed Steel Compression Member, Engineering, Materials Science - Arabian Journal for Science and Engineering DOI:10.1007/S13369-015-2015-0
[68] Vijayanand, S., & Anbarasu, M. (2017), Effect of Spacers on Ultimate Strength and Behavior of Cold-Formed Steel Built-up Columns. Procedia Engineering, n°103 pp 251-263 DOI: 10.1016/j.proeng.2016.12.205
[69] Zhang, P., & Alam, M. S. (2017) Experimental investigation and numerical simulation of pallet-rack stub columns under compression load. Journal of Constructional Steel Research n° 133 pp 282-299 DOI: 10.1016/j.jcsr.2017.02.023
[70] Baldassino N., Bernuzzi C., di Gioia A., Simoncelli M (2019) An experimental investigation on solid and perforated steel storage racks uprights, journal of constructional Steel Research DOI: 10.1016/j.jcsr.2019.01.008
[71] G. Zucco, P.M. Weather (2020) The Role of Symmetry in the Post-Buckling Behaviour of Structures, Proceedings of the royal society A: Mathematical, Physical and Engineering Sciences, n° 27, issue 2233 DOI: 10.1098/rspa.2019.0609
[72] Taranu G., Iacob S., Taranu N., (2025) Buckling Behavior of Perforated Cold-Formed Steel Uprights: Experimental Evaluation and Comparative Assessment Using FEM, EWM, and DSM, Buildings n° 15, issue 9 p 1561 DOI: 10.3390/buildings15091561
[73] de Almeida Neivahttps://www.scielo.cl/scielo.php?script=sci_arttext&pid=S0718-915X2022000200204&lng=p&nrm=iso&tlng=en - aff1 L. H. , Eliashttps://www.scielo.cl/scielo.php?script=sci_arttext&pid=S0718-915X2022000200204&lng=p&nrm=iso&tlng=en - aff2 G.C. , Juliane Aparecida Braz Starlinohttps://www.scielo.cl/scielo.php?script=sci_arttext&pid=S0718-915X2022000200204&lng=p&nrm=iso&tlng=en - aff3 J.A.B., Arlene Maria Cunha Sarmanho A.M.C., Alves V.N.,(2016) Industrial storage system continuous perforated uprights: a combined design proposal, Revista de la construcción, DOI: 10.7764/rdlc.21.2.204
[74] J.A.B., Arlene Maria Cunha Sarmanho A.M.C., Alves V.N.,(2016) Industrial storage system continuous perforated uprights: a combined design proposal, Revista de la construcción, DOI: 10.7764/rdlc.21.2.204
[75] Zhao O., Gardner L., Young B., (2016) Buckling of ferritic stainless steel members under combined axial compression and bending, Journal of Constructional steel research , vol. 117, pp. 35-48 DOI: 10.1016/j.jcsr.2015.10.003.
[76] Furukawa, M.N. & Malite, M., 2025. Experimental analysis of the mechanical behavior of steel storage rack base plate upright connections. Thin-Walled Structures, 214, 113340.
[77] Firouzianhaij, A., Gorji Azandariani, M., Usefi, N. & Samali, B., 2022. Performance of baseplate connections in CFS storage rack systems: an experimental, numerical and theoretical study. Journal of Constructional Steel Research, 196, 107421. https://doi.org/10.1016/j.jcsr.2022.107421.
[78] Nagy, Z. & Sánduly, A., 2022. Upright base connection impact on structural design of steel storage rack systems in seismic zones. In: F.M. Mazzolani, D. Dubina & A. Stratan (eds.), Proceedings of the 10th International Conference on Behaviour of Steel Structures in Seismic Areas – STESSA 2022, Lecture Notes in Civil Engineering, vol. 262, pp. 1124–1132. Springer, Cham. https://doi.org/10.1007/978-3-031-03811-2_125.
[79] Zhao, X., Huang, Z., Wang, Y. & Sivakumaran, K.S., 2019. Flexural behaviour of steel storage rack base-plate upright connections with concentric anchor bolts. Steel and Composite Structures, 33(3), pp.357–373. https://doi.org/10.12989/scs.2019.33.3.357.
[80] Bernuzzi, C., Draskovic, N. & Simoncelli, M., 2015. European and United States approaches for steel storage pallet rack design: Part 1 – Discussions and general comparisons. Thin-Walled Structures, 97, pp.308–320. https://doi.org/10.1016/j.tws.2015.08.012.
[81] Bernuzzi, C., Draskovic, N. & Simoncelli, M., 2015. European and United States approaches for steel storage pallet rack design. Part 2: Practical applications. Thin-Walled Structures, 97, pp.321–341. https://doi.org/10.1016/j.tws.2015.08.011.
[82] GB 50017- “Standard for Design of Steel Structures”
[83] GB 50018- “Technical Standard for Cold-Formed Thin-Walled Steel Structures”
[84] JIS B 8942:2021- Basic requirements for automated and non-automated storage systems
[85] Chaudhary S. Ur R., Mahmood A., Haque Md A, Comparative Analysis of Steel Component Section Classification and Local Buckling Design Methods in Chinese, European, and American Codes, International Journal of Research Publication and Reviews, November 2024 Vol 5, no 11, pp 4302-4312
[86] Pham L., Amirsardari A., Lee J., Gad E.F., “Reliability Analysis of Cold-Formed Steel Components”, PART 1, Eleventh International Conference on Advances in Steel Structures (ICASS’2023) DOI: 10.18057/ICASS2023
[87] Pham L., Amirsardari A., Lee J., Gad E.F., “Reliability Analysis of Cold-Formed Steel Components”, PART 2, Eleventh International Conference on Advances in Steel Structures (ICASS’2023) DOI: 10.18057/ICASS2023
[88] Faria, V.A.M., Freitas, M.S.R., Brandão, A.L.R. "Structural reliability of the design of pallet-rack columns via Direct Strength Method" (2025) Thin-Walled Structures, 213, art. no. 113294, DOI: 10.1016/j.tws.2025.113294.
[89] Shabhari, A., Jeyapragasam, V.V.K., Chandrasekar, D. "Local buckling behaviour of web perforated cold-formed steel lipped channel columns" (2024) Thin-Walled Structures, 205, art. no. 112448, DOI: 10.1016/j.tws.2024.112448.
[90] Peng Z., Shaira A.M. “Assessment of buckling strength curves in Direct Strength Method for estimating axial strengths of Cold-formed Steel members considering average yield stresses of cross-sections” (2023), Thin-Walled Structures, 188, art. no. 113743, https://doi.org/10.1016/j.tws.2023.110823.
[91] Isobe, D., Xie, B., Narayanan, U.N., Veeraraghavan, N. "A numerical investigation on methods to prevent progressive collapse of pallet rack systems subjected to impact loads" (2025) Thin-Walled Structures, 216, art. no. 113743, DOI: 10.1016/j.tws.2025.113743.
[92] Lewis GM (1991) Stability of rack structures. Thin Walled Struct n° 12 pp 163–174 DOI: 10.1016/0263-8231(91)90062-n
[93] Mohan, V., Prabha, P., Rajasankar, J., Iyer, N.R., Raviswaran, N., Nagendiran, V., & Kamalakannan, S.S., 2015. Cold-formed steel pallet rack connection: an experimental study. International Journal of Advanced Structural Engineering, 7(1), pp.55–68. https://doi.org/10.1007/s40091-015-0082-9
[94] Baldassino N., Bernuzzi C., (2000) Analysis and behaviour of steel storage pallet racks, Thin-walled structures n°37(4) pp 277-304 DOI: 10.1016/S0263-8231(00)00021-5
[95] Bernuzzi C, Castiglioni CA (2001), Experimental analysis on the cyclic behaviour of beam to column joints in steel storage pallet racks. Thin Walled Struct n°39 pp841–859 DOI: 10.1016/S0263-8231(01)00034-9
[96] Bajoria KM, Talikoti RS (2006), Determination of flexibility of beam to column connectors used in thin walled cold formed steel pallet racking systems, Thin-Walled Structures n°44 pp 372–380 DOI:10.1016/j.tws.2006.01.007
[97] Abdel-Jaber M., Beale R.G., Godley M.H.R., (2006) A theoretical and experimental investigation of pallet rack structures under sway, journal of constructional Steel Research DOI: 10.1016/j.jcsr.2005.04.008
[98] Ślęczka, L., & Kozlowski, A. (2008). Design of beam-to-column joints in steel storage pallet racks by testing and by component method. Archives of civil engineering, 54, 263-291.
[99] Godley M.H.R., Beale R.G., (2008) Investigation of the effects of looseness of bracing components in the cross-aisle direction on the ultimate load carrying capacity of pallet rack frames, Thin-walled structures, n° 46(7-9), pp. 848–854 DOI: 10.1016/j.tws.2008.01.011:
[100] Wang T., Zhao X., Chen Y.(2012) Experimental analysis of beam-to-upright connections in cold-formed steel storage pallet rack, 21st International Specialty Conference on Cold-Formed Steel Structures - Recent Research and Developments in Cold-Formed Steel Design and Construction DOI:10.18057/IJASC.2020.16.3.
[101] Bernuzzi C., Pieri A., Squadrito V. (2014) Warping influence on the static design of unbraced steel storage pallet racks, Thin-Walled Structures, n°79, pp 71-82 DOI: 10.1016/j.tws.2014.01.024
[102] Shah S.N.R. Hafizah R.S, Shariati M., Jumaat Z., (2015) Steel rack Connections: identification of most Influential factors and a comparison of stiffness design methods, Plos One DOI: 10.1371/journal.pone.0139422
[103] Shah S.N.R. Hafizah R.S, Shariati M., Jumaat Z., (2016) State-of-the-art review on the design and performance of steel pallet rack connections, Engineering failure analysis, DOI: 10.1016/j.engfailanal.2016.04.017
[104] Dai L., Zhao,X, Rasmussen K.J.R. (2018) Flexural behaviour of steel storage rack beam-to-upright bolted connections, Thin Walled Structures, n°124, pp 202-217 DOI: 10.1016/j.tws.2017.12.010
[105] Baldassino N., Bernuzzi C., di Gioia A., Simoncelli M (2019) An experimental investigation on solid and perforated steel storage racks uprights, journal of constructional Steel Research DOI: 10.1016/j.jcsr.2019.01.008
[106] Chen C., Shi L., Shariati M., Toghroli A., E. T., Bui D.T. Khorami M, (2019) Behavior of steel storage pallet racking connection-A review, Steel and Composite Structures, Vol. 30, No. 5 pp 457-469 DOI: 10.12989/scs.2019.30.5.457
[107] R. Vujanac, N. Miloradovic, S. Vulovic, A. Pavlovic (2020), A Comprehensive Study into the Boltless Connections of Racking Systems , Metals. DOI: 10.3390/met10020276
[108] Dai, L., Yao, H., Yan, S., Ren, C. "Progressive collapse of beam-to-upright subassemblies of steel storage racks under a column removal scenario" (2024) Thin-Walled Structures, 205, art. no. 112575, DOI: 10.1016/j.tws.2024.112575.
[109] A.N. Trouncer n, K.J.R. Rasmussen (2013) Flexural–torsional buckling of ultra light-gauge steel storage rack uprights, Thin-walled structures, vol. 81 pp 159-174, DOI: 10.1016/j.tws.2013.10.001
[110] T.Pekoz, K.Rao, “DESIGN OF INDUSTRIAL STORAGE RACKS” Cornell University, Ithaca, new rk usa
[111] M. Casafont, M. M. Pastor, F. Roure, J. Bonada , T. Peköz, M.ASCE, (2013) Design of steel storage rack columns via the direct strength method, Journal of Structural Engineering Volume 139, Issue 5 DOI: 10.1061/(ASCE)ST.1943-541X.0000620.

Advanced Steel Construction – Vol. 22 No. 5 (2026) 538–546
DOI:10.18057/IJASC.2026.22.5.5

NUMERICAL STUDY ON THE SEISMIC PERFORMANCE OF REPLACEABLE ENERGY-DISSIPATION CHANNEL STEEL JOINTS

Bi Zhang [1], Feng Song [2], Xue-Fei Sun [3] and Bao-Wen Zhang [4, *]

[1] *M.E. Rinker Sr. School of Building Construction, University of Florida, Gainesville, FL 32611, USA*
[2] *Sichuan College of Architectural Technology Chengdu, 610000, China*
[3] *G-Force Waterproofing & Restoration, LLC, 8011 NW 14th St, Doral, FL 33126, USA*
[4] *Department of Sustainable Resources Management, SUNY College of Environmental Science and Forestry, One Forestry Drive, Syracuse, NY 13210, USA*
** (Corresponding author: E-mail: bzhang2@esf.edu)*

ABSTRACT

To meet the requirements for post-earthquake recoverable functionality, a novel replaceable energy-dissipation channel-steel joint is proposed for rectangular steel–concrete composite structures. Finite element models were established using ABAQUS and validated through comparative analyses. Based on the validated model, the stress distribution and energy-dissipation ratio of the joint were investigated to clarify its force-transfer path, energy-dissipation mechanism, and failure mode. The hysteretic performance, skeleton curves, energy-dissipation capacity, and residual deformation characteristics were comprehensively evaluated, and the joint stiffness was classified according to Eurocode 4 (EN 1994). The simulation results show that the beam-end moment is effectively transformed into a tensile-compressive couple along the beam flanges, which is then transferred sequentially to the joint core through the beam flange, channel steel, ring plate, and steel sleeve. Shear force is transmitted via the beam web, channel steel, shear connectors, and sleeve, establishing a clear and efficient load-transfer mechanism. The joint region remained elastic throughout loading, conforming to the seismic design principle of "strong column–weak beam and strong joint–weak component." The addition of the steel sleeve significantly enhances joint stiffness and flexural capacity, relocating plastic hinges to the replaceable channel steel and thus achieving "damage control." Compared with a conventional ring-plate joint, the proposed joint exhibits a 32.4% increase in stiffness, a 27.2% improvement in flexural strength, and a 24.7% enhancement in ultimate rotation capacity. To satisfy the design criteria for rigid connections in renewable steel beam-column joints, the following ratios are recommended: ring-plate thickness to beam-flange thickness (tr/tb) not less than 1.33, channel-steel thickness to beam-flange thickness (tc/tb) not less than 0.89, beam-to-column stiffness ratio k not exceeding 0.39, and channel-steel length to beam height (Lc/hb) not exceeding 0.83.

ARTICLE HISTORY

Received: 24 August 2025
Revised: 22 January 2026
Accepted: 22 January 2026

KEYWORDS

Replaceable energy-dissipating channel steel;
Beam-column joint;
Concrete-filled square steel tube;
Seismic performance;
Finite element analysis

Copyright © 2026 by The Hong Kong Institute of Steel Construction. All rights reserved.

1. Introduction

Earthquake disasters, marked by their abrupt onset and significant destructive potential, frequently lead to substantial structural damage or complete functional failure in building systems almost immediately. Conventional seismic design philosophies predominantly prioritize maintaining structural integrity during infrequent, high-magnitude seismic events, with the primary objective of preventing collapse and ensuring occupant safety [1]. Nevertheless, recent catastrophic seismic occurrences have underscored that structures exhibiting an apparently undamaged exterior may still incur severe or irreparable damage to essential load-bearing elements, such as beams, columns, and beam-column joints. Illustrative examples include the 2008 Wenchuan earthquake in China, which resulted in near-total destruction of buildings within the epicentral zone [2]. The 2015 Gorkha earthquake in Kathmandu, Nepal, led to the destruction of approximately 500,000 residential units and caused significant damage to an additional 269,000 [3]. The 2016 Kumamoto earthquake in Japan resulted in the collapse of approximately 8,050 buildings and inflicted severe damage upon another 24,147 structures [4]. More recently, the 2023 Turkey-Syria earthquakes precipitated the collapse of over 85,000 buildings, with more than 230,000 others sustaining severe damage [5].

In recognition of the significant complexities and costs involved in post-disaster building restoration, the concept of designing structures with rapid recovery capabilities has emerged as a critical element in earthquake-resistant engineering. This methodology extends beyond the primary objective of safeguarding human life; it equally emphasizes the expeditious re-establishment of building functionality following seismic events. Within the United States, the Federal Emergency Management Agency's (FEMA) P-58 guideline, first promulgated in 2012 and subsequently revised in 2018, explicitly integrated parameters such as potential human casualties, structural damage severity, estimated repair expenditures, and restoration timelines into the assessment of building performance. Correspondingly, in China, the national standard GB/T 38591-2020 was enacted in 2020, providing a comprehensive methodology for evaluating the susceptibility of various building elements, assessing damage, estimating repair costs and durations, and categorizing the resilience classification of structures [7]. Subsequently, in 2024, the municipality of Beijing advanced this initiative by introducing a local standard dedicated to the evaluation of the seismic resilience and recovery potential of entire residential districts [8]. This development underscores the progressive establishment of a multi-tiered resilience assessment system, which operates from national and municipal levels down to the individual building scale.

To achieve the objective of constructing resilient buildings that facilitate rapid post-earthquake re-occupancy, the development of structural components exhibiting controllable and replaceable damage is imperative. Furthermore, the integration of fuse-like energy-dissipating elements, which localize inelastic deformation within readily replaceable units, is essential. This strategy markedly enhances both functional recoverability and seismic resilience [9,10]. Conventional beam-column joint configurations predominantly rely on on-site welding or hybrid bolted-welded connections, which inherently result in extended construction durations, complicate quality assurance processes, and present significant challenges for post-seismic repair. Post-earthquake investigations from major seismic events have consistently identified these joints as susceptible to brittle weld fractures, panel zone shear failures, localized column buckling, and potentially catastrophic outcomes such as overall structural instability or soft-story collapse [1,2,4,11-12]. In response to these shortcomings, a multitude of innovative steel beam-column connection designs have recently been developed, with a primary focus on augmenting energy dissipation capacity and ensuring the replace ability of damaged components. Specifically, external stiffened flange plate joints, sleeve or coupler connections, through-diaphragm connections, and extended end-plate joints represent prominent areas of current research [13-15]. While the aforementioned connection designs have demonstrated varying degrees of improvement in the seismic energy dissipation performance of beam-column joints, they have yet to comprehensively address the issue of damage to primary structural elements. Moreover, the inherent complexity of specific construction methodologies and the associated potential failure modes necessitate further rigorous evaluation and optimization.

Recent research has increasingly emphasized the development of replaceable or repairable fuse-type beam-column connections. The fundamental principle underlying these joint designs is the deliberate localization of plastic deformation and seismic-induced damage within designated, replaceable energy-dissipating elements, thereby safeguarding primary structural components from catastrophic failure [15-17]. For example, Zhao et al. [18] proposed a replaceable short beam segment fabricated from low-yield-point steel. Cyclic loading tests demonstrated its superior ductility and energy dissipation capacity; following an earthquake, the damaged segment could be expeditiously replaced to restore the joint's full functionality. Zhang et al. [19] developed a prefabricated beam-to-column joint incorporating replaceable U-shaped steel plates. Their investigation indicated that seismic damage was

confined to these plates, maintaining the elastic behavior of the principal beams and columns, while exhibiting excellent energy dissipation characteristics and facilitating post-earthquake repair. Xiong et al. [20] further introduced a replaceable short beam link, supported by both numerical and experimental studies confirming effective plastic deformation localization and enabling rapid component replacement post-seismic events. Although these advancements have enhanced the energy dissipation capabilities and replaceability of joints, significant challenges persist, encompassing complex detailing requirements, stringent assembly procedures, and difficulties associated with component replacement. The absence of standardized manufacturing and maintenance protocols remains a constraint, limiting their practical application. Consequently, there is a critical need for beam-column joint designs that are more straightforward to fabricate, simpler to install, and genuinely conducive to rapid replacement, aiming to surmount these existing limitations.

This study presents an innovative replaceable energy-dissipating joint system, designed to address the identified limitations in current practices. The system integrates a concrete-filled square steel tubular (CFST) column with an H-shaped steel beam, incorporating a standardized slotted channel steel fuse. The energy-dissipating component is fully prefabricated in a factory setting and assembled on-site utilizing high-strength bolts, thereby eliminating the necessity for field welding. This approach not only enhances construction efficiency and quality control but also facilitates the rapid replacement of damaged elements post-seismic events, significantly reducing repair complexity and associated costs. A comprehensive three-dimensional nonlinear finite element model was developed utilizing ABAQUS software to investigate the mechanical behavior of the proposed joint. This model was subjected to monotonic static loading and low-cycle reversed cyclic loading analyses to evaluate critical performance indicators such as load-bearing capacity, ductility, energy dissipation performance, failure mechanisms, and internal force transmission. Simulation results demonstrate that the novel connection enhances structural strength, deformation capacity, and energy dissipation, effectively confining plastic deformation and damage to the replaceable fuse region. This design substantially improves the post-earthquake reparability and reusability of steel frames, presenting a practical and cost-effective solution for resilient design and modular implementation in prefabricated steel structures.

2. Design details

2.1. Joint details and construction procedure

The proposed joint design in this paper represents an innovative approach to connecting CFST with steel beams, integrating a replaceable energy-dissipating channel steel. As depicted in Fig. 1, the assembly comprises a square CFST column, a connecting steel sleeve, a shear connector, ring plates, and an energy-dissipating channel steel, all interfacing with an H-shaped steel beam featuring dog-bone weakened sections. The connection mechanism involves positioning the sleeve on the column with bolts, followed by a welded connection, with initial welding steps including fillet welds at the edges and plug welds at the center of the sleeve. Subsequently, the shear connector and ring plates are welded to the sleeve. Notably, these components can be prefabricated, streamlining the construction process and enhancing overall efficiency.

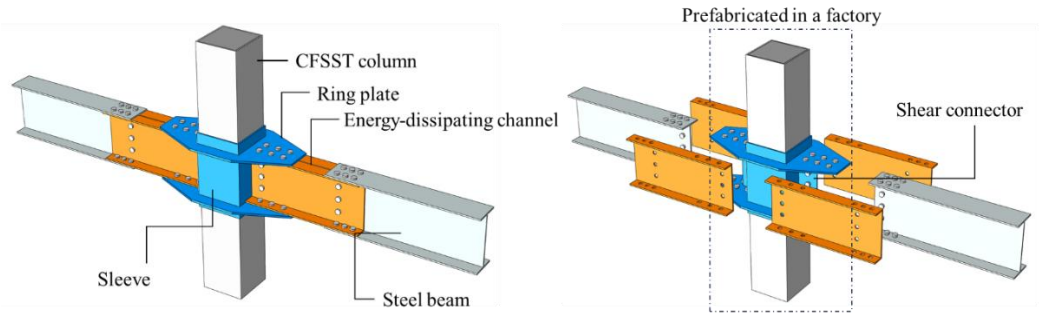


Fig. 1 Schematic diagram of the replaceable energy-dissipating C-shaped steel fuse joint

2.2. The design principle

The design methodology for the novel replaceable energy-dissipating channel steel connection joint parallels the concept of plastic hinge external shift, as depicted in Fig. 2. The bending moment (M) induced by an external load on a steel beam is directly proportional to the distance from the point of application to the beam's end. Assuming a constant cross-section of the steel beam, its bending resistance (Mu) remains constant. Conventionally, the plastic hinge would develop at the location where the ratio of M to Mu is maximum, typically the core area of the connection. The introduction of an outer ring plate enhances the stiffness and load-bearing capacity of the beam section adjacent to the core area, facilitating the relocation of the plastic hinge from the core area to the position of the energy-dissipating channel steel, thereby achieving an external shift of the plastic hinge.

The joint configuration adopted in this design employs a column joint format. The H-beam utilized exhibits dimensions of 300×150×6.5×9 mm, while the square steel tube column measures 250×250×8 mm. High-strength bolts, graded M22 and of the friction-type, are employed for assembly. The concrete specified for this design is of grade C60, with the steel tube composed of Q550 high-strength steel. All other components are fabricated from Q355 ordinary strength steel. Detailed calculations confirm that the beams, columns, and overall design adhere to the "strong column-weak beam" and "strong connection-weak member" principles as outlined in the "Seismic Design Code for Buildings" (GB50011-2010(2016)) [21]. The bolt hole spacing between components is in compliance with the specifications detailed in the "Steel Structure Design Standard" (GB50017-2017) [22]. Comprehensive dimensions for additional components, including gusset plates, channel steel, sleeves, and shear connectors, are provided in Fig. 3.

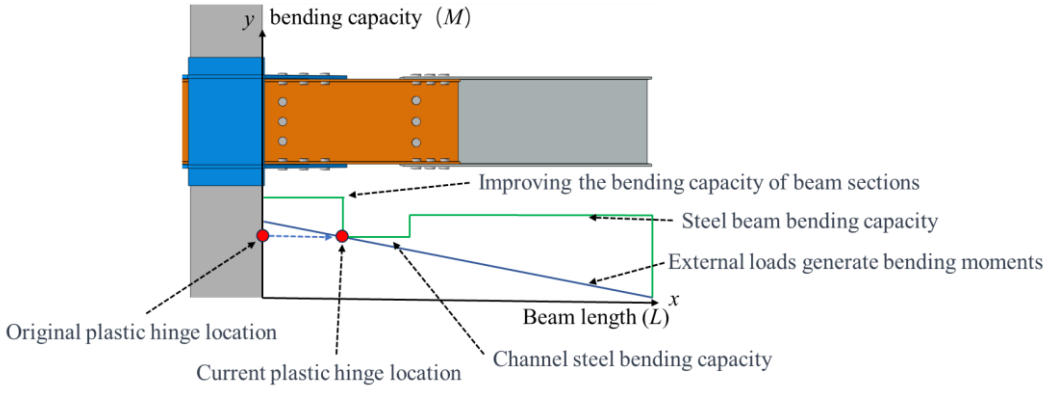


Fig. 2 Schematic of the plastic hinge shift principle

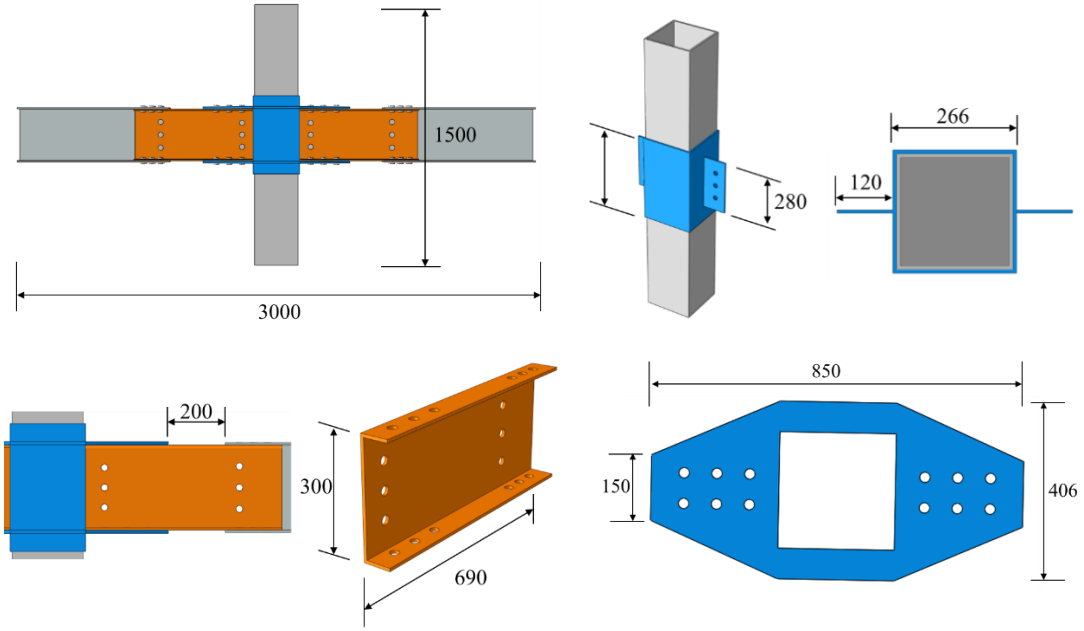


Fig. 3 Detailed dimensions of each component (unit: mm)

3. Finite element analysis

3.1. Material constitutive relationship

The elastic modulus for both the steel and high-strength bolts has been determined to be 2.06 ×105 N/mm2, with a Poisson's ratio of 0.3. The high-strength bolts exhibit a double linear isotropic hardening behavior, as illustrated in Fig. 4. Nominal values are employed for grade 10.9 high-strength bolts. Stiffness reduction factor α was taken as 0.0065, and the corresponding constitutive relationship is presented in Eq. (1).

$$\sigma_s = \begin{cases} E_s\varepsilon_s & \varepsilon_s \le \varepsilon_y \\ \sigma_y + k_1 E_s(\varepsilon_s - \varepsilon_y) & \varepsilon_y \le \varepsilon_s \le \varepsilon_u \\ \sigma_u & \varepsilon_s \ge \varepsilon_u \end{cases} \quad (1)$$

In the provided equation, εy denotes the yield strain, σu signifies the ultimate strength, and εu indicates the ultimate strain. The constitutive model commonly employed for ordinary steel is the one proposed in reference [23], which incorporates both the platform and hardening stages. The detailed constitutive relationship is depicted in Fig. 5 and formulated in Eq. (2).

$$\sigma = \begin{cases} E_s\varepsilon_s & 0 \le \varepsilon \le \varepsilon_e \\ f_p & \varepsilon_e \le \varepsilon \le \varepsilon_{e1} \\ f_p + E_1(\varepsilon - \varepsilon_{e1}) & \varepsilon_{e1} \le \varepsilon \le \varepsilon_{e2} \\ f_y + E_2(\varepsilon - \varepsilon_{e2}) & \varepsilon_{e2} \le \varepsilon \le \varepsilon_{e3} \\ f_u + E_3(\varepsilon - \varepsilon_{e3}) & \varepsilon_{e3} \le \varepsilon \le \varepsilon_u \end{cases} \quad (2)$$

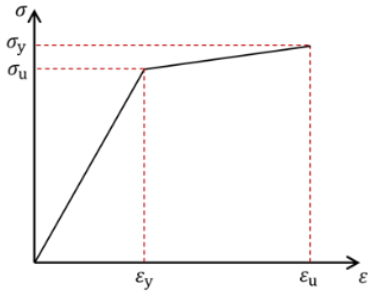


Fig. 4 The constitutive relationship of high-strength bolts

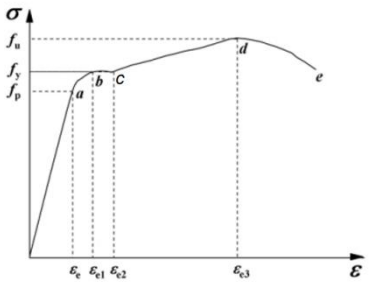


Fig. 5 The constitutive relationship of steel

In the formula, Es、E1、E2 and E3 denote the initial elastic modulus, tangent modulus in the elastic hardening stage, tangent modulus in the plastic hardening stage and tangent modulus in the necking descending stage, respectively; fp、fy and fu represent the yield strength, terminal stress in the elastic hardening stage and terminal stress in the plastic hardening stage, respectively; εe、εe1、εe2 and εe3refer to the yield strain, terminal strain at the end of yield plateau, terminal strain in the elastic hardening stage and terminal strain in the plastic hardening stage, respectively, εe=fp/Es. The mechanical properties of the steel are adopted from the data recommended in reference [24].

The constitutive model for concrete is selected as the plastic damage model. The constitutive curve is shown in Fig. 6. The parameters for the plastic indicators are set as follows: the dilation angle is taken as 38°, the eccentricity is taken as 0.1, the K value is taken as 0.66667, and the ratio of biaxial compressive to uniaxial compressive limit strength. f_b0/f_c0 is taken as 1.16, and the viscosity coefficient is taken as 0.00005.

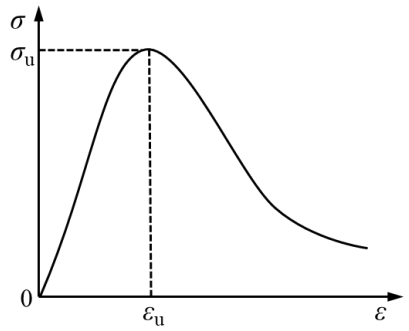


Fig. 6 The constitutive relationship of concrete

3.2. Model establishment

Fig. 7 delineates the boundary conditions, meshing, and contacts in the finite element model. The model incorporates key components such as steel tube, concrete, ring plates, sleeves, shear connectors, steel beams, channel steel, and bolts, all represented by C3D8R solid elements. To counteract the potential hourglass phenomenon in elements with reduced integration, an enhanced hourglass control mechanism is integrated into each element. Shear connectors, ring plates, and sleeves are coupled with steel tubes through Tie constraints. The interfacial interactions, including those between steel tubes and concrete, ring plates and steel beams, and shear connectors and channel steel, are defined by face-to-face contact conditions. In the normal interaction, a "hard contact" approach is employed, whereas the "Coulomb friction model" regulates the tangential interactions. The friction coefficient for the interface between steel tubes and concrete is specified as 0.60, with a coefficient of 0.35 assigned to all other interfaces.

In the structural framework, the mid-column joint is positioned at the inflection point of the beam and column. Consequently, hinged boundary conditions are implemented at the extremities of the column and the beam's loading location. To mitigate the risk of out-of-plane buckling at the joint, additional constraints are enforced within the joint's core area, with U3, UR1, and UR2 set to zero. At the column's apex and terminal points, U2 and UR3 degrees of freedom are allowed. Furthermore, axial loading is applied at the column's top, and reciprocating loading is exerted at the beam's end.

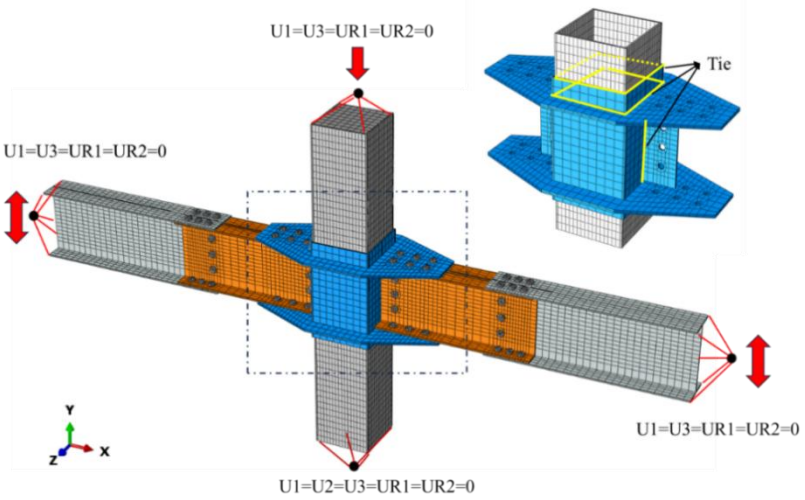


Fig. 7 Meshing and boundary conditions

3.3. Loading procedure

The cyclic loading protocol at the beam ends is formulated in accordance with the specifications outlined in AISC 341-16 [25], as illustrated in Fig. 8. The beams undergo a series of incremental vertical displacements in a reciprocating manner, achieving inter-story drift angles ranging from 0.00375 radians to 0.03 radians. Prior to reaching the 0.01 radian loading level, each displacement level is cycled through six times. At the 0.01 radian level, the cycle is repeated four times, and for subsequent loading levels, each is cycled twice. It is defined that vertical displacements applied in the direction of tensile force, as induced by the MTS, are deemed positive. Conversely, horizontal displacements applied in the direction of compressive force are considered negative.

3.4. Model verification

In order to validate the accuracy of the established finite element model, a simulation analysis was conducted, replicating the experimental procedures reported in references [26] . The joints examined in references exhibit a similar configuration to the one analyzed in this paper, and maintain a high degree of consistency in geometric parameters and material properties. Consequently, to validate the accuracy of the proposed modeling methodology, the selection of elements, mesh division, and boundary conditions for the verification model were consistently applied as described in Section 2.2. Figs. 9 and 10 provide a comparative analysis of the hysteresis curves obtained from the experiments cited in references [26] with the results of the finite element analysis.

The analysis of Figs. 9 and 10 provides substantial evidence that the finite element modeling methodology utilized in this paper exhibits a high level of agreement with the experimental hysteresis and skeleton curves. With respect to failure modes, the model successfully emulates the development of plastic hinges at the beam terminations and the deformation of the connectors at the beam ends. The error between the simulation and the specimen SCBL1-1 is 3.2% in peak load, 5.8% in initial stiffness, and 8.1% in cumulative energy dissipation. For specimen SCBL1-2, the discrepancies are 3.4% in peak load, 6.0% in initial stiffness, and 8.5% in cumulative energy dissipation. Given that the simulation adopts the fully continuous damage mechanics theory, all the above errors fall within an acceptable range. This correlation underscores the precision of the finite element modeling technique adopted in this study, thereby affirming its suitability for subsequent analytical applications.

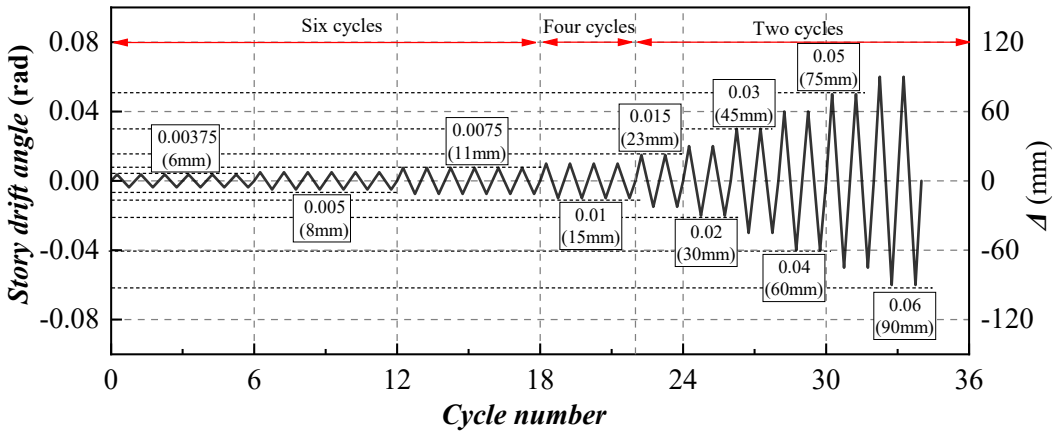


Fig. 8 Loading procedure

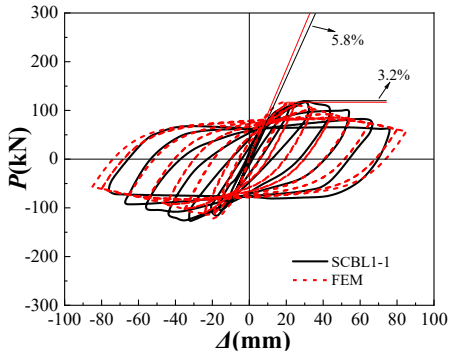


Fig. 9 Comparison with experimental results

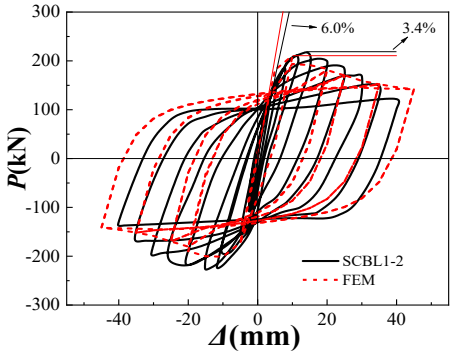


Fig. 10 Comparison with experimental results

4. Finite element analysis results

4.1. Typical member failure mode analysis

Figs. 11(a) and 11(b) illustrate the distribution of equivalent plastic strain and Mises stress as the member is loaded to a 4% interlayer displacement angle. It is evident that the stress and plastic strain are predominantly concentrated in the energy-dissipating section of the replaceable channel steel at the node. This observation confirms that the node effectively achieves the intended objective of controlled damage. Figs. 11(c) to (e) depict the progression of yielding in the flange of the energy-dissipating section of the channel steel at the joint when the beam end rotation angle, θ, reaches 1.5%. As the rotation angle increases to θ = 2%, the plastic deformation in the energy-dissipating section of the channel steel further evolves, culminating in the formation of a substantial plastic hinge section. Ultimately, upon reaching a beam end rotation angle of θ = 4%, the joint's load-bearing capacity diminishes to 85% of its peak value, with the failure mode being characterized by the collapse of the plastic hinge section within the energy-dissipating part of the channel steel.

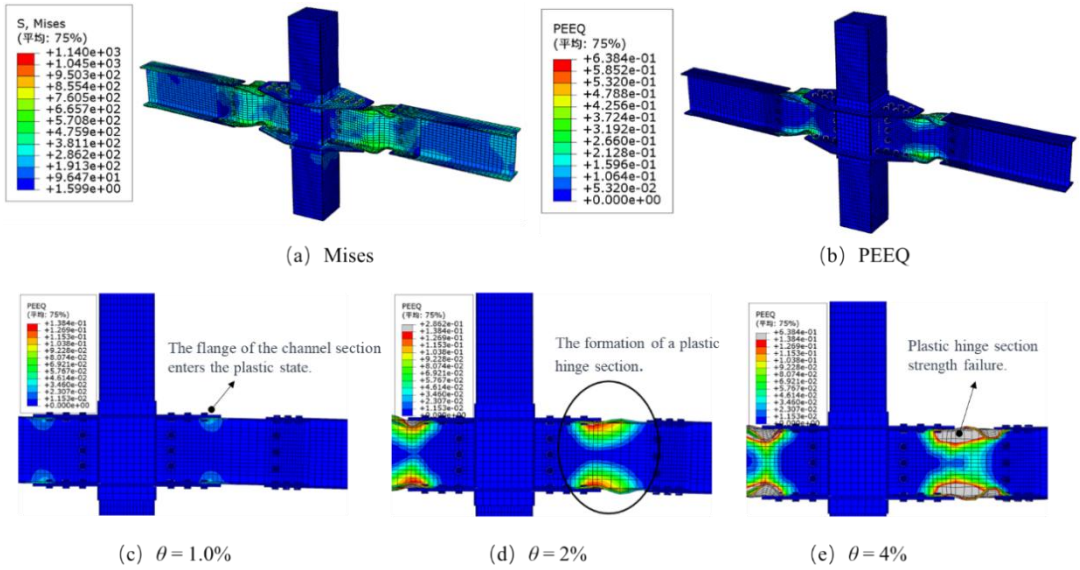


Fig. 11 Typical member failure mode diagram

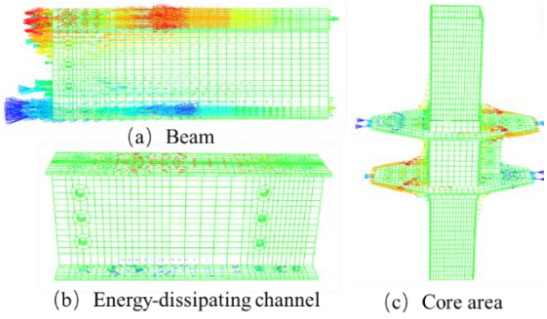


Fig. 12 Tensile and compressive stress transfer path

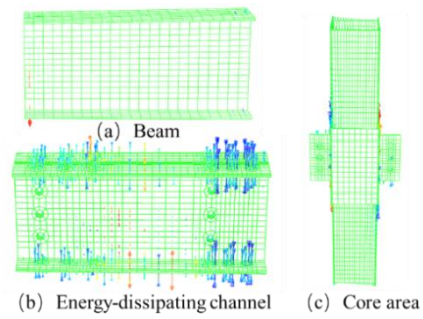


Fig. 13 Shear stress transfer path

4.2. Force transmission mechanism

Fig. 12 delineates the transmission pathway of tensile and compressive stress (S11) at the terminus of the beam. The bending moment at the beam's end is theoretically equivalent to a pair of tensile and compressive forces that are conveyed along the beam's flange. As depicted in the figure, these forces are channeled into the energy-dissipating channel steel via the beam flange. Subsequently, they are conveyed into the outer ring plate through the intermediary of bolts. From the outer ring plate, these forces are further transmitted into the sleeve, ultimately infiltrating the core area.

Fig. 13 provides a schematic representation of the transmission pathway for the vertical shear force (S22) at the beam end. As depicted, the primary route for the vertical shear force is along the beam's web, directed towards the node area. Within this region, the force is transferred to the energy-dissipating steel

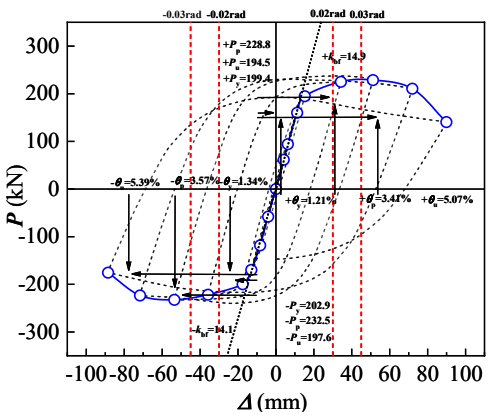
channel via high-strength bolts. These bolts, in turn, convey the force to the shear connectors, which ultimately transmit the force into the sleeves and the core area of the connection. The proposed connection form in this paper is characterized by a straightforward, unambiguous, and dependable force transfer path.

4.3. Hysteresis and skeleton curve

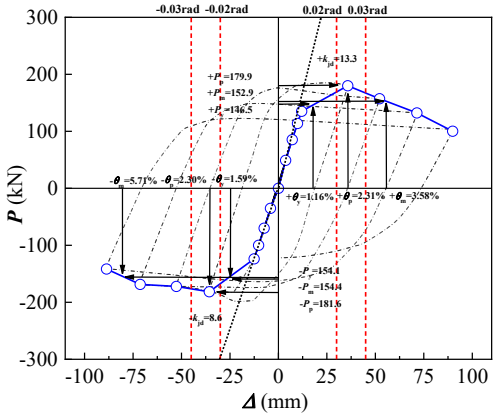
To elucidate the performance attributes of the novel replaceable energy-dissipating steel beam joint, a comparative finite element model was constructed. This model replicates the conventional outer ring plate joint with identical construction dimensions, utilizing the finite element modeling technique outlined in Section 2.2. Through the comparison of hysteresis and envelope curves for this joint, the seismic performance of the proposed innovative joint is subjected to an objective assessment.

Fig. 14(a) depicts the hysteresis curve of the novel replaceable energy-dissipating steel beam joint. Observations from the figure reveal a robust hysteresis loop, signifying a high energy dissipation capacity. Moreover, the area of the hysteresis loop increases under varying loading displacements. Post-peak load, the bearing capacity decays at a relatively slower pace, indicative of the new outer ring cover plate joint's robust plastic deformation capability. Fig. 14(b) presents the hysteresis and envelope curves of a conventional outer ring plate joint, maintaining identical beam, column, and ring plate dimensions. In contrast to the conventional joint, the proposed joint in this study exhibits an initial stiffness that is 32.4% greater, a flexural load-carrying capacity that is 27.2% higher, and an ultimate rotation angle increased by 24.7%. This comparison underscores the superior initial stiffness, flexural load-carrying capacity, and rotational capacity of the proposed replaceable energy-dissipating steel beam joint compared to the conventional outer ring plate joint.

The red dashed lines in the figures denote the specification in the Chinese Seismic Design Code for Buildings (GB50011-2016) [21], stipulating that the plastic inter-story displacement angle of multi-story steel frame structures must not surpass 0.02 radians. It is evident that prior to attaining the 0.02 inter-story displacement angle threshold, the joint's bearing capacity has not yet peaked, signifying a substantial strength reserve. Furthermore, the joint's ultimate rotation angle of 0.053 radians complies with the ductility criteria outlined in the American AISC seismic code, which mandates that the joint rotation angle should not be less than 0.03 radians.



(a) Replaceable energy-dissipating channel joint



(b) Conventional outer ring plate joint

Fig. 14 Hysteresis curve and skeleton curve

4.4. Energy dissipation capacity

The energy dissipation capacity of the joint is quantitatively evaluated by employing the equivalent viscous damping coefficient, as recommended in the Chinese Seismic Design Code for Buildings (GB50010-2016) [21]. The computational diagram for determining the equivalent viscous damping coefficient is depicted in Fig. 15, whereas the corresponding calculation formula is provided in Eq. 3.

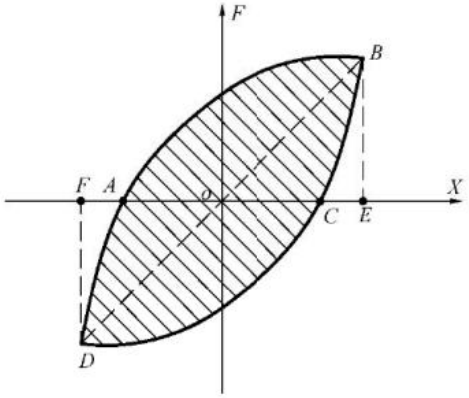


Fig. 15 Calculation diagram of energy dissipation coefficient

$$h_e = E/2\pi \tag{3}$$

$$E = S_{(ABC+CDA)}/S_{(OBE+ODF)} \tag{4}$$

Where: S(ABC + CDA) represents the area of the hysteresis loops under each level of load, which corresponds to the energy dissipated by the node. S(OBE + ODF) represents the area enclosed by the triangles OBE and ODF within one loading cycle.

In Fig. 16, the progression of the equivalent viscous damping coefficient for the joints is depicted. It becomes apparent that upon achieving a drift angle of 1%, the replaceable energy-dissipating channel steel joint exhibits a substantial increase in its energy dissipation capacity. The joint's equivalent viscous damping coefficient maintains an upward trend throughout the entire loading process. At drift angles of 1%, 2%, 3%, and 4%, the recorded equivalent viscous damping coefficients for the replaceable joint are 0.289, 0.403, 0.461, and 0.529, respectively. Conversely, the corresponding coefficients for the conventional outer ring plate joint are 0.045, 0.301, 0.450, and 0.463. The maximum viscous damping coefficient of the replaceable joint is approximately 1.14 times that of the conventional outer ring plate joint, underscoring the exceptional energy dissipation capacity of the proposed replaceable energy-dissipating channel steel connection joint.

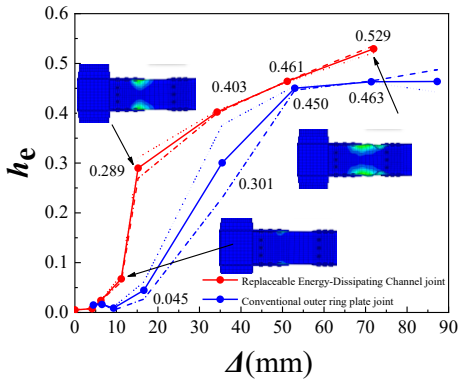


Fig. 16 Variation curves of equivalent viscous damping coefficient

4.5. Beam end rotation

Upon the application of load, a joint undergoes deformations across its various components, with the cumulative impact of these deformations resulting in the total displacement at the load-bearing end. Throughout the loading procedure, the displacement at the joint's beam-loading end can typically be dissected into three primary components: (1) Displacement at the beam-loading end attributable to the beam's intrinsic elastic or inelastic deformation, encompassing bending and shear deformations within the beam's plastic hinge region, as well as in the segments of the beam exterior to this zone. (2) Displacement at the beam-loading end resultant from column deformation, chiefly the bending deformation of the column. (3) Displacement at the beam-loading end induced by deformation in the core region, predominantly the shear deformation of the column in the panel zone, as depicted in Fig. 17.

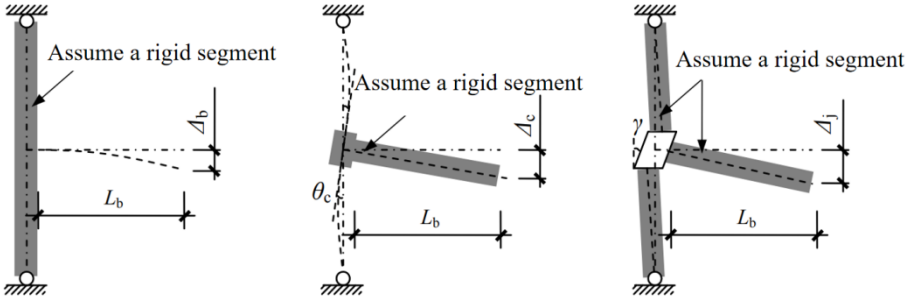


Fig. 17 Joint deformation schematic

The total displacement at the loading end of the beam can be expressed by the following Equation:

$$\Delta = \Delta_b + \Delta_c + \Delta_j \tag{5}$$

Where, Δb represents the displacement at the beam loading end caused by beam deformation, Δc is the displacement caused by column deformation, and Δj is the displacement caused by deformation in the joint core region. It should be noted that in concrete-filled steel tubular (CFST) column to steel beam joints, the core region deformation primarily manifests as macroscopic shear deformation. In addition to the conventional "shear" meaning, this macroscopic shear deformation in the core region actually includes the relative displacement between the beam end and the column wall face. This relative displacement is induced by the lateral compression of the column segment within the core region and the stretching/pulling of the steel tube wall. Since it is difficult to distinguish between the deformations caused by these two mechanisms, Δc and Δj can be obtained using the following method:

$$\Delta_c = \theta_c \times L_b \tag{6}$$

$$\Delta_j = \gamma_j \times L_b \tag{7}$$

Where, θc represents the rotation at the column end, γj is the shear deformation in the core region, and Lb is the length from the beam loading end to the column wall. Subtracting Δc and Δj from the total displacement at the beam loading end gives Δb.

Fig. 18 delineates the rotational composition at the beam-end of a replaceable energy-dissipating channel steel joint. In the absence of plastic deformation within the beam section throughout the entire loading procedure, the rotation induced by Δb is attributed to the plastic deformation of the channel steel. As depicted in the figure, prior to joint yielding, the core region is responsible for approximately 25.5% of the rotation. Post-yielding, the contribution of the core region to rotation decreases swiftly, amounting to roughly 1.2% of the total beam-end rotation. The rotation attributable to the column, ranging from 0.2% to 2.5%, is deemed negligible. The rotation resulting from the plastic deformation of the channel steel constitutes the predominant proportion, reaching approximately 98.6%. These results indicate that the employment of sleeves and high-strength materials enhances the shear stiffness and capacity of the joint panel zone, thereby preserving its near-elastic condition throughout the loading process. With the development of plastic deformation across the cross-section of the energy-dissipating channel steel, the joint manifests an optimal energy dissipation mechanism, where a yielding hinge forms and dissipates energy within the replaceable channel steel.

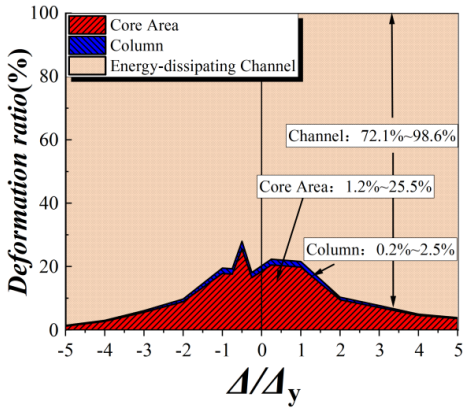


Fig. 18 Deformation ratio

4.6. Residual deformation

As per the FEMA-P58[27] specification in the United States, when the residual inter-story drift angle θr exceeds 0.5%, the structure becomes difficult to repair. The residual drift ratio θr is defined as the ratio of the irrecoverable displacement Δres of the beam-end loading point relative to the column surface to the distance Lb from the loading point to the column surface, after the cyclic loading at the specified load level is completed and the load is unloaded to zero. The calculation formula is shown in Eq. (8). However, for the replaceable energy-dissipating channel steel joint proposed in this study, due to the fact that plastic deformation is concentrated in the energy-dissipating segment of the channel steel and is easy to replace after an earthquake, it is not constrained by this limit. Fig. 19 illustrates the residual deformation of the joint at various loading levels. As shown in the figure, starting from a 2% inter-story drift angle, as the plastic deformation of the channel steel energy-dissipating segment progresses, a plastic hinge section gradually forms, resulting in a significant increase in residual deformation. By the time the joint reaches its ultimate state, the residual deformation is 62 mm, corresponding to θr= 4.1%, which is approximately seven times higher than the residual inter-story drift angle limit for conventional joints. This demonstrates that the replaceable energy-dissipating channel steel joint, with its unique design and energy-dissipating mechanism, exhibits excellent performance under seismic loads. The joint not only has high ductility and strong energy-dissipating capacity but also allows for rapid repair and reuse of the structure by replacing the energy-dissipating segment. Therefore, this joint has significant application value in earthquake engineering, effectively enhancing the seismic performance and reparability of structures while providing a new solution for the swift recovery of buildings after earthquakes.

$$\theta_r = \frac{\Delta_{res}}{L_b} \tag{8}$$

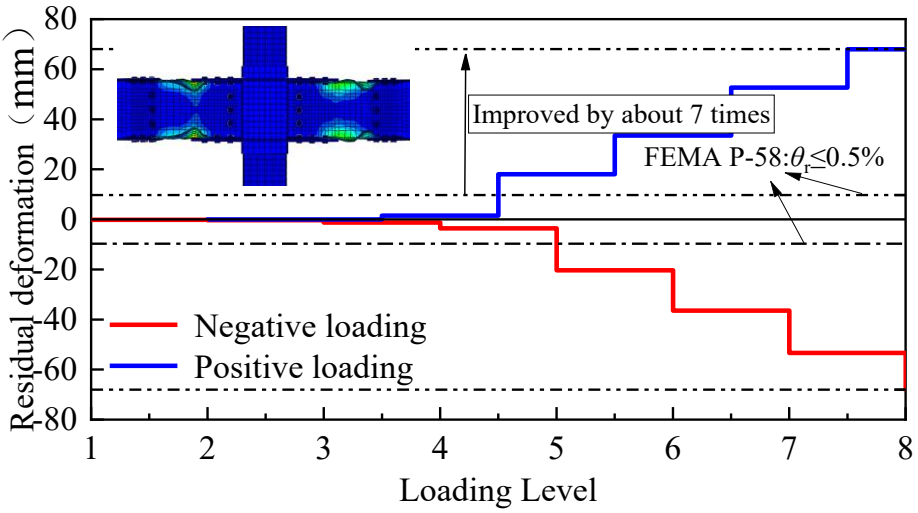


Fig. 19 Residual deformation

4.7. Stiffness determination

This study adopts the European specification EC4[28] for the stiffness classification of replaceable energy-dissipating channel steel joints, with specific classification methods provided in Table 1. The calculation formula for the initial rotational stiffness of the joint is shown in Eq. (9).

$$S_{j,ini} = M_e / \theta_e \tag{9}$$

In the Equation, Me represents the bending moment in the elastic segment of the M-θ curve, and θe represents the corresponding rotation angle.

Table1
Joint stiffness division

Stiffness determination	No lateral displacement structure	Structure with lateral displacement
Rigid	$S_{j,ini} \geq 8\,E_bI_b/L$	$S_{j,ini} \geq 25\,E_bI_b/L$
Semi-rigid	$8\,E_bI_b/L > S_{j,ini} > 0.5E_bI_b/L$	$25\,E_bI_b/L > S_{j,ini} > 0.5E_bI_b/L$
Pinned	$S_{j,ini} \leq 0.5\,E_bI_b/L$	$S_{j,ini} \leq 0.5\,E_bI_b/L$

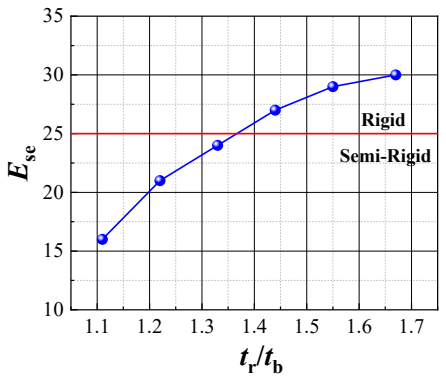
Note: E_bI_b is the flexural rigidity of the steel beam, and L is the length of the steel beam.

A finite element model is applied to conduct a parametric analysis of the stiffness of the proposed replaceable energy-dissipating channel steel joint, with parameters including: the ratio of outer ring plate thickness to beam flange thickness (tr/tb), the ratio of channel steel energy-dissipating segment length to beam height (Lc/hb), the ratio of channel steel thickness to beam flange thickness (tc/tb), and the column-to-beam linear stiffness ratio (k), as detailed in Table 2.

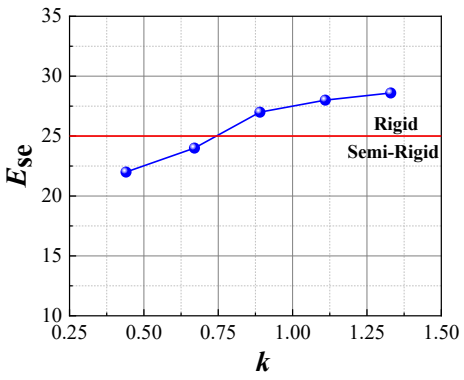
Table 2
Range of parameters on joint stiffness

Parameter Analysis	Parameter Values
t_r/t_b	1.11 1.22 1.33 1.44 1.55 1.67
L_c/h_b	0.33 0.50 0.67 0.83 1.00
t_c/t_b	0.44 0.67 0.89 1.11 1.33
k	0.23, 0.25, 0.31, 0.35, 0.39, 0.43

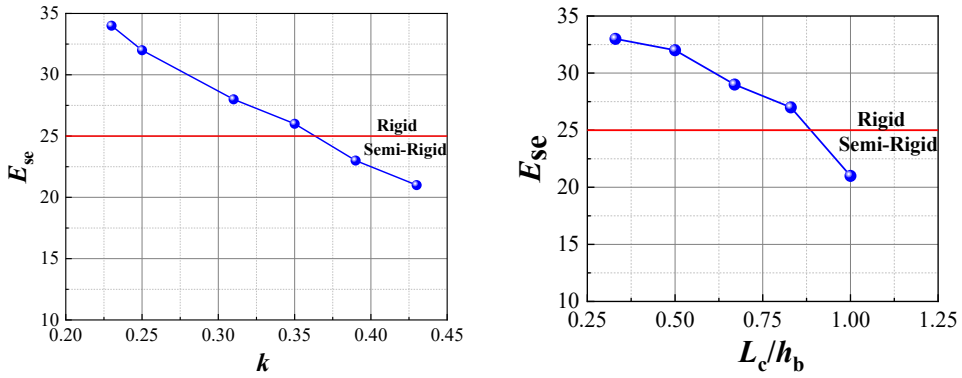
Parameter Analysis and Parameter Values. When the end moment M of the beam reaches 67% of the full-section plastic flexural bearing capacity Mp, the slope of the secant line of the curve represents the stiffness Ese. As shown in Fig. 20, the finite element analysis results for joint stiffness Ese indicate that the ratio of ring plate thickness to beam flange thickness (tr/tb) and the ratio of channel steel thickness to beam flange thickness (tc/tb) are positively correlated with joint stiffness. Conversely, the beam-to-column linear stiffness ratio k and the ratio of channel steel energy dissipation segment length to beam height (Lc/hb) are negatively correlated with joint stiffness. Based on the parameter analysis results, to satisfy the design requirements for replaceable energy dissipating channel steel connections and ensure a rigid joint, the following conditions should be met: the ratio of outer ring plate thickness to beam flange thickness (tr/tb) should not be less than 1.33, the ratio of channel steel thickness to beam flange thickness (tc/tb) should not be less than 0.89, the beam-to-column linear stiffness ratio k should not exceed 0.39, and the ratio of channel steel energy dissipation segment length to beam height (Lc/hb) should not exceed 0.83.



(a) t_r/t_b vs E_{se}



(b) t_c/t_b vs E_{se}



(c) k vs E_{se} (d) L_c/h_b vs E_{se}

Fig. 20 Parametric analysis on joint stiffness

5. Conclusions

In this paper, a novel CFST column to steel beam joint incorporating replaceable energy-dissipating channels is proposed. An extensive overview of the joint's configuration and the underlying design principles is provided. The joint's performance under various conditions, including failure modes, stress distribution, hysteretic behavior, and residual deformation, was evaluated utilizing the ABAQUS finite element analysis software. Furthermore, a comprehensive parametric analysis was carried out to assess the joint's initial stiffness, resulting in a systematic classification of joint types. The key conclusions derived from this study are presented below:

(1) The finite element analysis confirms the efficacy of the load transfer mechanism in the replaceable channel steel connection. Beam-end moments are predominantly conveyed through the channel flanges and ring plates, whereas shear forces are transmitted via the beam and channel webs. The integration of ring plates enhances the joint's flexural capacity by 30%, surpassing conventional designs, and strategically positions the plastic hinge within the energy-dissipating channel section. This is conducive to a controlled failure mode, aligning with damage-control objectives. The joint core, reinforced with high-strength steel and confined high-strength concrete, retains its elasticity, thereby augmenting shear stiffness and capacity. The channel section's progressive plastic deformation facilitates efficient energy dissipation through localized yielding in the intended plastic hinge zone.

(2) The proposed joint design in this study exhibits significant improvements over the conventional outer ring plate joint. It boasts an initial stiffness increase of 32.4%, a flexural load-carrying capacity enhancement of 27.2%, and an ultimate rotation angle increase of 24.7%. These enhancements underscore the superior performance of the proposed replaceable energy-dissipating steel beam joint in terms of initial stiffness, flexural load capacity, and rotational capacity when compared to traditional designs.

(3) In order to fulfill the design specifications for rigid connections in replaceable channel steel beam-column joints, it is advised to maintain the following ratios: the outer ring plate thickness to beam flange thickness (tr/tb) should be at least 1.33, the channel steel thickness to beam flange thickness (tc/tb) should be no less than 0.89, the beam-to-column linear stiffness ratio (k) must not exceed 0.39, and the ratio of the channel steel energy dissipation segment length to beam height (Lc/hb) should be limited to 0.83 or less.

References

[1] National standard of the People's Republic of China. GB50011-2010 Code for seismic design of buildings (2016 Edition) [S]. Beijing: China Construction Industry Press, 2016. (in Chinese)
[2] World Bank, Disaster Risk Management in Sichuan: Lessons from the 2008 Wenchuan Earthquake, World Bank Publications, 2008.
[3] National Reconstruction Authority (Nepal), Post Disaster Recovery Framework 2016-2020: Nepal Earthquake 2015, Kathmandu, Nepal, 2016.
[4] Architectural Institute of Japan, Preliminary Reconnaissance Report of the 2016 Kumamoto Earthquake, AIJ Press, Tokyo, Japan, 2016.
[5] United Nations Development Program (UNDP), Turkey-Syria Earthquake: Post Disaster Needs Assessment, UNDP Report, 2023.
[6] FEMA P 58 1, Seismic Performance Assessment of Buildings, Volume 1 – Methodology (Second Edition), FEMA, Washington, D.C., USA, 2018.
[7] National Standards of the People's Republic of China, GB/T 38591-2020 Evaluation Standard for Seismic Resilience of Buildings, Beijing: China Construction Industry Press, 2020. (In Chinese)
[8] Beijing Earthquake Agency, Technical Standard for Seismic Safety and Resilience Assessment of Urban Communities, Beijing Earthquake Agency Press, Beijing, China, 2024. (In Chinese)
[9] Men J, Li T, Zhou Q, Zhang H, Huang CH. Structural fuse performance and earthquake-resilient performance of beam-column joints with replaceable T-stub. Journal of Constructional Steel Research 2023; 206: 107943. https://doi.org/10.1016/j.jcsr.2023.107943.
[10] Zaker Esteghamati M, Farzampour A. Probabilistic seismic performance and loss evaluation of a multi-story steel building equipped with butterfly-shaped fuses. Journal of Constructional Steel Research 2020;172:106187. https://doi.org/10.1016/j.jcsr.2020.106187.
[11] Stevenson JR, Kachali H, Whitman Z, et al., "Preliminary observations of the impacts the 22 February Christchurch earthquake had on organizations and the economy: A report from the field (22 February–22 March 2011)," Report, New Zealand Society for Earthquake Engineering, Christchurch, New Zealand, 2011.
[12] Applied Technology Council (ATC), ATC-134: Performance of Buildings and Nonstructural Components in the 2017 Puebla-Morelos Earthquake. Redwood City, CA: ATC, 2017.
[13] Zheng XW, Xu S, Hou YZ, Chen R, Wang WM. Seismic performance of beam-to-column joints connected with combined angle steel-sleeve with the influence of beam web openings and slab effects. Structures 2025; 77: 109213. https://doi.org/10.1016/j.istruc.2025.109213.
[14] Ramirez Ortiz C, Areiza Palma G, Gutierrez Amador A, Ramirez Duque J, Cano Buitron R, Gonzales Escobar L. Seismic Behavior of a Steel Beam-to-Concrete-Filled Steel Tubular Column Connection Using External Diaphragms. Applied Sciences 2022; 12: 3618. https://doi.org/10.3390/app12073618.
[15] Ding C, Bai Y, Yang K, Zhang J. Cyclic behaviour of prefabricated connections for steel beam to concrete-filled steel tube column. Journal of Constructional Steel Research 2021; 176: 106422. https://doi.org/10.1016/j.jcsr.2020.106422.
[16] Shen Y, Christopoulos C, Mansour N, Tremblay R. Seismic Design and Performance of Steel Moment-Resisting Frames with Nonlinear Replaceable Links. J Struct Eng 2011; 137: 1107–17. https://doi.org/10.1061/(ASCE)ST.1943-541X.0000359.
[17] Richards PW, Oh SS. Cyclic Behavior of Replaceable Shear Fuse Connections for Steel Moment Frames. J Struct Eng 2019; 145: 04019156. https://doi.org/10.1061/(ASCE)ST.1943-541X.0002412.
[18] Zhao LY, Guo D, Yang YQ, Diao YS, Liu XL. Seismic performance and replaceability of steel frame structures with replaceable beam segments. Advanced Steel Construction 2024, 20(1), 69–80. https://doi.org/10.18057/IJASC.2024.20.1.8.
[19] Zhang X, Zhou B, Gao JD, et al. Numerical investigation on seismic performance of prefabricated steel beam-to-column connection with replaceable U-shaped plate. Advanced Steel Construction, 2024, 20(4), 397–405. https://doi.org/10.18057/IJASC.2024.20.4.7.
[20] Xiong L, Guo Z, Cai J, Jiang K, Li L. Seismic performance of the replaceable steel links with different short length ratios. Sci Rep 2024; 14: 29976. https://doi.org/10.1038/s41598-024-81336-8.
[21] GB50011-2010; Seismic Design Code of Building. China building industry press: Beijing, China, 2016. (In Chinese)
[22] National standard of the people's Republic of China.GB50017-2017 Steel structure design standard[s]. Beijing: China Construction Industry Press,2017. (in Chinese)
[23] Zhou J. Ren J. Feng Y. Tian W. Shi K. A modified parallel-sided shear zone model for determining material constitutive law. Int. J. Adv. Manuf. Technol. 2017, 91, 589–603. https://link.springer.com/article/10.1007/s00170-016-9717-7.
[24] Feng Y. Li W. Seismic performance of SMA-prestressed self-centering beam-column joints: Experimental and numerical study. J. Constr. Steel Res. 2025, 226, 109272. https://doi.org/10.1016/J.JCSR.2024.109272.
[25] American Institute of Steel Construction. ANSl/AISC 341-16 Seismic Provisions for Structural Steel Buildings[s]. chic ago, lllinois: 2016.
[26] Li G, Qiu Z, Yang Z, et al. Seismic performance of high strength concrete filled high strength square steel tubes under cyclic pure bending[J]. Advanced Steel Construction, 2020, 16(2): 112-123.
[27] FEMA P-58-1Seismic pertomance assessment buildings: volume 1-methodology [s].2nd Washington, D. C: Federal Emergency Management Agency, 2018.
[28] Design of composite steel and concrete structures-part1-1:general rules and rules for buildings:EUROCODE 4 (EC4) [S]. CEN:Brussels, Commission of European communities, 2004.

Advanced Steel Construction – Vol. 22 No. 5 (2026) 547–560
DOI:10.18057/IJASC.2026.22.5.6

EXPERIMENTAL AND NUMERICAL STUDY ON THE SEISMIC BEHAVIOUR OF DIFFERENT TYPES OF STRENGTHENED CONNECTIONS WITH SIDE PLATES

Wang Zhang [1, 2], Ai-Chao Lv [2], Qing-Qing Xiong [1, 2, *], Ao-Hua Liu [2] and Ya-Peng Wu [1, 2]

[1] *Key Laboratory of Roads and Railway Engineering Safety Control (Shijiazhuang Tiedao University), Ministry of Education, Shijiazhuang, China*
[2] *School of Civil Engineering, Shijiazhuang Tiedao University, Shijiazhuang, China*
** (Corresponding author: E-mail: xiongqingqing@stdu.edu.cn)*

ABSTRACT

To address the ductile fracture issue in steel beam flanges within traditional strengthened connections with side plates, three innovative connections were proposed and tested under quasi-static conditions. An evaluation of the seismic behaviour of the three novel connections was conducted. Additionally, a parametric analysis was conducted using the finite element model to evaluate how the arc radius of the connecting plates, the thickness of the cover plate and connecting plate, and variations in the extension length of the side plates affect the seismic performance of the specimens. The test results revealed that fracture failure occurred at the arc-expanded position near the side plates of Specimen NSP-1, which featured arc-expanded cover plates. In contrast, Specimens NSP-2 and NSP-3, which lacked arc-expanded cover plates, experienced failure at plastic hinges within the beam segments. Comparison of the test results revealed that Specimen NSP-3, which featured a strengthened connection with flush beam-flanged side plates, exhibited the best overall performance. The results of the finite element analysis indicated that, after increasing the radius of the arc of the connecting plate, a plastic hinge formed on the connecting plate, and a fracture occurred at the joint between the side plate and the connecting plate. Selecting appropriate thicknesses for the cover plate and connecting plate can improve the bearing capacity and initial stiffness. Additionally, the extension length of the side plates significantly affected the form of the plastic hinge.

ARTICLE HISTORY

Received: 1 July 2025
Revised: 29 January 2026
Accepted: 6 February 2026

KEYWORDS

CFST column;
Quasi-static tests;
Finite element analysis;
Beam-column joint;
Novel strengthened connection with side plates

Copyright © 2026 by The Hong Kong Institute of Steel Construction. All rights reserved.

1. Introduction

In recent years, concrete-filled steel tubular (CFST) members have gained widespread use in structural engineering because of the confining effect of steel tubes on concrete, as well as concrete's ability to delay the buckling of the steel tubes [1]. Rectangular concrete-filled steel tube (R-CFST) members offer the benefits of easy connection with beams and no indoor convex angle, and are commonly used in prefabricated multi-storey and high-rise buildings. During an earthquake, beam-column joints are subjected to shear forces, axial forces, and bending moments, making them vulnerable to damage. This damage affects the safety of the building. Therefore, the reliability of beam-column joints is crucial to the entire structure.

In the R-CFST structural system, the commonly used rigid and semi-rigid connection types include external-diaphragm connection [2-4], inner-diaphragm connection [5-6], diaphragm-through connection [7-8], and end-plate connections [9-10]. For example, Tong et al. [4] experimentally analysed the performance of beam-column joints with external-diaphragm connections. The experimental findings confirmed that employing small external diaphragms beyond the design code limits was feasible. Qin et al. [5] proposed and tested a novel inner-diaphragm connection. The findings showed that the connection exhibited good hysteretic behaviour and appropriate strength and stiffness, making it suitable for use in medium moment frames. Cho et al. [8] designed a cruciform diaphragm-through connection. Experimental studies showed that a thinner penetration plate can reduce beam flange stress and delay failure. Qu et al. [9] proposed a fully assembled end-plate connection and investigated its seismic performance. The research demonstrated that thicker plates significantly increase structural stiffness

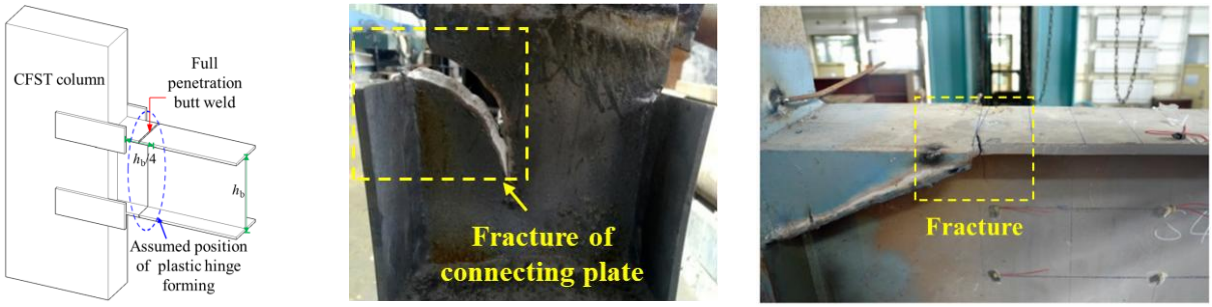
In addition to the aforementioned connection forms, the strengthened connection with the side plate is particularly suitable for residential steel structures. It changes the outer ring plate of the external-diaphragm connection on both sides in one direction to the vertical plate on the column wall. This connection form allows a portion of the beam's bending moment to be transferred directly to the column web through the side plates, addressing the issue of convex angles indoors. As a result, this connection form has been widely adopted across numerous new prefabricated steel structural building systems. However, Zhang et al. [11] conducted tests on the connections between L-shaped columns and H-beams, and a ductile failure mode manifested in the beam flange near the side plates. Zhang et al. [12] tested a strengthened side-plate connection with an arc transition. The results showed that ductile fracture also occurred in the arc transition section near the side plate.

To address ductile fracture at the ends of the side plates in traditional strengthened side-plate connections, researchers have optimized the joint structure to enhance performance. Kiamanesh et al. [13] proposed replacing the full-penetration butt welds with fillet welds to mitigate ductile fracture in the flange of the side-plate connection. The use of fillet welds is essentially a form of plate connection that involves lapping. The lapped portion increases the sectional modulus, which can move the plastic hinge outward. Ma et al. [14] replaced the rectangular side plates with trapezoidal ones and conducted experimental research; however, fracture damage still occurred at the ends of the side plates. Meanwhile, Zhang et al. [15] found that the fracture failure probability of beam flanges can be substantially reduced by using thicker connecting plates.

Despite numerous studies by scholars on strengthened connections with side plates to prevent ductile fracture failure in steel beams, the effectiveness of these methods remains unclear. Therefore, to solve this type of problem, according to the research by Kiamanesh et al.[13], the full-penetration butt welds at the beam flanges were converted to fillet welds by using cover plates and connecting plates (Fig. 1) and the outward movement of the plastic hinge is realized. The steel beam flanges are connected to the cover plates using fillet welds. The cover plates are 200 mm wide, while the steel beam flanges are 150 mm. In this case, the four-sided fillet weld connection between the steel beam and the cover plate can be completed in the factory. For on-site assembly, after the steel beam with the cover plates is transported to the construction site and hoisted into place, the steel beam web and the shear plate are first secured with temporary bolts. Once the connecting plate, which has been welded to the column flange, and the cover plate are connected by full-penetration butt welds, the temporary bolts are replaced with high-strength bolts, thereby completing the beam-column connection. Although there are also full-penetration butt welds here, they are not located in the plastic hinge zone. Therefore, the ductile fracture failure caused by the residual stress of the butt welds does not need to be considered. In the above innovative connection, because the connecting plate has the same width as the cover plate, the question of how to connect the connecting plates, the side plates, and the column flange has become a key problem that needs to be solved. Therefore, three different types of strengthened side-plate connection types were proposed, which were the connection with an arc-expanded connecting plate (AECP connection), the connection with slotted side-plates (SSP connection), and the connection with flush beam-flanged side plates (FBFSP connection), as shown in Fig. 2.

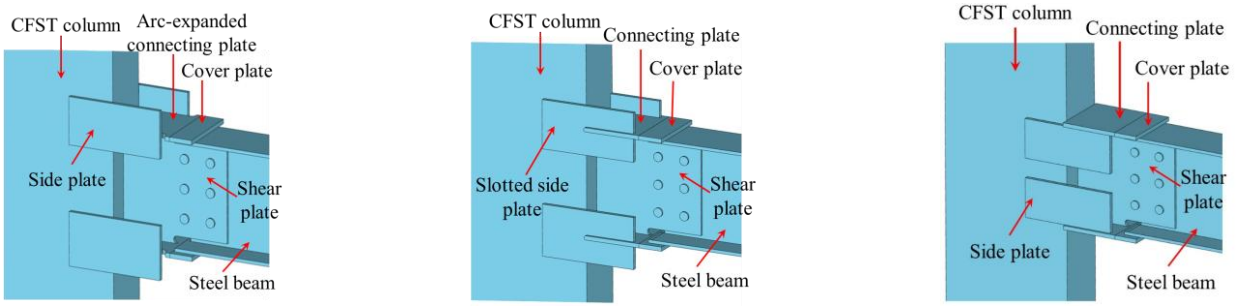
In the AECP connection scheme, the arc-expanded connecting plate is connected to the cover plate by a full-penetration butt weld. In the side-plate connection zone, the traditional side-plate reinforcement structure is retained. Therefore, the arc transition is adopted to reduce the connecting plate's width from 200 mm to 150 mm. In the SSP connection scheme, slots are cut in the side plates, and the connecting plates pass through them. The side plates and connecting plates are connected by full-penetration butt welds. In the FBFSP connection scheme, all side plates are moved towards the centre of the beam depth, so they are flush with the steel beam flanges, and the connecting plates and side plates are connected by full penetration butt welds. However, under this arrangement, the side plates become tension-bending and compression-bending components, which is slightly different from the previous two schemes.

In this study, three full-scale T-type joint specimens were designed, and cyclic loading tests were performed. The analysis included typical failure modes, hysteresis curves, skeleton curves, ductility, and other seismic performance indices. Based on experimental analysis, the performance evaluation of different side-plate connections was conducted. Finally, finite element models were constructed to analyse the influence of the radius of the arc of the connecting plate, the thickness of the cover plates and connecting plates, and the extension length of the side plates. The research findings will provide valuable data to support the development of the novel strengthened side-plate connection in prefabricated steel structures.



(a) Joint schematic diagram (b) Failure mode in reference [11] (c) Failure mode in reference [14]

Fig. 1 Failure of traditional side-plate reinforced connections



(a) AECP connection (b) SSP connection (c) FBFSP connection

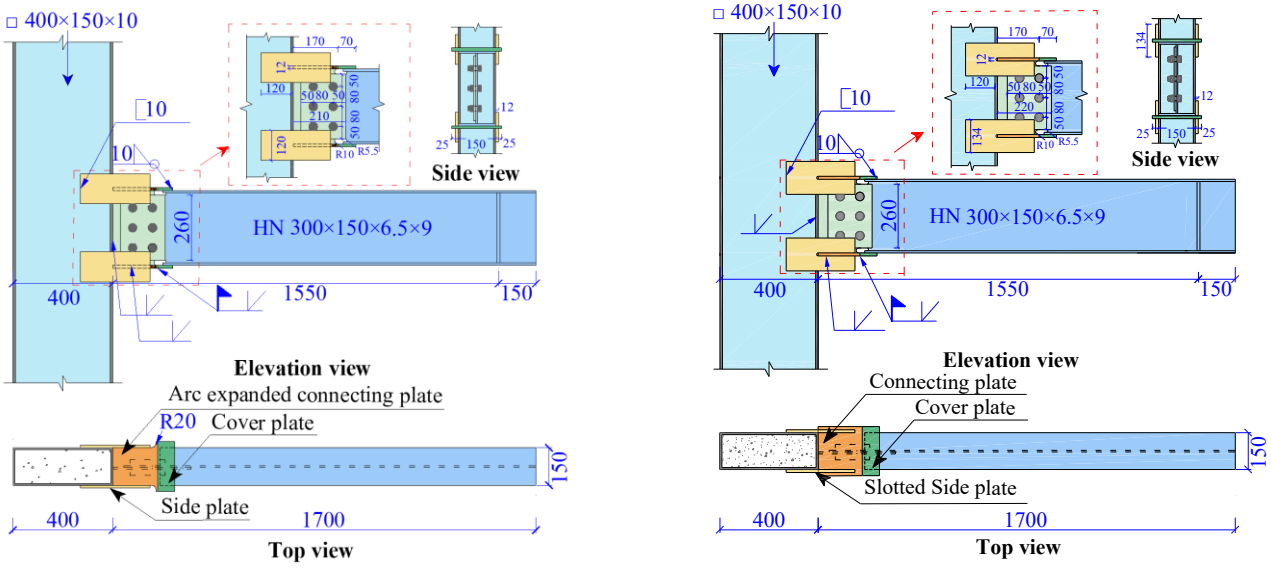
Fig. 2 Details of beam-column joints with strengthened side-plate connections

2. Experimental program

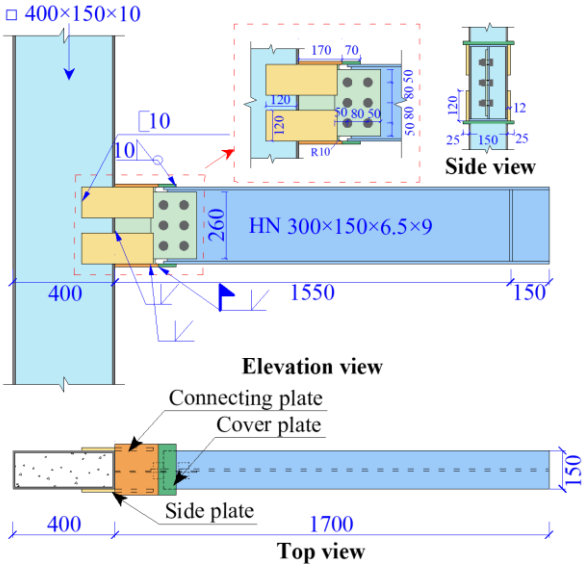
2.1. Dimensions and material properties

To study the seismic capacity of strengthened connections with side plates, three full-scale T-shaped beam-column joints were fabricated and subjected to quasi-static loading tests. The R-CFST columns measured 3000 mm in height, spanning from the ear plate's hole centre at the base to the top horizontal rod restraint position. The beam extended 1500 mm from the column flange to the loading point. Six M24 high-strength bolts were employed to connect the beam web to the shear plate. Detailed information is shown in Table 1 and Fig. 3. The arc radius in Specimen NSP-1 was set to 20 mm to ensure that the bending moment values at the connecting plate positions were the same when comparing the other specimens in the test. In all specimens, the connecting and cover plates, the side plates and the connecting plates were connected by full-penetration butt welds.

The specimens were made of Q355B steel. Samples extracted from steel plates of varying thickness were tested under axial tensile loading, as specified in standard GB/T 228.1 [16]. The results of the tensile test are shown in Table 2. According to standard GB 50010 [17], three 150 mm cubic concrete samples were cast concurrently. After undergoing the same curing conditions, the average compressive strength of the concrete cube samples was 50.3 MPa.



(a) Specimen NSP-1 (b) Specimen NSP-2



(c) Specimen NSP-3

Fig. 3 The detailed information of specimens (units: mm)

Table 1
Parameters of specimens (unit: mm)

Specimen No.	Connection type	Beam	Side plate	Connecting plate		Cover plate
				Dimension	Arc transition	
NSP-1	AECP	H300×150×6.5×9	120×280×12	150×170×12	Yes/r=20	200×70×12
NSP-2	SSP		134×280×12	200×170×12	No	
NSP-3	FBFSP		120×280×12	200×170×12	No	

Table 2
Tensile test results

Type	t	f_y	f_u	δ	ε_y	E
	mm	MPa	MPa	%	10^{-3}	MPa
Beam web	6.5	429.7	571.7	28.5	2.12	202400
Shear plate	8.0	433.3	592.3	23.5	2.10	206300
Beam flange	9.0	383.7	556.7	26.1	1.86	206100
Steel tube	10.0	368.3	512.0	30.8	1.80	204300
Side plate/ Connecting plate/ Cover plate	12.0	387.0	533.7	36.0	1.92	200900

Note: t is the thickness of the steel plate; f_y and f_u are the yield strength and ultimate strength, respectively; δ is the elongation at maximum stress; ε_y is the yield strain; E is the elastic modulus.

2.2. Test setup and instrumentation

The test setup is illustrated in Fig. 4. The specimen comprised a horizontally placed R-CFST column and a vertically arranged beam. At the column's base, an ear plate was hinged to a restraining device. The column was supported at the top by a rigid beam and two vertical rods, creating a one-way hinge condition.

To ensure stability during loading, the steel beam was equipped with lateral restraints placed at 2/3L from the column flange (where L represents the beam length). The beam-end loading scheme was adopted in the test [18]. A hydraulic loading system with a 200-ton capacity was mounted atop the column to apply axial force, and a 50-ton MTS actuator was used to provide cyclic loading. The column was initially subjected to a horizontal force of 1200 kN. The beam end was then subjected to cyclic horizontal loading as outlined in standard JGJ/T 101 [19]. The beam-end cyclic loading was regulated using a load-displacement hybrid control method, as presented in Fig. 5. Before yielding occurred, the beam end underwent load-controlled forces at 20%, 40%, 60%, and 80% of the yield force. Cyclic loading forces were applied, with each cycle repeated once. Displacement control was adopted after yielding and applied using integer multiples of the yield displacement (Δ), considering both positive and negative directions.

During the test loading, primary data were recorded, including horizontal forces and beam-end displacement. The layout of the linear variable displacement transducers (LVDTs) and dial indicators is shown in Fig. 4. Shear deformation in the panel zone was measured using dial indicators D1 and D2, while LVDT D3 measured beam-end displacement, which was then converted to beam-end rotation angle. Additionally, LVDTs D4 and D5 were used to assess the overall in-plane rotation of the specimen, and LVDTs D6 and D7 were employed to calculate the column's rotational angle. Strain gauges were arranged on the flanges and webs of the steel beams at the assumed plastic hinge locations to analyse the plastic development process of the steel beams. Strain gauges were placed at quarter-point positions across the width of the side plates, near the column flanges, to analyse the stress states of the side plates in different specimens.

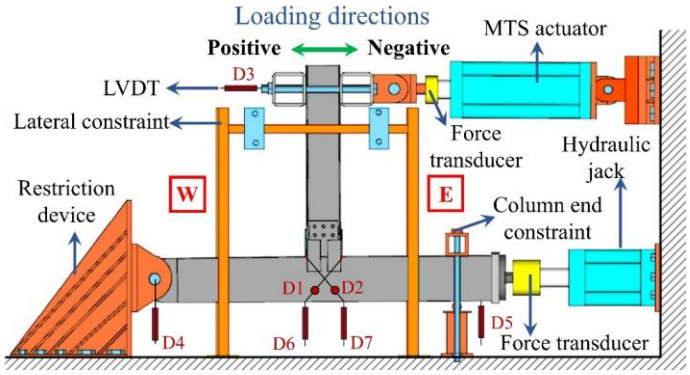


Fig. 4 Test setup

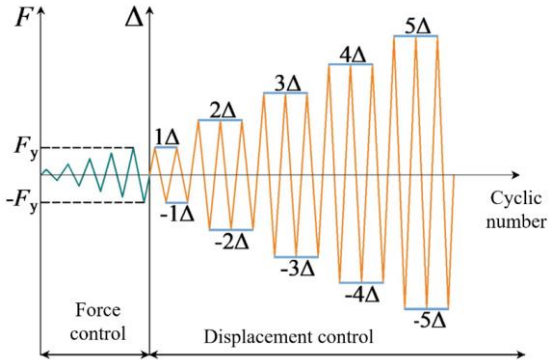
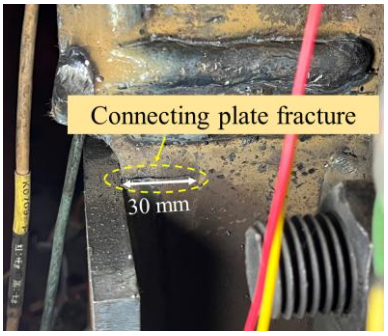


Fig. 5 Loading history

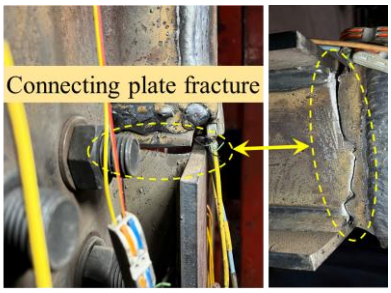
3. Test results

3.1. Failure progression

After three complete cycles at 2Δ (displacement of 24 mm) of a beam-end force applied to Specimen NSP-1, the arc transition of the connecting plate fractured locally, producing a fracture length of about 30 mm, as shown in Fig. 6(a). During the first loading cycle of 3Δ (displacement of 36 mm), the fracture penetrated the connecting plate, resulting in a significant reduction in beam-end force, as shown in Fig. 6(b). Fracture failure occurred at this location. A potential cause was a small arc radius, leading to inadequate resolution of stress concentration issues. Residual stress and welding defects may also have contributed to the fracture. The experimental phenomena observed in Specimens NSP-2 and NSP-3 were consistent. Upon completing the first cycle of 3Δ, with displacements of 30 mm and 36 mm, the compression flange of the steel beam commenced to exhibit minor buckling. Notably, the buckling position of the flange in Specimen NSP-2 was closer to the ends of the cover plates, as shown in Fig. 7(a) and Fig. 8(a). After the second cyclic positive load of 4Δ, with displacements of 40 mm and 48 mm, significant buckling of the west flange was observed, along with continuous buckling in the beam web. Following reverse-direction loading, the steel beam's western flange exhibited an unrecoverable residual deformation. At applied displacements of 6Δ in Specimen NSP-2 and 5Δ in Specimen NSP-3 (60 mm), the compression-side flanges buckled at distances of 60 mm and 90 mm from the end of the cover plate, as illustrated in Fig. 7(b) and Fig. 8(b). The experiment was terminated after the beam-end force was reduced to 85% of its maximum force [20].

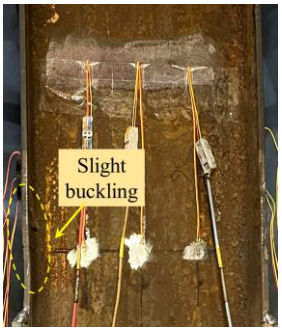


(a) Locally fracture (2Δ)

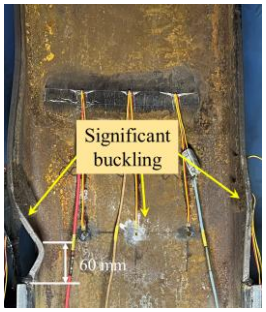


(b) Completely fracture (3Δ)

Fig. 6 Specimen NSP-1

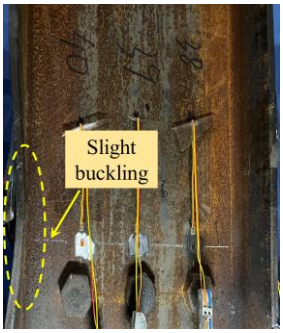


(a) Slight buckling (3Δ)

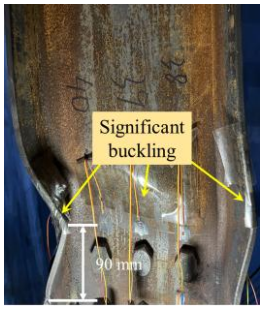


(b) Significant buckling (6Δ)

Fig. 7 Specimen NSP-2



(a) Slight buckling (3Δ)

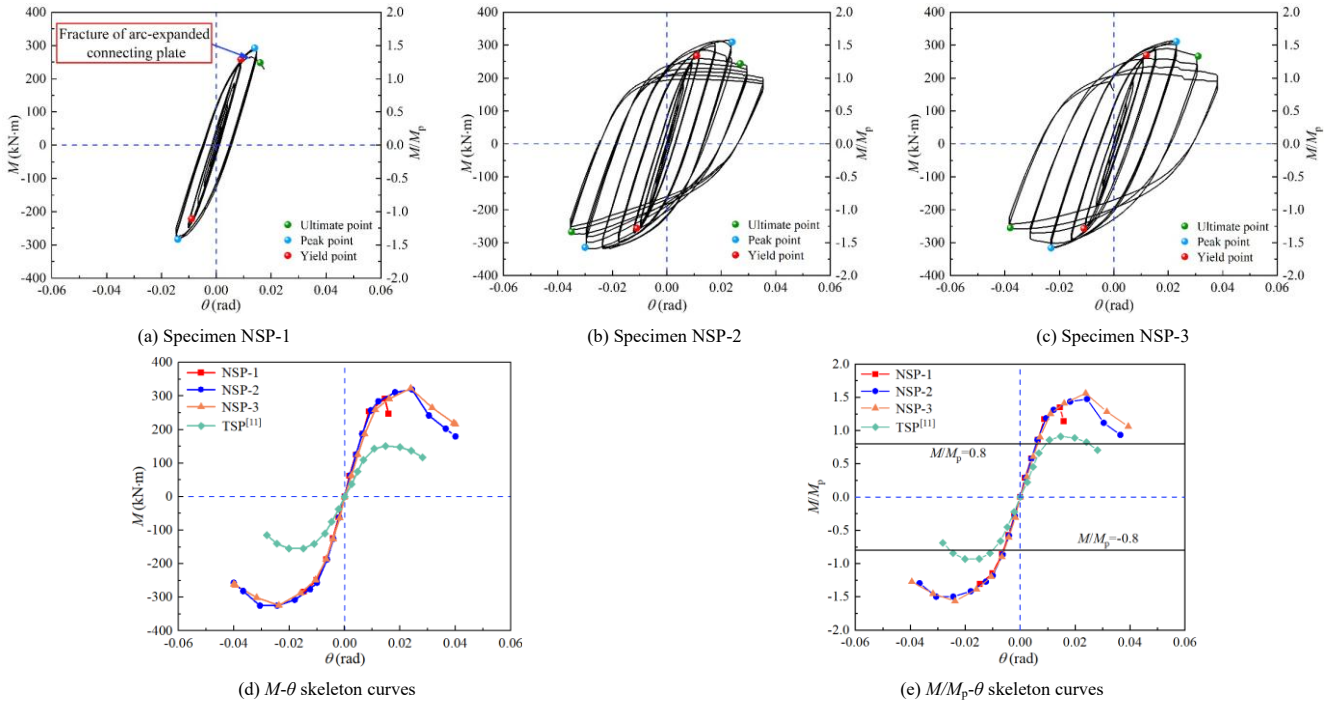


(b) Significant buckling (5Δ)

Fig. 8 Specimen NSP-3

3.2. Moment-rotation curves

Fig. 9 shows the moment-rotation curves of the specimens. The symbol M denotes the bending moment at the column flange, and M_p denotes the beam's full-section plastic moment. The inter-story drift angle (θ) was obtained by dividing the LVDT D3 reading by 1700 mm, the span from the loading position to the column centreline. The calculated full-section plastic moment (M_p) was 206.3 kN·m. Due to severe stress concentration in the arc-expanded connecting plate, Specimen NSP-1 failed prematurely, and the maximum M/M_p reached only 1.303. Specimens NSP-2 and NSP-3 showed good deformability, with hysteretic curves exhibiting a shuttle-shaped pattern. At plastic hinge failure, the maximum M/M_p values were 1.56 and 1.57, respectively. For traditional side-plate-strengthened connections, M/M_p ranges from 0.91 to 1.0 [11].



(a) Specimen NSP-1 (b) Specimen NSP-2 (c) Specimen NSP-3

(d) M-θ skeleton curves (e) M/M_p-θ skeleton curves

Fig. 9 Moment-rotation curves

According to the standard T/CECS 506 [21], the limit value of the column flange bending moment and the full-section plastic moment was given as shown in Eqs. (1)-(3).

$$M = M_{dp} + V_{dp}\left(l_{cp} + h_b/4\right) \tag{1}$$

$$M_{dp} = C_{pr} R_y M_p \tag{2}$$

$$V_{dp} = M_{dp} \Big/ \left(l - l_{cp} - h_b/4\right) \tag{3}$$

where C_{pr} is the steel bearing capacity coefficient, taken as 1.15; R_y is the steel overstrength coefficient, taken as 1.1; The total length comprising the connecting plate and cover plate is defined as l_{cp}, which measures 240 mm; h_b represents the beam depth; V_{dp} and M_{dp} represent the shear force and bending moment at the plastic hinge, respectively.

The ratio of the moment at the position of the column flange to the theoretical full-section plastic moment should satisfy the Eq. (4). The value of M/M_p was calculated as 1.58. Both Specimen NSP-2, featuring a slotted side-plate reinforced connection, and Specimen NSP-3, with a strengthened connection using flush beam-flanged side plates, show significant improvements over traditional strengthened side-plate connections. Furthermore, both specimens meet the requirements outlined in standard T/CECS 506-2018 [21] for strengthened connections, particularly regarding the ratio of column flange moments to the theoretical full-section plastic bending moments.

$$\frac{M}{M_p} \geq C_{pr} R_y \frac{l}{l - \left(l_{cp} + h_b/4\right)} \tag{4}$$

Fig. 9(d) shows the moment-rotation skeleton curves. The yield moment (M_y), yield beam-end rotation (θ_y), peak moment (M_m), peak beam-end rotation (θ_m), ultimate moment (M_u), ultimate beam-end rotation (θ_u), and initial stiffness (K_0) are listed in Table 3. The peak point (θ_m, M_m) is the point of maximum bending moment during loading. The ultimate point (θ_u, M_u) is defined as the point at which the bending moment decreases to less than 85% of the maximum moment resistance [22]. The values of θ_y and M_y were calculated using the energy equivalence method [23-24]. The steps for determining these values are as follows: First, draw a straight line L1 perpendicular to the Y-axis at the peak point B. Next, draw an inclined line from the origin that intersects the skeleton curve at point E and meets line L1 at point A. Verify that A1 (the area bounded by line OE and the skeleton curve) equals A2 (the area bounded by lines EA, AB, and the skeleton curve). Once this condition is met, draw a vertical line L2 from point A down to the X-axis. The intersection of line L2 and the skeleton curve gives point D, which represents the yield point, as illustrated in Fig. 10.

Table 3
Detailed test data (unit: M (kN·m), θ (rad), K_0 (kN·m·rad^{-1}))

Specimen No. & Loading direction		Yield State		Peak State		Ultimate State		K_0
		M_y	θ_y	M_m	θ_m	M_u	θ_u	
NSP-1	+	258.3	0.009	292.0	0.014	248.2	0.016	28140.6
	-	-221.7	-0.009	-283.7	-0.014	-	-	
NSP-2	+	276.6	0.011	319.4	0.025	271.6	0.028	28812.4
	-	-264.5	-0.011	-324.9	-0.031	-276.2	-0.035	
NSP-3	+	278.4	0.012	320.9	0.024	274.8	0.033	26925.4
	-	-265.5	-0.011	-326.8	-0.024	-263.6	-0.038	

The beam-end rotations of the three specimens at the peak state were 0.014, 0.02, and 0.024 rad, respectively. Specimens NSP-2 and NSP-3 met the requirements of standard GB 50011 [17] for inter-story drift in the elastic-plastic stage of steel frame structures, exceeding 1/50. In addition, when the inter-story drift reached 0.04, the flexural bearing capacity of specimens NSP-2 and NSP-3 was greater than $0.8M_p$, thereby meeting the requirements specified for the Special Moment Frame in AISC 341-10 [25].

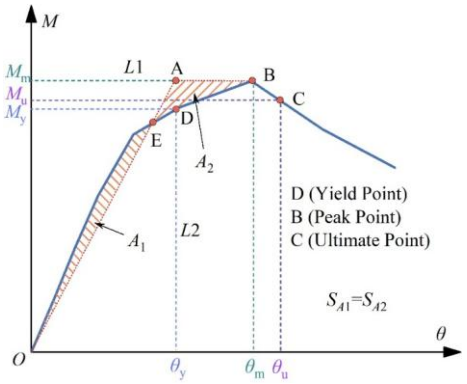


Fig. 10 Calculation method of the yield point

3.3. Ductility and energy dissipation analysis

Ductility coefficients (μ) were used to assess the deformation capacity of the three specimens [26]. They were calculated using the Eq. (5), listed in Table 4.

$$\mu = \frac{\theta_u}{\theta_y} \tag{5}$$

where θ_y and θ_u represent the angles of the beam end at yield and ultimate states, respectively.

Table 4 shows that the deformation capacities of Specimens NSP-1, NSP-2, and NSP-3 were 1.67, 2.92, and 3.03, respectively. The ductile fracture of Specimen NSP-1 occurred prematurely due to stress concentration at the curved transition zone, which limited the development of ductility. The ductility coefficients of Specimens NSP-2 and NSP-3 exceeded those of the joint specimens with steel beams and L-shaped composite columns [14]. During the early stages of loading, Specimen NSP-2 was slightly lower than that of the traditional side-plate strengthened joint, because the traditional joint could dissipate energy through fracture.

The energy dissipation capability of joint specimens can be characterized by the equivalent viscous damping coefficient (h_e), as shown in Eq. (6). The Fig. 11 presents the relationship between h_e values and beam-end rotation angles (θ). Table 4 shows the specimen's h_e under peak conditions. The h_e of Specimen NSP-2 with the slotted strengthened side-plate connection, and Specimen NSP-3 with the strengthened flush beam-flanged side-plate connection, improved significantly compared with the traditional strengthened connection with side plates [11].

$$h_e = \frac{1}{2\pi}\frac{S_{DEBF}}{S_{\Delta AOB} + S_{\Delta COD}} \tag{6}$$

where S_{DEBF}、$S_{\Delta AOB}$、$S_{\Delta COD}$ are the areas of the shapes DEBF、ΔAOB and ΔCOD in Fig. 12.

Table 4
Ductility and energy dissipation coefficient

Specimen No.	μ		$\bar{\mu}$	h_e					
	+	-		Δ	2Δ	3Δ	4Δ	5Δ	6Δ
NSP-1	1.67	-	1.67	0.073	0.190	-	-	-	-
NSP-2	2.46	3.18	2.82	0.081	0.129	0.239	0.309	0.362	0.394
NSP-3	2.67	3.45	3.06	0.105	0.191	0.276	0.377	0.416	-

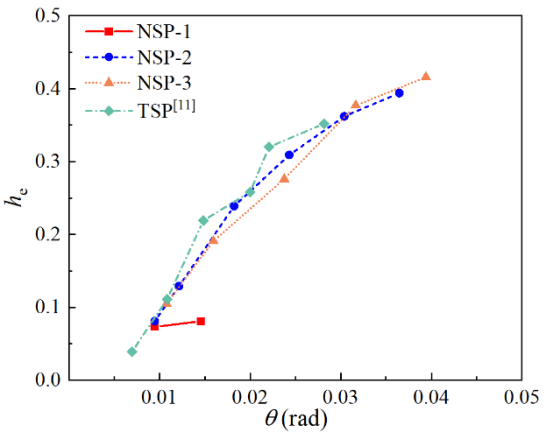


Fig. 11 The h_e-θ curves

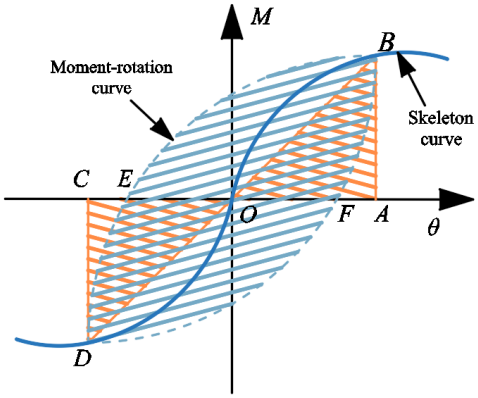


Fig. 12 Idealized hysteretic loop

3.4. Strength and stiffness

The strength degradation coefficient (λ_j) is a quantitative measure of the loss of specimens' load-bearing capacity, and can be calculated using Eq. (7).

$$\lambda_j = \frac{M_j^n}{M_j^1} \tag{7}$$

where n is the cycle frequency at the jth displacement level; M_j^n is the bending moment at the nth cycle under the jth displacement level; M_j^1 is the maximum moment at the first displacement level.

Fig. 13 shows the trend of the beam-end strength degradation coefficient after the specimen reaches its yield point. The value of λ_j for Specimen NSP-1 ranged from 0.95 to 1.06; for Specimen NSP-2, from 0.88 to 1.10; and for Specimen NSP-3, from 0.90 to 1.04. Specimen NSP-1 fractured prematurely due to stress concentration at the arc-expanded cover plates, leaving no further data being available for that specimen. After reaching the ultimate point, the strength-degradation curve of Specimen NSP-3 decreased at a slower rate overall, indicating better stability in its performance.

The parameter ξ_j, indicative of stiffness degradation, is mathematically represented as K_j divided by K_0, where K_j denotes the average loop stiffness and K_0 signifies the initial stiffness for each loading stage. The calculation method is delineated in Eqs. (8)-(10).

$$\xi_j = \frac{K_j}{K_0} \tag{8}$$

$$K_j = \frac{\sum_{i=1}^{n} K_j^i}{n} \tag{9}$$

$$K_j^i = \frac{|+M_j^i| + |-M_j^i|}{|+\theta_j^i| + |-\theta_j^i|} \tag{10}$$

where K_j^i denotes the hysteretic stiffness during the ith repetition at displacement level j; n denotes the total number of cycles at displacement level j; The peak flexural capacities achieved during positive ($+M_j^i$) and negative ($-M_j^i$) cyclic loading are recorded for each cycle i at level j, along with the corresponding maximum beam-end rotation angles ($+\theta_j^i$ and $-\theta_j^i$) for each loading direction.

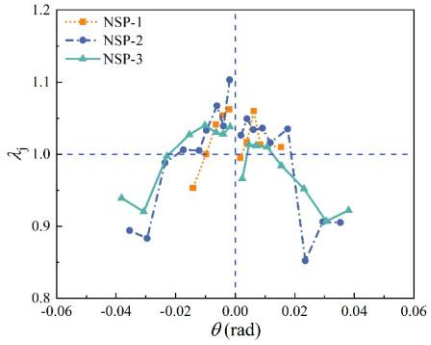


Fig. 13 Strength degradation

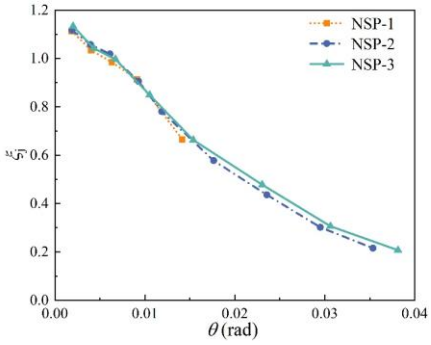


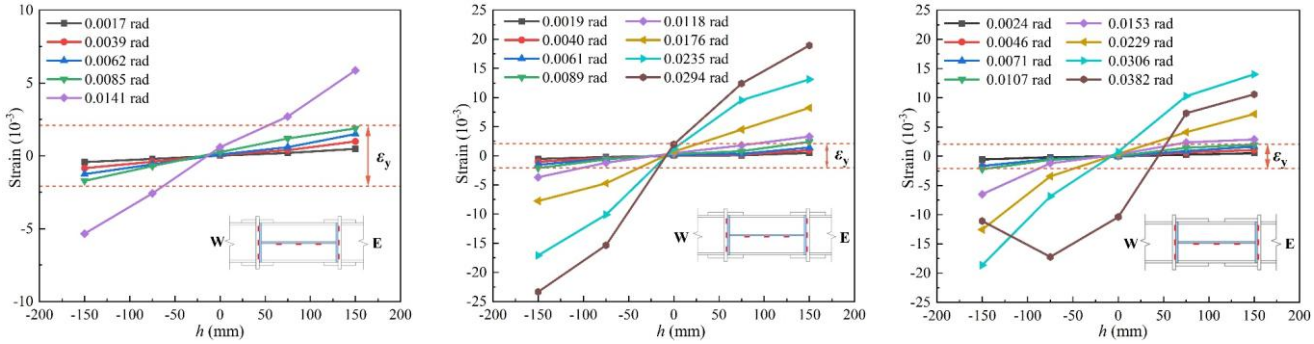
Fig. 14 Stiffness degradation

Fig. 14 shows the stiffness curves for each specimen. The stiffness-degradation patterns of Specimens NSP-2 and NSP-3 were generally similar. However, Specimen NSP-3 exhibited a slightly higher stiffness-degradation coefficient than Specimen NSP-2. The degradation in Specimen NSP-2 was more gradual, indicating that it retained greater stiffness during the post-yield phase. This characteristic is more advantageous for seismic performance.

3.5. Strain analysis

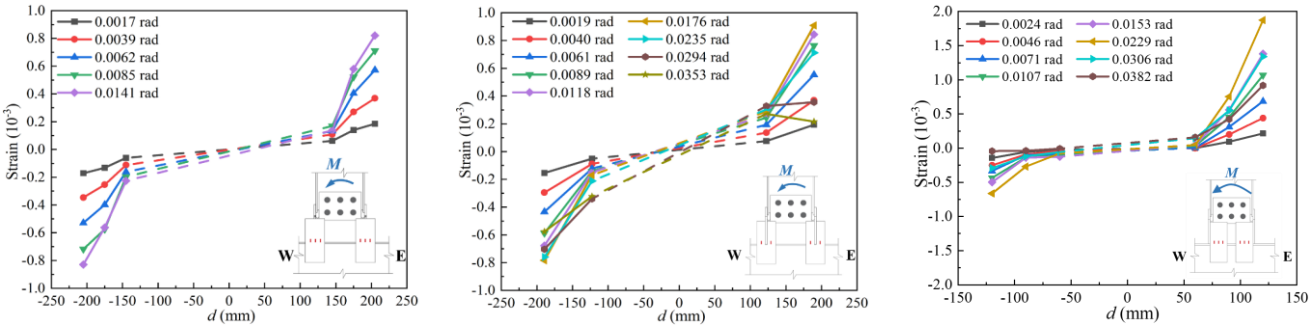
Fig. 15 shows the strain distribution of the beam section where plastic hinge failure occurred. Here, h denotes the vertical offset between the strain measurement location and the beam web's central axis. As shown in Fig. 15, the strain varies linearly across the beam depth. Specimen NSP-1 exhibited plasticity in the upper and lower quarters of the web at a beam-end rotation angle of 0.0141 rad, while the centre section remains elastic. At a beam-end rotation angle of 0.0294 rad, the strain at the centre of the web of Specimen NSP-2 exceeded the yield strain, initiating yielding across the entire cross-section. For Specimen NSP-3, the centre of the web did not yield at 0.0306 rad, but the specimen entered the full-section yield state when the angle reached 0.0382 rad. The reason for this result may be related to the stiffness of the connections.

Fig. 16 shows the strain distribution in the side plates of the specimens, with d denoting the distance between the strain measurement points on the top and bottom side plates, measured relative to the central axis of the beam depth. The figure shows that the strain evolution in the east- and west-side plates of each specimen exhibited opposing trends under applied loading. Additionally, the strain values for Specimens NSP-1 and NSP-2 on the east- and west-side plates were essentially symmetrical. However, the patterns of strain evolution were non-uniform across identical side plate specimens. Specifically, strain development was greater in areas farther from the panel zone and smaller closer to it. The strain values of the compressive and tensile side plates in Specimen NSP-3 showed significant differences. Strain developed much more weakly in the compressive side plate than in the tensile side plate. This discrepancy occurred because the concrete infill within the steel tube helped support the position of the compressive side plate. The column flange absorbed most of the force from the connecting plate. In contrast, the tensile side plate had to provide the required bearing capacity through tension, as the concrete's supporting effect was limited.



(a) Specimen NSP-1 (b) Specimen NSP-2 (c) Specimen NSP-3

Fig. 15 Development of strain distribution of steel beam



(a) Specimen NSP-1 (b) Specimen NSP-2 (c) Specimen NSP-3

Fig. 16 Strain distribution of the side plate

3.6. Beam section rotation angle analysis

In the test, the beam-end angle (θ) can be calculated using Eq. (11). The beam-end angle comprises the specimen's rigid rotation, the steel beam rotation angle (θ_b), the column rotation angle (θ_c), and the shearing rotation angle of the panel zone (θ_{pz}), as shown in Fig. 17. The specimen's rigid rotation can be calculated using the data measured by LVDTs D4 and D5. The values of LVDTs D4 and D5 were essentially zero and can be disregarded. Eq. (12). provides the method for calculating γ under reciprocating force conditions. Through the application of Eqs. (13)-(14), the rotation angle of the beam and column is determined. The relative rotation angle between beam and column can be determined through Eq. (15).

$$\theta = \frac{|\delta_3|}{L} \tag{11}$$

$$\theta_{pz} = \frac{1}{2}(\delta_1 + \delta_2)\frac{\sqrt{a^2+b^2}}{ab} \tag{12}$$

$$\theta_c = \frac{\delta_6 - \delta_7}{h_b} - \theta_{pz} \tag{13}$$

$$\theta_b = \theta - \theta_c - \theta_{pz} \tag{14}$$

$$\theta_{bc} = \theta_b - \theta_c \tag{15}$$

where δ_3 represents the displacement of the beam end as measured by the LVDT D3; L is the distance from the load application point at the beam end to the central axis of the column; δ_1 and δ_2 are the relative displacement of the diagonal points of the panel zone, measured by dial indicators D1 and D2, respectively; LVDTs D6 and D7 provided the displacement readings δ6 and δ7 respectively; h_b is the beam depth; a and b represent the horizontal and vertical dimension of the panel zone, respectively.

The values of θ at the peak state are shown in Table 5. Fig. 18 and Fig. 19 iillustrate the composition of the beam-end rotation angle. At the peak state, the panel zone rotation angle (θ_{pz}), column rotation angle (θ_c), and beam rotation angle (θ_b) of Specimen NSP-2 were 4.4×10^{-4} rad, 2.0×10^{-4} rad and 5.76×10^{-3} rad respectively, exceeding those of Specimen NSP-3. This discrepancy is attributed to the fact that the plastic hinge of Specimen NSP-2 was positioned closer to the cover plate.

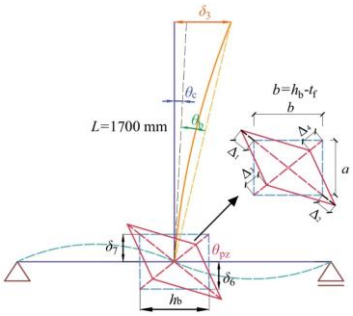


Fig. 17 Deformation of the joint specimen

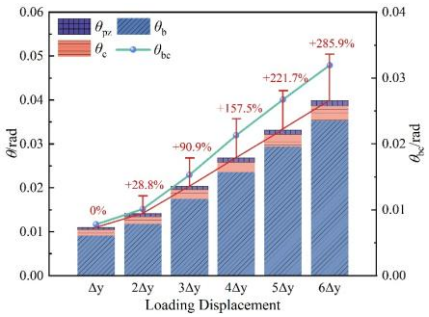


Fig. 18 Contributions of beam-end rotation of Specimen NSP-2

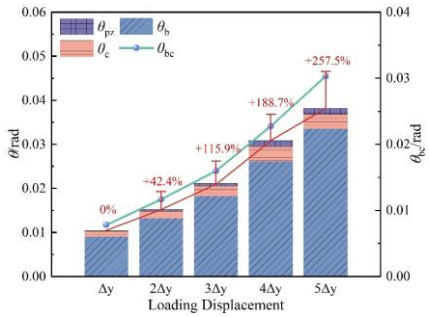


Fig. 19 Contributions of beam-end rotation of Specimen NSP-3

Table 5
Rotation angle of specimens under peak state

Specimen No.	θ/rad	θ_b/rad	θ_c/rad	θ_{pz}/rad
NSP-1	0.01403	0.00103	0.00163	0.00013
NSP-2	0.02650	0.02401	0.00249	0.00104
NSP-3	0.02294	0.01825	0.00229	0.00060

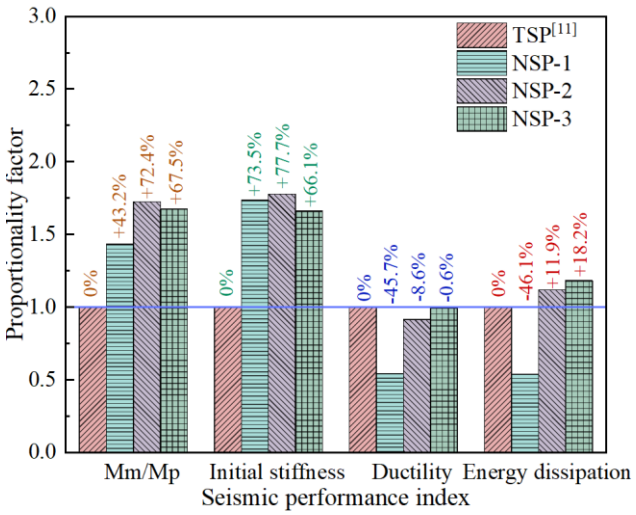


Fig. 20 Joint performance comparison diagram

3.7. Comprehensive performance evaluation

To assess the seismic performance of the three novel connections, a column diagram comparing the specimens was prepared, as shown in Fig. 20. The indicators of seismic performance include the ratio of maximum to full-section plastic moment (M_m/M_p), initial stiffness, ductility, and energy dissipation capacity. Based on experimental data for the traditional side-plate reinforced connection (TSP) referenced in [11], the TSP connection served as the reference specimen, with each parameter set to 1. This standardisation enabled a clearer assessment of the seismic performance parameters.

From the comparison results, it is evident that after normalisation with a TSP connection, the M_m/M_p and initial stiffness of the three specimens with novel side-plate connections are all higher than those of the traditional side-plate-reinforced specimens. In terms of ductility and energy dissipation capacity, Specimen NSP-1 shows the most significant decrease, while Specimen NSP-3 maintains similar ductility and shows an increase in energy dissipation capacity. Overall, the comprehensive performance of Specimen NSP-3 is better than that of the other two specimens with novel side-plate connections.

4. Finite element analysis

4.1. Modelling method and validation

Finite element modelling and experimental simulations were conducted using ABAQUS software. Fig. 21 offers detailed information about the finite element models (FEM). Various components, such as steel tubes, concrete, cover plates, beams, and high-strength bolts, were modelled using solid elements (C3D8R). The surface interaction approach was employed to establish the contact relationship, and a penalty function was utilised for tangential behaviour, with a contact friction coefficient of 0.6 [27] between the steel tube and the concrete. In the interactions between the shear plate and the bolt, the coefficient was assumed to be 0.3 [28], and tie constraints were employed to represent welds. Based on the grid sizes reported in references [29-31], the final mesh size for the steel, concrete, and steel tubes was set as 25 mm. The mesh size of the connecting plate and high-strength bolts was 5 mm. The boundary conditions of the finite element model were consistent with those of the experiment, as shown in Fig. 21.

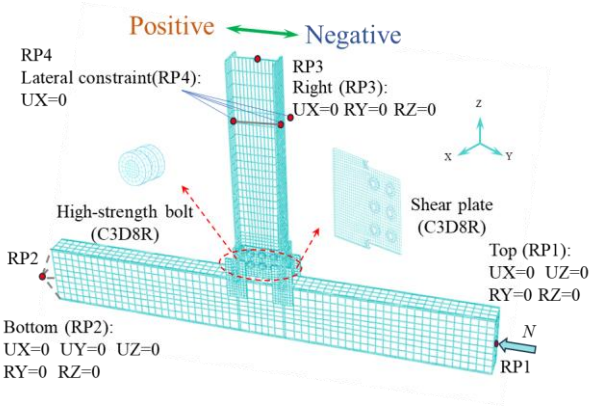


Fig. 21 Details of FEM

The Han's et al. confined concrete was applied to characterize mechanical behavior, as shown in Fig. 22. For concrete under tension, the constitutive relationship follows the formulations proposed by Shen et al. [32]. In the finite element model, the concrete damage plastic (CDP) model was used to simulate the failure behaviour of concrete, as shown in Eqs. (16)-(17).

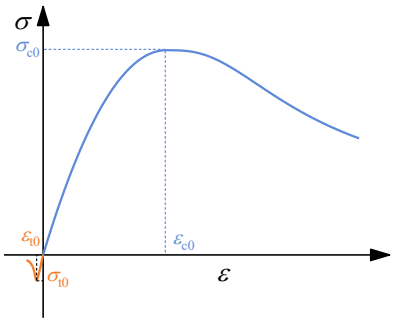


Fig. 22 σ-ε model for confined concrete

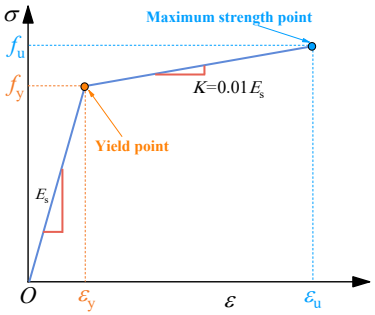


Fig. 24 σ-ε model of high-strength bolts

$$\sigma_s = \begin{cases} E_s\varepsilon & \varepsilon \le \varepsilon_a \\ -A\varepsilon^2 + B\varepsilon + C & \varepsilon_a < \varepsilon \le \varepsilon_b \\ f_y & \varepsilon_b < \varepsilon \le \varepsilon_c \\ f_y\left[1+\left(f_u/f_y\right)\dfrac{\varepsilon-\varepsilon_b}{\varepsilon_c-\varepsilon_d}\right] & \varepsilon_c < \varepsilon \le \varepsilon_d \\ f_u & \varepsilon_d < \varepsilon \end{cases} \tag{18}$$

where ε_a=0.8f_y/E_s; ε_b=1.5ε_a; ε_c=10ε_b; ε_d=25ε_b; A=0.2$f_y/(\varepsilon_b-\varepsilon_a)^2$; B=2$A\varepsilon_b$; C=0.8f_y+$A\varepsilon_a^2$-$B\varepsilon_a$; f_y and f_u represent the yield strength and ultimate strength of the steel in the test, respectively.

$$d_c = 1 - \frac{\sigma_c + 2\sigma_{c0}}{E_c\left[\left(2\sigma_{c0}/E_c\right)+\varepsilon_c\right]} \tag{16}$$

$$d_t = 1 - \frac{\sigma_t + 2\sigma_{t0}}{E_c\left[\left(2\sigma_{t0}/E_c\right)+\varepsilon_t\right]} \tag{17}$$

where d_c and d_t are the compressive and tensile damage parameters of confined concrete, while E_c denotes the elastic modulus of concrete.

Specimen NSP-1 fractured during the loading process. Here, the connecting plate adopted the true stress-strain curve (Fig. 23), and the metal ductile fracture damage was used to simulate the stiffness degradation of elements [34]. The stress-strain curves of other steel components (excluding high-strength bolts) adopted the engineering stress-strain curves, which was simplified into a multi-linear model [35-36], as shown in Fig. 25. The model's mechanical response at different phases is described by Eq. (18). The constitutive model parameters were calculated and listed in Table 6. To simulate the mechanical properties of high-strength bolts, a bilinear model was utilized [37-38], as shown in Fig. 24. A kinematic hardening model was also used for the steel material [39]. The comparison results of the failure modes and M-θ curves are shown in Fig. 26. It can be seen that the failure modes and M-θ curves predicted by this finite element method closely matched those observed in the test.

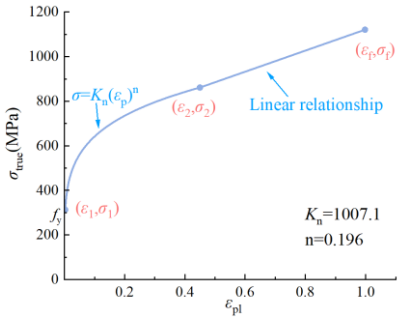


Fig. 23 True σ-ε model of steel [33]

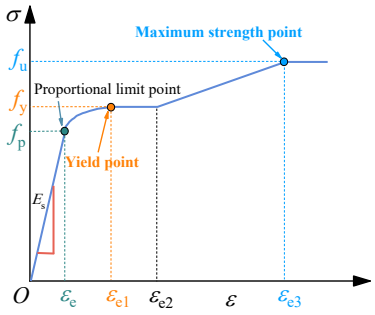
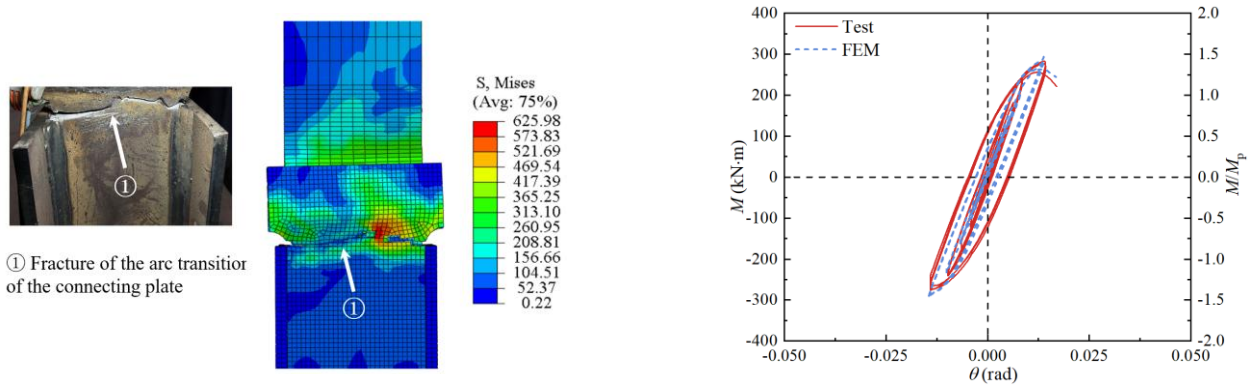


Fig. 25 Multi-linear σ-ε model of steel

Table 6
Calculation results of parameters A, B, C for each plate category

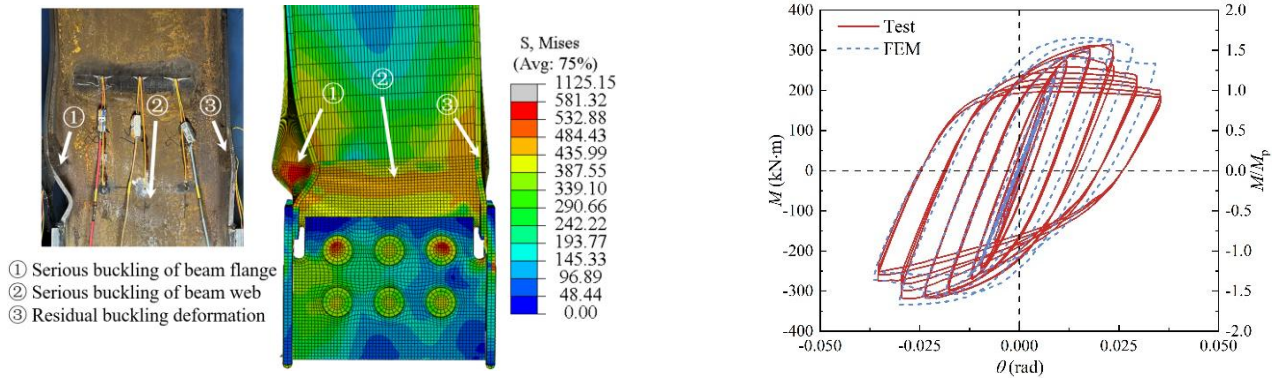
Type	t	f_y	ε_y	A	B	C
	mm	MPa	10^{-3}	$\times10^8$	$\times10^5$	
Beam web	6.5	429.7	2.12	1.235	6.180	-343.8
Shear plate	8.0	433.3	2.10	1.224	6.181	-346.9
Beam flange	9.0	383.7	1.86	1.384	6.184	-307.1
Steel tube	10.0	368.3	1.80	1.440	6.178	-294.4
Side plate/ Connecting plate/ Cover plate	12.0	387.0	1.92	1.371	6.179	-309.8



(a) Failure modes (b) Moment-rotation curves

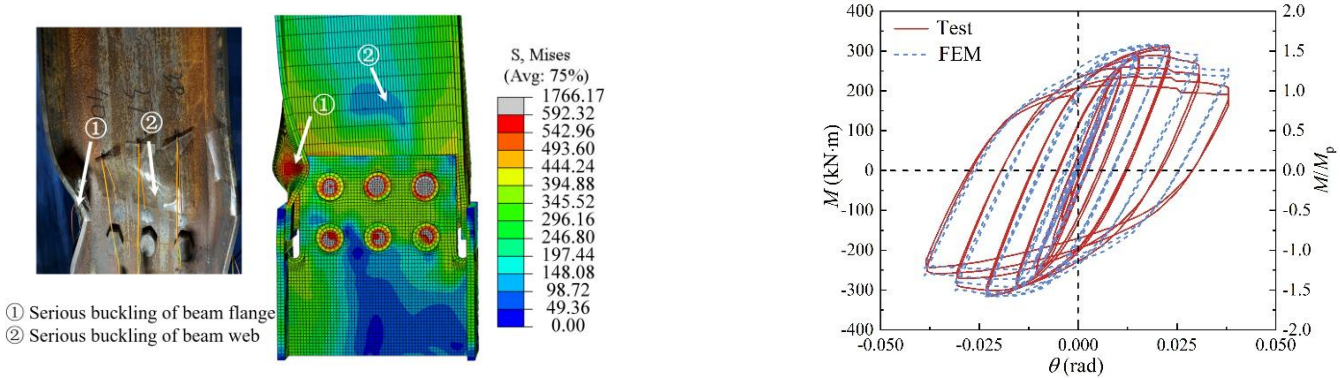
Fig. 26 Comparison between failure modes and *M-θ* curves of Specimen NSP-1

Considering that the finite element model using metal ductile fracture damage calculation was time-consuming and had low efficiency in conducting parametric analysis, and since Specimens NSP-2 and NSP-3 did not exhibit obvious fracture damage during the test, the engineering stress-strain relationship curves are still used for these two specimens without considering the influence of metal ductile fracture damage. The failure modes for Specimens NSP-2 and NSP-3 were similar, with both experiencing significant buckling at the plastic hinge. As Fig. 27 and Fig. 28 shows, the hysteresis loops from the experimental data closely match those from the numerical simulations. Table 7 summarises the comparison between the test and simulation results. The values of $M_{y,FEM}/M_y$, and $M_{m,FEM}/M_m$ ranged from 0.97 to 1.08 and 1.01 to 1.06, respectively. The error was within 10%, indicating that the numerical analysis results better reflect the specimens' mechanical response.



(a) Composition of failure modes (b) Composition of *M-θ* curves

Fig. 27 Composition of failure modes and *M-θ* curves of Specimen NSP-2



(a) Composition of failure modes (b) Composition of *M-θ* curves

Fig. 28 Composition of failure modes and *M-θ* curves of Specimen NSP-3

Table 7
Contrast data between FEM and test (unit: kN·m)

Specimen No.	Direction	M_y	$M_{y,FEM}$	$M_{y,FEM}/M_y$	M_m	$M_{m,FEM}$	$M_{m,FEM}/M_m$
NSP-1	+	250.0	242.7	0.97	282.6	293.6	1.03
	-	-214.5	-213.9	0.99	-274.5	-286.7	1.04
NSP-2	+	267.7	279.5	1.04	309.1	328.2	1.06
	-	-256.0	-276.3	1.08	-314.4	-334.1	1.06
NSP-3	+	269.4	271.2	1.01	310.5	316.9	1.02
	-	-256.9	-273.2	1.06	-316.3	-317.9	1.01

4.2. Parametric analysis

This section will further analyze how parameters such as the arc radius of connecting plates (r), the thickness of the cover plate ($t_{cov\text{-}p}$) and the connecting plate ($t_{con\text{-}p}$), as well as the extension length of the side plate (l_{sp}), influence the seismic performance of Specimen NSP-3.

4.2.1. Influence of arc radius of connecting plates

To further verify the influence of the arc radius dimension in Specimen NSP-1 on the hysteretic performance, the arc radius was set to 175 mm in accordance with the standard [40], as shown in Fig. 29. After increasing the arc radius, no ductile fracture occurred at the ends of the side plates. However, the connecting plate at the edge of the side plate also failed due to a fracture. Meanwhile, plastic hinges formed at the connecting plate and the cover plate. The formation of plastic hinges, together with welding residual stresses and welding defects generated during the butt weld process, adversely affected the butt weld at these positions. From the analysis of the moment-rotation curve, it can be seen that after increasing the arc radius, the peak point did not change significantly. However, beyond the peak, buckling deformation of the connecting plate led to ductile fracture between the connecting plate and the side plate, resulting in a rapid decrease in the ultimate bearing capacity, with no significant improvement in ductility and energy dissipation.

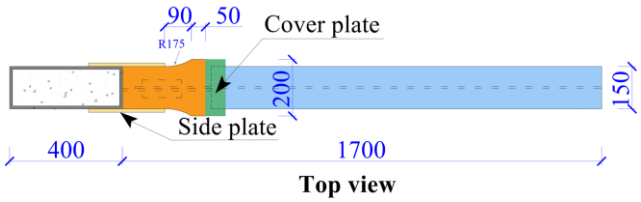
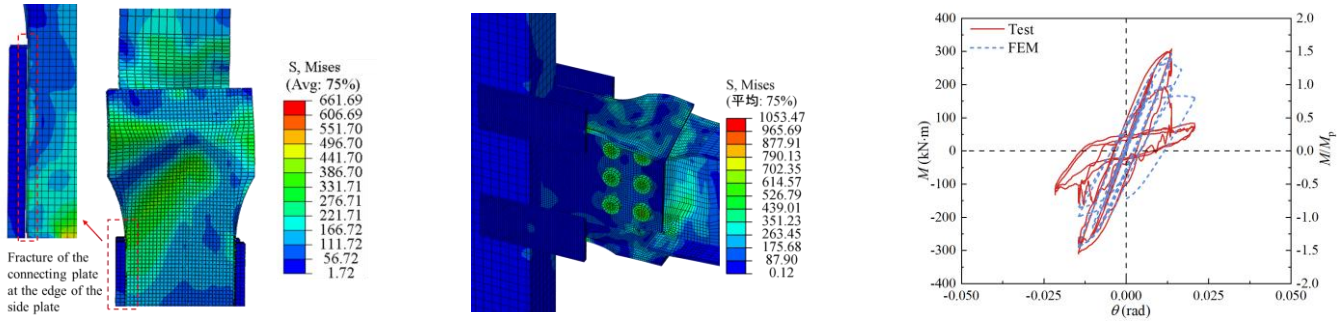


Fig. 29 Detailed information of Specimen NSP-1 with increased arc radius



(a) Failure modes (b) Moment-rotation curves

Fig. 30 Comparison of finite element results with varying arc radii

4.2.2. Influence of thickness of cover and connecting plates

To investigate how the $t_{cov\text{-}p}$ and $t_{con\text{-}p}$ affect performance, five different cover plate thicknesses were established for comparison and analysis: 8 mm (Model GLB-8), 10 mm (Model GLB-10), 12 mm (NSP-3), 14 mm (Model GLB-14), and 16 mm (Model GLB-16). The FE simulation assigned equivalent thickness values to both cover and connecting plates, and in the following text, the $t_{cov\text{-}p}$ is used to describe the thickness of both plate types.

The results are presented in Fig. 31 and Fig. 32, as well as in Table 8. The stress distribution, flexural capacity and stiffness were compared. Bending resistance is sensitive to $t_{cov\text{-}p}$. As $t_{cov\text{-}p}$ increased, the peak flexural capacity also increased. However, upon reaching a certain thickness, the rate of increase diminished. Furthermore, as $t_{cov\text{-}p}$ increased, the joint ductility initially improved but subsequently decreased.

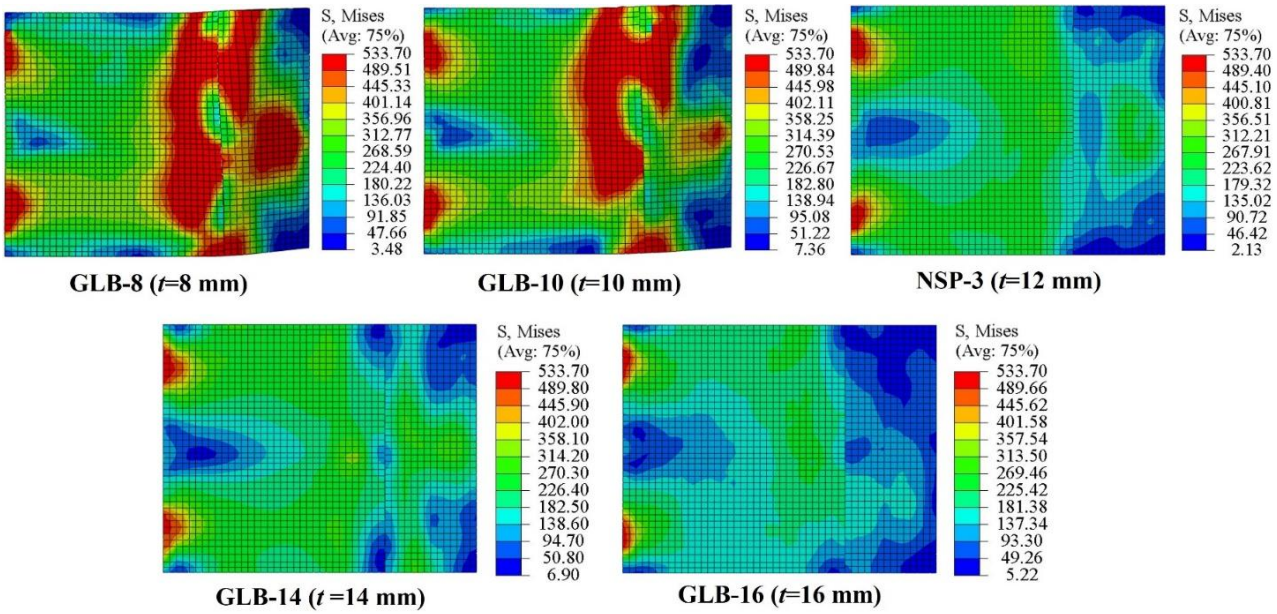
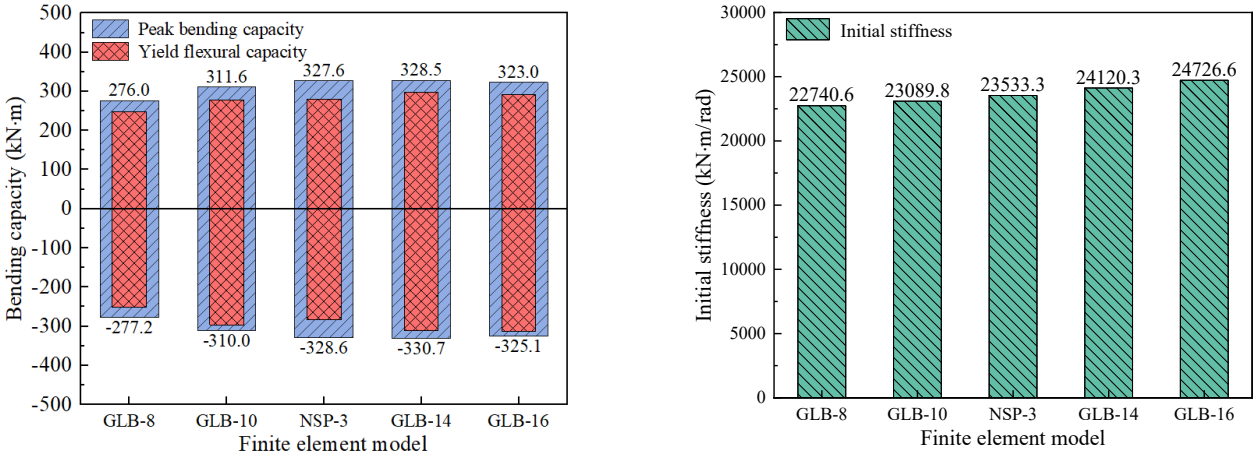


Fig. 31 Stress contour plot of the cover plate and connecting plate with different thicknesses (unit: MPa)



(a) Flexural capacity (b) Initial stiffness

Fig. 32 Contrast of the flexural capacity and initial stiffness

Table 8
Summary of data results for different $t_{cov\text{-}p}$

Specimens	Direction	Yield Point		Peak Point		Ultimate Point		K_0
		M_y	θ_y	M_m	θ_m	M_u	θ_u	
GLB-8	+	248.6	0.013	276.0	0.015	234.7	0.031	22740.63
	-	-251.1	-0.014	-277.2	-0.023	-235.6	-0.033	
GLB-10	+	278.5	0.014	311.6	0.023	264.7	0.036	23089.81
	-	-296.3	-0.016	-310.0	-0.023	-264.0	-0.040	
NSP-3	+	280.2	0.014	327.6	0.023	278.4	0.035	23533.26
	-	-282.4	-0.017	-328.6	-0.023	-279.3	-0.038	
GLB-14	+	297.7	0.014	328.5	0.023	279.2	0.035	24120.31
	-	-311.3	-0.017	-330.7	-0.023	-281.1	-0.038	
GLB-16	+	291.2	0.013	323.0	0.023	274.4	0.030	24726.62
	-	-312.6	-0.016	-325.1	-0.023	-276.3	-0.032	

Unit: M (kN·m), θ (rad), K_0 (kN·m·rad^{-1})

4.2.3. Influence of Side plate extension length

Numerical models were developed to evaluate the performance of Model NSP-3 with different side-plate outreach lengths. The models in this analysis had outreach lengths of 110 mm (Model CL-110), 130 mm (Model CL-130), 150 mm (Model NSP-3), and 170 mm (Model CL-170). The results are presented in Fig. 33, Fig. 34, and Table 9.

The data presented in these figures and tables indicated that altering the values of l_{sp} had no obvious influence on bearing capacity and only slight effects on initial stiffness. According to Fig. 33, the l_{sp} significantly affects where the plastic hinge forms. When the side plate had a shorter extension, buckling damage was more likely to occur at the junction between the connecting plate and the cover plate, which could easily lead to weld fractures. This situation was detrimental to seismic resistance. Conversely, when the side plate had a longer extension, the plastic hinge's buckling damage occurred in the steel beam segment, which is safer.

Table 9
Summary of data results for joints with different thicknesses of cover plates and connecting plates

Specimens	Direction	Yield Point		Peak Point		Ultimate Point		K_0
		M_y	θ_y	M_m	θ_m	M_u	θ_u	
CL-110	+	286.4	0.014	320.3	0.023	272.3	0.035	23770.30
	-	-302.8	-0.017	-320.0	-0.023	-272.0	-0.039	
CL-130	+	289.2	0.014	322.4	0.023	274.0	0.044	23878.35
	-	-305.8	-0.017	-324.1	-0.023	-275.5	-0.054	
NSP-3	+	280.2	0.014	327.6	0.023	278.4	0.035	23533.26
	-	-282.4	-0.017	-328.6	-0.023	-279.3	-0.038	
CL-170	+	294.5	0.014	326.5	0.023	277.6	0.036	24080.73
	-	-309.4	-0.017	-326.4	-0.023	-277.6	-0.038	

Unit: M (kN·m), θ (rad), K_0 (kN·m·rad^{-1})

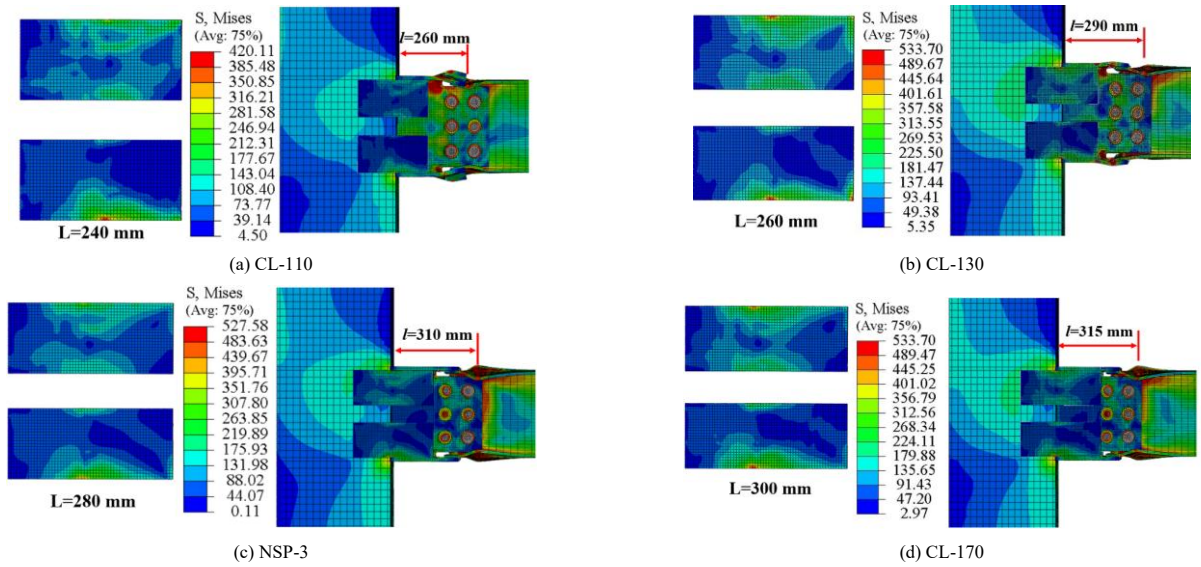


Fig. 33 Stress contour plot and plastic hinge locations with different side plate extensions (unit: MPa)

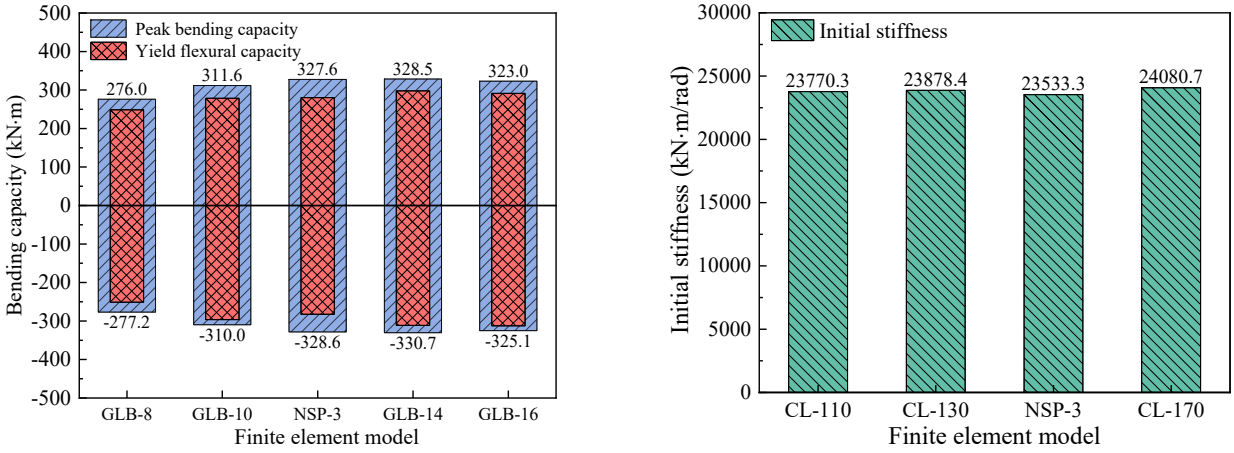


Fig. 34 Effect of different side plate outreach lengths on load carrying capacity and initial stiffness

5. Conclusion

To assess the seismic performance of novel strengthened connections with side plates, this study fabricated three T-shaped specimens and tested them, examining failure modes and comparing seismic performance indices. Additionally, verified FEM were employed to conduct a parametric analysis. Based on both the test results and the simulations, the main conclusions are:

1. In the three joint specimens featuring novel side-plate strengthened connections, the following observations were made: For Specimen NSP-1, at a story drift of 0.014, the arc-expanded connecting plate fractured. In this case, the beam segment did not develop a plastic hinge, resulting in an incomplete hysteresis curve. In contrast, plastic hinge failure occurred in the outer beam segment of the cover plate for Specimens NSP-2 and NSP-3. Both specimens exhibited full hysteresis curves, and Specimen NSP-3 exhibited the best performance.

2. The peak flexural capacities of Specimens NSP-2 and NSP-3 were nearly identical, with only a 0.44% difference between them. However, Specimen NSP-2 exhibited the highest initial stiffness, whereas Specimen NSP-3 demonstrated superior ductility and energy dissipation capacity. Both Specimens NSP-2 and NSP-3 meet the performance requirements for beam-column joints as outlined in the standard T/CECS506. Additionally, Specimens NSP-2 and NSP-3 comply with the SMF systems in AISC 341-10.

3. This study comprehensively estimated the seismic behaviour of four types of connections, including traditional side-plate reinforced connections. The overall performance of Specimen NSP-1, with the side-plate reinforced connection featuring arc-expanded connecting plates, was the poorest, while Specimen NSP-3 exhibited the best overall structural behaviour.

4. The numerical model accurately predicts the key mechanical properties and failure modes. Results from the parametric study showed that increasing the arc radius shifted the fracture position, but there was no significant improvement in bearing capacity, ductility, or energy dissipation. The joint's bearing capacity and stiffness were substantially affected by variations in the cover plate and connecting plate thicknesses. Varying the side plate outreach had minimal effects on bearing capacity and only slight effects on initial stiffness, but it had a considerable effect on the plastic hinge forms.

Acknowledgements

This work was sponsored by the National Natural Science Foundation of China (Grant Nos. 52308185 and 52008270); the Basic Research Project of Hebei Provincial Universities Sponsored by Shijiazhuang, China (Grant No.241790587A); the S&T Program of Hebei, China (Grant No. 22375409D); the Project of the Science and Technology Research Foundation of Hebei Colleges and Universities, China (Grant No. ZD2022040).

References

[1] LH Han. Concrete-Filled Steel Tubular Structures- Theory and Practice. Fourth edition. Beijing: China Science Publishing & Media Ltd. (CSPM), 2022. (in Chinese)
[2] C Vulcu, A Stratan, A Ciutina, D Dubina. Beam-to-CFT high-strength joints with external diaphragm. I: design and experimental validation. Journal of Structural Engineering, 2017, 143(5): 04017001.
[3] JF Li, B Mou, Z Wang. Cyclic behavior of column-to-column connections in novel prefabricated H-shaped steel beam to CFST column joint. Journal of Constructional Steel Research, 2023, 200: 107657.
[4] LW Tong, JF Huang, HL Wu, KY Wang, BP Dong. Experimental behavior of steel-beam to flat rectangular CFST column connections with small-sized external diaphragms. Journal of Constructional Steel Research, 2022, 198: 107520.
[5] Y Qin, ZH Chen, XD Wang. Experimental investigation of new internal-diaphragm connections to CFT columns under cyclic loading. Journal of Constructional Steel Research, 2014, 98(7): 35-44.
[6] NZ Zhang, S Jiang, XM Chen, LJ Bao, F Zhou, HT Zhao, G Shi. Experimental study on seismic behaviour of thick-flange steel beam to square CFST column joints with internal

diaphragms. Engineering Structures, 2024, 319: 118792.
[7] B Rong, YC Zhang, JY Sun, RY Zhang. Experimental and numerical research on hysteretic behavior of CFST frame with diaphragm-through connections. Journal of Building Engineering, 2022, 45: 103529.
[8] YH Cho, FY Wang, SY Seo, KS Lee, TS Kim. Experimental and numerical investigation of through-diaphragm in H-shaped steel beam to CFST column connections. Thin-Walled Structures, 2024, 199: 111852.
[9] XS Qu, JH Yan, QW Liu, YX Deng. Research on seismic behavior of CFST column-H-beam fully assembly joint. Structures, 2023, 58: 105525.
[10] Ali Koden, and Tuba Hatipoglu. Investigation of the behavior of weakened and strengthened steel column-beam connections under seismic effects. Advanced Steel Construction, 2014, 10: 1–13.
[11] W Zhang, ZH Chen, QQ Xiong, T Zhou, X Rong, YS Du. Experimental seismic behaviour of L-CFST column to H-beam connections. Steel and Composite Structures, 2018, 26(6): 793-808.
[12] YF Zhang, DF Zhang. Experimental study on the seismic behaviour of the connection between concrete-filled twin steel tubes column and steel beam. European Journal of Environmental and Civil Engineering, 2015, 19(3): 347-365.
[13] R Kiamanesh, A Abolmaali, M Ghassemieh. The effect of stiffeners on the strain patterns of the welded connection zone. Journal of Construction Steel Research, 2010, 66(1): 19-27.
[14] RQ Ma, PY Zhao, H Y Ban, et al. Behaviour of reinforced joints between steel beam and L-shaped wide limb composite column. Advanced Steel Construction, 2021, 17(1): 66-72.
[15] W Zhang, ZH Chen, QQ Xiong, T Zhou. Seismic optimization analysis of vertical stiffener connection to L-CFST column. Advanced Steel Construction, 2019, 15(1): 100-108.
[16] GB/T 228. Metallic Materials Tensile Testing Part 1: Method of Test at Room Temperature, National Standard of the People's Republic of China, Beijing, China, 2022. (in Chinese)
[17] GB 50010.. Code for Design of Concrete Structures, China Architecture & Building Press, Beijing, China, 2015. (in Chinese)
[18] GH Li, ZM Qiu, ZJ Yang, BW Chen and YH Feng. Seismic performance of high strength concrete filled high strength square steel tubes under cyclic pure bending. Advanced Steel Construction, 2020, 16.2: 112-123.
[19] JGJ/T101. Specification for Seismic Test of Buildings, China Architecture & Building Press, Beijing, China, 2015. (in Chinese)
[20] W Zhang, AH Liu, QQ Xiong, WB Wu. Research on the seismic performance of novel side-plate reinforced beam-column composite joints. Journal of Constructional Steel Research, 2024, 222: 108935.
[21] CECS506. Technical specification for joint in rectangular concret-filled steel tubular structures, China Association for Engineering Construction Standardization, China, 2018. (in Chinese)
[22] YL Yang, XG Liu, J Zhang, JP Liu, W Cheng. Behavior of large-scale connections between circular concrete-filled steel tubular columns and H-section steel beams. Advances in Structural Engineering, 2019, 1-13.
[23] QL Tao, B Niu, YY Guan, J Kong, CX Zhang, ZY Kong. Experimental and theoretical study on flexural behavior of high strength concrete encased steel beams with steel fibers. Structures, 2022, 41: 1359-1368.
[24] JQ Dong, SS Zheng, ZW Zhang, H Liu, YL Li. Experimental study on seismic performance of RC beam-CFST column joint combination using ECC. Engineering Structures, 2024, 312: 118188.
[25] ANSI/AISC 341-10, 2010, Seismic Provisions for Structural Steel Buildings, Chicago.
[26] XC Liu, YL Tao, XS Chen, FY Cui. Seismic performance of welded-bolted joint between double channel beam and CFST column. Engineering Structures, 2021, 247: 113202.
[27] LH Han, GH Yao, Z Tao. Performance of concrete-filled thin-walled steel tubes under pure torsion. Thin-Walled Struct, 2007, 45(1): 24–36.
[28] CY Liu, JH Qin, ZF Gong, H Wang, GK Zhou. Design and seismic performance analysis of a novel special-shaped steel tube concrete column steel beam joint. Advances in Structural Engineering, 2024, 27(11): 1922-1944.
[29] Y Cheng, YL Yang, JP Liu, WQ Nie, YF Chen. Seismic performance and design method of T-shaped CFST column to U-shaped steel-concrete composite beam joint with vertical stiffeners. Engineering Structures, 2023, 275: 115270.
[30] X Xu, R Cheng, P Yang, YL Yu. Experimental and numerical investigations on square CFST column to U-shaped steel-concrete composite beam joints with internal T-shaped diaphragms. Journal of Building Engineering, 2022, 60: 105172.
[31] YP Zhu, Y Zhang, JQ Shi. Finite element analysis of flexural behavior of precast segmental UHPC beams with prestressed bolted hybrid joints. Engineering Structures, 2021, 238(7): 111492.
[32] JM Shen, CZ Wang, JJ Jiang. Finite Element Analysis of Reinforced Concrete and Limit Analysis of Plate and Shell, Tsinghua University Press, Beijing, China, 1993 (in Chinese).
[33] FF Liao, W Wang, YY Chen. Experimental study to calibrate monotonic micromechanics-based fracture models of Q345 steel. Advanced Materials Research, 2011, 261, 545-550.
[34] HL Yu, DY Jeong. Application of a stress triaxiality dependent fracture criterion in the finite element analysis of unnotched Charpy specimens, Theoretical and Applied Fracture Mechanics, 2010: 54-62.
[35] ZQ Wang, WY Wang, C Gao. Experimental and numerical study on the load-bearing capacity of cold-formed stiffened high-strength steel box columns. Journal of Building Engineering, 2024, 83: 108412.
[36] LH Han, XL Zhao, Z Tao. Tests and mechanics model for concrete-filled SHS stub columns, columns and beam-columns. Steel and Composite Structures, 2001, 1(1): 51–74.
[37] YZ Lin, JC Yan, ZF Wang, CY Zhou. Experimental study, finite element simulation and theoretical analysis on failure mechanism of steel-concrete-steel (SCS) composite deep beams with UHPC, Engineering Structures, 2023, 286(12): 116124.
[38] ZW Zhang, D Li, HJ Wang, HL Qian, WQ Fang, XF Jing, F Fan. Study of mechanical properties of a novel column-beam-column prefabricated steel frame joint. Advanced Steel Construction, 2024, 20(4): 0–344.
[39] Kashan Khan, JB Yan. Numerical studies on the seismic behaviour of a prefabricated multi-story modular steel building with new-type bolted joints. Advanced Steel Construction, 2021, 17(1): 1–9.
[40] JGJ99. Technical specification for steel structures of tall building. China Architecture & Building Press, 2015. (in Chinese)

Advanced Steel Construction – Vol. 22 No. 5 (2026) 561–571
DOI: 10.18057/IJASC.2026.22.5.7

STUDY ON STRUCTURAL DAMAGE IDENTIFICATION USING SINGLE SENSOR DATA BASED ON TWO-DIMENSIONAL IMAGE AND CONVOLUTIONAL NEURAL NETWORK

Yu-Min He [1], Li Wang [1], Dan Luo [1,*], Nan Hu [1] and Yi-De Chen [2]

[1] *School of Mechanical and Electrical Engineering, Xi'an University of Architecture and Technology, Xi'an 710055, China*
[2] *Qinchuan Machine Tool & Tool Group Co., Ltd, Baoji 721009, China*
* *(Corresponding author: E-mail: 18634473182@163.com)*

ABSTRACT

This study aims to lower the cost of structural damage detection and reduce the number of measurement points and samples needed, while addressing the accuracy limitations of damage recognition methods based on one-dimensional time series signals. A Convolutional Neural Network that utilizes two-dimensional images from single-sensor data is proposed for damage identification. First, a finite element model of a large slender beam and a dataset of vibration signals are created. These signals are then transformed into two-dimensional images using the Continuous Wavelet Transform (CWT) and numerical coding. Next, the CNN and test models are developed with this dataset to study damage identification. The effects of noise and heterogeneous data — measuring points not involved in training — are further analyzed. Finally, the model's performance is evaluated using the extended steel beam dataset from the Kitami Institute of Technology in Japan. Cross-validation with two independent datasets and analysis of each measurement point's results show that the proposed model achieves high accuracy across both datasets, confirming its generalizability, practicality, and robustness against noise.

ARTICLE HISTORY

Received: 4 August 2025
Revised: 31 January 2026
Accepted: 6 February 2026

KEYWORDS

Single sensor;
Two-dimensional image;
Convolutional neural network;
Continuous wavelet transform;
Structural damage identification

Copyright © 2026 by The Hong Kong Institute of Steel Construction. All rights reserved.

1. Introduction

Due to human activities, operational loads, and environmental factors, engineering structures inevitably sustain damage during their service life. Structural Damage Detection (SDD) is an essential tool for ensuring the safety of in-service structures, playing a vital role in early damage detection and preventing accidents [1].

Traditional vibration-based damage detection methods mainly depend on changes in structural modal parameters like natural frequencies [2], mode shapes [3][4], and modal curvatures [5] to find damage. However, deriving high-order modal parameters needs dense sensor networks, and environmental noise and operational loads can affect the results, leading to measurement errors. These issues hinder the practical use of such methods in engineering.

Deep learning (DL) has recently emerged as a new method for processing and classifying data features, drawing significant attention in structural damage identification research [6]. Qin et al. [7] converted the multi-location damage identification problem into a multi-label classification task, using convolutional neural networks (CNN) to extract features, resulting in effective multi-location damage detection. Abdeljaber et al. [8]-[9] simulated structural damage by loosening nuts and used raw vibration signals from a steel grandstand frame as CNN inputs. Li et al. [10] proposed a damage identification method that combines time-frequency transformation with CNN, incorporating frequency-domain features of time-series signals as inputs. Yu et al. [11] employed a Deep Convolution Neural Network (DCNN) model to localise and quantify structural damage. Teng et al. [12] developed a transfer learning (TL)-based damage identification method that maintained high accuracy even in noisy conditions.

Although deep learning models have shown excellent performance in classifying one-dimensional time-series signals, their effectiveness in real-world engineering applications can be limited by environmental noise, limited training data, mechanical interference, and sensor errors. These issues can mask important information in the signals, ultimately reducing the accuracy of structural damage detection. Researchers have explored methods that utilize two-dimensional signal representations to address these challenges. Cofre-Martel et al. [13] proposed a CNN-based approach for damage localization and quantification by converting raw transmissibility functions into 2D images as inputs for the network. Similarly, Alazzawi et al. [14] investigated the detection, quantification, and localisation assessment of structural damage by converting structural vibration responses into RGB images as input for a CNN model. Luo et al. [15] developed a hybrid Gramian Angular Field (GAF)-CNN method that encodes time-series signals as 2D images, improving identification accuracy. Wang et al. [16] used wavelet transform and variational mode decomposition (VMD) to convert vibration responses into 2D representations, though their approach involves complex signal preprocessing. Liang et al. [17] introduced a multi-channel Markov transition field (MCMTF)-CNN framework that successfully detects structural damage using 2D image inputs.

In summary, while one-dimensional time-series data and two-dimensional images can be used as inputs for CNN models, damage-sensitive temporal signals often display nonlinear and non-stationary characteristics. Converting time-series signals into 2D images can offer more intuitive and comprehensive information for damage detection in large-scale complex structures, thereby boosting detection accuracy. Although deploying dense sensor arrays may improve identification efficiency and precision, it also raises economic costs. To overcome these challenges, this study introduces a CWT-CNN-based damage identification method that uses data from a single sensor. The proposed approach can directly analyze complex vibration signals without relying on additional prior knowledge or expert experience. The method's generalization ability, practical usefulness, and noise resistance are demonstrated through numerical simulations of large slender beams and real-world data from long steel girders.

2. Basic principle

2.1. Continuous wavelet transform（CWT）

The continuous wavelet transform enables the conversion of vibration signals into the time-scale domain, revealing how frequency content varies over time from raw vibration responses [18][19]. By selecting a basis function that matches the characteristics of the raw vibration response, the local features of one-dimensional time-series signals can be more effectively represented. For any given 1D time-series signal *x(t)*, the continuous wavelet transform (CWT) converts it into:

$$CWT(a,b) = \frac{1}{\sqrt{|b|}} \int_{-\infty}^{+\infty} x(t)\psi^*\left(\frac{t-a}{b}\right)dt \tag{1}$$

In the equation, b is the translation parameter, determining the position of the wavelet within the signal; a is the scale parameter, determining the magnitude of the wavelet's frequency; $\psi^*(t)$ is the complex conjugate of the wavelet function; $\psi(t)$ denotes the wavelet function (also termed the mother wavelet). Through continuous adjustment of the scale parameter a and the shift parameter b, the CWT enables multiresolution analysis of signals across different temporal and frequency scales.

The complex Morlet wavelet is employed as the mother wavelet for the continuous wavelet transform, which is composed of complex sine functions modulated by a Gaussian envelope. It ensures the optimal balance between temporal and frequency resolution.. Its mathematical is:

$$\psi(t) = \pi^{-1/4} e^{i\omega_0 t} e^{-t^2/2} \tag{2}$$

Where, ω_0 denotes the central angular frequency. The complex sine term corresponds to the signal's oscillatory behaviour in the frequency domain, whilst the Gaussian envelope function ensures the wavelet possesses finite support in the time domain. Through translation and scaling, a series of wavelet functions is obtained, expressed as:

$$\psi_{a,b}(t) = \frac{1}{\sqrt{a}}\psi(\frac{t-b}{a}) \tag{3}$$

In the complex Morlet wavelet, the scale parameter b satisfies the following mapping relationship with the corresponding maximum frequency f:

$$f = \frac{f_c}{a} \cdot f_s \tag{4}$$

Where, f_c denotes the centre frequency of the complex Morlet wavelet, while f_s denotes the signal sampling frequency. When a is large, the corresponding frequency is lower, resulting in a larger time-domain support interval and a narrower frequency-domain bandwidth; when a is small, the opposite occurs.

During feature construction, the magnitude of complex wavelet coefficients is employed to generate time-frequency amplitude spectrograms. This approach characterises the energy distribution characteristics at different time-frequency positions and avoids the influence of phase information on the stability of model training. These spectrograms are subsequently utilised to construct two-dimensional image features, serving as input for subsequent convolutional neural networks. This process enables the automatic extraction of time-frequency features from raw vibration signals.

The Continuous Wavelet Transform (CWT) automatically adjusts parameters a and b based on the features of the one-dimensional time series signal, providing a representation with adaptability and multi-resolution capabilities. Fig.1 illustrates the complete CWT process for transforming a 1D time series signal into a 2D image.

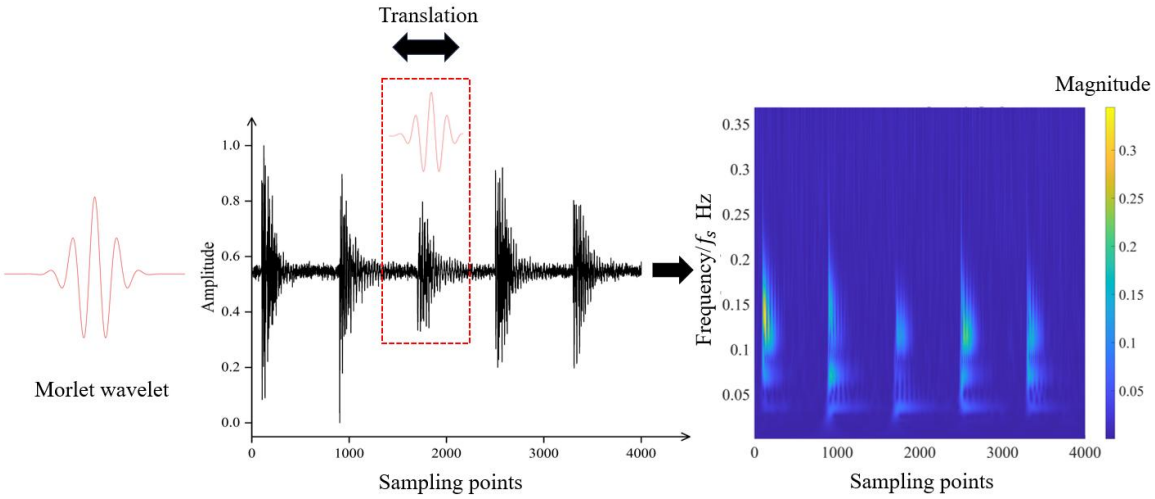


Fig. 1 CWT transformation process

2.2. Convolutional neural networks（CNN）

The CNN model primarily consists of an input layer, convolutional layers, pooling layers, and fully connected layers [20]. Its architecture is illustrated in Fig. 2.

Different kernel filters extract hierarchical features from input images in the convolutional layers, which are combined and forwarded to subsequent layers. The convolution operation can be mathematically expressed as:

$$Z^k = \sigma(W^k * A^{k-1} + b^k) \tag{5}$$

Where Z^k denotes the pixel values of the input image at layer k; k represents the layer index; σ is the activation function; W^k corresponds to the convolutional kernel weights; $*$ indicates the convolution operation; A^{k-1} represents the activated output from the $(k-1)$-th convolutional layer; b^k is the bias term.

The pooling layer, found after convolutional layers, performs downsampling on the extracted features. Using max-pooling or average-pooling operations, it simplifies feature representations while reducing the complexity of parameters-effectively easing the computational load in subsequent layers and lowering overfitting risks. Both convolutional and pooling layers are vital parts of hierarchical feature extraction in CNN architectures. The pooling operation can be formally expressed:

$$O^{k+1} = f_{pool}(A^k) \tag{6}$$

Where O^{k+1} denotes the output of the $(k+1)$-th pooling layer; $f_{pool}(\cdot)$ $(\cdot)$ represents the pooling function; A^k is the activated output from the k -th convolutional layer.

After convolutional and pooling layers, the fully-connected (FC) layer combines the extracted features and flattens them into a 1D vector. This processed feature representation is then mapped to the classification labels. The operation can be formally expressed as:

$$y = \sigma(W \cdot x + b) \tag{7}$$

Where y is the output vector; σ denotes the activation function; W represents the weight matrix; x is the input feature vector; b is the bias vector.

When a CNN model performs classification tasks, a Softmax layer is typically added after the fully connected layer. This layer converts raw outputs into a probability distribution, normalizing each class score to the range [0,1] while making sure that the total of all outputs equals 1, resulting in an n×1 vector (where n is the number of classes). The Softmax function is defined as:

$$q = Softmax(x_i) = \frac{e^{x_i}}{\sum_{j=1}^{n} e^{x_j}} \tag{8}$$

Where q represents the probability of the i -th class; x_i denotes the raw output (logit) of the i -th class; $\sum_{j=1}^{n} e^{x_j}$ is the exponential sum of raw outputs across all n classes, serving as the normalization term.

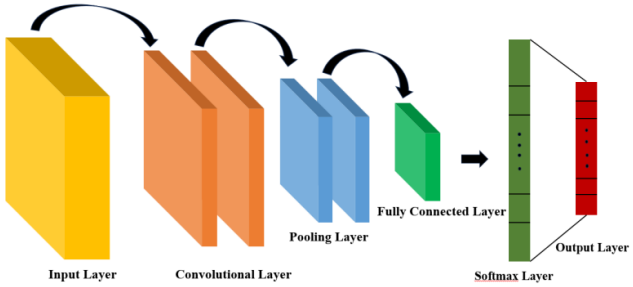


Fig. 2 CNN model structure

The classification layer, situated at the end of the CNN model, has neurons equal to the number of target classes. It computes the loss by comparing the Softmax-derived probability distribution with ground-truth labels, measuring the difference between predicted and actual values. A lower loss indicates better model performance in damage detection.

2.3. Structural damage identification method using CWT-CNN

This paper introduces a CWT-CNN-based framework for structural damage detection to address the dual challenges of reducing sensor deployment and enhancing damage detection accuracy. As shown in Fig. 3, the workflow includes the following key steps:

First, the original vibration response of the structure is converted into a two-dimensional image using CWT. Second, this two-dimensional image is input into a convolutional neural network for feature learning and effective extraction. Finally, structural damage information is classified through the Softmax layer. The effectiveness of the proposed method is further validated by a comparison of one-dimensional time-series signals, grayscale images (GSI), and CWT images. CWT images provide clearer representations of the practical information contained in vibration signals, while convolutional neural networks have strong capabilities for feature extraction. Combining these methods effectively enhances the accuracy of structural damage detection, offering a new and efficient solution for identifying structural damage.

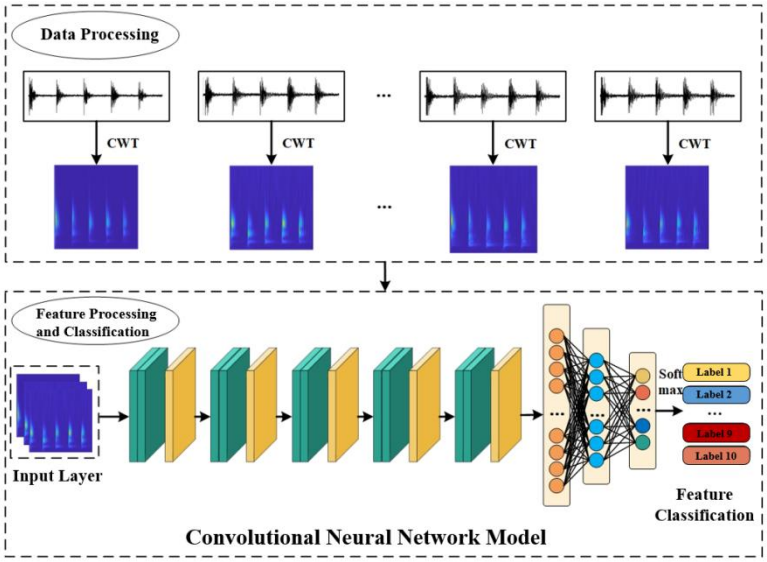


Fig. 3 CWT-CNN model structural damage identification process

3. Numerical simulation of large-scale slender beam structures

3.1. Finite element model

The finite element model of the large slender beam is constructed using beam elements, as shown in Fig.4. The model includes 50 regular members, with six selected members identified as damaged. The material properties of the structure are: elastic modulus E =210 GPa, density ρ =7850 kg/m³, and Poisson's ratio μ =0.3. The boundary condition is set as "fixed support-fixed support", and the damping ratio is ζ=0.02. In this study, structural damage is simulated by decreasing the stiffness of the damaged members, applying a uniform 50% reduction in the elastic modulus to represent 50% damage.

The model's modal dynamic analysis is performed using ABAQUS (SIMULIA Inc., Providence, RI, USA). Ten data sampling points (A1 to A10) are set up with a sampling frequency of 200Hz. Set five excitation points, namely B1 to B5, and sequentially apply 500N pulse excitation. Raw vibration responses are collected at different data sampling points. Each excitation sampling time is 20 seconds. Each individual signal generated at the data sampling point includes 4000 data points. Select the first 3969 data points as a sample.

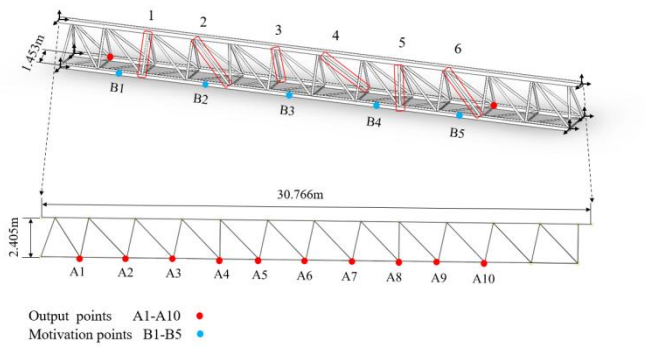


Fig. 4 Finite element modeling of large slender beam structures

3.2. Dataset construction

Ten damage conditions are defined based on the structure's different damage locations and states, as shown in Table 1. Each damage condition contains 200 vibration signal samples, and the samples are divided into training, validation and test sets in a ratio of 7:1:2 . The data from various conditions are labeled with different numerical tags, and the labeled dataset is used as input for the CNN model.

Table 1
Structural damage condition setting for large slender beam structures

Case Number	Damaged Member	Damage State
1	/	Intact
2	1	Single Damage
3	2	Single Damage
4	3	Single Damage
5	4	Single Damage
6	1,2	Double Damage
7	2,3	Double Damage
8	3,4	Double Damage
9	1,3,5	Multiple Damage
10	2,4,6	Multiple Damage

In practical engineering applications, sensor output signals naturally include certain noise levels caused by mechanical vibrations and component friction [21-23]. The signal-to-noise ratio (SNR), which is the ratio of signal power to noise power expressed in decibels (dB), is defined by Eq. (9).

$$SNR = 10log\frac{P_s}{P_n} \tag{9}$$

where P_s represents the signal power and P_n denotes the noise power. To simulate noise interference in real engineering environments, this study adds Gaussian white noise with signal-to-noise ratios (SNR) of 9 dB, 5 dB, and 1 dB to the one-dimensional time-series signals obtained from ABAQUS simulations.

3.3. Signal processing

The one-dimensional time series signals are normalized to the range [0, 1] using Eq. (10) to enhance data consistency.

$$y = \frac{x - \min(x)}{\max(x) - \min(x)} \tag{10}$$

The normalised vibration signal is converted into two-dimensional image with time-frequency domain characteristics via the CWT, with the image resolution set to 256×256 pixels. Additionally, the vibration signal is converted into a GSI and CWT time-frequency diagram using a numerical encoding method for comparative analysis.

One-dimensional time-domain signals can be converted into greyscale images through linear mapping, with signal values sequentially forming image pixels. The grayscale levels comprise 256 gradations, i.e., [0,255], where 0 denotes black and 1 denotes white. Each pixel's grayscale value represents the corresponding time-domain signal value at that position. To obtain $M \times M$ GSI, where the length of the one-dimensional time-domain signal is M^2, $P(j,k)$denotes the two-dimensional image pixel value, with $j,k \in [1,M]$, as shown in Eq. (11).

$$P(j,k) = F_{round}\left\{\frac{X((j-1)\times M+k) - Min(X_i)}{Max(X_i) - Min(X_i)} \times 255\right\} \tag{11}$$

In the equation, $F_{round}(\cdot)$ denotes the rounding function; $X_i = \{x_1, x_2, \ldots, x_n\}$ represents the time series of a one-dimensional time signal; the process of converting a one-dimensional time-domain signal into a GSI is illustrated in Fig. 5.

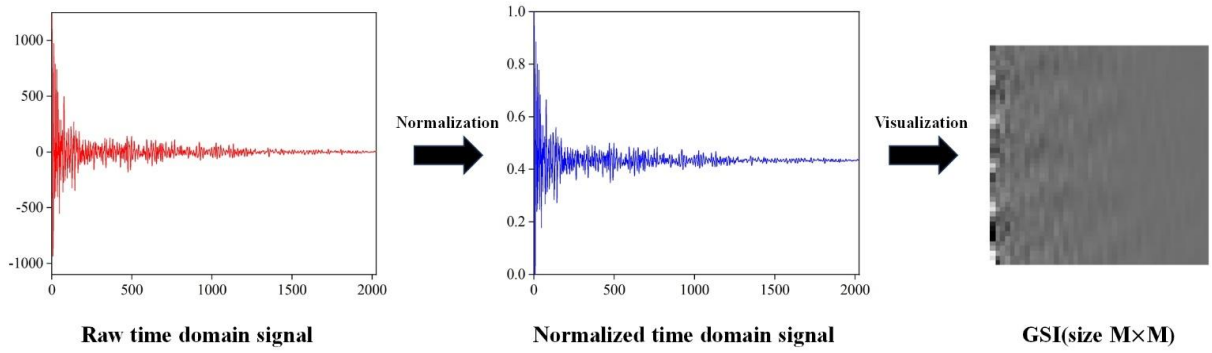


Fig. 5 GSI Conversion Process

A two-dimensional image representing each noise level under operating condition 1 is presented for illustration, as shown in Fig. 6.

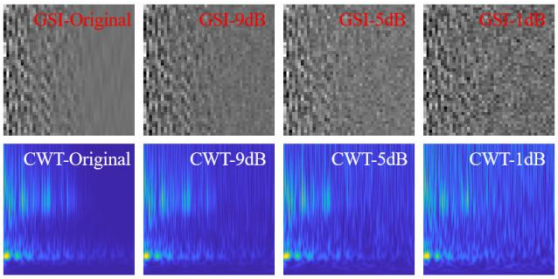


Fig. 6 Two-dimensional image display at each noise level

A supplementary ablation study is conducted analysing the impact of varying CWT image resolutions in the 2D-CNN. While maintaining consistent network architecture, training strategy, and data partitioning methods, four different CWT time-frequency images—64×64, 128×128, 256×256, and 512×512—as inputs for the 2D-CNN. Comparative analysis is performed on their training convergence characteristics, classification accuracy, and computational cost. The experimental results are presented in Fig. 7.

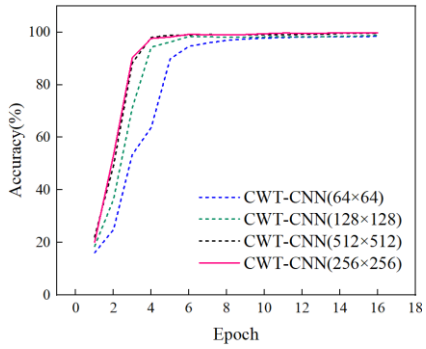


Fig. 7 Experimental results for different CWT image resolutions

Experimental results indicate: at 64×64 and 128×128 resolutions, while models achieve effective training, their convergence rates are markedly slower than the 256×256 input scenario due to constrained expression of time-frequency structural details, accompanied by a certain degree of decline in final classification accuracy. The 256×256 resolution strikes the optimal balance between convergence speed and classification performance, enabling the model to converge rapidly while achieving higher and more stable recognition accuracy. When image resolution is further increased to 512×512, the model's final classification accuracy remains largely comparable to that achieved at 256×512. However, computational time and graphics memory consumption increase significantly, markedly raising training and inference costs without delivering substantial performance gains. Based on the aforementioned ablation study results, this paper ultimately selects 256×256 CWT time-frequency images as the input size for the 2D-CNN. This configuration effectively controls computational complexity while ensuring the integrity of time-frequency feature representation, embodying a reasonable trade-off between performance and efficiency.

3.4 Notation table

The mathematical signs and meanings used in this paper are shown in Table 2.

Table 2
Notation table

Sign	Meaning
b	Translation parameters
a	Scale parameter
ψ(t)	Mother wavelet
ω_0	Central angular frequency
f	Pseudo-frequency
k	Number of storeys
σ	Activation function
y	Output vector
x	Input vector

4. CNN model establishment and testing

4.1. CNN model development and testing

The 2-D CNN model constructed herein employs ten convolutional layers, five pooling operations, and three fully connected layers. The stride for each convolutional layers is set to 1, all convolutional layers employ the Same padding method, and with the ReLU activation function is uniformly applied. Batch Normalisation (BN) layers are inserted between convolutional and ReLU layers to normalise the batch size of feature outputs from hidden layers. Maximum pooling is employed in pooling layers to reduce feature map dimensions and enhance the model's feature extraction capability. The initial learning rate is set to 0.001, decreasing by 20% per training iteration. The batch size is fixed at 32 samples. Stochastic Gradient Descent (SGDM) is employed as the optimisation function to update the network parameters. Furthermore, a Dropout layer is inserted between fully connected layers with a dropout rate of 0.5 to prevent model overfitting ; L2 regularisation is applied with a regularisation coefficient of 0.00001, reducing weight values by adding a penalty term proportional to the square of the weights to minimise model error. A Softmax layer and classification layer are placed at the model's output to classify damage conditions.

Additionally, shallow machine learning models, including BPNN, 1-D CNN, and GSI-CNN are established for comparison with the proposed model. The BPNN and 1-D CNN models employed one-dimensional time-series signals as input. The BPNN comparison model employed two hidden layers with 150 and 100 neurons respectively. Each hidden layer employs a non-linear activation function to enhance the model's feature representation capability. The number of output layer neurons matched the damage category count, with multi-class classification achieved via the Softmax function. The 1-D CNN maintains identical network depth and training parameter settings to the 2-D CNN. The network parameters for both 1-D CNN and 2-D CNN models are detailed in Table 3.

Table 3
Model network parameters

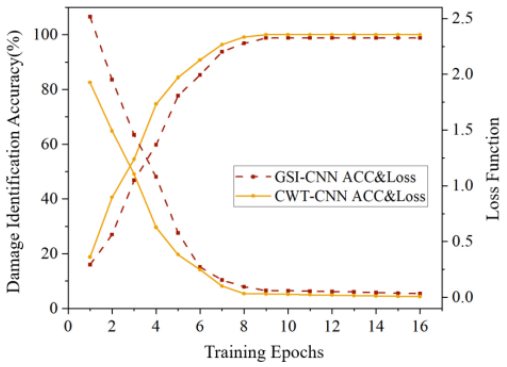
Network model	Name	2-D CNN	1-D CNN
Feature extraction	Convolution layer	Conv2D（64@5×5）	Conv1D（64@5）
	Convolution layer	Conv2D（64@5×5）	Conv1D（64@5）
	Pooling layer	MaxPool（4×4）	MaxPool（4）
	Convolution layer	Conv2D（128@3×3）	Conv1D（128@3）
	Convolution layer	Conv2D（128@3×3）	Conv1D（128@3）
	Pooling layer	MaxPool（2×2）	MaxPool（2）
	Convolution layer	Conv2D（256@3×3）	Conv1D（256@3）
	Convolution layer	Conv2D（256@3×3）	Conv1D（256@3）
	Pooling layer	MaxPool（2×2）	MaxPool（2）
	Convolution layer	Conv2D（512@3×3）	Conv1D（512@3）
	Convolution layer	Conv2D（512@3×3）	Conv1D（512@3）
	Pooling layer	MaxPool（2×2）	MaxPool（2）
	Convolution layer	Conv2D（512@3×3）	Conv1D（512@3）
	Convolution layer	Conv2D（512@3×3）	Conv1D（512@3）
	Pooling layer	MaxPool（2×2）	MaxPool（2）
Feature Classification	Fully connected layer	FC1（1024）	FC1（1024）
	Dropout layer	Dropout（0.5）	Dropout（0.5）
	Fully connected layer	FC2（512）	FC2（512）
	Dropout layer	Dropout（0.5）	Dropout（0.5）
	Fully connected layer	FC3（10）	FC3（10）
	Fully connected layer	Softmax	Softmax

In constructing two-dimensional convolutional neural networks, this paper employs a 2-D CNN as the unified backbone architecture, achieving comparisons between different models solely by altering the input feature format and channel count. When employing greyscale images as input, the GSI-CNN model is constructed with 1 input channel. When employing the Gram angle field as input, the GADF-CNN and GASF-CNN models are constructed with the number of input channels set to 3. When employing the continuous wavelet transform (CWT) as the input for the frequency domain, a CWT-CNN model is constructed with the number of input channels set to 3.

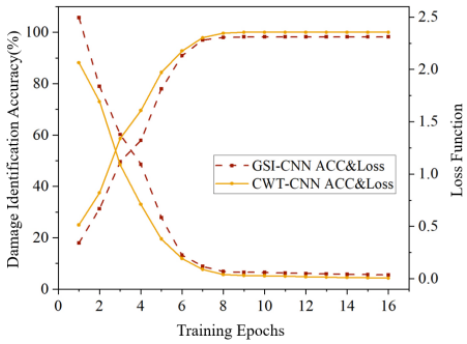
4.2. Training

The training setup is as follows: The computer hardware runs on a 64-bit Windows 11 OS, equipped with an Intel i7-11800H @ 2.30 GHz CPU and an NVIDIA GTX 3060 graphics card. The program operates on the PyTorch framework with Python 3.9.

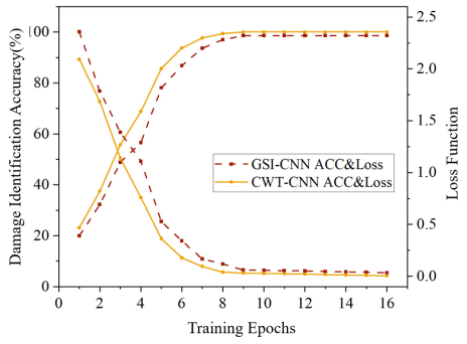
The training process used data from measurement points A1, A5, and A10, over 16 epochs. During training, both models continuously learned and optimized until they reached convergence. The validation accuracy and loss function curves for GSI-CNN and CWT-CNN are shown in Fig.8.



(a) Measurement point A1



(b) Measurement point A5



(c) Measurement point A10

Fig. 8 Damage recognition accuracy and loss function curves of various models for the numerical simulation dataset

As shown in Fig.8, both 2D image-based models achieved consistent damage detection accuracy after eight training epochs, with their loss function curves steadily declining. This confirms that neither GSI-CNN nor CWT-CNN showed signs of overfitting. When using CWT time-frequency images as network input, the accuracy curves consistently outperformed those of GSI grayscale images, while the loss function curves continued to decrease steadily.

These results highlight the superior structural damage identification performance of the CWT-CNN model.

4.3. Numerical simulation results

To assess the generalization ability of the proposed model, vibration signals without added Gaussian white noise are input into each model for damage identification analysis. Each model is tested five times with datasets at different noise levels, and the average damage identification accuracy is computed, as shown in Fig.9.

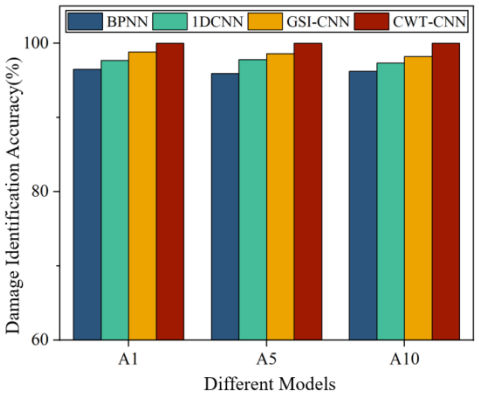
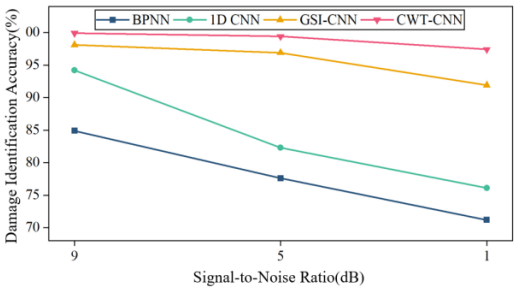


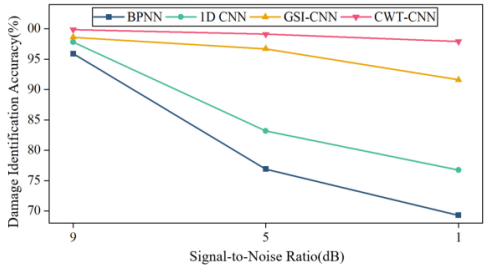
Fig. 9 Damage recognition accuracy across measurement points (numerical)

As shown in Fig.9, when employing the vibration response from a single sensor as model input, the CWT-CNN model achieves the highest recognition accuracy, with the highest damage identification accuracy reaching up to 100%. In comparison, the GSI-CNN model attained a maximum accuracy of 98.80%. The recognition results of the GSI-CNN and FDGSI-CNN models ranged between 95.50% and 98%. These results demonstrate that 2D image-based inputs significantly enhance damage detection accuracy, and the CWT time-frequency image input model exhibits substantially better fitting capability for damage data compared to GSI-based models.

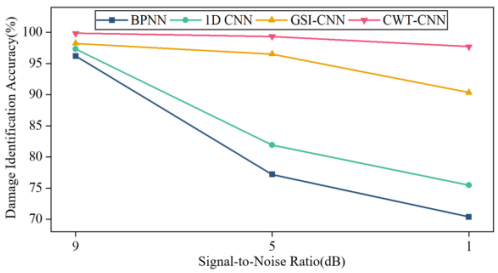
To assess the noise robustness of the proposed model, vibration signals with added Gaussian white noise are input into each model for damage detection. Each model is tested five times on datasets with different noise levels, and the average damage identification accuracy is reported Fig.10.



(a) Measurement point A1



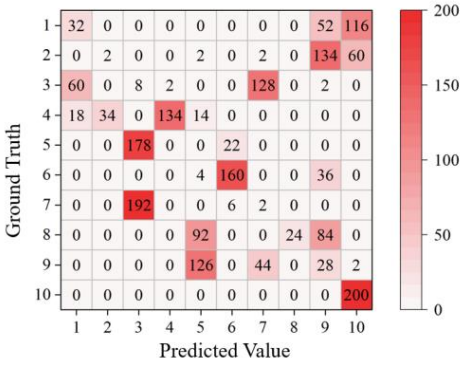
(b) Measurement point A5



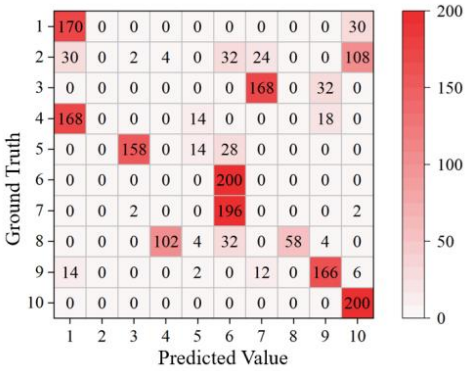
(c) Measurement point A10

Fig. 10 Damage recognition accuracy vs. noise levels (numerical simulation)

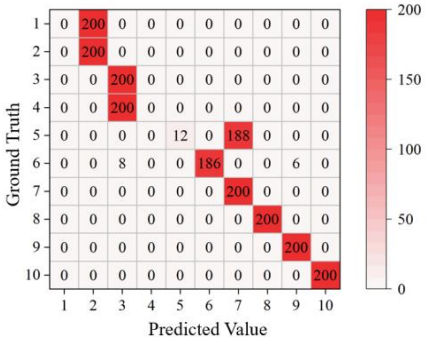
As shown in Fig.10, the 2D image-based identification methods have obvious advantages over traditional 1D time-series signal approaches at different noise levels. This is because 2D images offer a more complete representation of temporal and frequency information compared to 1D signals. Additionally, the CWT-CNN model shows better noise robustness than GSI-CNN, thanks to the CWT time-frequency diagrams' ability to capture both the time-frequency features and transient aspects of vibration signals, providing a richer and more detailed set of information for feature extraction.



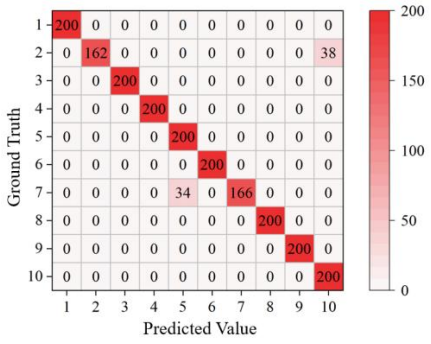
(a) BPNN



(b) 1D-CNN



(c) GSI-CNN



(d) CWT-CNN

Fig. 11 Confusion matrix for heterogenous signal identification in numerical simulation datasets

To test the reliability of the model presented in this paper, data from the A3 measurement point, which is not involved in training, is used to test the data from the A1 measurement point that had been trained. To analyse the classification results of different models for heterogeneous signals, confusion matrices are plotted for each of the four models. Column labels denote the true values of damage conditions, while row labels represent the predicted values of damage conditions. This indicates that the trained model can only recognise data from the measurement points included in the training set. In practical engineering applications, if data from surrounding measurement points can be utilised to compensate for missing data at the target measurement points, this would significantly enhance the reliability of the damage detection system. The CWT time-frequency map can depict the evolution of energy in different frequency bands over time in transient responses with variable time – frequency resolution. This enables the identification of damage-induced alterations in time-frequency structure, thereby fully exploiting the time-frequency structural characteristics inherent in transient vibration signals. Fig. 11 (a)-(c) shows the confusion matrices for different models, with limited identification accuracies of 29.50%, 40.40%, and 69.90%, respectively. When used as inputs to the models, they substantially improve identification accuracy. As shown in Fig. 11 (d), the CWT-CNN model achieves 96.40% accuracy in its confusion matrix, meeting the precision requirements for structural damage assessment identification.

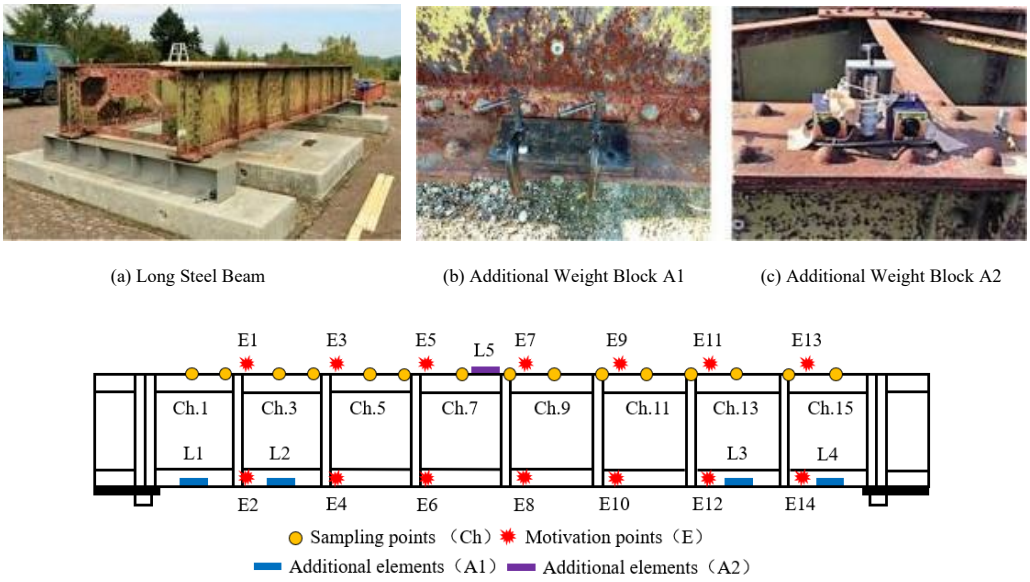
5. Experimental results analysis

5.1. Data sources

To validate the practicality of the CWT-CNN model, experimental testing is conducted using the extended steel beam dataset from Kitami Institute of Technology [24]. The steel beam measures 6.45 m in length, 1.994 m in width, and 0.775 m in height, with its physical model shown in Fig.12(a). Fifteen accelerometers served as data sampling points (Ch. 1 to Ch. 15), along with fourteen excitation points (E1 to E14). Five different locations (L1 to L5) are designated on the beam, where additional weights A1 or A2 could be attached to simulate minor changes in mass or stiffness; the weights A1 and A2 are shown in Figs. 12(b) and (c), respectively. The vibration test layout is depicted in Fig.12(d). The sampling frequency is 10 kHz. Each excitation sampling time is 0.6 seconds. Each individual signal generated at the data sampling point includes 6000 data points. Select the first 2025 data points as a sample. There are 6 damage conditions, each with 1080 samples, as shown in Table 4.

Table 4
Structural damage condition settings for long steel beam structures

Case	Damage State
1	Healthy state
2	Added mass A1 at Position L1
3	Added mass A1 at Position L2
4	Added mass A1 at Position L3
5	Added mass A1 at Position L4
6	Added mass A2 at Position L5



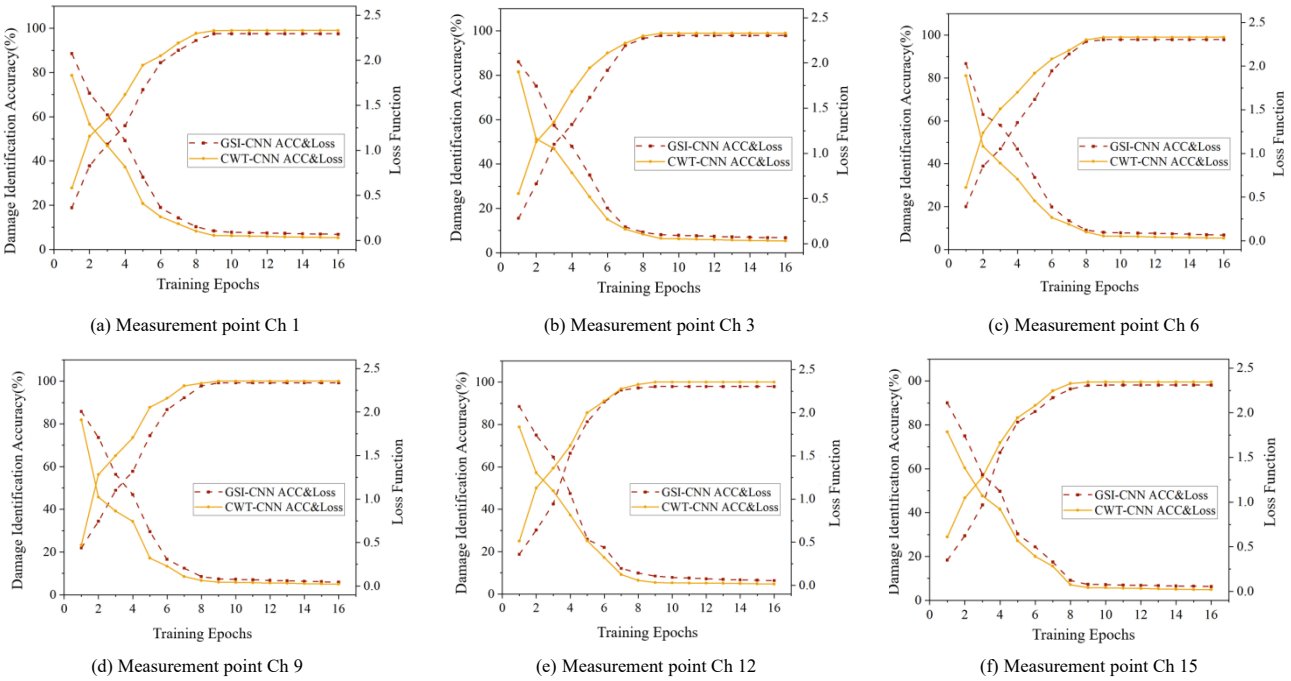
(a) Long Steel Beam (b) Additional Weight Block A1 (c) Additional Weight Block A2

(d) Vibration Test Layout

Fig. 12 Damage data acquisition experimental arrangement

5.2. Identification study using 1D time-series signals and 2D images

To verify whether channel information leakage has occurred, acceleration responses from individual sensors at Ch.1, Ch.3, Ch.6, Ch.9, Ch.12, and Ch.15 under excitation points E1, E2, E3, and E4 are selected as test samples. For each damage condition, the samples are divided into training, validation, and test sets in a ratio of 7:1:2. While maintaining the same training configurations and network parameters, the validation accuracy and loss function curves of GSI-CNN and CWT-CNN across six measurement points are shown in Fig.13.

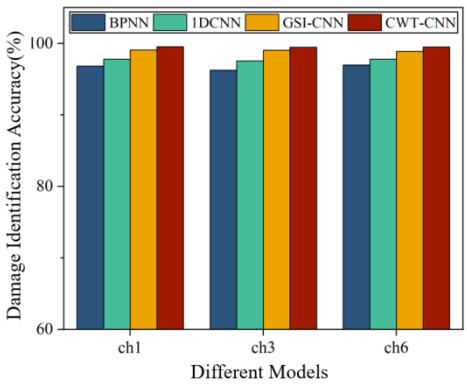


(a) Measurement point Ch 1 (b) Measurement point Ch 3 (c) Measurement point Ch 6

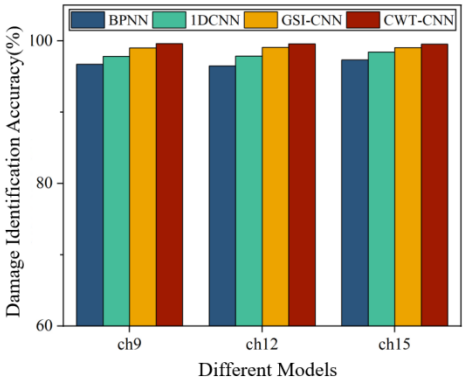
(d) Measurement point Ch 9 (e) Measurement point Ch 12 (f) Measurement point Ch 15

Fig. 13 Damage recognition accuracy and loss function curves for various models on the extended steel beam dataset

As shown in Fig. 13, the models exhibit rapid convergence as training epochs increase. After nine epochs, the damage detection accuracy curves for both 2D image input methods plateau, with the CWT-CNN model reaching the highest accuracy (up to 100%), followed by the GSI-CNN model (peak accuracy of 99.17%). Models using 1D time-series signals achieve 95% and 98% accuracy. These results confirm that 2D image inputs significantly improve damage detection accuracy; CWT time-frequency diagrams outperform grayscale images (GSI) derived from direct signal encoding. The superior performance of CWT is due to its dual time-frequency representation, which maintains temporal sequence information, uncovers frequency-domain features, and extracts complex details not visible in pure time-domain analysis. To ensure statistical reliability, all four models from Section 3.1 underwent five repeated tests, with average accuracy values shown in Fig.14.



(a) Measurement point Ch 1、3、6



(b) Measurement point Ch 9、12、15

Fig. 14 Damage detection accuracy across extended steel beam measurement points

As shown in Fig. 14, the CWT-CNN model achieved average damage identification accuracies of 99.55%, 99.48%, 99.51%, 99.60%, 99.56%, and 99.54% across six different measurement points, all surpassing other tested models. This confirms that the CWT-CNN model can maintain high damage identification accuracy when processing real structural vibration signals. The experimental results indicate that using 2D images as model input consistently yields higher damage identification accuracy than models based on 1D time-series signals, demonstrating the advantages of 2D image-based identification methods in capturing complex features and improving recognition performance.

To evaluate the model's true performance under unseen excitation conditions, experiments are conducted using a leave-one-out cross-validation (LOCO) protocol. The design is as follows: based on single-sensor data from measurement points ch.9 and ch.12, six damage scenarios are set for each measurement point, and a total of 1080 samples are set across all damage categories. The 195 data points from channel E4 are designated as the test set, while the 885 data points from channels E1 – E3 formed the training set. Classification accuracy on the test set served as the evaluation metric for the model's cross-source generalisation capability. The experiment is conducted five times, yielding an average recognition accuracy of 97.35% on the test set for ch.9 and 96.13% for ch.12, both meeting structural damage identification requirements. By strictly isolating training and test excitation sources, this experiment effectively prevented channel information leakage, validating the model's adaptability and robustness under unknown excitation conditions.

T-Distributed Stochastic Neighbor Embedding (t-SNE) is a nonlinear manifold learning algorithm [25] that effectively visualizes the reduction of high-dimensional data. Due to the black-box nature of deep learning models with many parameters, interpreting the classification results theoretically is challenging. To assess the feature extraction capability of the CWT-CNN model, the t-SNE algorithm is employed to visualize the features extracted from the network's output. Using vibration responses from a single sensor (Ch . 9) as input, the t-SNE visualization results are shown in Fig.15.

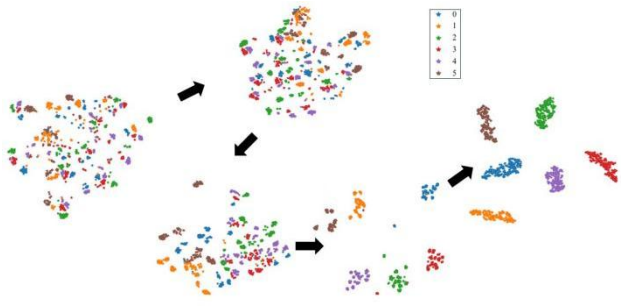


Fig. 15 CWT-CNN model feature extraction visualization

As shown in Fig.15, the classification states of the six working conditions appear very disorganized and complex when no model training is conducted. In contrast, the classification performance significantly improves after training, with each damage type forming clear, well-separated clusters that demonstrate excellent identifiability.

To validate the superiority of CWT time-frequency images, a comparative analysis is conducted using grayscale images (GSI), Gramian Angular Difference Field (GADF), and Gramian Angular Summation Field (GASF) as alternative 2D representations. Using the same model architectures, the test results from various image input methods are evaluated with Precision, Recall, and F1-score metrics. The macro-averaged results are shown in Fig.16.

As shown in Fig.16, the CNN model using CWT time-frequency images as input outperformed all other image-based CNN models across all evaluation metrics, with the CWT-CNN achieving perfect 100% scores in every indicator. Additionally, while the GADF-CNN maintained metrics above 98.50%, GSI-CNN and GASF-CNN's performance is limited to the 97%-98.50% range. The CWT-CNN demonstrates superior performance over other models in damage feature extraction and classification tasks.

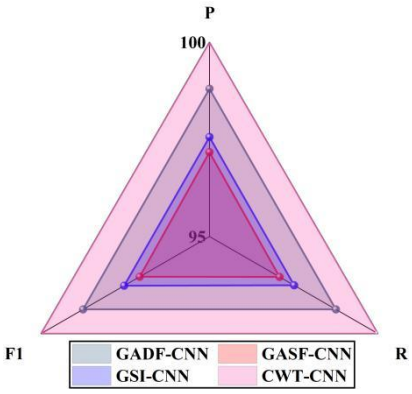
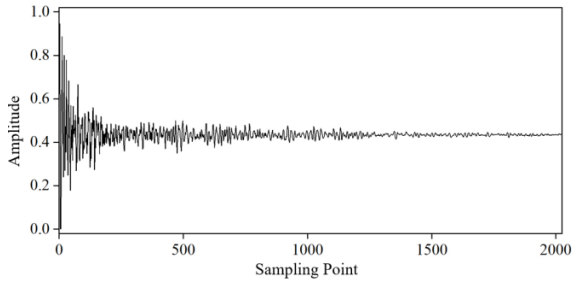


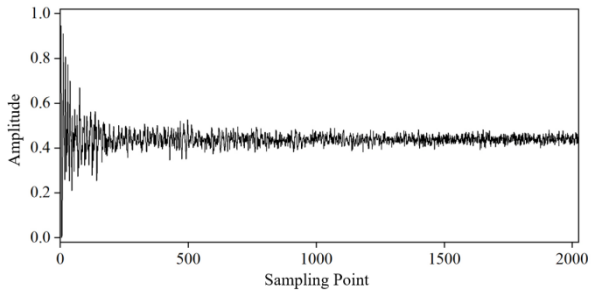
Fig. 16 Comparison of model performance by input image type (Unit: %)

5.3. Research on noisy data identification

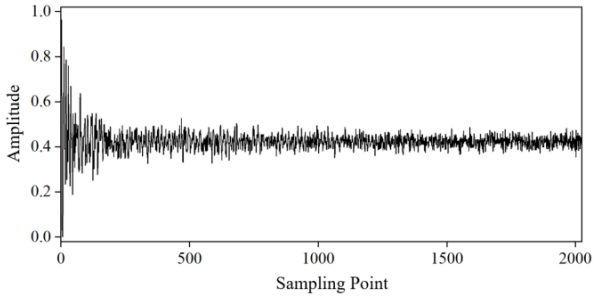
To assess the noise robustness of the proposed model, Gaussian white noise with signal-to-noise ratios (SNR) of 9 dB, 5 dB, and 1 dB is added to the original extended steel beam dataset to simulate real engineering conditions. The sample characteristics at different noise levels are shown in Fig.17. As noise intensity increases, the random components and interference errors in the original signal become significantly more prominent, further affecting the inherent features of the vibration signals.



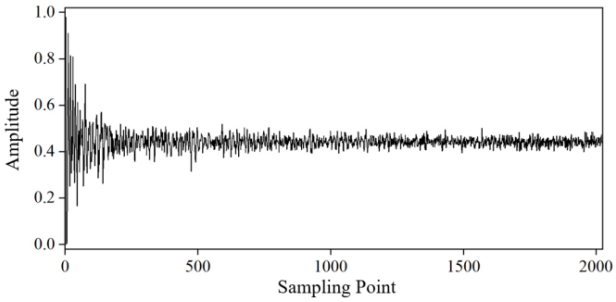
(a) Noise-Free



(b) 9dB



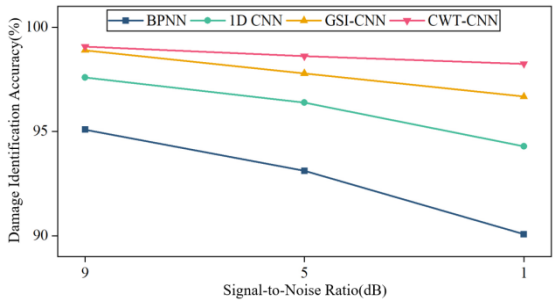
(c) 5dB



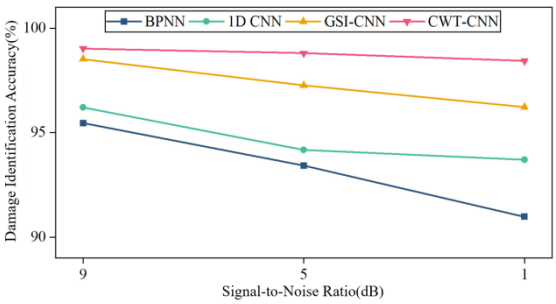
(d) 1dB

Fig. 17 Characterization of noisy data samples

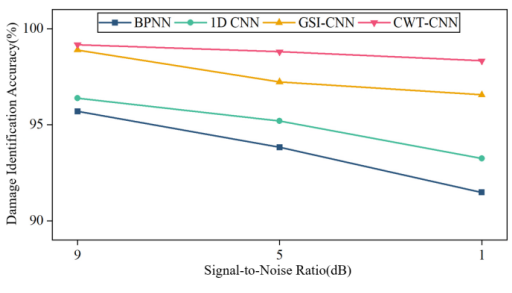
The vibration signals with varying noise levels are used to train and evaluate each model's recognition performance under noisy conditions. Five repeated tests are performed for each model at each noise level, and the average damage identification accuracy is calculated, as shown in Fig.18.



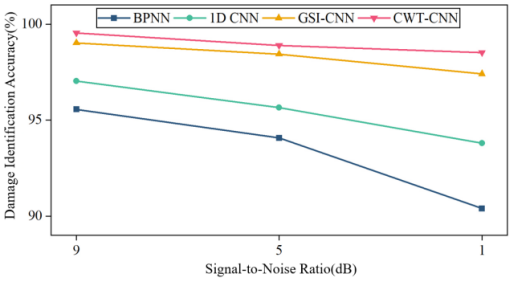
(a) Measurement point Ch1



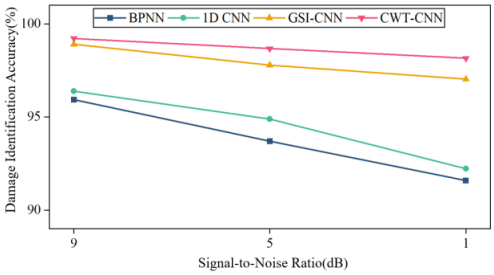
(b) Measurement point Ch 3



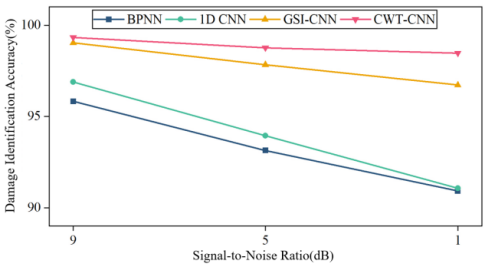
(c) Measurement point Ch 6



(d) Measurement point Ch 9



(e) Measurement point Ch 12



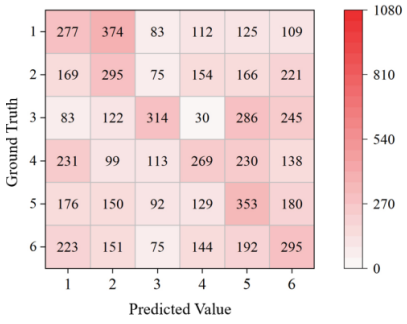
(f) Measurement point Ch 15

Fig. 18 Damage accuracy under noise effects

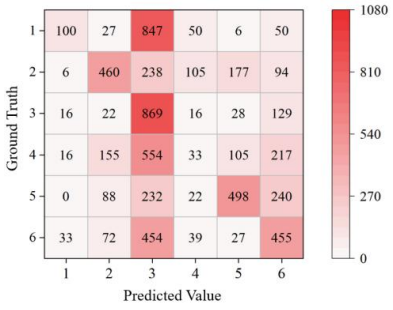
As shown in Fig.18, all models exhibit decreasing recognition accuracy as noise levels increase, although the CWT-CNN model is significantly less affected by degradation than the others. A detailed analysis at six measurement points under 1 dB noise conditions shows that the 2D image-based CWT-CNN and GSI-CNN models achieve average recognition accuracies of 98.36% and 96.77%, respectively. In comparison, the 1D-CNN and BPNN models only reach 93.05% and 90.91%. This performance advantage stems from the inherent ability of CWT time-frequency diagrams to distinguish and filter key signal features while reducing redundant noise through their frequency-domain representation, as confirmed by experimental validation of the method's excellent noise robustness.

5.4. Research on cross-source dataidentification

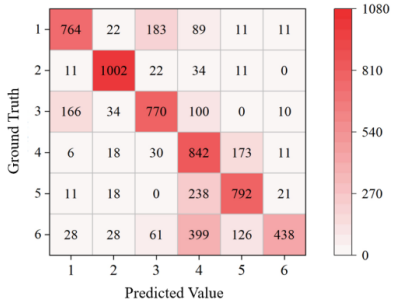
To verify the reliability of the proposed model, the data from the Ch. 4 measurement point (not used in training) is employed to test the model trained on Ch. 1 data. Fig. 19(a)-(c) presents the confusion matrices of the comparative models, which achieved identification accuracies of just 28.72%, 37.26%, and 71.11%, respectively. In contrast, Fig. 19(d) shows the confusion matrix of the CWT-CNN, with a significantly higher accuracy of 98.61%. The experimental results confirm the effectiveness of the proposed method in improving cross-source data identification.



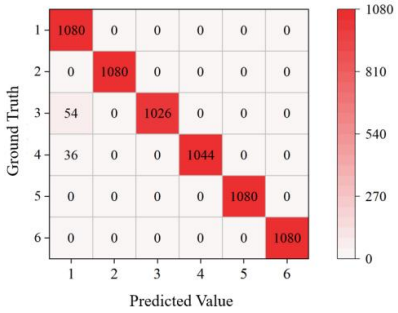
(a) BPNN



(b) 1D-CNN



(c) GSI-CNN



(d) CWT-CNN

Fig. 19 Heterogeneous signal classification matrix

6. Conclusions

This paper introduces a new method for structural damage identification aimed at reducing costs and addressing the limitations of one-dimensional time-series signal inputs, such as limited damage detection accuracy, poor noise robustness, and weak reliability. The CWT-CNN model is evaluated on two separate datasets: a numerical simulation of a large slender beam and field testing of a long steel beam. The simulation involved positive structural damage, while the field test identified harmful damage. A detailed analysis of single-sensor identification results showed that the CWT-CNN achieved high damage detection accuracy in cross-validation across both datasets, leading to the following conclusions:

(1) For the raw data from both independent datasets, the CWT-CNN model achieved over 99% identification accuracy using single-sensor measurements, while the GSI-CNN model attained over 98% accuracy. This demonstrates

significantly better generalization ability compared to traditional network models trained on one-dimensional time-series inputs. Additionally, CWT time-frequency diagrams provide a more comprehensive information representation than GSI, enhancing feature extraction accuracy.

(2) When Gaussian white noise with signal-to-noise ratios (SNRs) of 9 dB, 5 dB, and 1 dB is added to the original data, the 2D image-based identification methods demonstrated significantly higher accuracy than traditional 1D time-series signal approaches for noisy data. The performance advantage of CWT-CNN became especially apparent as noise levels increased. A detailed analysis of all measurement points showed that, in the numerical simulation dataset, CWT-CNN achieved identification accuracies of 99.87%, 99.28%, and 97.67%, respectively, across different noise levels. Meanwhile, the extended steel beam dataset achieved 99.26%, 98.76%, and 98.36% accuracy.

(3) Network models that use one-dimensional time-series inputs exhibited poor performance when identifying untrained samples, while two-dimensional image-based methods significantly improved accuracy. Specifically, the CWT-CNN achieved cross-source data identification rates of 96.40% and 98.61%, demonstrating a clear enhancement over other tested models.

The CWT-CNN can analyze damage signals directly without needing additional prior knowledge or expert input. Also, the proposed method uses fewer measurement points, which greatly lowers the cost of structural damage detection. We plan to extend the CWT-CNN in future research to locate unknown damage, further increasing its practical usefulness.

Acknowledgments

This research was supported by Shaanxi Provincial Key Research and Development Program of China (2024GX-YBXM-305, 2024GX-YBXM-178) and National Natural Science Foundation of China (No. 52475531).

References

[1] TENG Z Q, TENG S, ZHANG J Q, et al. Structural Damage Detection Based on Real-Time Vibration Signal and Convolutional Neural Network. Applied sciences, 2020, 10(14), e4720.
[2] TOAN N T, KHIEML K. A novel method for crack detection in beam-like structures by measurements of natural frequencies[J]. Journal of Sound and Vibration, 2014, 333(18).
[3] LI L, YUAN Y C. Damage detection for frame beams based on changes in mode rotary angles[J]. Journal of Vibration and Shock, 2019, 38(01): 180-186.
[4] WANG M, WENG S, YU X S, et al. Structural damage identification based on time-varying modal mode shape of wavelet transformation[J]. Journal of Vibration and Shock, 2021, 40(16): 10-19.
[5] PENG H B, ZHANG Q Q, DAN M. Research on damage recognition of blade-disc structure based on improved curvature modal[J]. Machine Tool & Hydraulics,2020,48(6):99-106.
[6] ZHANG X Y, FU Q, HUANG Q, et al. Fault Identification Method of Centrifugal Pump Bearing Based on CWT-CNN[J]. Machine Tool & Hydraulics,2024, 52(12): 202-207.
[7] QIN S Q, SU S, YANG R. Structural damage identification based on multi-label convolution neural networks[J]. Journal of Architecture and Civil Engineering, 2024,41(03): 108-119.
[8] ABDELJABER O, AVCI O, KIRANYAZ S, et al. Real-time vibration-based structural damage detection using one-dimensional convolutional neural networks[J]. Journal of Sound and Vibration, 2017, 388: 154-170.
[9] ABDELJABER O, AVCI O, KIRANYAZ M S, et al. 1-D CNNs for structural damage detection: Verification on a structural health monitoring benchmark data[J]. Neurocomputing, 2018, 275:1308-1317.
[10] LI Z F, KANG S, WANG Z F, et al. Structural damage identification based on time-frequency transform and convolutional neural network[J]. Journal of Disaster Prevention and Mitigation Engineering,2023,43(06):1275-1283.
[11] YU Y, WANG C, GU X, et al. A novel deep learning-based method for damage identification of smart building structures [J]. Structural health monitoring, 2019, 18(1): 143-163.
[12] TENG H, KANG S, WANG Z F, et al. Research on structural damage identification based on deep learning [J]. World Earthquake Engineering, 2023, 39(03): 68-74.
[13] COFRE-MARTEL S, KOBRICH P, DROGUETT E L, et al. Deep Convolutional Neural Network-Based Structural Damage Localization and Quantification Using Transmissibility Data[J]. Shock and Vibration, 2019:1-27.
[14] ALAZZAWI O, WANG D. Deep convolution neural network for damage identifications based on time-domain PZT impedance technique[J]. Journal of Mechanical Science and Technology, 2021, 35(4).
[15] LUO Y P, WANG L K, GUO X et al. GAF-CNN based structural damage recognition using single sensor data[J]. Journal of Vibration, Measurement & Diagnosis, 2022, 42(01): 169-176+202-203.
[16] WANG Q X, LI X J, REN Y J, et al. Study on structural damage identification based on VMD-WT-CNN[J]. Journal of Qingdao University of Technology, 2023, 44(04).
[17] LIANG T, YE T P, LI S W, et al. Combining multi-channel MTF and CNN for frame structure damage recognition[J]. Journal of Vibration, Measurement & Diagnosis, 2024, 44(02): 217-224+404-405.
[18] LIANG X J. Research on structural damage recognition based on piezoelectric sensing technology and deep learning[D]. Guangzhou: Guangzhou University, 2023.
[19] LIANG R J, RAN F, YU C L, et al. Recognition of gearbox operation fault state based on CWT-CNN[J]. Journal of Aerospace Power, 2021, 36(12): 2465-2473.
[20] TANG Y H, ZHANG C Y, ZHANG D D, et al. Bearing fault identification based on credible multi-scale quadratic attention convolutional neural network[J/OL]. Computer Integrated Manufacturing Systems:1-17[2024-07-12].
[21] HERNANDEZ-GARCIA M R, MASRI S F. Application of statistical monitoring using latent-variable techniques for detection of faults in sensor networks[J]. Journal of Intelligent Material Systems & Structures, 2014, 25（2）: 121-136.
[22] HUANG H B, YI T H, LI H N. Sensor fault diagnosis for structural health monitoring based on statistical hypothesis test and missing variable approach[J]. Journal of aerospace engineering, 2017, 30(2): B4015003.
[23] Song T X, Huang J C, Liu S Q, et al. Gear fault diagnosis method based on DWT and 2D-CNN in small samples[J/OL]. Computer Integrated Manufacturing Systems:1-15[2024-07-22]. http://kns.cnki.net/kcms/detail/11.5946.TP.20230423.1131.004.html.
[24] ZHANG Y, MIYAMORI Y, MIKAMI S, et al. Vibration-based structural state identification by a 1 1-dimensional convolutional neural network[J]. Computer -Aided Civil and Infrastructure Engineering, 2019, 34(9): 822-839.
[25] V. LAURENS. Accelerating t-SNE using tree-based algorithms[J]. Journal of Machine Learning Research, 2014, 15(1): 3221-3245.

Advanced Steel Construction – Vol. 22 No. 5 (2026) 572–581
DOI:10.18057/IJASC.2026.22.5.8

MECHANICAL PROPERTIES AND RELIABILITY ASSESSMENT OF POST-FIRE HIGH-STRENGTH STEEL

Zi-Hao Xiong [1], Qing-Rui Deng [1], Ming-Yu Zhu [1], Yu-Feng Zhang [1] and Pan Chen [2, *]

[1] *School of Civil Engineering, Wuhan University, Wuhan, 430072, PR China*
[2] *School of Civil Engineering, Hubei Engineering University, Xiaogan, 432000, PR China*
** (Corresponding author: E-mail: chenpan@hbeu.edu.cn)*

ABSTRACT

Steel structures represent one of the most prevalent structural systems in modern construction, with high-strength steel (HSS) increasingly adopted for its superior performance characteristics. A comprehensive understanding of the post-fire mechanical properties of steel structures is essential for safety assessment due to their inherent thermal sensitivity. However, previous studies have not adequately considered the uncertainty in the mechanical properties of post-fire HSS. This study addresses this research gap by conducting 90 tensile tests on various grades of HSS exposed to different temperatures. The results demonstrate that the ultimate and yield strength of all HSS grades remained relatively stable after exposure to 300 °C, decreased moderately after exposure to 550 °C and 680 °C, and exhibited significant degradation after exposure to 800 °C. Furthermore, the post-fire yield strength of HSS can be represented by a normal distribution, verified by four statistical hypothesis tests. The research established a resistance attenuation function for post-fire HSS and evaluated the reliability of post-fire HSS under six load levels. These findings provide a reference for safety assessment and repair decision-making for fire-damaged HSS structures.

ARTICLE HISTORY

Received: 26 July 2025
Revised: 27 January 2026
Accepted: 6 February 2026

KEYWORDS

High-strength steel;
Post-fire;
Mechanical properties;
Reliability

Copyright © 2026 by The Hong Kong Institute of Steel Construction. All rights reserved.

1. Introduction

Steel structures have been extensively employed in buildings such as stadiums, airports, and bridges due to their lightweight characteristics, superior mechanical properties, and ease of maintenance[1-3]. In recent years, with the increasing prevalence of long-span and high-rise steel structures, high-strength steel (HSS) has gained broader application[4-6] compared to low-carbon steel due to its cost-effectiveness and enhanced strength-toughness balance[7-9]. Building fires continue to cause property losses annually[10-12], and the structural performance of steel buildings is significantly compromised under fire exposure[13], highlighting the critical importance of fire-resistant design research for steel structures. Damaged structures can either be directly reused or rehabilitated through reinforcement, an approach that effectively mitigates resource waste[14-16]. Precise damage evaluation and scientifically informed repair strategies fundamentally depend on understanding the material's residual mechanical properties after fire exposure. Consequently, investigating the post-fire performance of HSS and evaluating its post-fire safety and reusability are of paramount importance.

Numerous studies have investigated the degradation mechanisms of mechanical properties in conventional post-fire steels[17-19]. Tao et al.[17] analyzed the post-fire behavior of structural steels, quantifying residual elastic modulus, residual yield strength, and residual ultimate strength. Through experimental investigation of Q235 steel, Ding et al.[18] established comprehensive relationships for post-fire Poisson's ratio, and tensile stress-strain behavior. However, existing studies have demonstrated that fire-resistant design principles cannot be directly extrapolated from conventional steels to HSS due to their distinct material responses[20], necessitating dedicated research on HSS post-fire mechanical properties. Aziz and Kodur[7] examined the material characteristics of A572 steel both during and after elevated temperatures, revealing that air-cooling versus water-quenching affects residual strength when cooling from 600 °C or higher. Qiang et al.[8] investigated post-fire S460 and S690 steels, developing two distinct predictive equations for evaluating post-fire mechanical performance. Nevertheless, these studies overlooked the inherent variability and uncertainty in post-fire mechanical properties, which necessitates a systematic reliability assessment approach in the context of conventional steels. Xing et al.[21] conducted reliability analysis for HK40 steel under thermal conditions, while Wang and Xia[22] employed the First-Order Second-Moment (FOSM) method to verify reliability of post-fire Q345. Given the current absence of reliability studies on post-fire HSS, it is imperative to investigate the performance degradation patterns of fire-exposed HSS, develop statistical models, and conduct comprehensive reliability analyses.

This study systematically investigates the degradation mechanisms and statistical modeling of post-fire performance in HSS, with particular emphasis on reliability assessment under varying temperature exposures. A comprehensive experimental program involving post-fire tensile tests was conducted on 90 HSS specimens. The specimens were exposed to five temperature levels selected based on metallurgical framework: ambient temperature, 300 ℃, 550 ℃, 680 ℃ and 800 ℃. The analysis focused on quantifying degradation patterns of key mechanical properties, including yield strength and ultimate tensile strength, leading to the development of an empirical formulation for predicting post-fire yield strength. The statistical characteristics of material strength were rigorously determined through probabilistic analysis. Furthermore, structural reliability assessments were performed considering multiple safety levels, as quantified by selected safety factors, to evaluate the post-fire reliability of HSS components.

2. Experimental overview

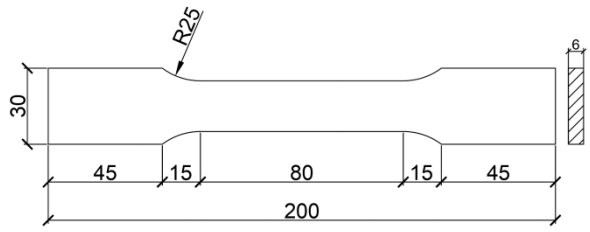
2.1. Experimental design

Experimental materials comprised three grades of HSS: Q460, Q550 and Q690. All steels were produced via the quenched and tempered (QT) process and sourced from a single production batch per grade to ensure consistency in the initial microstructure and chemical composition. The chemical compositions and elemental proportions of each steel grade are detailed in Table 1.

Table 1
Chemical composition of HSS

HSS	Chemical compositions（%×100）																A_{c1}	A_{c3}
	C	Si	Mn	P	S	Al	Als	Nb	Ti	V	B	N	Cu	Ni	Cr	Mo	(℃)	(℃)
Q460	7	4	126	1.8	0.34	5.7	5.3	3.2	5.1	0.2	0.01	0.36	1.6	1.4	3.5	0.6	711	858
Q550	4.84	14.95	103	1.4	0.4	-	-	-	-	-	-	-	-	-	-	-	716	872
Q690	7	9	165	1.2	0.1	-	3	0.2	12.7	0.4	0.02	0.37	3	2	29	0.6	713	861

As illustrated in Fig. 1, standard tensile specimens were fabricated in accordance with *Standard Test Methods and Definitions for Mechanical Testing of Steel Products* (ASTM A370-19)[23]. The experimental program comprised 15 sets of specimens (6 specimens per set), totaling 90 test units. The grouping scheme, tabulated in Table 2, follows an A-B labeling convention where: A represents the steel grade identifier (Q460/Q550/Q690) and B represents the peak temperature exposure level (ambient, 300 ℃, 550 ℃, 680 ℃, 800 ℃). All tensile specimens were extracted from 6 mm thick steel plates, with their longitudinal axes aligned parallel to the rolling direction (longitudinal orientation). It is acknowledged that mechanical properties can exhibit directionality due to rolling texture; therefore, the data reported in this study characterize the material performance in the longitudinal direction.



(a) Standard tensile specimen dimension



(b) Cutting process

Fig. 1 Standard tensile specimen

Table 2
Mechanical properties of post-fire HSS

Samples	Grade	Peak temperatures (°C)	Yield strength (MPa)		Ultimate strength (MPa)	
			Mean	Standard deviation	Mean	Standard deviation
Q460-20	Q460	20	597.41	6.910	679.34	7.144
Q460-300		300	604.78	18.242	675.50	11.727
Q460-550		550	582.58	13.444	642.27	12.555
Q460-680		680	524.51	6.963	578.50	6.060
Q460-800		800	353.40	8.275	450.48	4.418
Q550-20	Q550	20	649.24	7.483	724.70	6.153
Q550-300		300	667.79	13.563	740.79	12.788
Q550-550		550	627.62	9.852	692.72	9.827
Q550-680		680	561.62	5.897	624.90	4.361
Q550-800		800	363.21	6.705	497.30	5.277
Q690-20	Q690	20	760.28	6.103	802.35	6.228
Q690-300		300	804.59	13.756	844.42	11.836
Q690-550		550	734.16	10.938	772.06	10.281
Q690-680		680	675.04	7.489	730.52	7.613
Q690-800		800	383.91	6.897	512.04	6.369

The experimental results demonstrate that steel exhibits blue brittleness within the 180 ~ 370 ℃ temperature range. In this critical temperature interval, accelerated diffusion of interstitial atoms pins dislocations and restricts their movement, leading to increased strength and reduced ductility[24, 25]. When steel is exposed to temperatures between the blue brittleness range and the A_{C1} critical point, the high-density dislocation networks in cold-worked microstructures are progressively replaced by strain-free equiaxed grains. This reduces dislocation density and results in a decrease in strength[24, 26]. The A_{C1} temperature denotes the onset of austenite formation from ferrite during heating, whereas A_{C3} represents the completion of ferrite-to-austenite transformation. Above A_{C1}, ferrite and pearlite dissolve into austenite. Subsequent slow cooling to ambient temperature allows the austenite to decompose into equilibrium ferrite-pearlite structures. Notably, coarsening of cementite lamellae in pearlite and the formation of coarse mixed microstructures during annealing both contribute to significant strength loss[24, 27]. These critical phase transformation temperatures (A_{C1} and A_{C3}) were determined using Andrews' empirical formulae[28], derived from steel chemical composition:

$$A_{C1} = 723 - 10.7Mn - 16.9Ni + 29.1Si + 16.9Cr + 290As + 6.38W \quad (1)$$

$$A_{C3} = 910 - 203\sqrt{C} - 15.2Ni + 44.7Si + 104V + 31.5Mo + 13.1W \quad (2)$$

The calculated A_{C1} and A_{C3} values for each steel grade are systematically presented in Table 1. Based on this metallurgical framework, four fire exposure temperatures (300 ℃, 550 ℃, 680 ℃, 800 ℃) were strategically selected along with an ambient control group (20 ℃) to comprehensively investigate the residual mechanical properties of post-fire HSS.

2.2. Heating and cooling protocol

The heating and cooling tests were conducted using a SD202047 high-temperature electric furnace at Wuhan Wuce Laboratory, as shown in Fig. 2. The furnace employs resistance wires for heating, and temperature was monitored by integrated sensors. Each standard tensile specimen was suspended within the furnace chamber using iron wires to ensure uniform heat exposure. To ensure uniform heating, the furnace interior was lined with thermal ceramic fiber rock wool as insulation. After closing the furnace door, fire-resistant cotton was applied to seal the upper and lower openings. The specimen was heated at a rate of 20 °C/min, complying with EN1993-1-2 requirements (2-50 °C/min)[29]. When reaching the predetermined fire exposure temperature, the furnace maintained constant temperature for 20 minutes before stopping heating, allowing the specimen to cool naturally to room temperature inside the furnace[30]. This approach was adopted based on several considerations. First, the cooling method below the A_{C1} temperature has a relatively minor influence on the resulting strength and ductility, with the most significant microstructural

changes and mechanical property losses occurring during cooling from temperatures above this critical range[31-33]. Since a number of the test scenarios involved heating to temperatures at or below this threshold, furnace cooling was deemed a reasonable and consistent method for those cases. Second, furnace cooling allows for a controlled cooling process, avoiding the safety risks such as rapid quenching, which was crucial for ensuring experimental safety and repeatability. Furthermore, furnace cooling effectively represents a "worst-case" scenario in terms of strength loss, thereby helping to establish a reliable lower-bound estimate of residual capacity for conservative design assessment.

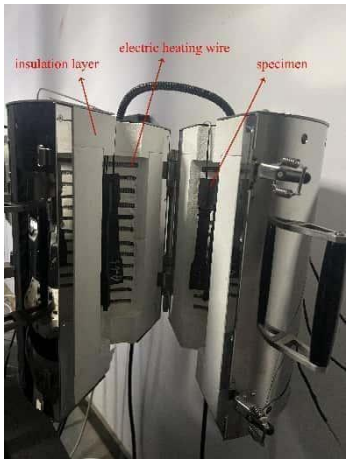


Fig. 2 Electric furnace

2.3. Uniaxial tensile testing

The material tensile tests were conducted using a 60-ton electronic universal testing machine at the Structural Engineering Laboratory of the School of Civil Engineering, Wuhan University, as shown in Fig. 3. Following ASTM A370-19[23] protocols, displacement-controlled monotonic loading was applied at a consistent rate of 2 mm/min throughout all tests. Load-displacement data were automatically acquired by the testing system's data acquisition module. The derived mechanical properties for all specimen groups are comprehensively presented in Table 2.

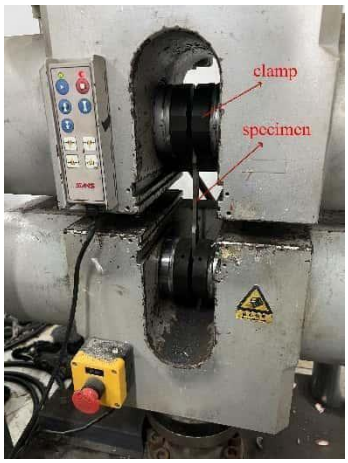


Fig. 3 Uniaxial tensile testing

3. Test results

3.1. Macroscopic features and failure modes

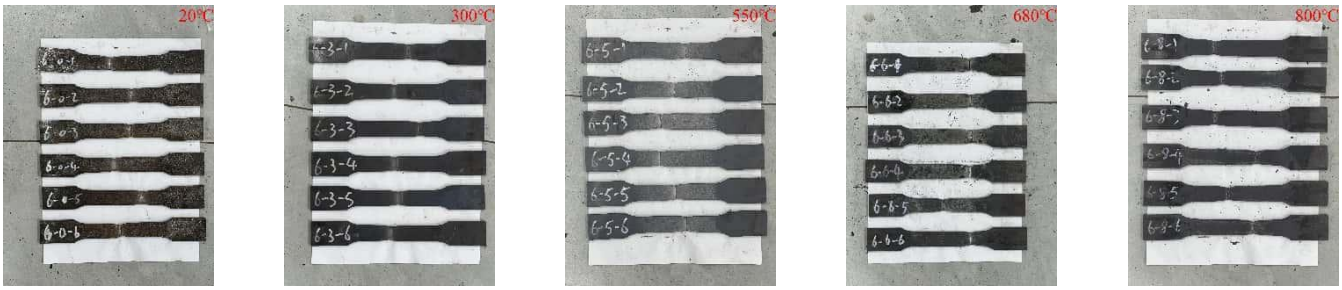
Fig. 4 demonstrates the apparent characteristics and failure modes of all specimens. Visual examination revealed that specimens cooled from 300 °C exhibited a distinctive blue appearance with a thin oxide layer formed on the surfaces. Upon cooling from 550 °C, the color of all specimens transitioned to light brown. When cooled from 680 °C, small fragments of oxide layer spalled off from all specimens. After cooling from 800 °C, significant spalling of oxide layers occurred in all specimens. All specimens exhibited characteristic necking deformation without evidence of brittle fracture, demonstrating that the HSS retained substantial ductility even after exposure to various elevated temperatures.



(a) Q460



(b) Q550



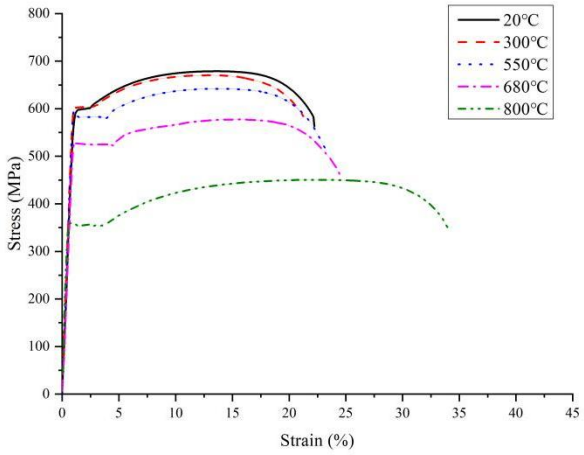
(c) Q690

Note: The specimen identification system in Fig. 4 follows the format A-B-C, where:
- A indicates the steel grade (4 = Q460, 5 = Q550, 6 = Q690)
- B represents the maximum exposure temperature (0 = ambient temperature, 3 = 300 ℃, 5 = 550 ℃, 6 = 680 ℃, 8 = 800 ℃)
- C denotes the specimen number within each group (1-6, with six specimens per group)

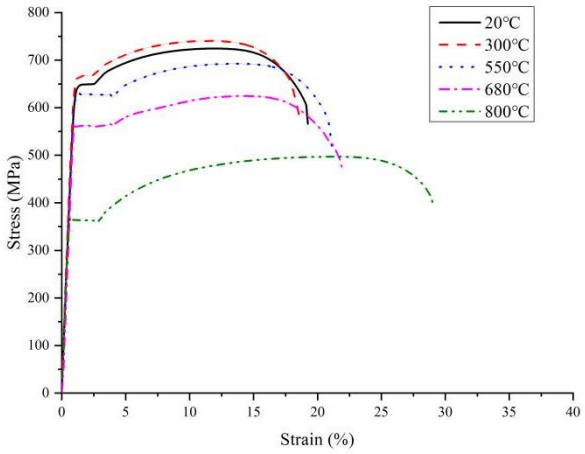
Fig. 4 Macroscopic features and failure mode

3.2. Stress-strain curves

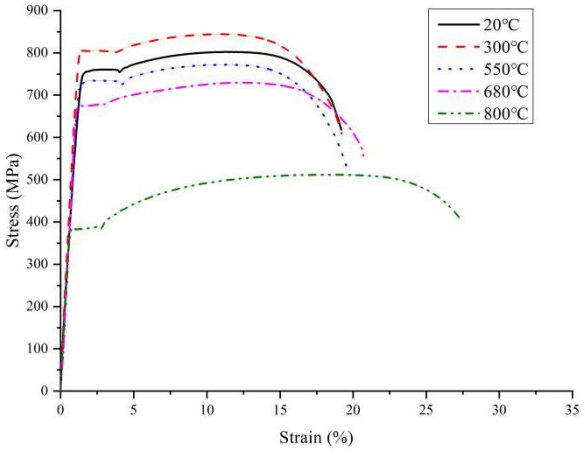
Fig. 5 illustrates the representative stress-strain curves for various HSS grades after exposure to elevated temperatures. The evolution patterns of stress-strain relationships across different HSS grades demonstrate a remarkably high degree of consistency. After high-temperature exposure, the shapes of their stress-strain curves remain comparable to those at room temperature, continuing to exhibit distinct yield plateaus and strain-hardening stages. Notably, following exposure to 300 ℃, the yield and strain-hardening plateau levels of all HSS are observed to slightly increase compared to room-temperature conditions. However, as the exposure temperature rises further, these plateau levels gradually decline. After exposure to 800 ℃, both yield and strain-hardening plateaus decrease significantly, accompanied by a substantial enhancement in ductility, thereby effectively transforming the mechanical behavior to resemble that of conventional mild steel.



(a) Q460



(b) Q550



(c) Q690

Fig. 5 Stress-strain curves

3.3. Post-fire material properties

3.3.1. Yield strength

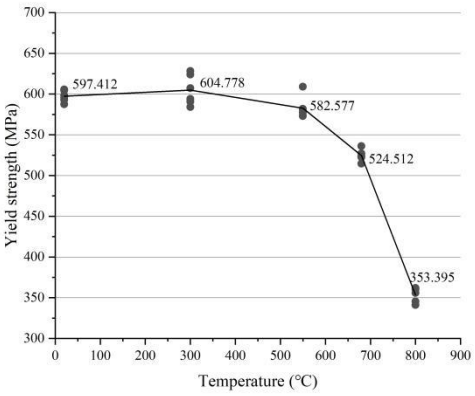
In this study, the nominal yield strength is adopted as the yield strength of the specimens, using the average cross-sectional area of the specimens to approximate their actual cross-sectional area. The nominal yield strength can be expressed by Eq. (3):

$$f_{y,T} = \frac{F_{y,T}}{A_T} \tag{3}$$

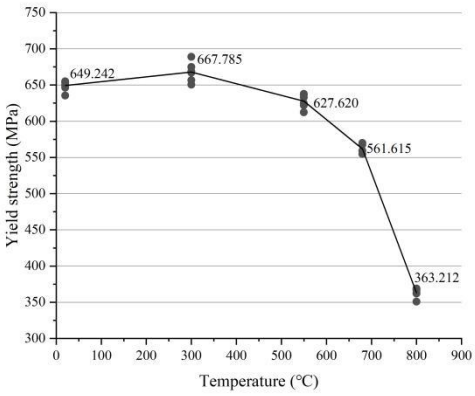
where $F_{y,T}$ and A_T represent the yield load and average cross-sectional area of the post-fire HSS, respectively.

Fig. 6 illustrates the variation in yield strength and corresponding standard deviations for different grades of HSS. Those data reveal that all HSS grades exhibit similar patterns in both yield strength evolution and standard deviation changes across the temperature spectrum. For Q460 specimens, the yield strengths after exposure to ambient temperature, 300 ℃, 550 ℃, 680 ℃ and 800 ℃ are 597.41, 604.78, 582.58, 524.51 and 353.40 MPa, respectively; For Q550 specimens, the corresponding yield strengths are 649.24, 667.79, 627.62, 561.62 and 363.21 MPa; For Q690 specimens, the values are 760.28, 804.59, 734.16, 675.04 and 383.91 MPa. All steel grades show minimal yield strength variation after 300 ℃ exposure, moderate reduction after 550 ℃ and 680 ℃ treatments, and significant strength decline following 800 ℃ exposure. This phenomenon can be interpreted based on established metallurgical principles: at 550 ℃ and 680 ℃, the observed gradual strength degradation is consistent with the recrystallization processes in cold-deformed microstructures, which progressively reduce dislocation density with increasing temperature. At 800 ℃, the austenite formed during heating would decompose into softer equilibrium phases during subsequent slow cooling, with the coarsening of microstructural features contributing to strength loss. These mechanistic frameworks, widely supported by literature on high-strength structural steels[34,35], provide a coherent explanation for the mechanical performance trends observed in this study. It is acknowledged that the specific microstructural changes are inferred from these established principles, as our experimental program was primarily focused on mechanical performance assessment.

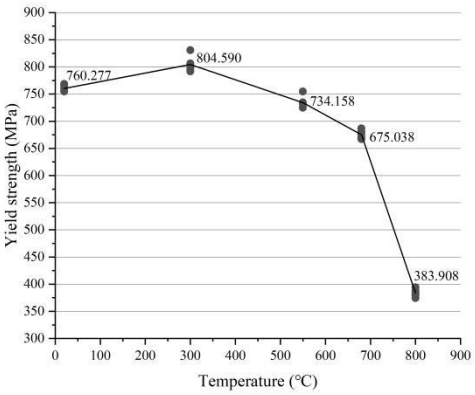
For Q460 specimens, the standard deviations of yield strength after exposure to ambient temperature, 300 ℃, 550 ℃, 680 ℃ and 800 ℃ are 6.910, 18.242, 13.444, 6.963 and 8.275 MPa, respectively; For Q550 specimens, the corresponding standard deviations are 7.483, 13.563, 9.852, 5.897 and 6.705 MPa; For Q690 specimens, the values are 6.103, 13.756, 10.938, 7.489 and 6.897 MPa. All HSS grades exhibit larger yield strength standard deviations after 300 ℃ and 550 ℃ exposures compared to ambient temperature specimens, while their standard deviations return to levels comparable with ambient temperature groups following 680 ℃ and 800 ℃ treatments. This behavior may be attributed to the increased material heterogeneity caused by C and N atom pinning dislocations at 300 ℃ and inhomogeneous recrystallization of cold-deformed microstructures at 550 ℃. At 680 ℃, approaching the A_{C1} temperature of these steels, the recrystallization process nears completion, restoring material uniformity to levels similar to ambient conditions.



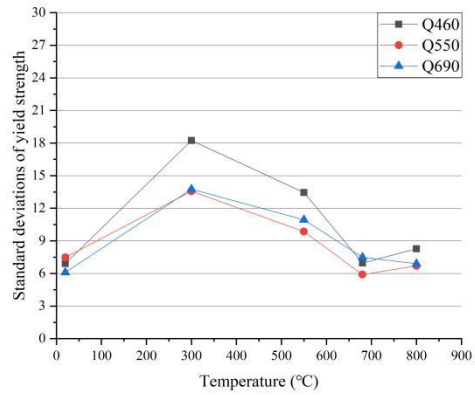
(a) Yield strength of Q460



(b) Yield strength of Q550



(c) Yield strength of Q690

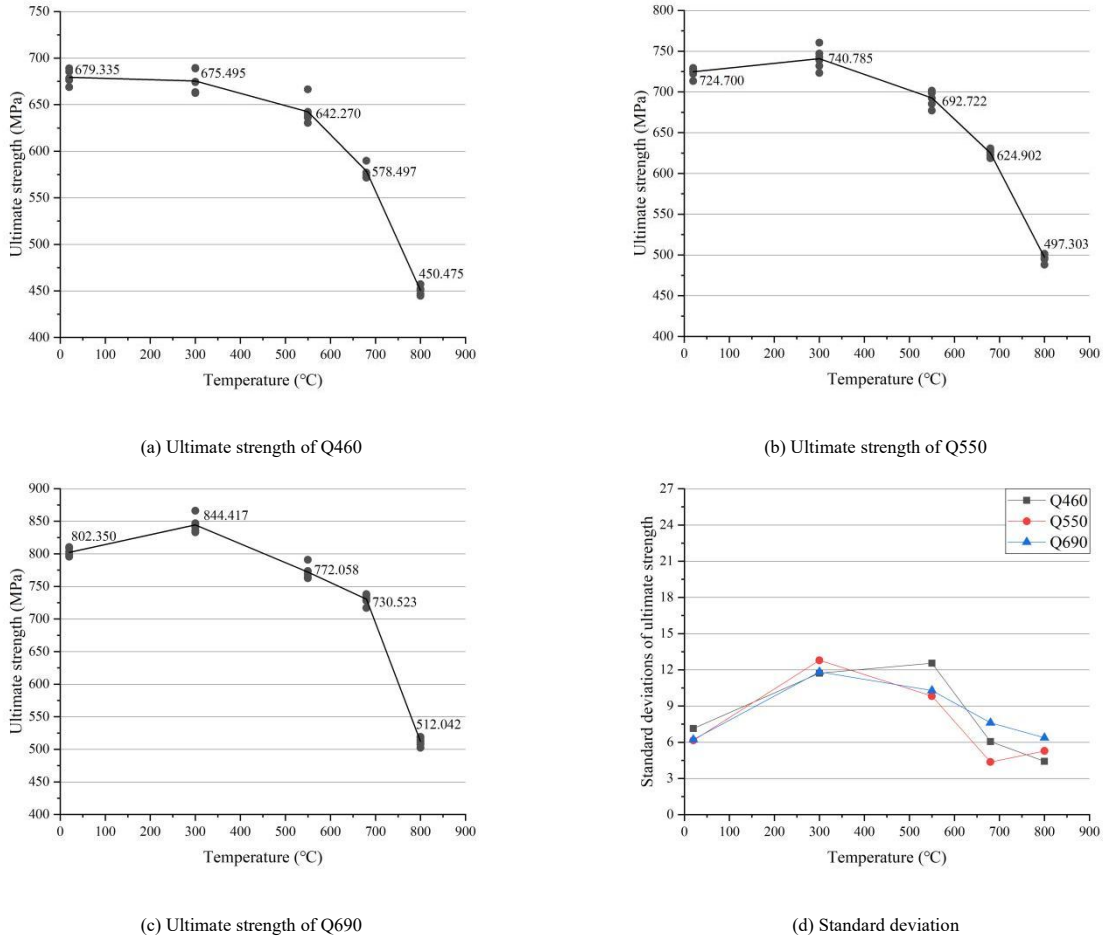


(d) Standard deviation

Fig. 6 Yield strength of HSS and its standard deviation

3.3.2. Ultimate strength

Fig. 7 presents a comprehensive analysis of ultimate strength variations and their associated standard deviations across different HSS grades. Those data reveal remarkably consistent patterns in both ultimate strength evolution and standard deviation changes across all tested steel grades. For Q460 specimens, the ultimate strengths after exposure to ambient temperature, 300 ℃, 550 ℃, 680 ℃ and 800 ℃ are 679.34, 675.50, 642.27, 578.50 and 450.48 MPa, respectively; For Q550 specimens, the corresponding ultimate strengths are 724.70, 740.79, 692.72, 624.90 and 497.30 MPa; For Q690 specimens, the values are 802.35, 844.42, 772.06, 730.52 and 512.04 MPa. Similar to the yield strength behavior, all steel grades show minimal variation in ultimate strength after 300 ℃ exposure, moderate reduction following 550 ℃ and 680 ℃ treatments, and significant strength decline after 800 ℃ exposure. The explanation for this phenomenon is similar to section 3.3.1.



(a) Ultimate strength of Q460

(b) Ultimate strength of Q550

(c) Ultimate strength of Q690

(d) Standard deviation

Fig. 7 Ultimate strength of HSS and its standard deviation

For Q460 specimens, the standard deviations of ultimate strength after exposure to ambient temperature, 300 ℃, 550 ℃, 680 ℃ and 800 ℃ are 7.144, 11.727, 12.555, 6.060 and 4.418 MPa, respectively; For Q550 specimens, the corresponding values are 6.153, 12.788, 9.827, 4.361 and 5.277 MPa; For Q690 specimens, the values are 6.228, 11.836 MPa, 10.281, 7.613 and 6.369 MPa. Similarly, all HSS grades exhibit larger ultimate strength standard deviations after 300 ℃ and 550 ℃ exposures compared to ambient temperature specimens, while their standard deviations return to levels comparable with ambient temperature groups following 680 ℃ and 800 ℃ treatments. The explanation for this phenomenon is similar to section 3.3.1.

4. Reliability assessment

Reliability assessment constitutes the cornerstone of probabilistic limit state design methodology, providing a systematic framework for integrating various sources of uncertainty, including material property variability, geometric parameter tolerances, and analytical model approximations. This design philosophy has been adopted by multiple international structural design standards, including the *General Principles on Reliability for Structures* (ISO 2394-2015)[36], the *Eurocode — Basis of Structural Design* (EN 1990-2010)[37], and the *Unified Standard for Reliability Design of Engineering Structures* (GB 50153-2008)[38]. In accordance with structural reliability principles, the Chinese design code *Standard for Design of Steel Structures* (GB 50017-2017)[39] employs conservative percentile values as characteristic values to reduce the material yield/ultimate strengths obtained through testing. Resistance partial factors are further applied to derive design values from these characteristic values. For calculating the load-bearing capacity of steel structures, the design methodology incorporates load effect coefficients, with the axial force design value mathematically expressed as the product of an equivalent coefficient (α)[39-41], the material tensile strength, and the cross-sectional area of the structural member.

4.1. Statistical model for yield strength of post-fire HSS

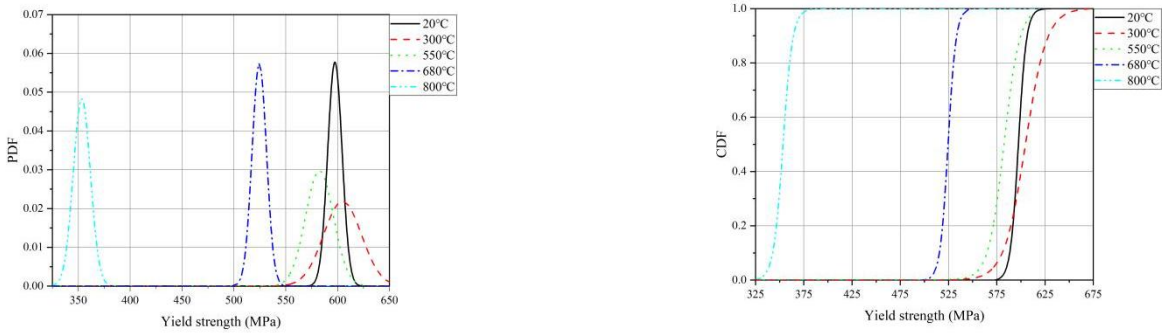
The steel structural limit state design typically considers material yielding rather than ultimate strength attainment[42]. The experimental results presented in preceding sections demonstrate that yield strength data for each specimen group (defined by identical steel grade and temperature exposure conditions) exhibit distinct statistical characteristics. Significantly, the standard deviation of HSS yield strength shows vital temperature-dependent variations, necessitating careful redefinition of its probabilistic distribution parameters for accurate reliability assessment.

In accordance with the *Unified Standard for Reliability Design of Engineering Structures* (GB 50153-2008)[38], material property design parameters and their associated probability distribution functions must be rigorously determined through statistical parametric estimation and formal hypothesis testing of experimental data. Within this framework, characteristic strength values are defined as the 5th percentile of the statistically confirmed probability distribution. This validates the normality assumption through four hypothesis testing methodologies—Shapiro-Wilk test, Kolmogorov-Smirnov test, Anderson-Darling test, and Lilliefors test—applied to experimental datasets with a significance level of 0.05. In Table 3, all specimen groups demonstrate compliance with normal distribution, evidenced by p-values exceeding 0.05 across tests. The table presents test statistics and corresponding p-values for each method, confirming the validity of the normality assumption for subsequent reliability analyses.

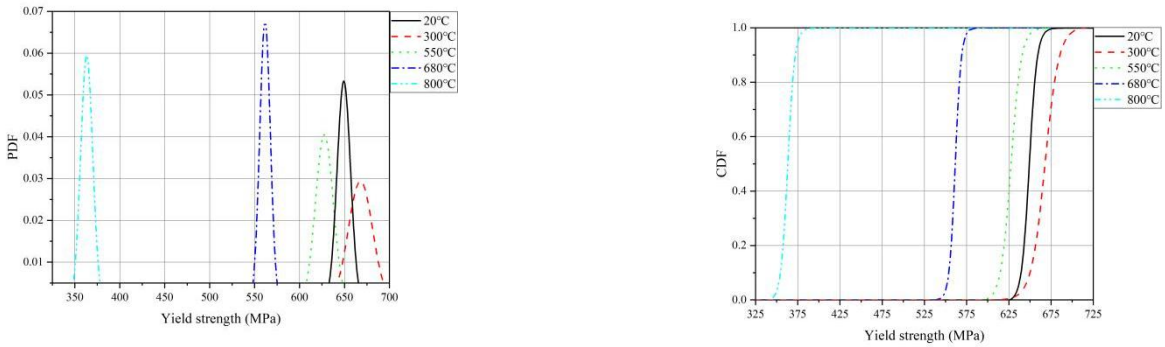
The probability density functions (PDFs) and cumulative distribution functions (CDFs) of yield strength are illustrated in Fig. 8, with their mean values and standard deviations (for each specimen group) derived from experimental data. The PDFs and CDFs exhibit consistent temperature-dependent evolution patterns across all HSS grades. At 300 ℃, the PDF peaks shift downward along the vertical axis with flattened distributions, indicating comparable mean yield strengths but increased standard deviations. Under 550 ℃ exposure, the peaks migrate leftward and downward, accompanied by further distribution flattening, signifying slight reductions in mean yield strength alongside elevated standard deviations. For specimens subjected to 680 ℃ and 800 ℃, the PDF peaks shift leftward with similar distribution shapes, demonstrating significant mean strength reductions while maintaining comparable standard deviations across these high-temperature conditions.

Table 3
Results of the normal distribution hypothesis tests of the yield strength of post-fire HSS

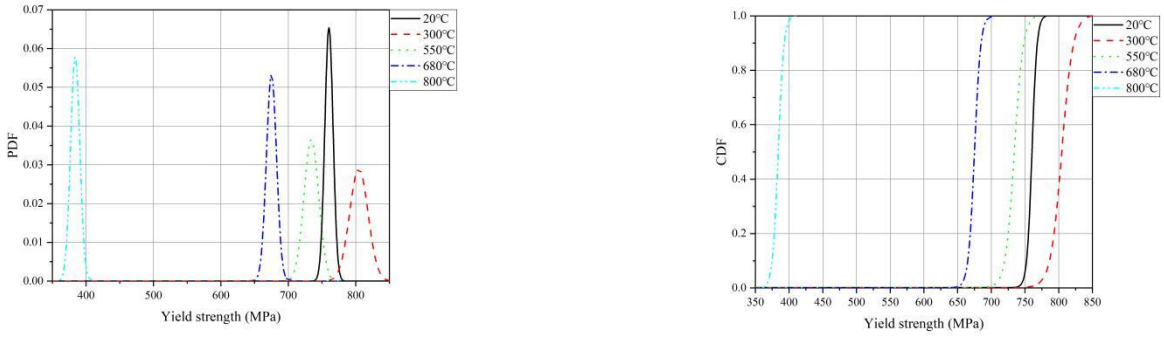
Grade	Samples	S-W test		K-S test		A-D test		Lilliefer test	
		Statistic	P value	Statistic	P value	Statistic	P value	Statistic	P value
Q460	Q460-20	0.957	0.799	0.177	1	0.191	0.817	0.177	0.2
	Q460-300	0.908	0.421	0.221	0.979	0.307	0.439	0.221	0.2
	Q460-550	0.740	0.016	0.353	0.360	0.756	0.022	0.353	0.02
	Q460-680	0.935	0.616	0.215	1	0.341	0.354	0.215	0.2
	Q460-800	0.890	0.317	0.284	0.642	0.379	0.275	0.284	0.135
Q550	Q550-20	0.821	0.090	0.234	0.906	0.516	0.111	0.234	0.2
	Q550-300	0.975	0.924	0.148	1	0.178	0.858	0.148	0.2
	Q550-550	0.929	0.576	0.200	1	0.256	0.573	0.200	0.2
	Q550-680	0.869	0.222	0.326	0.455	0.494	0.126	0.326	0.05
	Q550-800	0.838	0.125	0.260	0.762	0.484	0.135	0.260	0.2
Q690	Q690-20	0.849	0.156	0.275	0.685	0.448	0.174	0.275	0.157
	Q690-300	0.840	0.131	0.287	0.625	0.507	0.118	0.287	0.127
	Q690-550	0.813	0.077	0.316	0.493	0.567	0.079	0.316	0.061
	Q690-680	0.927	0.560	0.234	0.907	0.271	0.529	0.234	0.2
	Q690-800	0.991	0.991	0.146	1	0.147	0.926	0.146	0.2



(a) Q460



(b) Q550



(c) Q690

Fig. 8 PDFs and CDFs of yield strength

4.2. Reliability assessment of post-fire HSS

The probability that the limit state function (or performance function) is non-positive is estimated as follows:

$$Z = g(R,S) = R(T) - S = 0 \tag{4}$$

where S represents the load effect; $R(T)$ denotes the resistance of steel members after exposure to a specific maximum temperature T. According to the *Standard for Design of Steel Structures* (GB 50017-2017)[39], this study defines $R(T)$ as the post-fire yield strength, which can be mathematically expressed as:

$$R(T) = g(T)R_0 \tag{5}$$

where R_0 represents the resistance of steel at ambient temperature, and $g(T)$ denotes the resistance degradation function.

This study adopts the unified equation for residual yield strength after elevated temperatures proposed by Chen and Young[43] (as shown in Eq. (6)), with coefficients a, b, c, and n calibrated against HSS test results. The calibrated coefficients are provided in Eq. (7).

$$\frac{f_{y,T}}{f_{y,normal}} = a - \frac{(T-b)^n}{c} \tag{6}$$

The resistance degradation function $g(T)$ is:

$$g(T) = \begin{cases} 1 & 20°C \le T \le 400°C \\ 1 - \dfrac{(T-400)^{3.5}}{2.65\times10^9} & 400°C < T \le 800°C \end{cases} \tag{7}$$

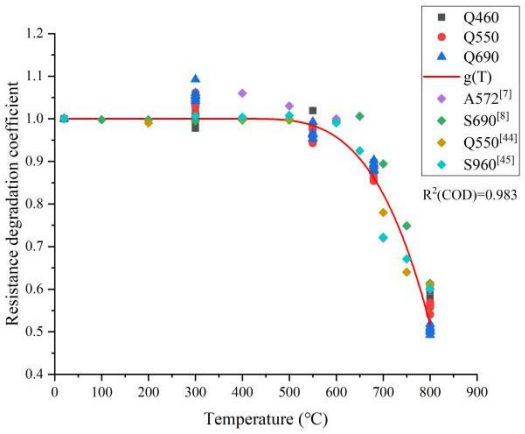


Fig. 9 Resistance degradation function

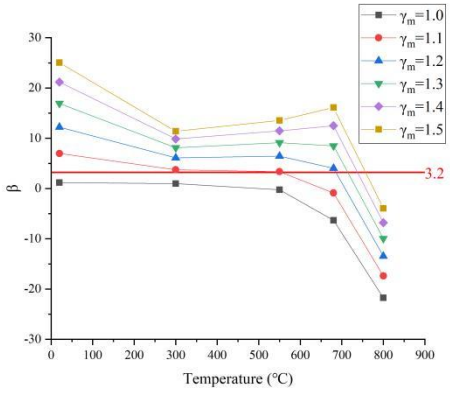
The resistance degradation function $g(T)$ for HSS after cooling from elevated temperatures was compared with experimental data from References[7, 8, 44, 45], as shown in Fig. 9. The comparative analysis demonstrates that this function provides accurate predictions of post-fire yield strength across various grades of HSS, thereby validating the reliability of the experimental methodology and data presented in this work.

It is emphasized that the resistance degradation function is applicable within a specific scope. It is applicable to HSS with nominal yield strengths up to 960 MPa, following exposure to temperatures up to 800 °C and subsequent furnace cooling. Caution is advised against extrapolating the model beyond these conditions, particularly for: (1) temperatures exceeding 800 °C; (2) very high-strength grades (e.g., ≥ Q960); (3) ultra-thin plate sections.

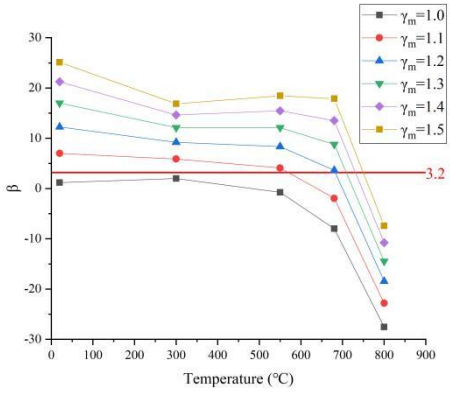
In this study, the load effect S in Eq. (4) is a random variable. One objective of this work is to investigate the post-fire material safety factor γ_m (i.e., the ratio of mean value to design value) for steel tubes, for which a series of trial material safety factors (from 1.0 to 1.5 in increments of 0.1) are assigned for reliability estimation. When the safety factor is 1.0 ($S = R_0$), the statistical data of S (normal distribution) can be obtained from corresponding experimental tests on non-fire-exposed specimen groups (i.e., the mean [standard deviation] values of S for Q460, Q550 and Q690 specimens are 586.04 MPa [6.78 MPa], 636.93 MPa [7.34 MPa] and 750.24 MPa [6.02 MPa], respectively). This approach serves as a first-order analytical simplification for the purpose of this study. It is based on two key considerations: (1) the applied (design) load is determined for "standard" steel members (i.e., at ambient temperature), and (2) it is assumed that the load effect on steel tubes after fire exposure is assumed not to diminish. The assumptions establish a consistent analytical baseline, allow the subsequent reliability analysis to isolate and clearly attribute changes in the reliability index (β) predominantly to the degradation of material resistance caused by fire exposure, rather than to concurrent variations in load effects. For material safety factors greater than 1.0, the mean value of S can be simply determined as R_0 / γ_m. It is acknowledged that this constitutes a simplification. The primary aim of the developed framework is to perform a relative reliability assessment to evaluate the trend of safety index degradation with increasing fire temperature, not to compute absolute reliability indices for specific post-fire design situations. If Z in Eq. (4) follows a marginal normal distribution, the reliability index β given in Eq. (8) may serve as a common measure of reliability. According to the first-order second-moment (FOSM) method, β can be expressed as:

$$\beta = \frac{\mu_R - \mu_S}{\sqrt{\sigma_R^2 + \sigma_S^2}} \tag{8}$$

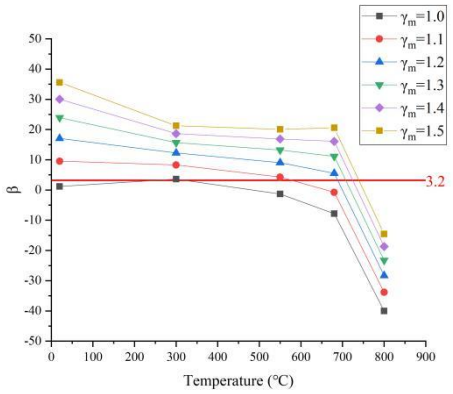
where μ and σ represent the mean value and standard deviation of resistance (denoted by subscript R) or load effect (denoted by subscript S), respectively. The reliability index β can be readily correlated with the corresponding failure probability as $P = \Phi(-\beta)$, where Φ is the standard normal cumulative distribution function. Fig. 10 illustrates the variations in reliability index as a function of temperature under different load effect conditions.



(a) Q460



(b) Q550



(c) Q690

Fig. 10 Variations in reliability index as a function of temperature

The target reliability index for evaluating the post-fire resistance predictions in this study was set at $\beta = 3.2$. This value was adopted with the *Unified Standard for Reliability Design of Engineering Structures* (GB 50153-2008)[38]. Specifically, for building structural components under persistent design situations for ultimate limit states, this standard specifies a minimum β value of 3.2 for ductile failure modes when the safety class is Level II. While some codes allow lower β for assessment, the adoption of $\beta = 3.2$ in this study is because this widely accepted design-life target inherently incorporates a margin of safety that can account for additional uncertainties inherent in post-fire conditions—such as material inhomogeneity, residual stresses, and the accuracy of fire temperature estimation—which may not be fully quantified in a deterministic analysis.

As demonstrated in Fig. 10, when the load level remains below R_0 /1.3, the reliability index consistently exceeds the target value for members exposed to temperatures up to 680 °C. However, after exposure to 800 °C, even with an elevated material safety factor of γ_m =1.5, the calculated reliability index remains significantly below the stipulated target threshold.

As discussed previously, an equivalent coefficient α integrating both load effect factors and material partial factors was proposed for computing structural design bearing capacity. The α values specified in the Chinese code[39], European code[40], and American code[41] are 0.7, 0.72, and 0.75 respectively, with corresponding $\gamma_m \approx 1.4$. Reliability indices corresponding to the load level R_0 /1.4 were determined from Fig. 10, enabling verification of whether codified safety margins adequately safeguard fire-exposed steel tube structures. Below 680 °C, the β values for Q460, Q550, and Q690 steels substantially exceed the target $\beta = 3.2$. In contrast, post-800 °C specimens demonstrate β values critically below 3.2, revealing that HSS fail to satisfy structural safety requirements under extreme thermal conditions. This necessitates implementing strengthening and rehabilitation measures for fire-damaged structures exhibiting such reliability deficits.

5. Conclusions

(1) The yield and ultimate strength of various grades of HSS show minimal change after exposure to a maximum temperature of 300 °C, while the standard deviations of yield and ultimate strength increase compared to room temperature specimens. After exposure to a maximum temperature of 550 °C, both yield and ultimate strength decrease slightly, with their standard deviations further increasing relative to room temperature specimens. Following exposure to a maximum temperature of 680 °C, the yield and ultimate strength exhibit further reduction, while their standard deviations become comparable to those of room temperature specimens. After exposure to a maximum temperature of 800 °C, both yield and ultimate strength demonstrate significant decline, with their standard deviations remaining similar to those observed in room temperature specimens.

(2) The study derived a resistance degradation function for post-fire HSS, and comparisons with extensive experimental data demonstrate that the proposed degradation function effectively captures the variation patterns of yield strength in HSS subjected to different temperatures. It should be noted that the proposed function is applicable within a defined scope. This can be referenced and selected for engineering design applications.

(3) A probabilistic analysis was conducted on the yield strength of post-fire HSS. Four commonly used hypothesis testing methods were employed to validate the normal distribution characteristics of the yield strength. The reliability analysis results indicated that for structures exposed to temperatures up to 680 °C, the material safety factor of 1.4 specified in Chinese design codes satisfies the required safety level; However, after exposure to higher temperatures, steel structures exhibit significantly increased failure risks, and consequently, strengthening and repair measures should be implemented for damaged structures.

Acknowledgments

The authors gratefully acknowledge the financial support provided by the National Natural Science Foundation of China (Grand No. 51978539; 51708240).

Reference

[1] Tian C, Jiang J, Zhang Z, et al. Post-fire mechanical properties of corroded steel under different cooling methods[J]. Thin-Walled Structures, 2025: 113329. https://doi.org/10.1016/j.tws.2025.113329

[2] Song L X, Li G Q, Wang Y C. Experimental study on the effects of whole heating cycle on post-fire behavior of restrained high strength structural steel columns[J]. Journal of Building Engineering, 2023, 70: 106385. https://doi.org/10.1016/j.jobe.2023.106385

[3] Xu C Y, Zhang X Y, Zhang J H, et al. Post-fire behavior of double-sided stainless-clad bimetallic steels[J]. Thin-Walled Structures, 2024, 203: 112128. https://doi.org/10.1016/j.tws.2024.112128

[4] Ban H, Shi G. A review of research on high-strength steel structures[J]. Proceedings of the Institution of Civil Engineers-Structures and Buildings, 2018, 171(8): 625-641. https://doi.org/10.1680/jstbu.16.00197

[5] Xue X, Shi Y, Zhou X, et al. Experimental study on the properties of Q960 ultra–high–strength steel after fire exposure[J]. Structures, 2023, 47: 2081-2098. https://doi.org/10.1016/j.istruc.2022.12.034

[6] Cai W, Li G Q. Experimental study on post-fire mechanical properties and fracture behavior of Q690 steel[J]. Thin-Walled Structures, 2023, 193: 111253. https://doi.org/10.1016/j.tws.2023.111253

[7] Aziz E M, Kodur V K. Effect of temperature and cooling regime on mechanical properties of high-strength low-alloy steel[J]. Fire and Materials, 2016, 40(7): 926-939. https://doi.org/10.1002/fam.2352

[8] Qiang X, Bijlaard F S K, Kolstein H. Post-fire mechanical properties of high strength structural steels S460 and S690[J]. Engineering Structures, 2012, 35: 1-10. https://doi.org/10.1016/j.engstruct.2011.11.005

[9] Chen Z, Lu J, Liu H, et al. Experimental study on the post-fire mechanical properties of high-strength steel tie rods[J]. Journal of Constructional Steel Research, 2016, 121: 311-329. https://doi.org/10.1016/j.jcsr.2016.03.004

[10] Ban H, Zeng Z, Yang L, et al. Post-fire mechanical properties of 316L+ Q355 stainless-clad bimetallic steels[J]. Structures, 2025, 78: 109359. https://doi.org/10.1016/j.istruc.2025.109359

[11] Lyu X, Zhang P, Wang Y Z, et al. Axial performance of ultra-high strength concrete filled double-skin circular steel tube columns after exposure to fire[J]. Structures, 2025, 79: 109311. https://doi.org/10.1016/j.istruc.2025.109311

[12] Zhang Z, Guo T, Wang S, et al. Experimental study on post-fire properties of steel wires of bridge suspender[J]. Structures, 2021, 33: 1252-1262. https://doi.org/10.1016/j.istruc.2021.04.099

[13] Garlock M, Paya-Zaforteza I, Kodur V, et al. Fire hazard in bridges: Review, assessment and repair strategies[J]. Engineering Structures, 2012, 35: 89-98. https://doi.org/10.1016/j.engstruct.2011.11.002

[14] Avent R R. Guide for Heat-Straightening of Damaged Steel Bridge Members: Final Draft of the AASHTO Guidelines[R]. Federal Highway Administration (US), 2008. https://rosap.ntl.bts.gov/view/dot/51757

[15]Maraveas C, Fasoulakis Z, Tsavdaridis K D. Post-fire assessment and reinstatement of steel structures[J]. Journal of Structural Fire Engineering, 2017, 8(2): 181-201. https://doi.org/10.1108/JSFE-03-2017-0028

[16] Azhari F, Heidarpour A, Zhao X L. On the use of Bernstain-Bézier functions for modelling the post-fire stress-strain relationship of ultra-high strength steel (Grade 1200)[J]. Engineering Structures, 2018, 175: 605-616. https://doi.org/10.1016/j.engstruct.2018.08.088

[17] Tao Z, Wang X Q, Uy B. Stress-strain curves of structural and reinforcing steels after exposure to elevated temperatures[J]. Journal of Materials in Civil Engineering, 2013, 25(9): 1306-1316. https://doi.org/10.1061/(ASCE)MT.1943-5533.0000676

[18] Ding F X, Yu Z W, Wen H L. Experimental research on mechanical properties of Q235 steel after high temperature treatment[J]. Journal of Building Materials, 2006, 9(2): 245-249.
[19] Outinen J. Mechanical properties of structural steels at high temperatures and after cooling down[M]. Helsinki University of Technology, 2007. https://aaltodoc.aalto.fi/items/e6f71813-55e9-4ac1-a6ab-1c215983ec41
[20] Zeng X, Wu W B, Huo J S, et al. Residual mechanical properties of Q890 high-strength structural steel after exposure to fire[J]. Construction and Building Materials, 2021, 304: 124661. https://doi.org/10.1016/j.conbuildmat.2021.124661
[21] Xing L I, Zhao J I E, Shen F Z, et al. Reliability analysis and life prediction of HK40 steel during high-temperature exposure[J]. International Journal of Pressure Vessels and Ping, 2006, 83(10): 730-735. https://doi.org/10.1016/j.ijpvp.2006.07.006
[22] Wang W Y, Xia Y. Design parameters and reliability analysis of Q345 steel axial loading member under high temperature[J]. Journal of Chongqing University, 2018, 41(11): 31-41. http://dx.doi.org/10.11835/j.issn.1000-582X.2018.11.004
[23] ASTM. A370–19. Standard Test Methods and Definitions for Mechanical Testing of Steel Products[S]. ASTM International, Philadelphia 2019. https://dlvn.vn/uploads/files/A370-22.pdf
[24] Xiong M X, Liew J Y R. Experimental study to differentiate mechanical behaviours of TMCP and QT high strength steel at elevated temperatures[J]. Construction and Building Materials, 2020, 242: 118105. https://doi.org/10.1016/j.conbuildmat.2020.118105
[25] Dolzhenkov I E. The nature of blue brittleness of steel[J]. Metal Science and Heat Treatment, 1971, 13(3): 220-224. https://doi.org/10.1007/BF00652795
[26] E.J. Mittemeijer. Recovery, recrystallization and grain growth, Fundamentals of Materials Science[M]. Springer, Berlin, Heidelberg, 2010. https://link.springer.com/content/pdf/10.1007/978-3-030-60056-3.pdf
[27] Yu Y, Chen Z, Liu H, et al. Effects of strength-weakening oriented heat treatment on structural steel and its application on steel plate shear walls[J]. Construction and Building Materials, 2017, 151: 827-839. https://doi.org/10.1016/j.conbuildmat.2017.06.096
[28] Andrews K W. Empirical formulae for the calculation of some transformation temperatures[J]. Journal of the Iron and Steel Institute, 1965: 721-727. https://cir.nii.ac.jp/crid/1571980075716504064
[29] Eurocode 3: Design of Steel Structures - Part 1-2: Structural fire design[S]. 2024.
[30] EN ISO 6892-2:2018, Metallic materials. Tensile testing, Method of test at elevated temperature, 2018.
[31] Azhari F, Heidarpour A, Zhao X L, et al. Mechanical properties of ultra-high strength (Grade 1200) steel tubes under cooling phase of a fire: An experimental investigation[J]. Construction and Building Materials, 2015, 93: 841-850. http://dx.doi.org/10.1016/j.conbuildmat.2015.05.082
[32] Li G Q, Lyu H, Zhang C. Post-fire mechanical properties of high strength Q690 structural steel[J]. Journal of Constructional Steel Research, 2017, 132: 108-116. http://dx.doi.org/10.1016/j.jcsr.2016.12.027
[33] Azhari F, Apon A A H, Heidarpour A, et al. Mechanical response of ultra-high strength (Grade 1200) steel under extreme cooling conditions[J]. Construction and Building Materials, 2018, 175: 790-803. https://doi.org/10.1016/j.conbuildmat.2018.04.191
[34] Zhang C, Wang R, Song G. Post-fire mechanical properties of Q460 and Q690 high strength steels after fire-fighting foam cooling[J]. Thin-Walled Structures, 2020, 156: 106983. https://doi.org/10.1016/j.tws.2020.106983
[35] Kang L, Wu B, Liu X, et al. Experimental study on post-fire mechanical performances of high strength steel Q460[J]. Advances in Structural Engineering, 2021, 24(12): 2791-2808. https://doi.org/10.1177/13694332211010601
[36] ISO 2394. General principles on reliability for structures, The International Organization for Standardization[S]. Switzerland, 2015.
[37] EN 1990 2010. Eurocode—Basis of structural design, European committee for standardization[S]. British, 2010.
[38] GB 50153-2008. Unified standard for reliability design of engineering structures[S]. China Architecture & Building Press, Beijing, 2009. (In Chinese).
[39] GB 50017-2017. Standard for design of steel structures[S]. China Architecture & Building Press, Beijing, 2018. (In Chinese).
[40] Eurocode 3. Design of steel structures-part 1-1: generalrules and rules for buildings: EN 1993-1-1: 2005[S]. London: British Standards Institution, 2005.
[41] Specification for structural steel buildings. ANSI /AISC360-10. Chicago: American Institute of Steel Construction[S]. 2010.
[42] Melchers R E. The effect of corrosion on the structural reliability of steel offshore structures[J]. Corrosion Science, 2005, 47(10): 2391-2410. https://doi.org/10.1016/j.corsci.2005.04.004
[43] Chen J, Young B. Stress–strain curves for stainless steel at elevated temperatures[J]. Engineering Structures, 2006, 28(2): 229-239. https://doi.org/10.1016/j.engstruct.2005.07.005
[44] Song L X, Li G Q. Processing and cooling effects on post-fire mechanical properties of high strength structural steels[J]. Fire Safety Journal, 2021, 122: 103346. https://doi.org/10.1016/j.firesaf.2021.103346
[45] Qiang X, Bijlaard F S K, Kolstein H. Post-fire performance of very high strength steel S960[J]. Journal of Constructional Steel Research, 2013, 80: 235-242. https://doi.org/10.1016/j.jcsr.2012.09.002

Advanced Steel Construction – Vol. 22 No. 5 (2026) 582–596
DOI:10.18057/IJASC.2026.22.5.9

THE LOAD-BEARING CAPACITY OF LATTICED COLUMN OF ELECTRIC BRIDGE-TYPE SCAFFOLD UNDER ECCENTRIC COMPRESSION

Li-Jun Ma [1, 3, 4], Hong-Bo Liu [1, 2], Hai-Jiang Zhang [2, *], Yi-Fan Liu [2], Jian-Dong Li [2] and Tian-Qi Hao [2]

[1] *State Key Laboratory of Hydraulic Engineering Intelligent Construction and Operation, Tianjin University, Tianjin 300072, China*
[2] *School of Civil Engineering, Hebei University of Engineering, Handan 056038, China*
[3] *Central Research Institute of Building and Construction Co., Ltd., MCC Group, Beijing, 100088, China*
[4] *China Formwork and Scaffold Association, Beijing, 100088, China*
** (Corresponding author: E-mail: zhjiang1994@sina.com)*

ABSTRACT

The application of electric bridge-type scaffold in the construction of high-rise structures and urban renewal is growing rapidly. To investigate the load-bearing capacity of stand latticed column of electric bridge-type scaffold under eccentric compressive loading, the latticed column specimen experimental tests and FEM simulations of columns subjected to eccentric concentrated forces were conducted, and the design formula was proposed. The longitudinal square tube with toothed steel strip bearing the eccentric compression showed the local branch component buckling, and the specimens presented the extremum point instability and elastic-plastic buckling. The local branch component buckled as the layers n was 1-2, the global-local interactive buckling occurred as the layers n was 3-4, and the overall flexural buckling dominated as the layers n exceeded 5. The eccentricity of the concentrated force exerted by the self-weight of the construction platform, the load of building materials, and the driving motor cannot be ignored. The lacing bar should not be thinner than 10mm to avoid the instability of bracing component. The longitudinal tube with toothed steel strip bearing the eccentric concentrated force showed the maximum Mises stress and tended to buckle. Based on the correlation equation, the ultimate load-bearing capacity of latticed column of electric bridge-type scaffold under eccentric compression could be calculated theoretically, and the results indicated that the correlation equation in this paper was reliable to calculate the ultimate load-bearing capacity.

ARTICLE HISTORY

Received: 3 December 2025
Revised: 31 January 2026
Accepted: 6 February 2026

KEYWORDS

Electric bridge-type scaffold;
Latticed column;
Buckling;
Ultimate load-carrying capacity;
Eccentric compression

Copyright © 2026 by The Hong Kong Institute of Steel Construction. All rights reserved.

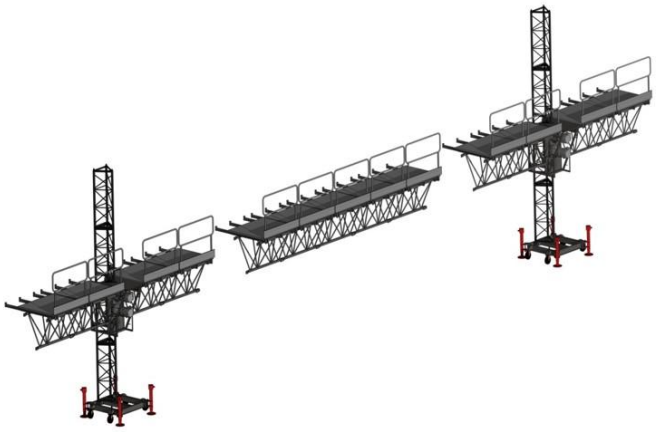
1. Introduction

Electric bridge-type scaffold was a mechanized platform suitable for high-altitude operations, which consisted of the base system, mast system, operation platform, protective system, control system, etc. It transported workers and construction materials to different height levels through the movement of gears and racks on the mast. Electric bridge-type scaffold originated in Europe, and was also known as a mast climbing work platform (MCWP) abroad. It was widely used in Europe, the United States, Canada, Australia, China, and other countries. Electric bridge-type scaffold was often used as an aerial work platform and was widely applied in residential maintenance for urban renewal, as well as in the construction of chimney silos, bridge piers, nuclear power projects, and wind power facilities, as shown in Fig. 1. The electric bridge-type scaffold had many advantages compared with the traditional tube-coupler or disk-lock scaffold[1-4], such as the good load-bearing capacity and security, modularization and easy installation, economy benefit and wide adaptability, and mechanization. Therefore, the electric bridge-type scaffold had gradually been irreplaceable to support the workers and transport the building materials mechanically in the modern practical construction process.

The stand latticed column, which was assembled by multiple standard column segments with generally the height of 1.5m, was the most load-bearing important component to transform the load of workers and materials from the operation platform to the foundation. The security of electric bridge-type scaffold was largely determined by the stability of stand latticed column. As shown in Fig. 1c, the operating platform typically consisted of a steel structure frame ranging from 1.5 meters to over 10 meters in length, allowing for the walking and placement of construction materials weighing up to tons. It was supported by a drive motor, and the drive motor was bore by the toothed steel strip welded on one of the three longitudinal steel tubes. Therefore, the stand latticed column of electric bridge-type scaffold was under the eccentric compressive load, and its ultimate load-bearing capacity under eccentric compression should be focused on.

In the previous literature, the load-bearing performance of other types of scaffolds, such as the tube-coupler scaffold[2, 3, 5, 6], disc-lock scaffold[1, 4] and door-type scaffold[7-10] were studied comprehensively through the joint rotational tests[11, 12], full-scale scaffold experimental tests, FEM analysis and corresponding theoretical analysis[13]. The loading mode included the vertical compression[7], lateral horizontal compression[1, 4] and dynamic impact[14]. However, due to various constraints, no relevant institutions had conducted research on the load-bearing capacity of electric bridge-type scaffold, which made the failure modes and ultimate resistance of latticed column of electric bridge-type scaffold under eccentric compression be confused. The previous studies and conclusions about the bearing performance of latticed column under compression, such as the profile steel built-up column[15-17], multi-tube latticed steel column[18-20] and concrete-filled steel tube latticed column[21-23], could not be directly applied to the latticed steel column of electric bridge-type scaffold, because there was some differences in load-bearing conditions, structural forms, and material types between electric bridge scaffolds and other types of lattice columns. Due to the above inadequate research, the design formula about the ultimate load-carrying capacity of stand latticed column of electric bridge-type scaffold under eccentric compressive loading was missing, which limited the further application of the electric bridge-type scaffold in practical engineering.

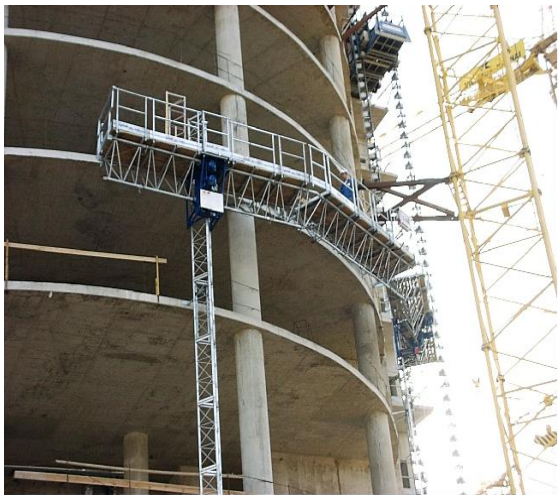
Addressing the research gap mentioned above, this paper investigated the load-bearing capacity of stand latticed column of electric bridge-type scaffold under eccentric compressive loading. The experimental tests of standard 1-layer and 2-layers latticed column specimen under eccentric compression were conducted. The FEA of latticed column of electric bridge-type scaffold under eccentric compression considering various column layers and geometric layout were carried out. Furthermore, the existing codes to estimate the ultimate load-bearing capacity of stand latticed column of electric bridge-type scaffold under eccentric compression were evaluated. The results of this paper provided an important reference for the design, monitoring, and engineering application of electric bridge-type scaffold.



(a) Composition of electric bridge-type scaffold



（b）Electric bridge-type scaffold used for urban renewal



（c）Electric bridge-type scaffold used for new construction



(d) Electric bridge-type scaffold used for bridge maintenance



(e) Electric bridge-type scaffold used for chimney

Fig. 1 The composition and practical application of electric bridge-type scaffold

2. Experimental investigation

2.1. Specimen design

Due to the spatial and height constraints of the experimental loading device, two 1-layer specimens (height was 1.5m, numbered as LC1-1L and LC2-1L) and two 2-layers specimens (height was 3m, numbered as LC1-2L and LC2-2L) were prepared to test the load-carrying capacity of eccentrically loaded latticed column of electric bridge-type scaffold experimentally. The bolt holes were provided on the angle steels at both ends of the standard 1-layer column, allowing for the connection of another set of components through bolts to construct 2-layer and multi-layer columns.

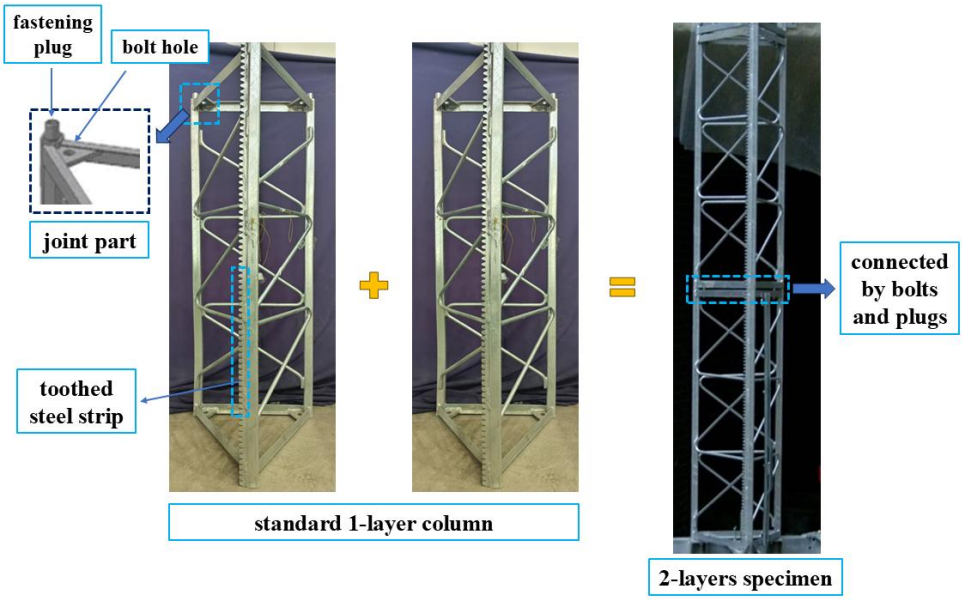
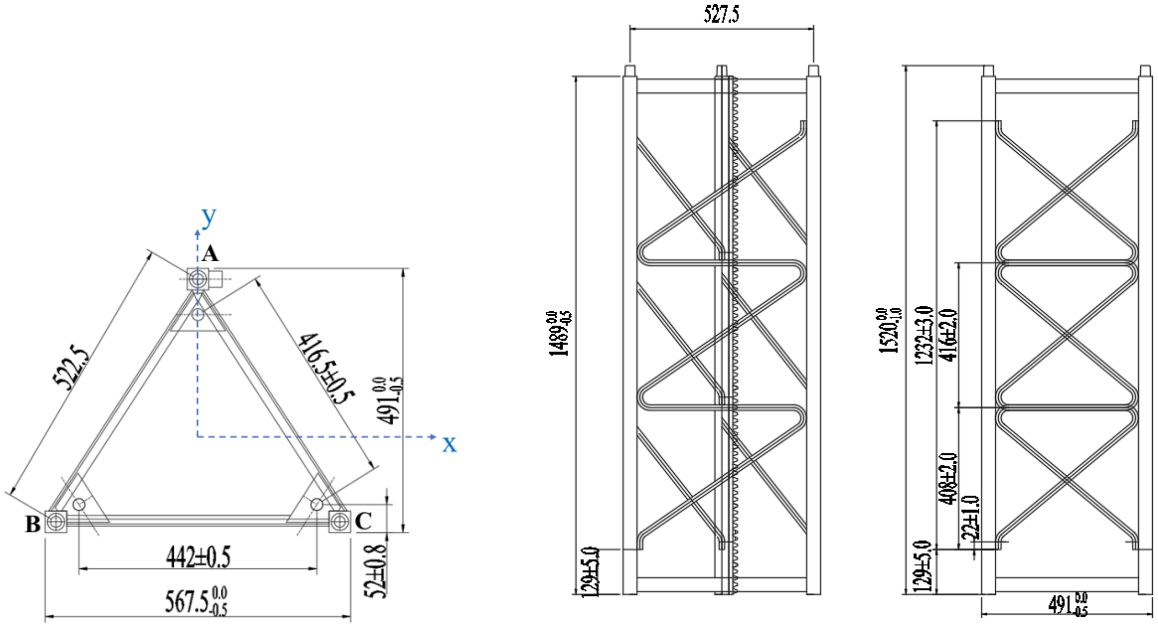


Fig. 2 The standard 1-layer and 2-layers latticed column specimens of electric bridge-type scaffold

The column component was made of Chinese Q355 steel with the yield stress of 355MPa and elasticity modulus of 206GPa. As shown in Fig. 2 and Fig. 3, the standard 1-layer latticed column was composed of three longitudinal steel tubes with the square cross-section of □ 40 × 5mm, among which, a longitudinal square tube was welded with a toothed steel strip, which bore the construction load transmitted from the construction operation platform through gear connection. It should be noted that the eccentric pressure from the drive motor was loaded on the longitudinal square tube welded with the toothed steel strip. The three longitudinal square tubes were connected by the lacing bars, which was the plain round steel bar with diameter of 15mm and was welded to the square tubes. The plain round bar was continuous and cold bent at the welding point. On the two ends of the standard 1-layer latticed column, the column section was strengthened by the three horizontal steel angles with the section of ∟40×20×3mm, which was located at the connection part between the standard 1-layer columns of the muti-layers column. As shown in Fig. 3a, the eccentric pressure was loaded at the longitudinal square tube A, and the latticed column section was bent around the x-axis. As shown in Fig. 3b, the height of one standard 1-layer column was 1.5m, and the distance between two horizontal lacing bars was about 416mm.



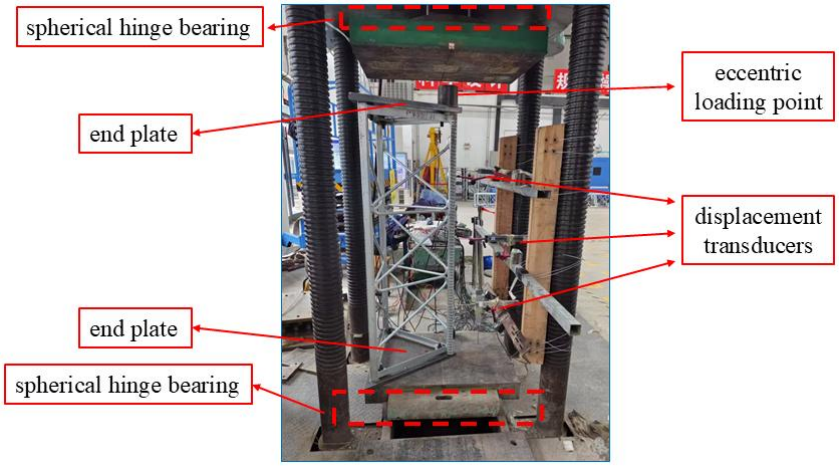
(a) The cross-sectional geometric features (mm) (b) The side-view geometric features (mm)

Fig. 3 The geometric features of the standard 1-layer latticed column of electric bridge-type scaffold (mm)

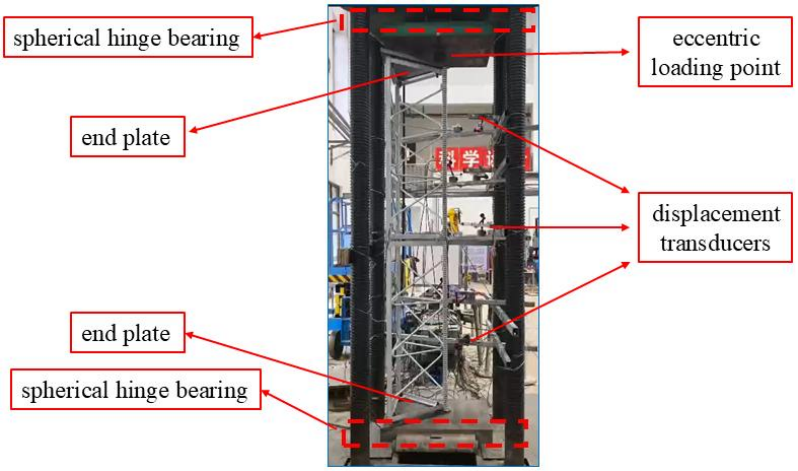
2.2. Test setup and loading procedure

As shown in Fig. 4, the eccentric compressive loading was applied through the 5000kN long column testing machine. The steel column located at the end of the longitudinal square tube A was welded to the upper end plate. The axis of the loading device coincided with the axis of the small steel column at end A, so as to apply an eccentric compressive load to the longitudinal square tube welded with the toothed steel strip, which was consistent with the actual loading conditions. The compressive loading was applied from the testing machine to the latticed column through the spherical hinge bearing.

To ensure full contact between the equipment and eliminate non-elastic deformation caused by installation gaps, the pre-loading of 20% of ultimate strength was carried out. To observe the failure phenomenon clearly, the displacement-controlled loading with the loading rate of 0.5mm/min was used. The latticed column specimens would be considered as instability failure when the eccentric compressive force N reached the peak value and started to decline. The eccentric compressive force N in the loading process and corresponding peak value could be recorded automatically by the long column testing machine.



(a) The eccentric compressive loading tests of 1-layer latticed column



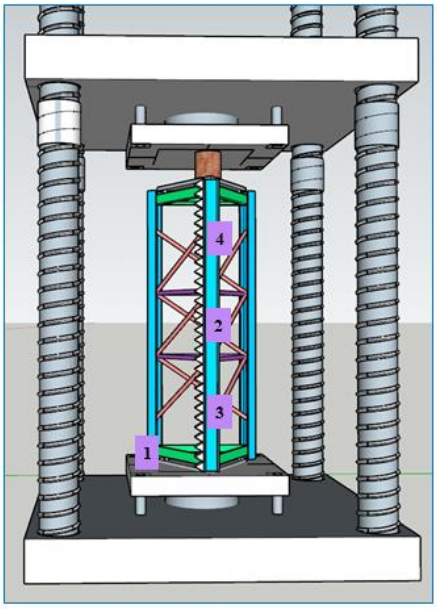
(b) The eccentric compressive loading tests of 2-layers latticed column

Fig. 4 The eccentric compressive loading test setup of latticed column of electric bridge-type scaffold

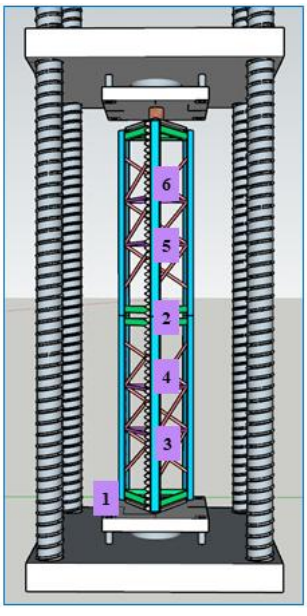
2.3. Instrumentation

The axial deformation of lower end plate and the lateral deformation of longitudinal square tube A in both x and y directions were monitored in real time through the YWD-300mm displacement transducers, and the measuring points were presented in Fig. 5. Because the eccentric pressure was applied on the longitudinal square tube A with toothed steel strip that tended to buckle, its lateral deformation in both x and y directions at some equal-division points (point 2-6) was focused on, as shown in Fig. 5. The compression displacement Δ was measured by the displacement transducers at point 1.

The tubes' strain was measured and recorder by the BX120-5AA electric resistance strain gauge. To monitor the data fluctuations of each lattice column, the axial strain of longitudinal square tubes along the compressive loading direction at 1/4, 1/2 and 3/4 height of latticed column specimen was focused on.



(a) 1-layer latticed column specimen



(b) 2-layers latticed column specimen

Fig. 5 The measuring points of axial and lateral deformation of latticed column specimen under eccentric compression

3. Analysis of experimental results

3.1. Experimental phenomenon analysis and failure modes

Fig. 6-7 represented the experimental failure phenomenon of standard 1-layer and 2-layers latticed column specimens under the eccentric compressive force applied on longitudinal square tube A with toothed steel strip. It was observed that both the standard 1-layer and 2-layers latticed column specimens showed the failure mode of branch component buckling. The longitudinal square tube A with toothed steel strip bearing the eccentric compressive force buckled firstly and suddenly, and presented the most lateral deformation in x and y direction. At the ultimate failure, the buckling deflection at the center of the mast was significant, causing the welded joints of the tooth steel strips made of different materials to fail and separate from the longitudinal square tube A, as shown in Fig. 6. The branch component buckling of 2-layers latticed column specimens occurred in the mid-span, as shown in Fig. 7. The ultimate load-bearing capacity of a single branch component was less than that of the whole latticed column section, so the branch component buckling occurred earlier than the whole column under the eccentric compressive force, which would be discussed in detail in section 5.1.

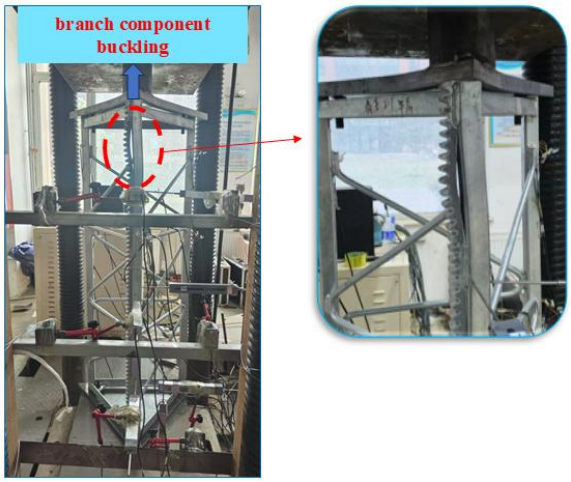
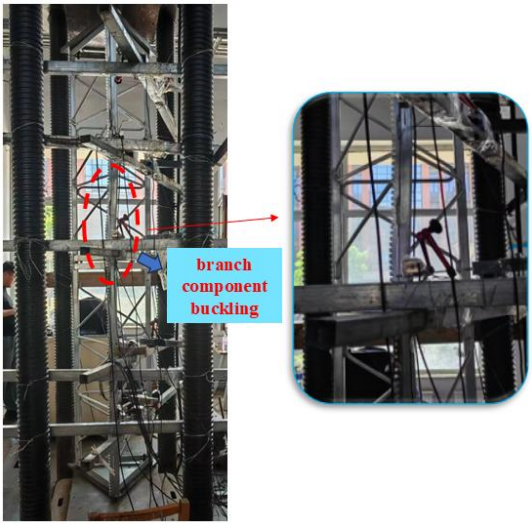
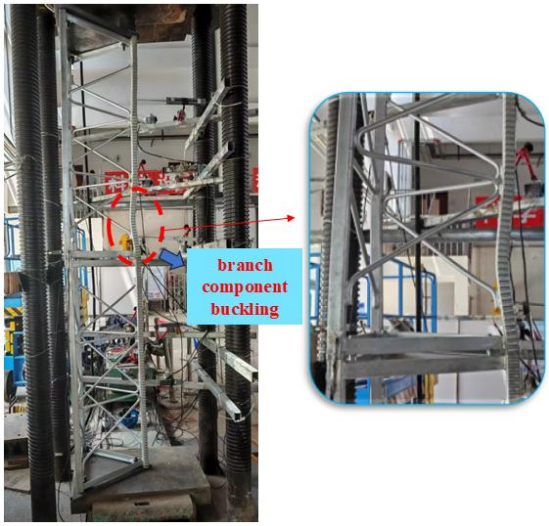


Fig. 6 Experimental buckling mode of standard 1-layer latticed column of electric bridge-type scaffold

Because the latticed column specimens failed mainly due to the buckling of longitudinal square tube A with toothed steel strip bearing the eccentric compression, its lateral deformation was focused on and presented, as shown in Fig. 8. It was shown that the lateral deformation in y direction was positive or negative, which was irregular. But the lateral deformation in x direction was approximately bow-shaped, which was determined by the increased strength provided by the toothed steel strip welded on one side of longitudinal square tube A. The final deformation of longitudinal square tube A was consistent with its initial lateral deformation, which was also consistent with its initial imperfection. The branch component at buckling site would present the most lateral deformation, and its values would be extracted and analyzed.

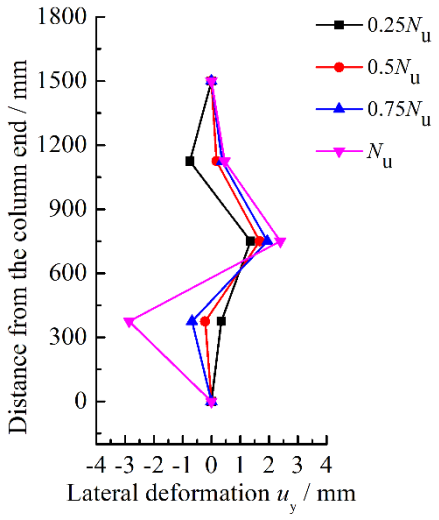


(a) Specimen LC1-2L

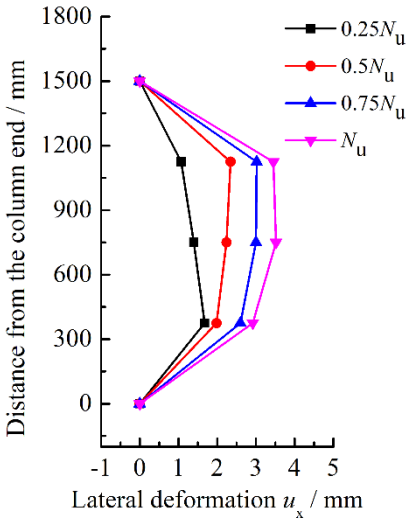


(b) Specimen LC2-2L

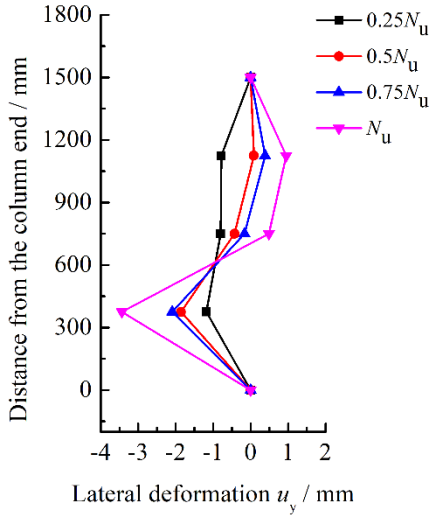
Fig. 7 Experimental buckling mode of 2-layers latticed column of electric bridge-type scaffold



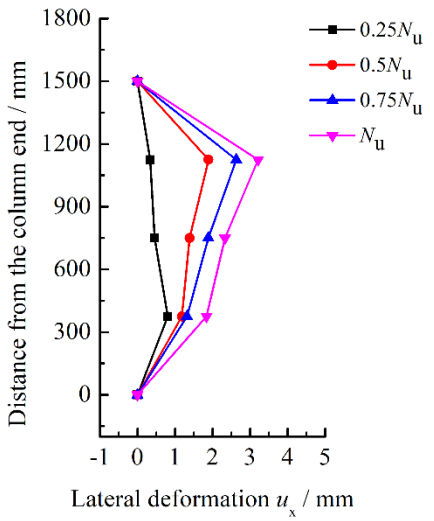
(a) Lateral deformation u_y of specimen LC1-1L



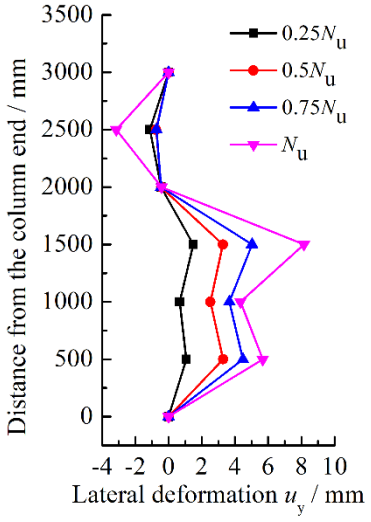
(b) Lateral deformation u_x of specimen LC1-1L



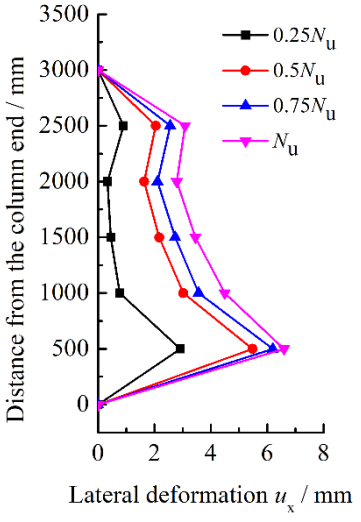
(c) Lateral deformation u_y of specimen LC2-1L



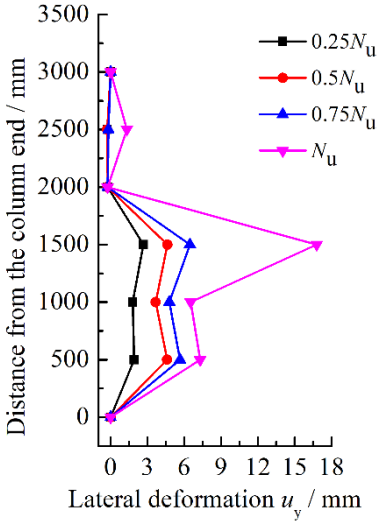
(d) Lateral deformation u_x of specimen LC2-1L



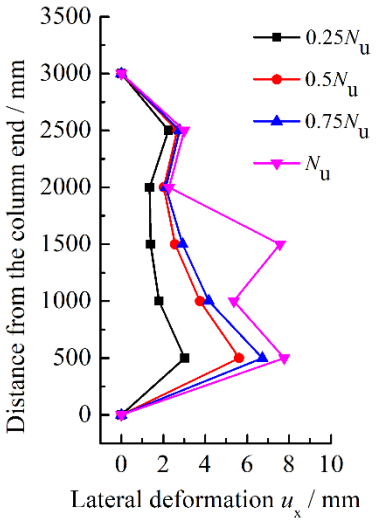
(e) Lateral deformation u_y of specimen LC1-2L



(f) Lateral deformation u_x of specimen LC1-2L



(g) Lateral deformation u_y of specimen LC2-2L



(h) Lateral deformation u_x of specimen LC2-2L

Fig. 8 The lateral deformation of longitudinal square tube A with toothed steel strip under eccentric compression

3.2. Ultimate load-bearing capacity analysis

The ultimate load-bearing capacity N_u of latticed column specimens under eccentric compression was listed in Table 1. Fig. 9-10 represented the experimental tested compression force N-compression displacement Δ curves and the compression force N-maximum lateral deflection δ curves. It was concluded from Fig. 9-10 that both the 1-layer and 2-layers latticed column specimens presented the feature of extremum point instability because the gradual decrease in compressive force after the peak. The stiffness of 2-layers latticed column specimens under eccentric compression was less than that of the

1-layer specimen. The maximum compression displacement Δ_{max} and maximum lateral deflection δ_{max} of latticed column specimens under eccentric compression corresponding to the ultimate strength N_u were listed in Table 1.

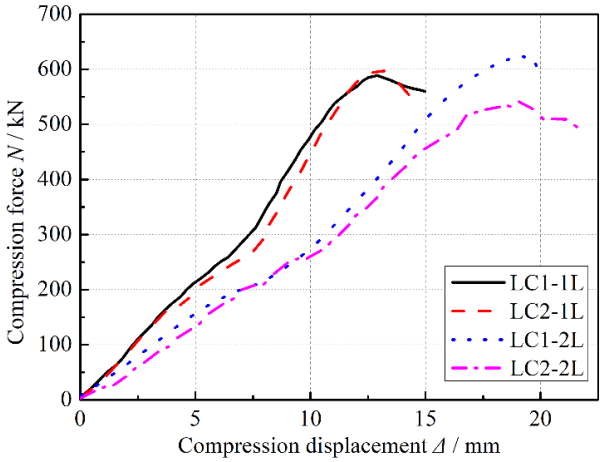


Fig. 9 The tested compression force *N*-compression displacement *Δ* curves

Table 1 and Fig. 11 also presented the tested average value of ultimate strength $N_{u,a}$ of the same latticed column specimens under axial compression. It was shown that the ultimate strength N_u under eccentric compression was about 60% of the ultimate strength $N_{u,a}$ under axial compression due to the additional bending moment caused by the eccentric load.

From Fig.6-8, it was concluded that both the 1-layer and 2-layers were subjected to eccentric compression, and their respective steel pipe components A would experience local buckling failure. Therefore, increasing the column layers from 1 to 2 didn't reduce the ultimate strength N_u because the ultimate load-bearing capacity was determined by the local branch tube component A and the geometric parameters of the single longitudinal square tube buckling remained unchanged for the 1-layer and 2-layers column specimens, as shown in Table 2. Besides, the ultimate strength calculated by the branch component buckling and overall column buckling respectively, were also listed in Table 2. It could be seen that the ultimate strength calculated by the branch component buckling was less than that calculated by overall column buckling, thus the local branch component buckling occurred earlier than the overall column buckling.

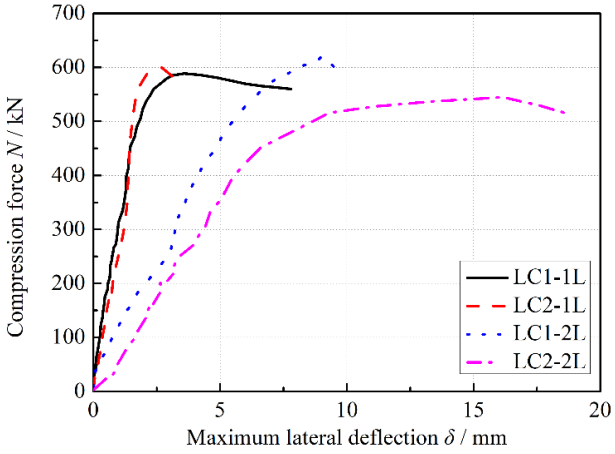


Fig. 10 The tested compression force *N*-maximum lateral deflection *δ* curves

Table 1
The experimental tested results of the 1-layer and 2-layers latticed column specimens of electric bridge-type scaffold

Specimens	Ultimate strength N_u of column under eccentric compression (kN)	Ultimate strength $N_{u,a}$ of column under axial compression (kN)	Maximum compression displacement Δ_{max} (mm)	Maximum lateral deflection δ_{max} (mm)
LC1-1L	588.63	954.80	12.90	3.58
LC2-1L	600.91		13.10	2.77
LC1-2L	622.94	1046.89	19.26	9.08
LC2-2L	544.72		19.16	16.16

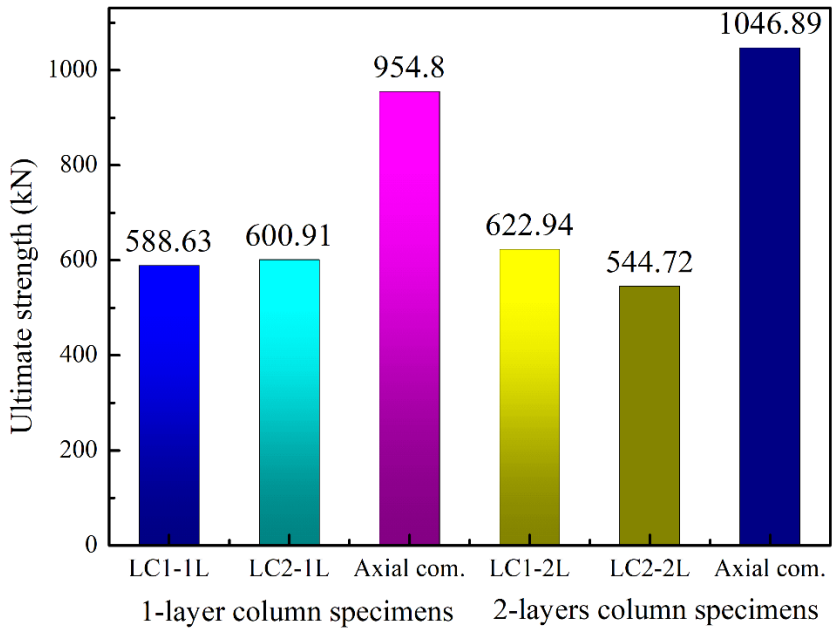
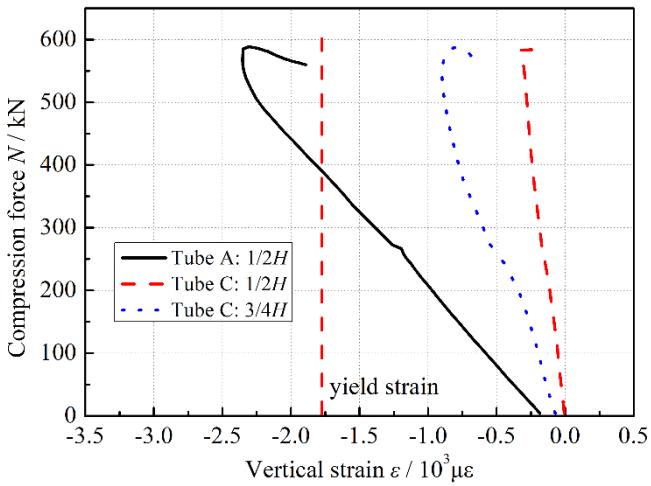


Fig. 11 The comparison of ultimate strength of 1-layer and 2-layers latticed column specimens between under eccentric and axial compression

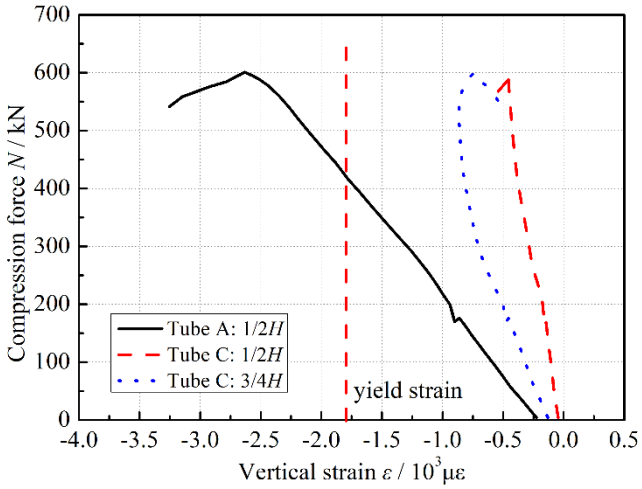
Table 2
The calculation of ultimate strength based on the single longitudinal square tube buckling

Specimens	Length l_{s0} between two consecutive horizontal bars (mm)	Radius of gyration a branch component i_s (mm)	Slenderness ratio of a branch component λ_1	Stability factor φ in GB50017	Calculated ultimate strength by branch component buckling (kN)	Calculated ultimate strength by overall column buckling (kN)
LC1-1L	400	14.43	27.72	0.921	228.92	233.19
LC2-1L						
LC1-2L						230.55
LC2-2L						

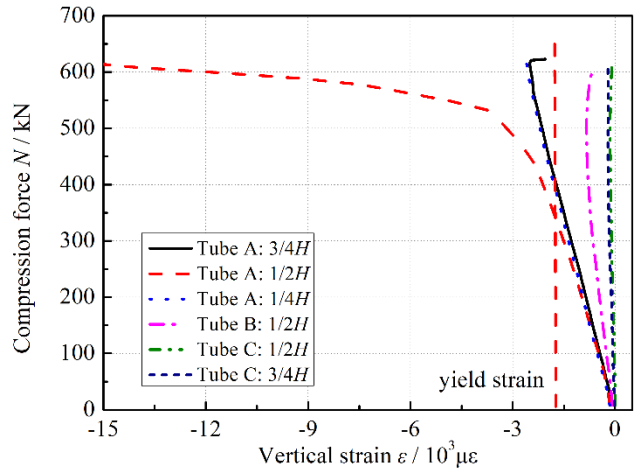
Fig. 12 presented the evolution of vertical strain ε of longitudinal square tubes with eccentric compression force N. Some representative equal-division points were focused on, as described in section 2.3. It was illustrated that the vertical strain ε of longitudinal square tube A bearing the eccentric compression was most developed, which was consistent with the failure mode of local buckling of branch tube component A. The longitudinal square tube A was yielded and failed under the eccentric compression, which indicated the elastic-plastic buckling of latticed column specimens.



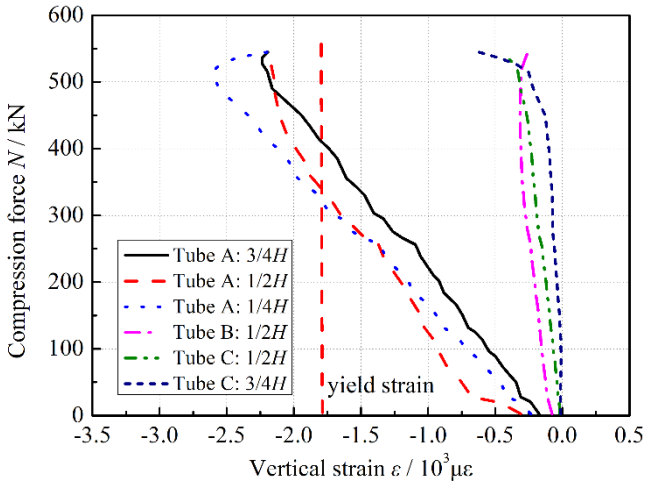
(a) Specimen LC1-1L



(b) Specimen LC2-1L



(c) Specimen LC1-2L



(d) Specimen LC2-2L

Fig. 12 The tested eccentric compression force N-vertical strain ε curves at representative equal-division points

4. Numerical analysis

4.1. FEM establishment of latticed column of electric bridge-type scaffold

Using the finite element analysis software ABAQUS, a finite element model of the lattice column was established by selecting materials reasonably, determining element types, interface treatment, and mesh division settings, as shown in Fig. 13. Considering the geometric dimensions of longitudinal square tube, steel lacing bar and ended steel angle components, the three-dimensional 2-node linear beam element B31 was adopted. The cross-section with the geometric dimensions of longitudinal square tube, lacing bar and ended angle components was assigned to the linear beam element, respectively. Based on the practical assembly process of multi-layers latticed column, the 1-layer column model was established firstly, and then was copied and merged at the longitudinal tubes' end point to establish the 2-layers and multi-layers column models.

The material true yield stress and elasticity modulus (see Table 3) obtained by the tension tests of dog-bone specimens were applied. The ideal elastoplastic constitutive model of the Q355 carbon steel was inputted. As shown in Fig. 13, two reference points were set at the end of longitudinal square tube A, which simulate bearing the eccentric concentrated force. Then, the nodes at the longitudinal tube's end were coupled to the reference point to simulate the practical end restraint. The DOFS of two reference points were restrained respectively, as shown in Fig. 13.

Table 3
The materials properties of latticed column members applied in FEM

Components	Yield strength (MPa)	Ultimate strength (MPa)	Elasticity modulus (GPa)	Elongation
Longitudinal square tubes Lacing bars	470	579	206	21%

The Static, Riks analysis was conducted considering the material nonlinearities and large deformation to calculate the ultimate load-bearing capacity. Based on the Chinese standard GB50017[24] and the European code Eurocode 3[25], the initial imperfection such as the initial eccentricity, initial bending and welding residual stress could be included comprehensively in the initial bow-shape deformation with the maximum of $H/500$. Therefore, the bow-shape deflection with the maximum of $H/500$ was used as the initial imperfection of latticed column model. Most unfavorably, the direction of initial deflection should be opposite to the initial eccentricity of eccentric concentrated force.

The comparison of buckling modes between the tested and FEA results was represented in Fig. 14. It was illustrated that the branch component buckling of longitudinal square tube A bearing the eccentric concentrated force could be simulated well, which was quite similar to the experimentally tested buckling mode.

The FEA calculated ultimate load-bearing capacity was also compared to the theoretically calculated by Chinese standard GB50017 (discussed in detail in section 5.2) to further verify the established FEM, as shown in Fig. 15. It could be seen that the ultimate load-bearing capacity N_u calculated by the established FEM was very consistent with the theoretical calculation results at multiple process nodes of curve fitting. Therefore, the load-carrying performance of latticed column of electric bridge-type scaffold under eccentric compression could be accurately calculated by the established FEM in Fig. 13.

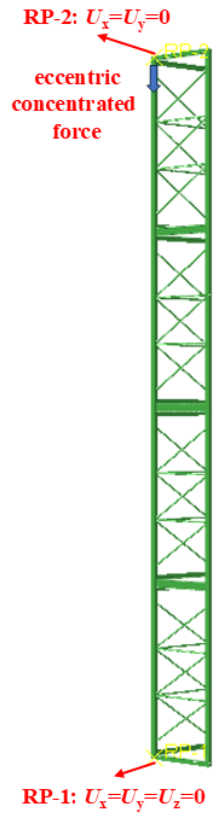
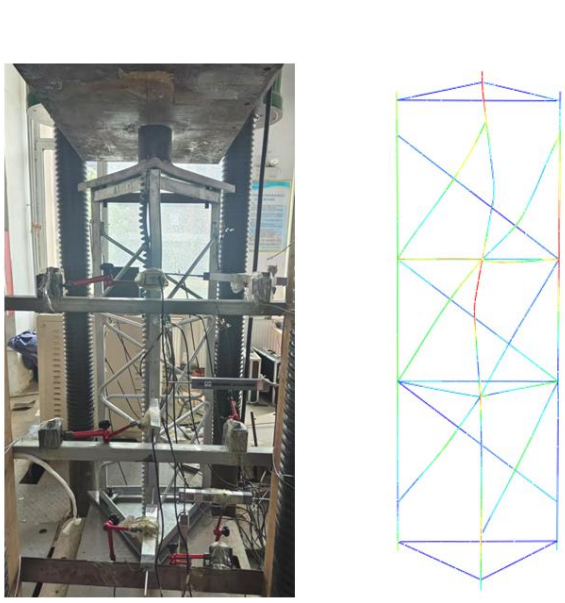
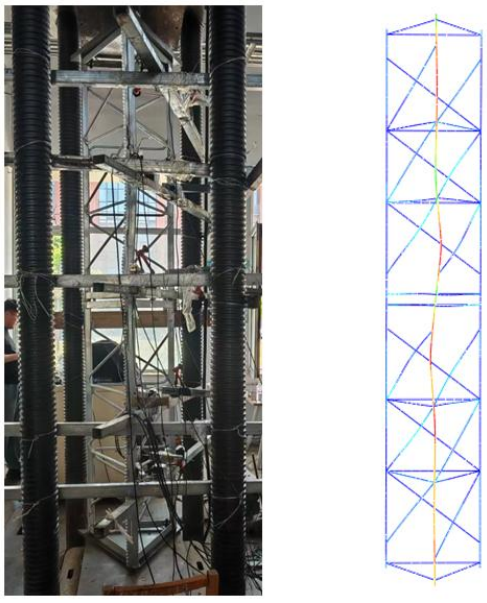


Fig. 13 The FEM of latticed column of electric bridge-type scaffold (took 4-layers latticed column model as example)



(a) 1-layer latticed column



(b) 2-layers latticed column

Fig. 14 Comparison of buckling modes between the tested and FEA results

4.2. Effects of number of latticed column layers

The design height of electric bridge-type scaffold in engineering applications could reach up to 150m. Therefore, the total height H of the lattice column FEM correspondingly changed from 1.5m to 150m, and the number of layers n changed from 1 to 100. As shown in Fig. 14, when the number of layers n was 1 and 2, the buckling of local branch component bearing the eccentric compression occurred. When the number of layers n was 3 and 4, the global-local interactive buckling occurred, as shown in Fig. 16a. As the number of layers reached 5, the overall flexural buckling with symmetrical single-wave shape would dominate, as shown in Fig. 16b-c. As the number of layers n increased, the ultimate strength calculated by overall flexural buckling decreased gradually due to the more serious of initial imperfection, and it was easier for the occurrence of overall flexural buckling than the local branch buckling, thus the buckling mode would convert.

The decrease trend of ultimate load-bearing capacity N_u with number of latticed column layers n under eccentric compression was represented clearly in Fig. 15. The overall initial geometric defect given to the latticed column FEM would accumulate as the number of layers n increased, and the P-δ effect would get serious, thus the ultimate load-bearing capacity N_u of latticed column FEM under eccentric compression was reduced gradually.

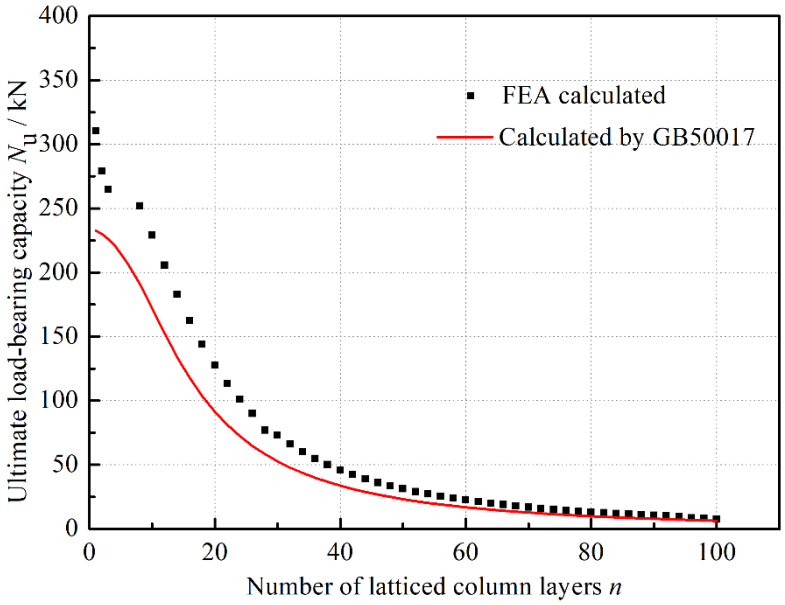
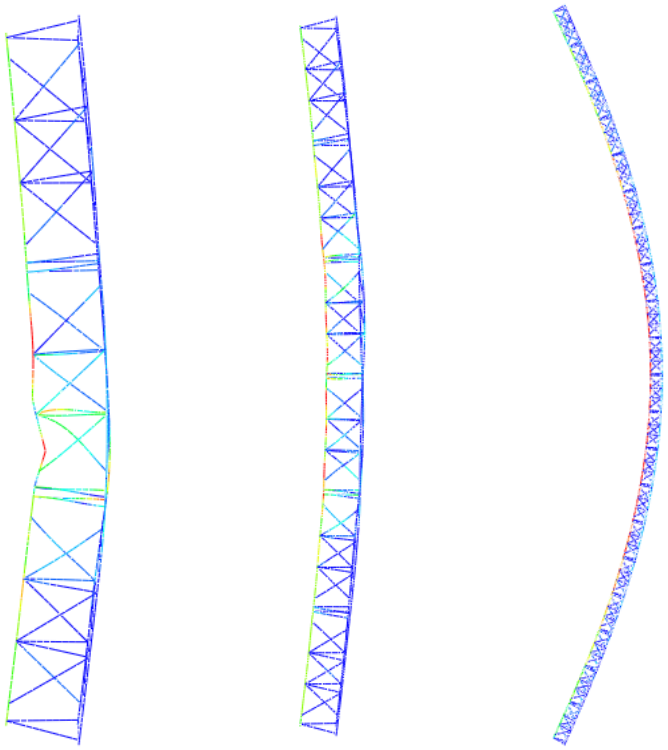


Fig. 15 Comparison of the ultimate load-bearing capacity of latticed column by FEA and theoretically calculated

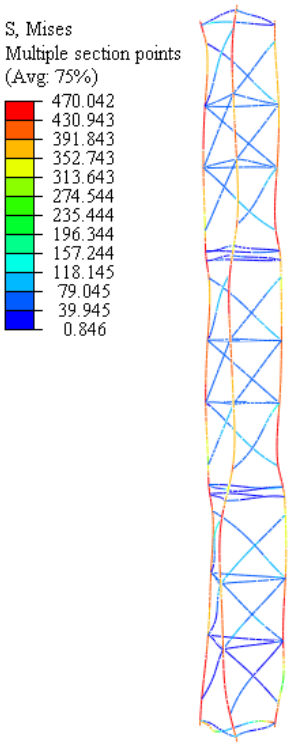


(a) 3-layers (b) 6-layers (c) 20-layers

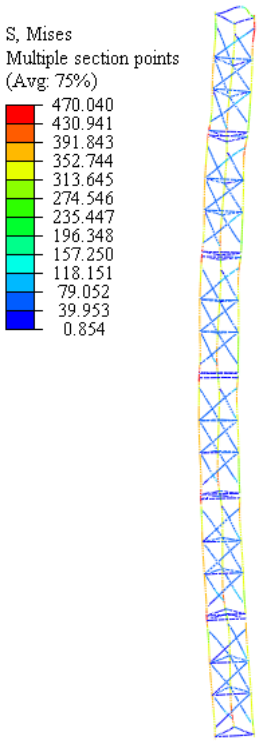
Fig. 16 Effects of number of layers *n* on the buckling modes of latticed column FEM

4.3. Effects of eccentricity of concentrated pressure

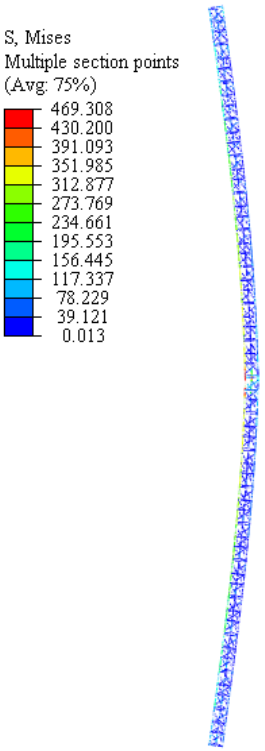
The latticed column FEM under axial compression was also calculated, and the calculated buckling modes, Mises stress contour and ultimate load-bearing capacity were compared to that under eccentric compression, as shown in Fig. 17 and Fig. 18. It could be observed that the pressure was uniformly distributed on the three longitudinal square tubes for the axial compression FEM. However, for the eccentric compression FEM, the eccentric concentrated force was mainly carried by the longitudinal tube A with toothed steel strip that had high Mises stress and tended to buckling, and the other two longitudinal pipes only bore a small amount of pressure and had limited participation in bearing capacity due to their large eccentricity. As the number of layers *n* was relatively small, the decrease of ultimate load-bearing capacity caused by the eccentricity of concentrated force was very much. As the number of layers *n* was large and the total height of latticed column was large correspondingly, the eccentric distance of the concentrated force was relatively small corresponding to the initial imperfection of bow-shape deformation, thus the decrease of ultimate load-bearing capacity induced by the eccentricity of concentrated force was insignificant. In conclusion, the eccentricity of concentrated force applied by the drive motor of electric bridge-type scaffold could not be neglected.



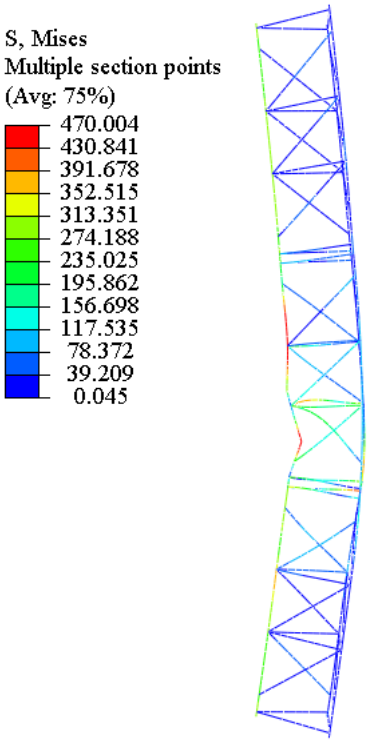
(a) 3-layers, axial compression



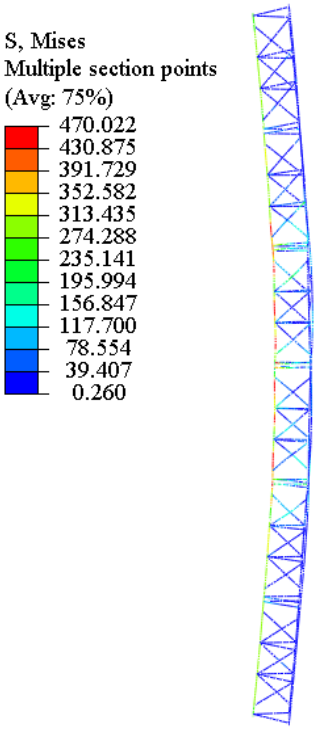
(b) 6-layers, axial compression



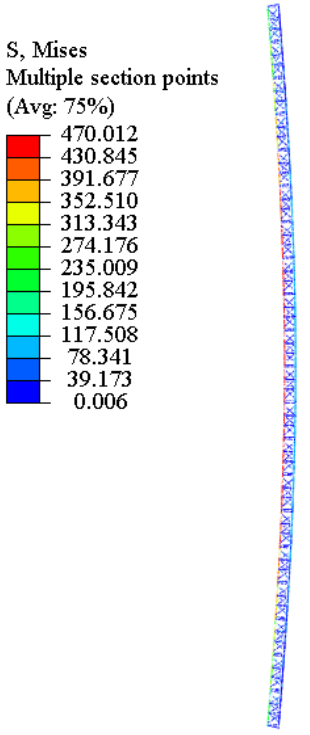
(c) 20-layers, axial compression



(d) 3-layers, eccentric compression



(e) 6-layers, eccentric compression



(f) 20-layers, eccentric compression

Fig. 17 Comparison of the buckling modes and Mises stress contour between the axial and eccentric compression FEM

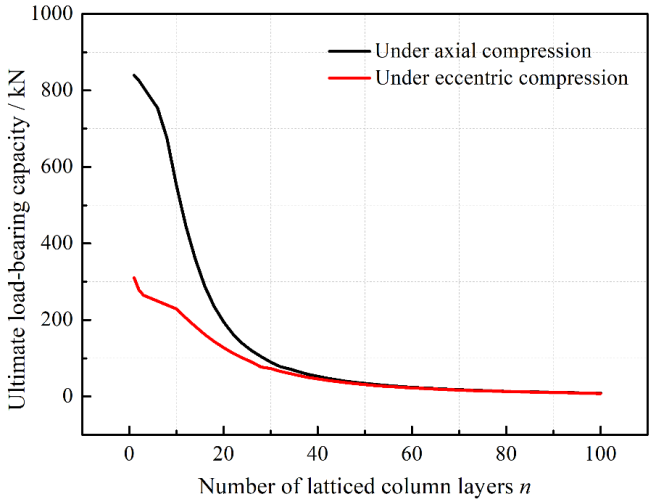


Fig. 18 Comparison of the ultimate load-bearing capacity between the axial and eccentric compression FEM

4.4. Effects of longitudinal square tube's cross-section

Fig. 19 represented the effects of longitudinal square tube's cross-section on the ultimate load-bearing capacity N_u of latticed column under eccentric compression. Three cases of cross-section 30×5mm, 40×5mm and 50×5mm were studied in Fig. 19. It was shown that the ultimate load-bearing capacity N_u would decline very much due to the local branch component buckling as the longitudinal square tube's cross-section was too thin for the few-layers latticed column. The effects of longitudinal tube's cross-sectional area on the ultimate load-bearing capacity N_u was obvious for the few-layers latticed column, which should be fully considered in the design.

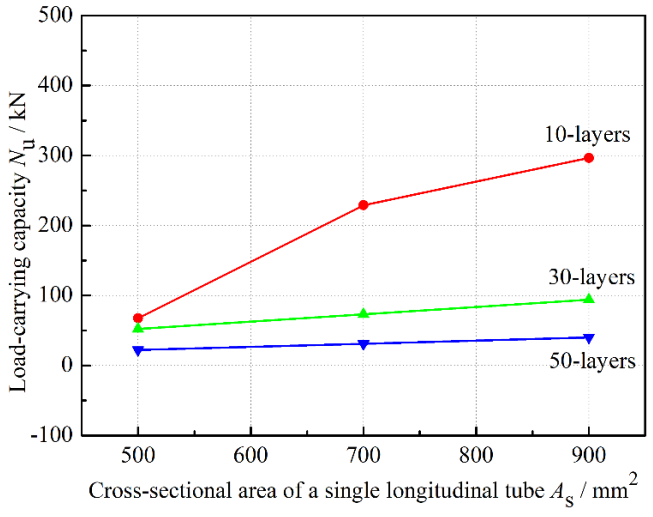


Fig. 19 Effects of longitudinal square tube's cross-section on the load-carrying capacity under eccentric compression

4.5. Effects of lacing bar's diameter

Fig. 20 presented the effects of lacing bar's diameter d_x on the ultimate load-bearing capacity N_u of latticed column under eccentric compression. For the 10-layers FEM, when the diameter d_x was 5mm, the tension bars underwent severe bending deformation and cannot effectively constrain lateral displacement, resulting in the inability to calculate. For the 30-layers FEM, the load-bearing capacity N_u would decrease significantly as the diameter d_x was 5mm. In conclusion, the lacing bar should not be thinner than 10mm to avoid the instability of bracing component. Increasing the lacing bar's diameter d_x from 15mm was insignificant for the ultimate load-bearing capacity N_u.

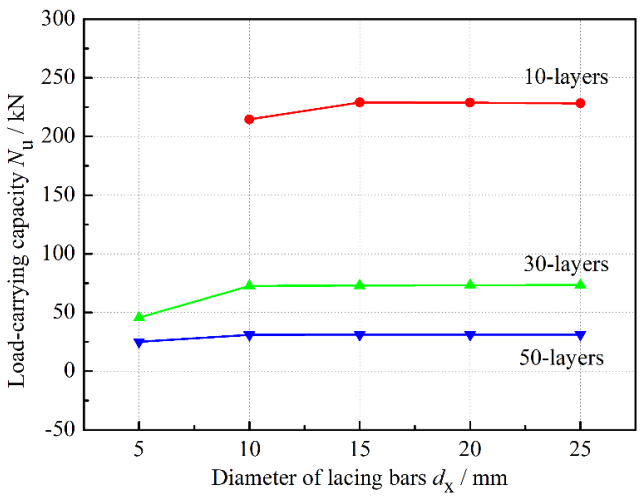


Fig. 20 Effects of lacing bar's diameter on the load-carrying capacity under eccentric compression

4.6. Effects of length l_{s0} between two consecutive horizontal bars

Fig. 21 showed the effects of branch component slenderness ratio λ_1 on the ultimate load-bearing capacity N_u of latticed column under eccentric compression. The length l_{s0} between two consecutive horizontal bars was considered as three cases of 300mm, 400mm and 600mm based on the geometric dimensions of a standard latticed column. For the 10-layers FEM, the ultimate load-bearing capacity N_u was decreased obviously as the length l_{s0} was increased to 600mm because the stability of local branch component was not guaranteed. Decreasing the length l_{s0} was meaningless for the ultimate load-bearing capacity N_u of latticed column under eccentric compression. Therefore, it was reasonable for the standard latticed column with the length l_{s0} of 400mm between two consecutive horizontal bars.

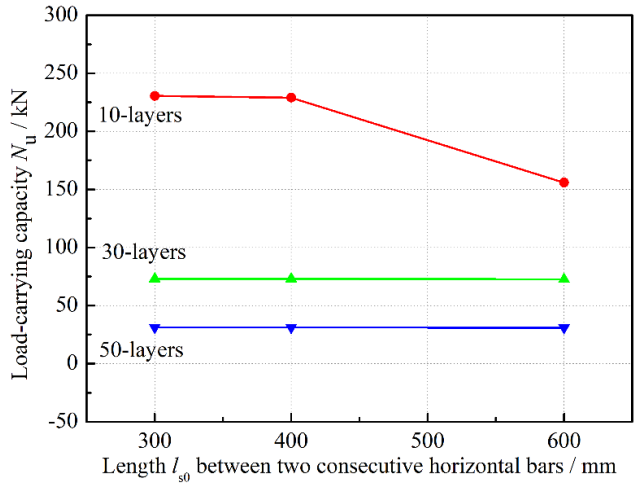


Fig. 21 Effects of length l_{s0} between two consecutive horizontal bars on the load-carrying capacity under eccentric compression

4.7. Effects of bracing component's form

Fig. 22 showed the effects of bracing component's form on the ultimate load-bearing capacity N_u of latticed column under eccentric compression. The batten plate built-up column FEM was established and three cases of batten plate dimensions (6×60mm, 10×100mm and 12×140mm) were considered. The results indicated that the cross-sectional form of the supporting components has almost no significant effect on the ultimate load-bearing capacity N_u of the lattice column. Especially for the 30-layers and 50-layers FEM models under eccentric loads, the main force was transmitted through longitudinal components, and the shear resistance capacity had little effect on the ultimate load-bearing capacity N_u.

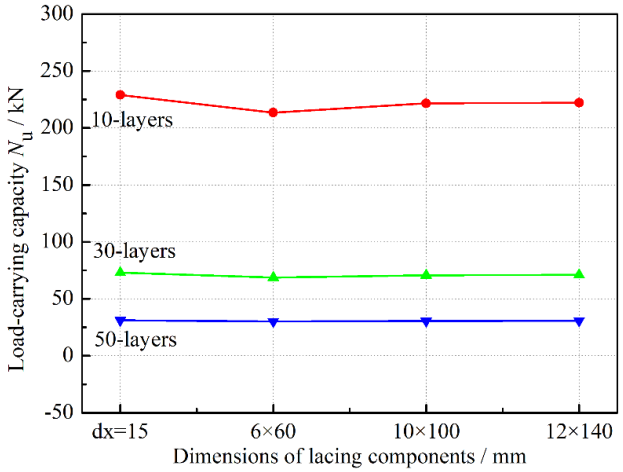


Fig. 22 Effects of bracing component's form on the load-carrying capacity under eccentric compression

5. Design formula for latticed column of electric bridge-type scaffold under eccentric compression

5.1. Demarcation of local branch buckling and overall column buckling under eccentric compression

The axial pressure N_A carrying by the longitudinal square tube A welded with toothed steel strip could be calculated by Eq. (1):

$$N_A = N\frac{y_2}{a} + \frac{M_x}{a} \tag{1}$$

where N was the total eccentric concentrated force, a was the distance between the longitudinal tube A center and axis of longitudinal tube B-C, y_2 was the distance between the axis x and axis of longitudinal tube B-C, M_x was the bending moment carrying by the column cross-section. As shown in Fig. 23, there was the following equation:

$$a = y_1 + y_2 \tag{2}$$

where y_1 was the distance between the axis x and axis of longitudinal tube A.

As for the latticed column of electric bridge-type scaffold in this paper, the relationship between the eccentric compression N and bending moment M_x was:

$$M_x = N \times y_1 \tag{3}$$

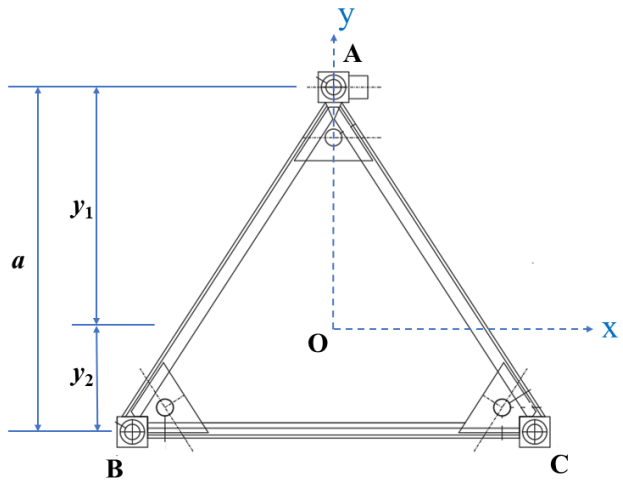


Fig. 23 Cross-sectional parameters of latticed column of electric bridge-type scaffold

Combining Eq. (1)-(3), the following equation could be obtained:

$$N_A = N \tag{4}$$

$$N_B = N_C = N - N_A = 0 \tag{5}$$

where N_B and N_C were the axial pressure carrying by the longitudinal square tube B and C, respectively. Eq. (4)-(5) was also consistent with the FEM results, as shown in Fig. 17. Therefore, when the local branch buckling occurred, the ultimate load-bearing capacity N_u was determined by the branch component slenderness ratio λ_1 of longitudinal square tube A.

Based on the branch component slenderness ratio λ_1, the ultimate load-bearing capacity N_u could be calculated according to the formula of axial compression member in code GB50017-2017[24]:

$$N_u = \varphi A f \tag{6}$$

$$\varphi = \begin{cases} 1-\alpha_1\lambda_n^2 & \lambda_n \le 0.215 \\ \dfrac{1}{2\lambda_n^2}\left[\left(\alpha_2+\alpha_3\lambda_n+\lambda_n^2\right)-\sqrt{\left(\alpha_2+\alpha_3\lambda_n+\lambda_n^2\right)^2-4\lambda_n^2}\right] & \lambda_n \succ 0.215 \end{cases} \tag{7}$$

$$\lambda_n = \frac{\lambda_1}{\pi}\sqrt{\frac{f_y}{E}} \tag{8}$$

where φ was stability factor, A was the total gross section area of a latticed column, f was the specified design stress of steel, α_1—α_3 was the parameters according to the groups of column buckling curves and α_1=0.65, α_2=0.965 and α_3=0.3 herein, λ_n was the non-dimensional slenderness ratio, E was the material elasticity modulus, f_y was the material yield stress.

The ultimate load-bearing capacity N_u was also calculated based on the overall column buckling, which would be discussed in detail in section 5.2. The ultimate load-bearing capacity N_u of latticed column of electric bridge-type scaffold under eccentric compression calculated based on the local branch buckling and overall column buckling, respectively, were represented in Fig. 24. It was illustrated that the ultimate load-bearing capacity N_u calculated based on the overall column buckling would be less than that based on the local branch buckling as the number of layers n reached three. Therefore, as the number of column layers n was between 1-2, the local branch buckling would occur and the ultimate load-bearing capacity N_u should be calculated based on the local branch buckling; as the number of column layers n exceeded 3, the overall column buckling would occur and the ultimate load-bearing capacity N_u should be determined based on the overall column buckling.

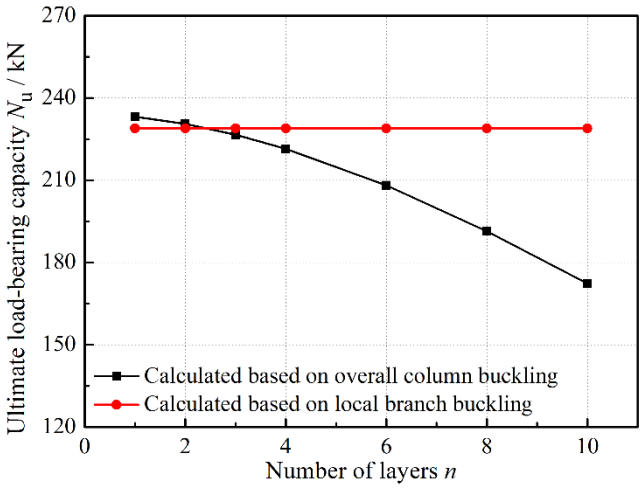


Fig. 24 Comparison of ultimate load-bearing capacity N_u calculated based on the local branch buckling and overall column buckling

5.2. Existing codes for ultimate load-bearing capacity of latticed steel column under eccentric compression

As for steel beam column members, its ultimate load-bearing capacity N

for the overall column buckling in the bending moment plane could be calculated based on the correlation equation[26]:

$$\frac{N}{\varphi_x Af}+\frac{\beta_{mx}M_x}{W_{1x}f\left(1-\varphi_x N/N'_{Ex}\right)}=1 \tag{9}$$

$$N'_{Ex}=\frac{\pi^2 EA}{1.1\lambda_x^2} \tag{10}$$

where N was the design resistance of eccentric compressive member, φ_x was stability factor around x-axis, which should be determined by the modified slenderness ratio λ_m. A was the total gross section area of a latticed column, f was the specified design stress of steel, β_{mx} was the equivalent moment factor and β_{mx} =1 here, M_x was the bending moment around x-axis, W_{1x} was the modulus of section around x-axis, E was the material elasticity modulus, λ_x was the global slenderness ratio of a latticed column around x-axis. It should be noted that the edge yield criterion and Eq. (6)-(8) for stability of axially compressed members were applied in the derivation of Eq. (9)-(10).

As for the solid-web compression-bending member, the plasticity development was allowed, and Eq. (9) was modified as[24]:

$$\frac{N}{\varphi_x Af}+\frac{\beta_{mx}M_x}{\gamma_x W_{1x}f\left(1-0.8N/N'_{Ex}\right)}=1 \tag{11}$$

where γ_x was sectional plastic development coefficient around x-axis and γ_x =1.05 here.

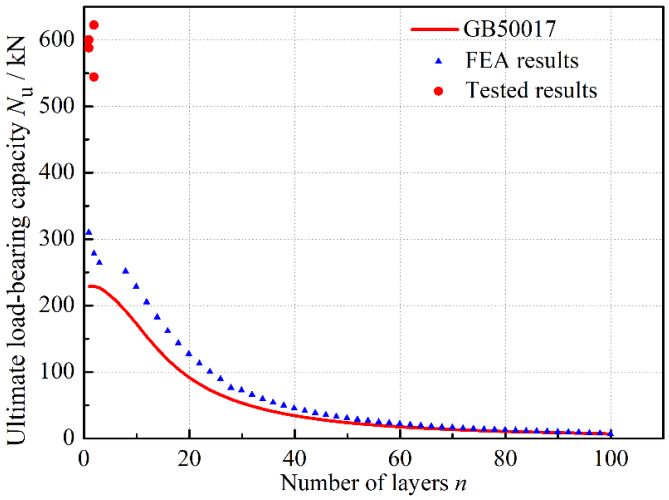
As for the latticed steel column, the plasticity development was not allowed. In Chinese code GB50017-2017, the Eq. (9) was revised as[24]:

$$\frac{N}{\varphi_x Af}+\frac{\beta_{mx}M_x}{W_{1x}f\left(1-N/N'_{Ex}\right)}=1 \tag{12}$$

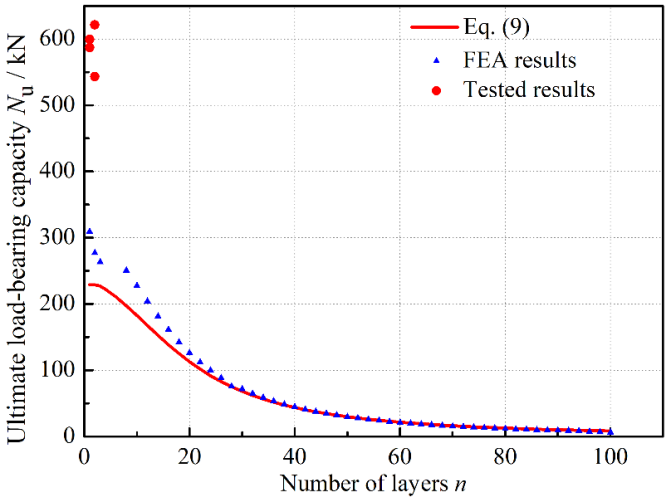
5.3. Comparing FEA and tested results with existing codes

Based on the discussions in section 5.1 and 5.2, the ultimate load-bearing capacity N_u of latticed column of electric bridge-type scaffold could be calculated theoretically. According to the regular operating height of electric bridge-type scaffold in practical engineering, the 1-100 layers latticed column were calculated theoretically based on Eq. (9), Eq. (11) and Eq. (12), respectively.

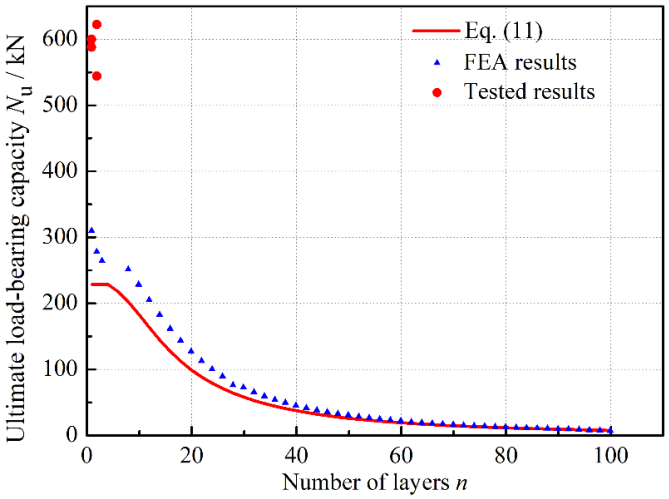
As for the latticed column of electric bridge-type scaffold carrying the eccentric concentrated force, the relationship between the eccentric compression N and bending moment M_x existed, as shown in Eq. (3) and Fig. 23. Therefore, the determined value of ultimate load-bearing capacity N_u could be calculated, which was compared to the FEA and tested results, as shown in Fig. 25.



(a) Comparison with Chinese code GB50017-2017 (Eq. (12)) – no plasticity development, φ_x was removed



(b) Comparison with Eq. (9) – initial correlation equation



(c) Comparison with Eq. (11) - plasticity development was allowed, φ_x was revised to 0.8

Fig. 25 Comparing FEA and tested results with existing codes

It was shown that the FEA and tested points were all above the theoretical line in Fig. 25a-c, indicating that Eq. (9), Eq. (11) and Eq. (12) were reliable to calculate the ultimate load-bearing capacity N_u of latticed column of electric bridge-type scaffold under eccentric compression. As for the many-layers latticed column, the FEA calculated N_u was very close to theoretical line by Eq. (9), Eq. (11) and Eq. (12). However, as the number of layers n was little, the FEA calculated N_u was higher than the theoretical line because the initial imperfection was overestimated in FEM. The experimentally tested results were much higher, because the initial imperfection of 1-layer and 2-layers specimens was very small and the cross-sectional plasticity was fully developed. The ratio of the experimental ultimate bearing capacity to the code-predicted value for each group of specimens was calculated, and the results showed that the experimental values were 2.28-2.61 times the code-predicted values, with an average of 2.45 times. The calculated quantitative reserve capacity in this paper could provide a reference for the optimization of relevant code provisions and the design of structures with higher safety requirements.

The element type effects of FEM model should also be discussed. The B31 linear beam element was adopted according to the components' slender rob shape. The research results showed that there was nearly no difference about the numerical results of latticed column between the simplified beam element and solid element.

Comparing Eq. (9), Eq. (11) and Eq. (12), the ultimate load-bearing capacity N_u calculated by Eq. (12) in GB50017-2017 was smallest due to the removement of parameter φ_x in the second term and the plasticity development was not considered. The ultimate load-bearing capacity N_u calculated by Eq. (11) was middle because the parameter φ_x was replaced by 0.8 in the second term, although the sectional plastic development coefficient was considered. The results calculated by Eq. (9) was the maximum.

6. Conclusions

In order to study the load-bearing mechanism of different structural forms of latticed column in electric bridge-type scaffold under eccentric compression, the latticed column specimen experimental tests and FEM bearing the eccentric concentrated force were conducted. Furthermore, the design formula for latticed column of electric bridge-type scaffold under eccentric compression was proposed. The following main conclusions were obtained:

(1) The experimental results showed that the longitudinal square tube with toothed steel strip subjected to eccentric compression force would experience partial buckling of the branch components. Both the 1-layer and 2-layers latticed column specimens presented the feature of extremum point instability and elastic-plastic buckling.

(2) The local branch component bearing the eccentric compression buckled as the number of layers n was 1-2. The global-local interactive buckling occurred as the number of layers n was 3-4. The overall flexural buckling with symmetrical single-wave shape dominated as the number of layers exceeded 5.

(3) The eccentricity applied by the driving motor was crucial for estimating the bearing capacity, and its impact needed to be clearly considered in the design.

(4) The lacing bar should not be thinner than 10mm to avoid the instability of bracing component. It was reasonable for the standard latticed column with the length l_{s0} of 400mm between two consecutive horizontal bars. The load-carrying capacity was hardly affected as the lacing bar was replaced by the batten plate.

(5) The eccentric concentrated force was mainly carried by the longitudinal tube with the toothed steel strip (high Mises stress zone), while the other two longitudinal tubes were subjected to less force, indicating uneven load distribution.

(6) The determined value of ultimate load-bearing capacity N_u of latticed column under eccentric compression of electric bridge-type scaffold could be calculated theoretically based on the correlation equation. The FEA and tested points were all above the theoretical line, indicating that the correlation equation in this paper were reliable to calculate the ultimate load-bearing capacity N_u of latticed column of electric bridge-type scaffold under eccentric compression.

In current research, the eccentric pressure was applied directly to the longitudinal tube A with the toothed steel strip through the 5000kN long column testing machine, and the lateral tie members were not considered in the tests, which was different from the practical electric bridge-type scaffold. In the future research, the experimental tests of the entire scaffold with the latticed column and truss girder considering the lateral tie members in the practical construction site would be conducted. Besides, the latticed column made of high-strength steel would be tested to study its bearing performance.

Acknowledgements

This work was supported by Hebei Natural Science Foundation of China (Grant No. E2025402005).

References

[1] Liu H, He Y, Zhang H, et al. Experimental and analytical studies on the lateral bearing performance of disk lock steel tubular scaffold under horizontal load [J]. Structures, 2025, 78: 109290.

[2] Chen Z, Lv J, Liu H, et al. Experimental and analytical studies on stability of ultra-strong thin-walled steel tube and coupler scaffolds [J]. Engineering Structures, 2023, 275: 115255.

[3] Liu H, Jia L, Wen S, et al. Experimental and theoretical studies on the stability of steel tube-coupler scaffolds with different connection joints [J]. Engineering Structures, 2016, 106: 80-95.

[4] Liu H, Hao T, Zhang H, et al. Experimental and theoretical investigation on the lateral bearing capacity of disk-lock scaffold [J]. Journal of Constructional Steel Research, 2026, 236: 109936.

[5] Liu H, Zhao Q, Wang X, et al. Experimental and analytical studies on the stability of structural steel tube and coupler scaffolds without X-bracing [J]. Engineering Structures, 2010, 32: 1003-1015.

[6] Liu H, Chen Z, Wang X, et al. Theoretical analysis and experimental research on stability behavior of structural steel tube and coupler falsework with X-bracing [J]. Advanced Steel Construction, 2010, 6(4): 949-962.

[7] Chan J L Y, Lo S H. Stability design of system scaffold with differential settlement [J]. Structures, 2020, 27: 1467-1478.

[8] Weesner L B, Jones H L. Experimental and analytical capacity of frame scaffolding [J]. Engineering Structures, 2001, 23: 592-599.

[9] Peng J L, Pan A D, Rosowsky D V, et al. High clearance scaffold systems during construction —I. Structural modelling and modes of failure [J]. Engineering Structures, 1996, 18(3): 247-257.

[10] Peng J L, Pan A D, Rosowsky D V, et al. High clearance scaffold systems during construction —II. Structural analysis and development of design guidelines [J]. Engineering Structures, 1996, 18(3): 258–267.

[11] Zheng Y, Guo Z. Investigation of joint behavior of disk-lock and cuplok steel tubular scaffold [J]. Journal of Constructional Steel Research, 2021, 177: 106415.

[12] Pieńko M, Bazik-Borowa E. Numerical analysis of load-bearing capacity of modular scaffolding nodes [J]. Engineering Structures, 2013, 48: 1–9.

[13] Dong J, Liu H, Lei M, et al. Effective length correction factor of disc-buckle type scaffolding by considering joint bending stiffness and geometrical size [J]. PLOS ONE, 2022, 17(10): e0276340.

[14] Lu Z, Zhang M, Guo C. Dynamic performance of high supporting formwork under horizontal impact load [J]. International Journal of Simulation and Process Modelling, 2019, 14(5): 407-420.

[15] Hu C, Cheng R, Wang Y, et al. Buckling behavior of thin-walled cold-formed steel latticed column with lacings under axial compression [J]. Thin-Walled Structures, 2024, 205: 112574.

[16] Dar M A, Sahoo D R, Pulikkal S, et al. Behaviour of laced built-up cold-formed steel columns: Experimental investigation and numerical validation [J]. Thin-Walled Structures, 2018, 132: 398-409.

[17] Kalochairetis K E, Gantes C J, Lignos X A. Experimental and numerical investigation of eccentrically loaded laced built-up steel columns [J]. Journal of Constructional Steel Research, 2014, 101: 66-81.

[18] Chen X M, Xia J W, Xu B, et al. Performance of a novel built-up column composed of four cold-formed tubes [J]. Proceedings of the Institution of Civil Engineers-Structures and Buildings, 2020, 173(10): 730-745.

[19] Guo Y L, Zhang B H, Zhao S Y, et al. Ultimate resistance design of shuttle-shaped steel tubular latticed columns [J]. Journal of Structural Engineering, 2014, 140: 1-10.

[20] Guo Y, Wang J. Instability behavior and application of prismatic multi-tube latticed steel column [J]. Journal of Constructional Steel Research, 2009, 65: 12-22.

[21] Yang Z M, Chen J, Pandey M. Compressive behavior and design calculations of CFST slender columns with latticed annular steel part [J]. Journal of Constructional Steel Research, 2024, 223.

[22] Yang Y F, Liu M, Hou C, et al. Behaviour of four-legged square CFST latticed members under lateral cyclic loading [J]. Journal of Constructional Steel Research, 2019, 156: 54-74.

[23] Yang Y F, Liu M, Fu F. Experimental and numerical investigation on the performance of three-legged CFST latticed columns under lateral cyclic loadings [J]. Thin-Walled Structures, 2018, 132: 176-194.

[24] GB50017-2017. Code for design of steel structures [S]. Beijing: China Architecture & Building Press, 2017.

[25] BS EN 1993-1-12. Eurocode 3: design of steel structures: Part 1-1: general rules and rules for buildings [S]. London: BSI, 1993.

[26] Zhang Y, Zhou X. Principles of steel structure design [M]. Beijing: Higher Education Press, 2020.

Advanced Steel Construction – Vol. 22 No. 5 (2026) 597–602
DOI:10.18057/IJASC.2026.22.5.10

MECHANICAL PERFORMANCE OF TERMINAL EQUIPMENT IN ULTRA-HIGH VOLTAGE SUBSTATIONS

Le-Tian Wang [1], Ke Xin [1], Jun-Ming Zhang [2], Jun-Xiang Xu [1], Guan-Jun Chai [3] and Hui-Huan Ma [2, *]

[1] *Shandong Electric Power Engineering Consulting Institute CoRP..Ltd., Jinan, China*
[2] *School of Civil Engineering, Sun Yat-Sen University, Zhuhai, China*
[3] *CCCC Guangzhou Dredging Co., Ltd., Guangzhou, China*
** (Corresponding author: E-mail: mahh5@mail.sysu.edu.cn)*

ABSTRACT

Failures of UHV terminal clamps can lead to insulation accidents and substantial economic losses. To overcome the limitations of conventional mechanical assessments, this study develops a three-dimensional finite element (FE) model of two representative connectors—a SY-500/45A terminal equipment clamp and an NY-1600K compression-type strain clamp—to investigate their mechanical response under bolt preload and representative combined loading conditions. The model explicitly incorporates bolt preload, the resulting bending effects, surface-to-surface contact with friction at the toothed clamp–anchor interface, and elastic–plastic material behavior of aluminum and steel. The numerical results resolve the global and local stress fields, clarify the load-transfer path from the outer teeth toward the inner core, and identify geometry-sensitive hotspots around the bolt holes and the steel-anchor connection. Bolt preload generates markedly non-uniform stresses and local yielding that dominate subsequent responses, while superposed mechanical actions further intensify the von Mises stress at tooth roots and at geometric discontinuities, highlighting the need to control assembly preload and bending in design carefully. Based on these findings, potential engineering measures, such as controlling preload, increasing the effective contact radius, and smoothing tooth-root fillets, are suggested as promising ways to alleviate stress concentration and improve the in-service reliability of UHV terminal clamps.

ARTICLE HISTORY

Received: 3 December 2025
Revised: 13 April 2026
Accepted: 22 April 2026

KEYWORDS

Terminal equipment;
Mechanical performance;
Substation hardware;
Finite element modeling;
Power systems

Copyright © 2026 by The Hong Kong Institute of Steel Construction. All rights reserved.

1. Introduction

Against the backdrop of rapid economic growth, China's demand for energy has been increasing substantially. Ultra-high voltage (UHV) substations, serving as critical infrastructure for long-distance power transmission, play an indispensable role in supporting modern industrial development and daily operations. However, in practical engineering, terminal failures frequently lead to insulation accidents, resulting in significant safety hazards and economic losses. In conventional high-voltage substations, conductor cross-sections are relatively small, and the mechanical loads transmitted to hardware remain far below their ultimate capacity. As a result, the mechanical performance of substation connectors and clamps has historically received less attention compared with electrical insulation and seismic reliability [1]. However, operational evidence from ultra-high voltage (UHV) substations shows that insulation faults caused by tensile fractures of terminal hardware have already occurred, suggesting that mechanical reliability can become a critical weak link in modern power systems. For large-section flexible busbars, the actual forces applied to terminal clamps often differ significantly from those predicted by simplified analytical formulas, calling into question the applicability of hardware designed according to traditional substation assumptions. Recent international studies on extra-high-voltage connectors and busbar systems have likewise shown that connectors and clamps are often among the most vulnerable substation components and that their detailed electro-mechanical behavior under realistic service conditions remains insufficiently characterized [2-7].

Previous research on terminal equipment has mainly focused on failure mechanisms and defect characterization. In terms of failure mechanisms, Aydar [8] combined SEM surface analysis with X-ray mappings of copper-clad aluminum wires and showed that abrasion grooves, tensile cracks, copper-layer delamination and pit-type corrosion act as local stress raisers and preferred sites for crack initiation, even when the bulk microstructure appears normal. In terms of defect characterization, Karabay et al. [9] conducted a systematic failure analysis of wire breaks in aluminum conductors and linked early fractures on transmission lines to casting shrinkage porosity and embedded oxide particles in the feedstock, demonstrating that such metallurgical defects markedly reduce fatigue life and often govern overall fracture behavior. More targeted studies have examined strain (tension) clamps, another critical class of substation hardware. Sun et al. [10] analyzed failed strain clamps from a 500 kV transmission line and found that ice-induced overload and local contact defects led to stress concentrations and crack propagation at the steel-anchor interface, a pattern consistent with earlier fracturing-case reports for 500 kV compact lines and strain clamps as well as numerical failure analyses of contact-resistance deterioration [11-13]. Zhang et al. [14] investigated the crimping quality of strain clamps using non-destructive testing techniques and finite-element analysis, demonstrating that insufficient compression and hidden voids in the aluminum sleeve markedly decrease ultimate tensile strength; complementary electro-thermal and thermo-mechanical studies further indicate that such manufacturing and contact defects can induce local overheating and accelerate deterioration of the clamp–conductor interface, thereby aggravating the risk of fatigue and fracture under service loads [15-17]. To improve quality assessment,Ouyang et al. [18] developed an ultrasonic pulse-echo method to detect internal positioning defects and evaluate on-site crimping reliability, while Zhang et al.[14] proposed an X-ray image-based method that estimates crimping quality using equivalent cross-sectional stiffness. In addition, finite-element and experimental investigations of hydraulic and NXJ-type strain clamps further confirm that local stress distribution in the crimped region and degradation of the steel-anchor segment govern the ultimate tensile strength and failure modes of the fittings [19-21].

Although considerable progress has been made in elucidating failure mechanisms and characterizing manufacturing and service-induced defects in substation hardware, existing research typically examines clamps only under specific failure scenarios—such as tensile pull-out, icing overload, or vibration fatigue—while little attention has been given to the coupled effects of bolt preload and service-like tensile loading, and to the resulting three-dimensional tensile–compressive stress state of substation terminal clamps. Studies focusing on UHV-substation equipment clamps remain limited, especially concerning how preload-induced local plasticity may act as an inherent initial defect and influence subsequent mechanical behavior under multi-directional loads.

To address these gaps, this study establishes detailed three-dimensional finite element models of two representative UHV substation terminal devices—a compression-type equipment clamp (SY-500/45A) and a compression-type strain clamp (NY-1600K). The objective of this study is to investigate their mechanical response under the combined effect of bolt preload and representative service-like loading conditions, with particular emphasis on preload-induced local plasticity, three-dimensional stress redistribution, and geometry-sensitive critical regions. The main contribution of this work is a refined numerical characterization of how preload and external actions jointly govern the stress concentration and deformation behavior of representative UHV terminal fittings. Section 2 introduces the classification and configuration of substation terminal equipment and describes the two selected clamps. Section 3 presents the finite element modelling strategy, including material constitutive models, contact definitions, meshing schemes and boundary conditions. Section 4 analyses the mechanical performance of the clamps under bolt preload and under representative combined loading states based on the numerical simulations.

2. Overview of substation terminal equipment

In practical engineering, substation hardware serves the functions of

fixation, connection, and conduction. Depending on the application scenario, hardware can generally be categorized into substation hardware and transmission line hardware. This paper focuses specifically on substation hardware. Owing to variations in the types of connected equipment, conductors, and installation positions, substation hardware exhibits a wide diversity in form and design. Considering the extensive variety of substation hardware used in engineering practice, two representative types are selected for analysis in this study.

2.1. SY-500/45A (150×150)

The compression-type single-conductor equipment clamp is a commonly used substation hardware, typically applied for phase-to-phase connections or interconnections between circuit breakers. As shown in Fig. 1, the SY-500/45A (150×150) examined in this study is designed for connecting a single LGJ-500/45 conductor, with its plate section measuring 150 mm × 150 mm. The connection between the clamp and the conductor is achieved through compression fixing, whereas its connection to equipment such as circuit breakers is realized via high-strength bolts.

2.2. NY-1600K

While the first type is an equipment clamp, the NY-1600K is a compression-type strain clamp. Strain clamps serve as three-way connecting components, primarily used for linking transmission conductors, downleads, and tension insulator strings. As shown in Fig. 2, the NY-1600K is a compression-type strain clamp intended for use with JLHN58K-1600 conductors. The upper conductor is connected by compression, while the lower part is attached to a drainage plate or a single-conductor clamp using high-strength bolts. Connection to the tension insulator string is achieved via a steel anchor. The steel anchor and the tension insulator string are fastened together through a steel ring.

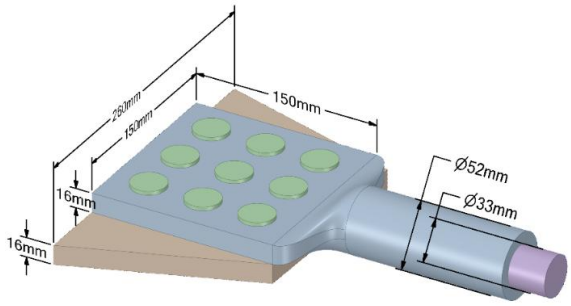


Fig. 1 SY-500/45A (150×150) model

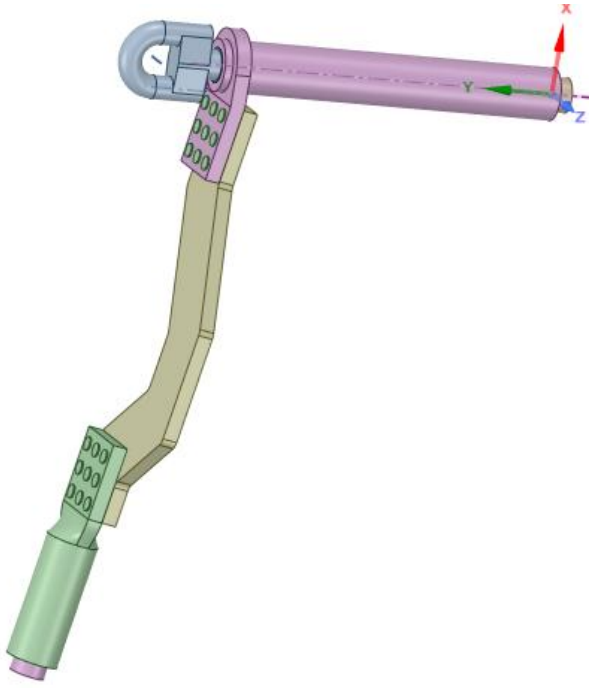


Fig. 2 NY-1600K model

3. Finite element modeling

3.1. Material parameter settings

In this study, aluminum components are modeled using a bilinear elastic-plastic constitutive curve with kinematic hardening rule [22]. The material parameters were adopted from commonly used engineering values and design specifications reported in GB 50017-2017 and GB 50429-2007 .[23, 24].The elastic modulus is set to 70 GPa, the Poisson's ratio to 0.33, and the yield strength to 100 MPa. Pure copper components in terminal equipment are modeled with an ideal elastic-plastic constitutive relation as a simplified engineering approximation. This treatment is adopted to capture the onset of yielding while keeping the constitutive description concise. The strain-hardening behavior of copper is not explicitly considered in the present model and should be incorporated in future studies when detailed material calibration data are available. The bolts used in the terminal equipment are modeled as linear-elastic steel components, with an elastic modulus of 200 GPa and a Poisson's ratio of 0.3. This simplification is adopted because the present study mainly focuses on the stress redistribution and local concentration in the clamp body and anchor-connected regions. Possible localized yielding in the bolts under high preload is not explicitly considered here and should be addressed in future refined analyses. Conductors and other fixed hardware are treated as rigid bodies. Particularly, for expanded conductors, deformable body modeling is still employed to capture their mechanical behavior.

3.2. Contact and mesh settings

The contacts between the clamp and the terminal plate, the clamp and the fixing bolts, as well as the terminal plate and the fixing bolts, are all defined as frictional contacts. Due to the lack of dedicated friction tests for this type of hardware, the friction coefficient is uniformly set to 0.3, which lies within the range commonly adopted in finite-element modeling of preloaded bolted joints and electrical connector contacts [3, 25-27]. The connection between the clamp and the conductor is established through compression, which makes relative sliding unlikely under the applied gripping force. Therefore, the conductor–clamp interface is modeled as a bonded contact. In the model, all parts except the conductors are meshed using SOLID187 elements. Given their regular geometric shape, the conductors are modeled with SOLID186 elements, while rigid bodies are represented by MASS21 elements.

Mesh densities are varied according to the geometric dimensions and structural importance of each component. For equipment clamps, the junction between the tubular and plate sections is regarded as a weak region. Meanwhile, the bolts are relatively small compared with terminal plates (M18 bolts are typically used). For these critical areas, a mesh size of 5 mm is applied, while non-critical areas are meshed with a size of 20 mm. Rigid body components are not meshed. The configured mesh is shown in Fig. 3.

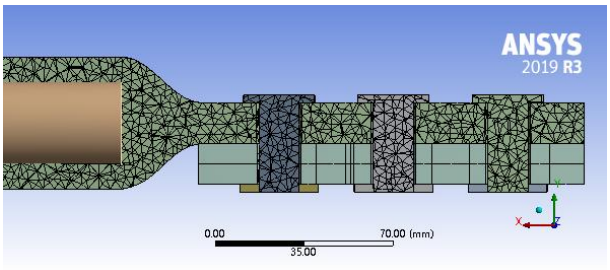


Fig. 3 Mesh of solution region

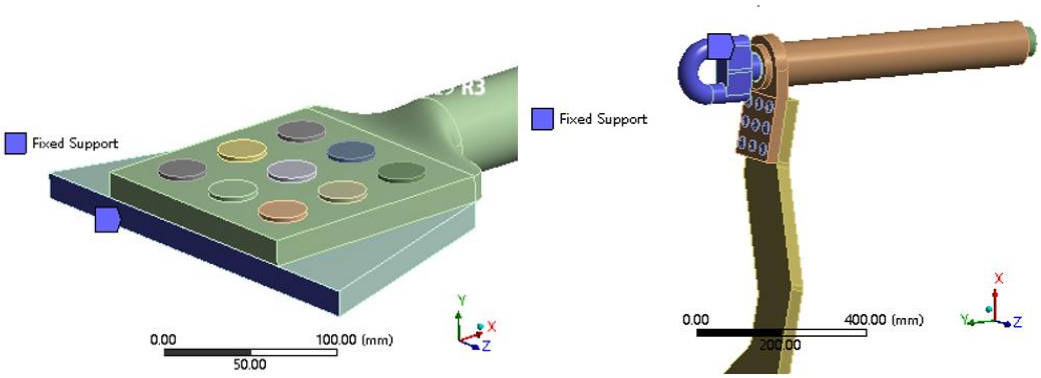
3.3. Boundary conditions

The connection methods of different clamps with other equipment or conductors vary in practical engineering applications. Accordingly, the boundary conditions of the two clamps analyzed in this study are also different.

For ordinary compression-type single-conductor clamps such as SY-500/45A (150×150), the clamp is typically connected directly to the terminal plate via bolts, and the terminal plate is generally connected to comparatively stiff external equipment. In the present model, this connection is idealized as a fixed constraint to represent the dominant restraint provided by the connected system and to obtain a conservative estimate of local stress concentration in the clamp. It should be noted, however, that the actual support may exhibit a certain degree of flexibility in service. Therefore, the side of the terminal plate connected to the circuit breaker is modeled as a fixed constraint, as shown in

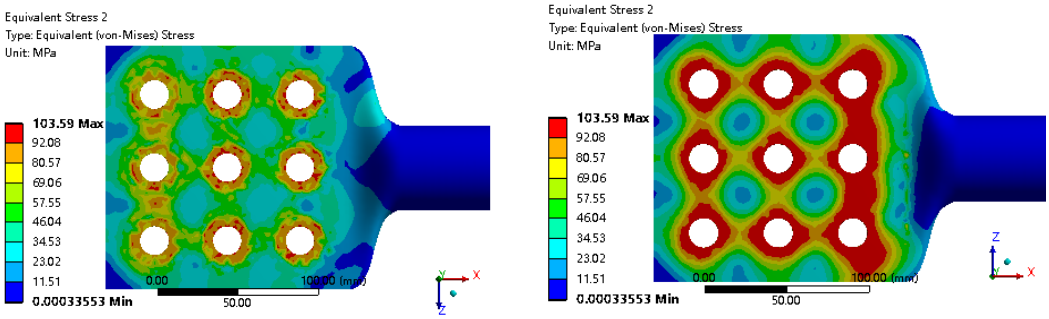
Fig. 4(a).

For strain clamps such as NY-1600K, the tubular section is usually connected to long conductors. The tensile force applied to this part is significantly greater than that on the lower drainage plate or single-conductor clamp section. Therefore, in this study, the annular section of the steel anchor of the NY-1600K is assumed to be a fixed constraint, as shown in Fig. 4(b).

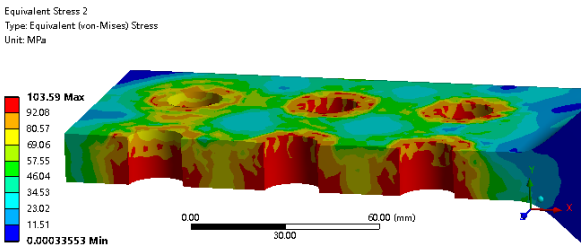


(a) SY-500/45A Fixed constraint position (b) NY-1600K Fixed constraint position

Fig. 4 Fixed constraint position



(a) Top view (b) Bottom view



(c) Section view

Fig. 5 von Mises stress contour (MPa)

4. Mechanical performance analysis

4.1. Mechanical response of the equipment clamp under bolt preload

It has been observed that when clamps are installed with the preload specified by the aforementioned standards during construction, initial defects may be introduced. To illustrate this issue, the equipment clamp SY-500/45A (150×150) is taken as an example. The numerical analysis results under preload alone are shown in Fig. 5. According to the structural characteristics of the SY-500/45A (150×150), the side without direct contact with the terminal plate is defined as the upper surface, while the side with the terminal connection is defined as the lower surface. Since pure aluminum exhibits greater ductility compared with structural steel, the fourth strength criterion is applied, and the von Mises stress distribution is examined.

As shown in Fig. 5, the overall stress distribution within the clamp under bolt preload is highly non-uniform, and the stress has already reached the yield strength of pure aluminum (100 MPa). Further analysis reveals that the specified bolt preload is 80 kN, whereas the bolt hole diameter is only 16 mm and its depth is 60 mm. Even with the use of bolt washers, which have a diameter of approximately 28 mm, the concentrated preload near the bolt hole causes the surrounding clamp material to yield, resulting in localized plastic deformation and creating an “imprint” effect. In practical engineering applications, such indentation marks are frequently observed, as shown in Fig. 6.

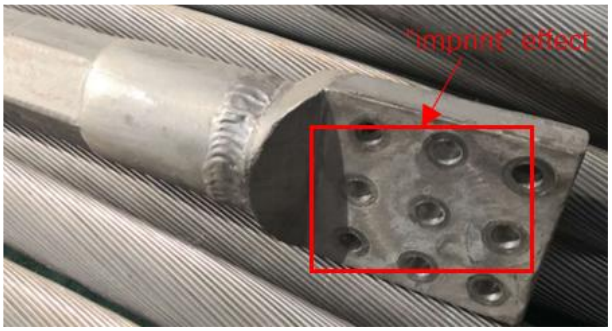
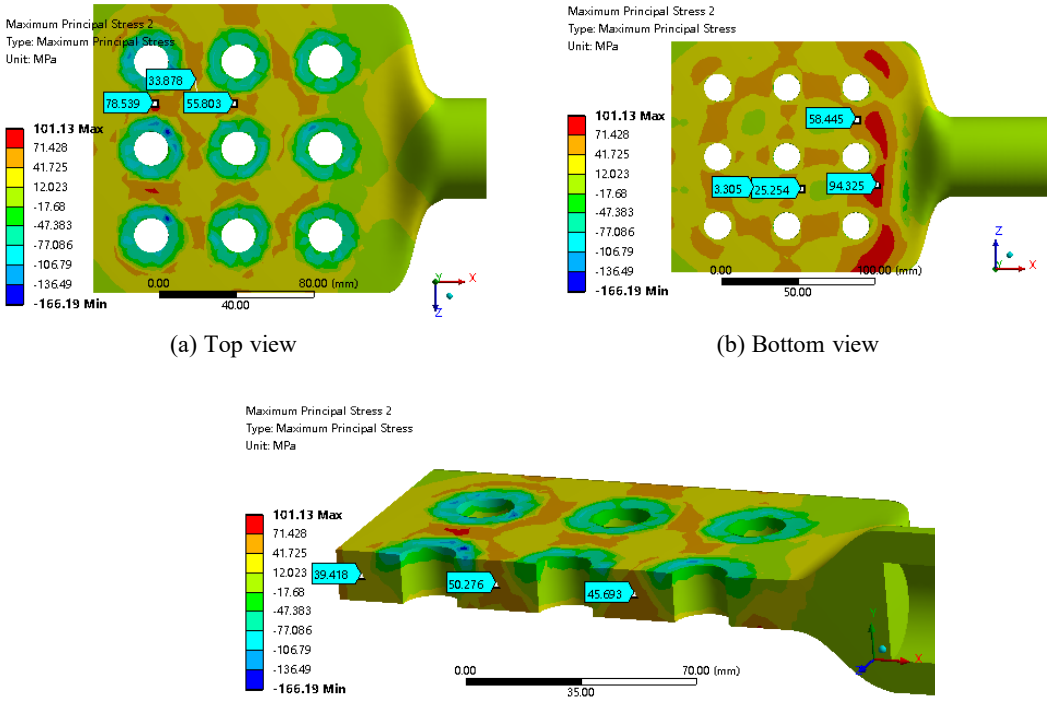


Fig. 6 Indentation observed on the clamp in practical engineering

The yielding of the clamp under bolt preload inevitably affects its load-bearing capacity when subjected to external forces. Therefore, a clamp

connected with high-strength bolts can be regarded as an initially imperfect component. Meanwhile, since localized yielding occurs in the clamp material under preload, and given that the "indentations" observed in practical engineering do not generally impair functionality, it would be unreasonable to regard the clamp as having failed at this stage. Given that in engineering practice clamp failure is typically defined as tensile fracture, the maximum principal stress is analyzed in this study.

As shown in Fig. 7, the majority of the clamp material does not experience tensile yielding under preload. However, because the bolts impose a localized compressive force, internal stress equilibrium leads to the development of tensile stresses in the material between bolt holes. In certain localized regions, these tensile stresses approach or even reach the yield strength. Consequently, if external loads further induce tensile stress in these areas, tensile failure is likely to occur once the tensile strain reaches a critical threshold.



(a) Top view

(b) Bottom view

(c) Section view

Fig. 7 Maximum principal stress contour (MPa)

This phenomenon is clearly observed when extracting and examining the normal stresses on the upper and lower surfaces. Under the bolt preload, the internal stress state of the clamp is highly non-uniform. After examining the stress states at various regions, it is found that at least three distinct stress states exist under preload conditions:

(1) Triaxial compressive state near the bolt holes. The areas at the bolt hole walls and where the clamp directly contacts the bolt washers are subjected to direct compressive forces. By extracting the magnitudes and orientations of the three principal stresses, it is evident that the material near the bolt holes is in a triaxial compressive state. Fig. 8 shows an enlarged sectional view of the stress distribution around the bolt holes.

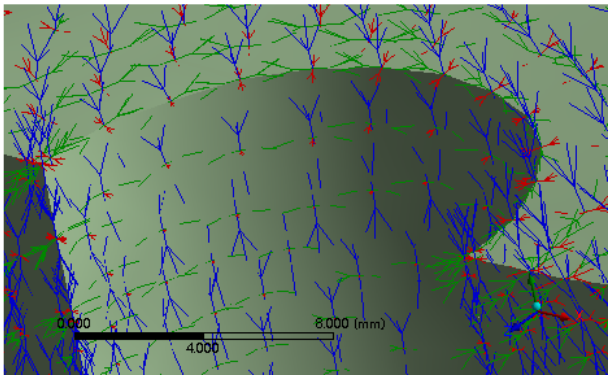


Fig. 8 The stress state near the bolt

(2) Biaxial tensile state on the upper surface. Since bolt preload acts as a localized compressive force, the material located between two adjacent bolt holes is subjected to tensile stresses. Since the upper surface is a free surface with no stress in the normal direction, the stress state in and near this region is characterized as biaxial tension, as shown in Fig. 9.

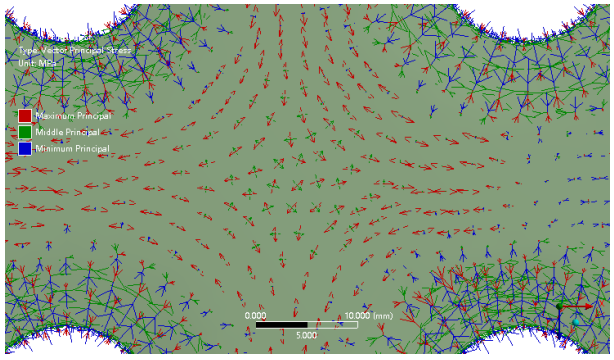


Fig. 9 The upper surface in a state of biaxial tension

(3) Biaxial tensile and uniaxial compressive state on the lower surface. Similar to the upper surface, the region between adjacent bolt holes on the lower surface is also subjected to biaxial tensile stresses. However, unlike the upper surface, the terminal plate transfers the non-uniform compressive force applied by the bolt on the opposite side to the clamp itself. According to Saint-Venant's principle, the non-uniform pressure exerted by the bolt is transmitted through the terminal plate and becomes relatively uniform. As a result, the material near the lower surface exhibits a stress state characterized by biaxial tension and uniaxial compression, as shown in Fig. 10.

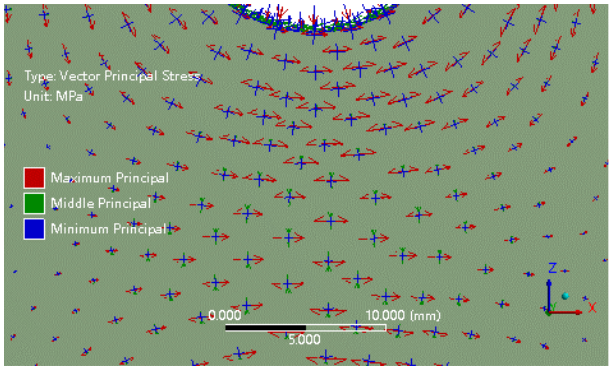


Fig. 10 Local stress state on the lower surface

Although the local stress states vary significantly across the clamp and no single scalar quantity can fully characterize failure in all regions, von Mises stress is adopted in this study as a practical indicator of local yielding in ductile metallic regions, whereas the maximum principal stress is used to identify regions with elevated tensile-fracture tendency under highly non-uniform multiaxial stress states.

4.2. Mechanical performance of terminal equipment under combined loads

Building on the preload analysis in the previous subsection, this part examines representative combined loading conditions that are consistent with actual service states. If the load corresponding to the weakest capacity of a clamp is defined as the "critical load," then, in most cases, the stress distribution and failure mode of the clamp under a single "critical load" are not substantially different from those under complex loading conditions that include the same "critical load" in practical engineering. For typical single-conductor clamps, based on their usage in actual projects and on the deformation patterns observed under bolt preload, the critical action can be regarded as the bending effect generated by the bolt preload and the service-like tensile loads.

For strain clamps, due to their unique structural features, this type of fitting cannot withstand significant bending moment. In line with their actual service conditions, a tensile stress of 35 MPa is applied to the upper conductor-connecting section, while a tensile stress of 1.5 MPa is applied to the lower conductor-connecting section, in order to investigate their mechanical performance. The model and calculation results are shown in Fig. 11 and Fig. 12. Analysis indicates that, aside from stress concentrations caused by bolt preload, the regions of highest stress occur at the midsection of the steel anchor and at the interface between the steel anchor and the main body of the strain clamp. The results further show that at the connection between the steel anchor and the clamp body, stress concentrations develop at the toothed section farthest from the steel ring. According to the sectional stress contour, the internal stress distribution in this region is also non-uniform, with a crescent-shaped low-stress zone appearing on the side away from the steel ring, surrounded by high-stress regions. Similar high-stress regions and corrosion-induced damage at the steel-anchor segment have been reported in field failure analyses of 500 kV transmission-line clamps, underscoring the practical relevance of this critical location [10, 19].

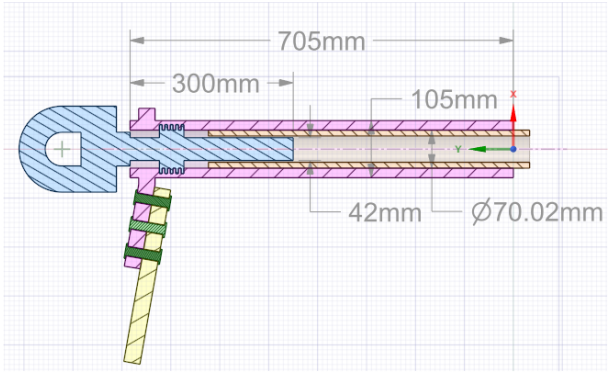
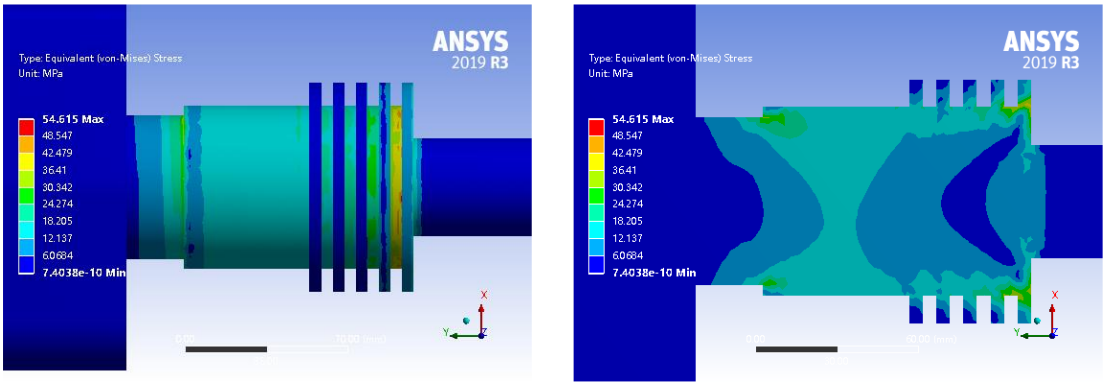


Fig. 11 Partial dimensions of the strain clamp



(a) Side view (b) Section view

Fig. 12 Stress contour of the steel anchor connection (MPa)

Further analysis of the internal stress states reveals that, at the steel anchor connection, the midsection is subjected to tensile stress while the ends are under compression, as shown in Fig. 13. The strain clamp and the steel anchor are joined through a toothed structure, whereby the load is transferred from the main body of the clamp to the steel anchor from the outside inward through the interlocking teeth. Under this load transfer mechanism, a "bulging" effect develops on the side of the connection farthest from the steel ring, which in turn creates an arch-shaped low-stress zone within the material. Since this "arch-shaped" region contains material, the bulging tendency induces compressive stresses in the internal material. Moreover, as both the clamp body and the steel anchor are rotationally symmetric about the central axis, this compressive stress acts three-dimensionally. According to Saint-Venant's principle, the stress state in the steel anchor transitions toward a uniform tensile condition in regions farther from the connection. The spatial transition between these two stress states gives rise to an internal low-stress zone within the steel anchor. Consequently, the most critical regions of the strain clamp in service are the connection between the steel anchor and the clamp body, as well as the contact surface of the clamp body adjoining the anchor. The most vulnerable point lies at the inner side of the outermost toothed section, where the most severe stress concentration occurs. Overall, the most critical stress concentrations in the two types of terminal fittings are located around the bolt-hole region of the equipment clamp and at the steel-anchor–clamp interface of the strain clamp, especially near the inner side of the outermost toothed section. Similar transitions from highly non-uniform local stresses in the vicinity of bolt interfaces to nearly uniform axial tension away from the joint have also been reported in detailed three-dimensional simulations of mechanically preloaded multi-bolt joints, which corroborates the Saint-Venant-type smoothing behavior inferred for the steel anchor region in this study [26, 28].

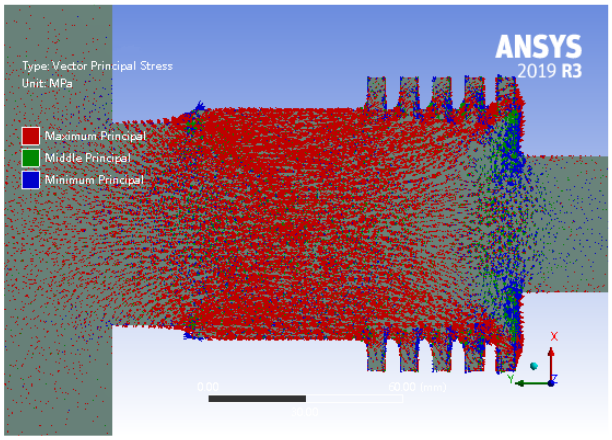


Fig. 13 Stress state at the steel–anchor interface

The global displacement field of the strain clamp under the combined loading condition is obtained from the numerical simulations. To better visualize the deformation pattern, the displacement is magnified 1700 times, as shown in Fig. 14. The results indicate that the maximum displacement occurs near the connection between the steel anchor and the clamp body, while the deformation in the remaining regions is relatively small. This implies that the joint region governs the overall deformation behavior and should therefore be given particular attention in structural design and safety assessment.

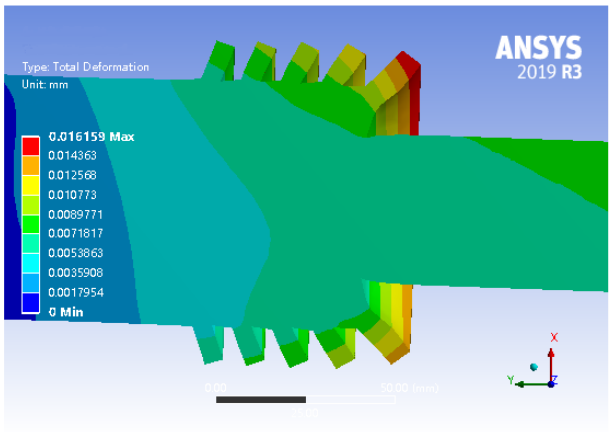


Fig. 14 Displacement state (magnified 1700 times, mm)

5. Conclusions

Based on a three-dimensional finite element analysis of typical terminal equipment used in UHV substations, the following conclusions can be drawn.

(1) The proposed finite element model, which considers elastic-plastic material behavior, contact interactions, and bolt preload, captures mechanical features that are consistent with engineering observations reported in practice, including the highly non-uniform stress distribution and local indentation tendency around bolt holes. The model therefore provides a useful numerical basis for evaluating the mechanical behavior of terminal clamps, although further experimental validation is still needed.

(2) High-strength bolt preload has a dominant influence on the initial state of terminal hardware. Even before external loads are applied, localized plasticity and typical multiaxial stress states form near the bolt holes, meaning that the fittings enter service with pre-existing residual stresses and plastic zones which should be considered in design and assessment.

(3) Under representative combined loading conditions, the stress and deformation of terminal equipment are strongly non-uniform, and the joint regions govern the overall response. Stress and displacement concentrate mainly near the bolt holes, at the tubular–plate junction and at the steel-anchor–clamp interface, which should therefore be regarded as key locations for strength verification and inspection.

(4) For the NY-1600K strain clamp, the most critical region is the steel-anchor–clamp interface and the inner side of the outermost toothed section on the side away from the steel ring, where severe local stress concentration and large deformation occur. This is consistent with reported field failure positions, and suggests that optimizing tooth geometry, increasing effective contact area, controlling assembly preload and enhancing corrosion protection in this region are mechanically motivated measures that may help improve the in-service reliability of such fittings, although their quantitative effectiveness should be verified in future parametric studies.

References

[1] Hwang H. H. M. and Huo J. R., “Seismic fragility analysis of electric substation equipment and structures,” Probabilistic Engineering Mechanics, vol. 13, no. 2, pp. 107–116, 1998
[2] Abomailek C., Riba J., Capelli F., and Moreno-Eguilaz M., “Fast electro-thermal simulation of short-circuit tests,” IET Generation Trans & Dist, vol. 11, no. 8, pp. 2124–2129, 2017.
[3] Angadi S. V., Jackson R. L., Pujar V., and Tushar M. R., “A Comprehensive Review of the Finite Element Modeling of Electrical Connectors Including Their Contacts,” IEEE Transactions on Components, Packaging and Manufacturing Technology, vol. 10, no. 5, pp. 836–844, 2020.
[4] Capelli F., “Development of high-capacity substation connectors compatible with HTLS technology,” Ph.D. Thesis, Universitat Politècnica de Catalunya, 2017.
[5] Capelli F., Riba J.-R., and Pérez J., “Three-Dimensional Finite-Element Analysis of the Short-Time and Peak Withstand Current Tests in Substation Connectors,” Energies, vol. 9, no. 6, p. 418, 2016.
[6] Guan X.Y., Shu N.Q., Kang B., and Zou M.H., “Multiphysics Analysis of Plug-In Connector Under Steady and Short Circuit Conditions,” IEEE Transactions on Components, Packaging and Manufacturing Technology, vol. 5, no. 3, pp. 320–327, 2015.
[7] Hernández-Guiteras J., Riba J.-R., and Romeral L., “Improved design of an extra-high-voltage expansion substation connector through magnetic field analysis,” Simulation Modelling Practice and Theory, vol. 43, pp. 96–105, 2014.
[8] Aydar E., “Surface Defects and Corrosions Developed on Copper Clad Aluminium Wires Investigated by Scanning Electron Microscope Analysis and X-Ray Mappings.,” Acta Microscopica, vol. 31, no. 2, pp. 1–8, 2022.
[9] Karabay S., Ertürk A. T., Zeren M., Yamanoğlu R., and Karakulak E., “Failure analysis of wire-breaks in aluminum conductor production and investigation of early failure reasons for transmission lines,” Engineering Failure Analysis, vol. 83, pp. 47–56, 2018.
[10] Sun M.C., Tan C., Zhang C.Q., Yang C., and Li H.Q., “Analysis of Strain Clamp Failure on 500 kV Transmission Line,” MSCE, vol. 06, no. 04, pp. 47–56, 2018.
[11]Cai X., “Analysis on 500 kV Compact Transmission Line Strain Clamps Fracturing Accident,” North China Electric Power, vol. 3, pp. 36–38, 2003.
[12] Li X.H., Wu H.L., Ding H., and Zhu C.L., “Simulation and failure analysis of strain clamp failed caused by deterioration of contact resistance,” in Recent Advances in Structural Integrity Analysis-Proceedings of the International Congress (APCF/SIF-2014)(Woodhead Publishing, 2014), 2014, pp. 212–217.
[13] Zhao J.K., Zhao J.L., Xu L., Qin J.L., and An K.Y., “Cause Analysis and Preventive Measures for Breaking of Strain Clamp in 500 kV Transmission Line,” in The proceedings of the 16th Annual Conference of China Electrotechnical Society, Singapore: Springer, 2022, pp. 931–940.
[14] Zhang W., Liu Y.S., Li S., and Tang J., “Analysis on the crimping quality of overhead transmission line conductors considering equivalent cross-sectional stiffness,” AIP Advances, vol. 12, no. 10, p. 105321, 2022.
[15] Dong X.C., Qu F.R., Li Y.F., Fang B.L., Wang Y.Q., and Liu G., “Experimental analysis of temperature distribution in high-voltage strain clamp,” in 2018 12th International Conference on the Properties and Applications of Dielectric Materials (ICPADM), May 2018, pp. 829–832.
[16] He W.X., Feng Y., Wu S.L., and Wang W., “Mechanical–Thermal–Electrical Coupling Modeling and Temperature Rise Characteristic of a Parallel Groove Clamp With Improved Representation of Contact Interactions,” IEEE Transactions on Components, Packaging and Manufacturing Technology, vol. 13, no. 3, pp. 356–364, 2023.
[17] Jin Y.A., Quan M.Y., Yan S.J., Yan Y.Y., Cui M., and Liu Y., “Analysis of overhead transmission lines fusing failure due to poor contact between conductors and clamps,” Engineering Failure Analysis, vol. 118, p. 104858, 2020.
[18] Ouyang K.J., Yang X.W., Zhan L., Xie Z.L., Huang J., and Xiao L.H., “Quality test of clamping connection of transmission lines across tensile line,” presented at the Vibroengineering Procedia, EXTRICA, 2018, pp. 156–160.
[19] Liu W.K., Cao X.H., Hu Y.J., Li D., and Xie Y., “Failure Analysis of the Strain Clamp Steel Anchor Corrosion of a 500 kV Transmission Line,” E3S Web of Conferences, vol. 252, 2021.
[20] Ye Z.F., Pang K., Du Y.X., Zhao G.F., Huang S., and Zhang M., “Simulation Analysis of the Tensile Mechanical Properties of a Hydraulic Strain Clamp-Conductor System,” Advances in Materials Science and Engineering, vol. 2020, no. 1, p. 4591812, 2020.
[21] Zhou Y.T., Zhou Z.Q., Wang J.G., Luo H.J., Zhang J., and Hu J.Y., “Study on Cracking of Aluminum Alloy Strain Clamps for 500kV Transmission Line,” Solid State Phenomena, vol. 279, pp. 10–15, 2018.
[22] Tsakmakis C., “Original ArticleKinematic hardening rules in finite plasticity Part I: A constitutive approach,” Continuum Mech Thermodyn, vol. 8, no. 4, pp. 215–231, 1996.
[23] Ministry of Housing and Urban-Rural Development of the People’s Republic of China, Code for Design of Steel Structures (GB 50017-2017). Beijing: China Architecture & Building Press, 2017.
[24] Ministry of Housing and Urban-Rural Development of the People’s Republic of China, Code for Design of Aluminum Alloy Structures (GB 50429-2007). Beijing: China Architecture & Building Press, 2007.
[25] Krolo P., Grandić D., and Bulić M., “The Guidelines for Modelling the Preloading Bolts in the Structural Connection Using Finite Element Methods,” Journal of Computational Engineering, vol. 2016, no. 1, p. 4724312, 2016.
[26] Li B.K., Gong Y., Xiao H., Gao Y.K., and Liang E.Q., “A Two-Dimensional Model for Pin-Load Distribution and Failure Analysis of Composite Bolted Joints,” Materials, vol. 14, no. 13, p. 3646, 2021.
[27] Sarka F., “Modelling possibilities of bolt connections with finite element method,” Design of Machines and Structures, vol. 13, no. 1, pp. 97–107, 2023.
[28] Zhang J.H., Zheng J., Zeng J.J., Yang G., and Tong M.B., “Thermal and Mechanical Stress Analysis in Aircraft Hybrid Panels with Multi-Bolt Joints,” Materials, vol. 17, no. 8, p. 1872, 2024.